Analysis of alkali-treated $Cu(In,Ga)Se_2$ solar cells with numerical simulations and capacitive spectroscopy

Zur Erlangung des akademischen Grades eines

DOKTORS DER INGENIEURWISSENSCHAFTEN

von der KIT-Fakultät für
Elektrotechnik und Informationstechnik
des Karlsruher Instituts für Technologie (KIT)

genehmigte

DISSERTATION

von

M.Sc. Tim Helder
geb. in Donaueschingen

Tag der mündlichen Prüfung:	22.05.2023
Hauptreferent:	Prof. Dr.-Ing. Michael Powalla
Korreferent:	Prof. Dr. rer. nat. Uwe Rau

Erklärung

Ich versichere wahrheitsgemäß, die Dissertation bis auf die dort angegebene Hilfe selbständig angefertigt, alle benutzten Hilfsmittel vollständig und genau angegeben und alles kenntlich gemacht zu haben, was aus Arbeiten anderer und eigenen Veröffentlichungen unverändert oder mit Änderungen entnommen wurde.

Tim Helder

Kurzfassung

Das globale Ziel dieser Arbeit war es, ein präzises digitales Modell einer Cu(In,Ga)Se_2 (CIGS)-Solarzelle aufzubauen. Dazu wurde eine Simulationssoftware entwickelt, die es ermöglicht, grundlegende Charakteristiken des Heteroübergangs abzubilden. Aufbauend auf den fundamentalen Drift-Diffusions Gleichungen wurden die wichtigsten physikalischen Zusammenhänge in die Software implementiert, um eine CIGS-Solarzelle auf der Ebene der Halbleiterphysik zu beschreiben. Dabei sollten die verwendeten Materialparameter möglichst nahe an der Realität liegen. Viele Parameter sind bekannt, eine große Unsicherheit liegt jedoch in der Beschreibung der elektrischen Defekte im CIGS-Halbleiter. Diese führen über Shockley-Read-Hall (SRH)-Rekombination zu dem dominanten Leistungsverlust in der Solarzelle. Im CIGS-Material können diese Defekte eine Vielzahl von möglichen Ursprüngen haben und je nach Prozess oder Beschichtungsanlage unterschiedlich auftreten. Eine genaue Beschreibung im numerischen Modell ist jedoch unabdingbar, um die genauen Verlustmechanismen und die Höhe der Verluste zu spezifizieren.

Für eine genaue und umfassende Kenntnisse über die Defekte im CIGS-Material, wurden CIGS-Schichten aus verschiedenen Anlagen, hergestellt mit unterschiedlichen Prozessarten, untersucht. Dazu wurden innerhalb dieser Arbeit Deep Level Transient Spectroscopy (DLTS)-Messungen für die Verwendung an CIGS Solarzellen angepasst. DLTS stellt eine sehr sensitive Methode dar, Störstellen in Halbleiter-Materialien äußerst exakt zu vermessen. Für genaue und belastbare Messungen wurde eine spezielle Messprozedur entwickelt sowie geeignete Werte der Messparameter identifiziert. Damit wurden schlussendlich die charakteristischen Eigenschaften Defektdichte, energetische Lage, Wirkungsquerschnitt und Defekttyp in den unterschiedlichen Proben bestimmt. Die Ergebnisse konnten dann als Input-Parameter in der Software übernommen werden und so die Defekte auf numerischer Ebene abgebildet werden.

Ein zentraler Punkt dieser Arbeit war es außerdem, mit Hilfe des numerischen Models den Einfluss von Rubidium, das durch ein Rubidiumfluorid (RbF) postdeposition treatment (PDT) Schritt eingebracht wurde, auf die Defekte und deren Eigenschaften zu untersuchen. Dazu wurden im ersten Schritt grundlegende Messungen an vereinfachten CIGS-Proben ohne Bandlücken-Gradienten durchgeführt, die mit unterschiedlichen Alkalielementen behandelt wurden. Dadurch konnten den einzelnen Alkalielementen charakteristische Signaturen in den DLTS-Messungen zugeordnet werden.
Mit dieser Grundlage wurden verschiedene Probenreihen an CIGS-Solarzellen aus einer produktionnahen Inline-Beschichtungsanlage vermessen. Im CIGS-Material konnten zwei signifikante Störstellen (ein Minoritätendefekt und ein Majoritätendefekt) in der Mitte der Bandlücke identifiziert werden, die aufgrund ihrer energetischen Lage, potentielle Rekombinationszentren darstellen. Es konnte nachgewiesen werden, dass eine PDT-Behandlung des CIGS-Materials die Defektdichte des einen Minoritätsdefekts um den Faktor drei reduziert, der Majoritätsdefekt jedoch nicht beeinflusst wird. Dieses unterschiedliche Verhalten konnte auf den räumlichen Ursprung der Defekte zurückgeführt werden. Während der vom PDT beeinflusste Defekt wahrscheinlich an Korngrenzen vorliegt, wo das Rubidium vorzugsweise segregiert, ist der zweite Defekt homogen in der Schicht verteilt. Die experimentellen Ergebnisse wurden in numerischen Simulationen verifiziert und Strategien für weitere Entwicklungsschritte ausgearbeitet.

Aktuell von großem Interesse ist die Entwicklung von (Ag,Cu)(In,Ga)Se_2 (ACIGS)-Solarzellen, bei denen ein Teil des Kupfers durch Silber substituiert wird. In ACIGS-Zellen mit geringem Silberanteil konnten ähnliche Defekte wie im CIGS nachgewiesen werden, einen Einfluss auf diese durch ein RbF-PDT konnte jedoch nicht direkt verifiziert werden. Das ist zum Großteil auf ein starkes Signal von einem Dotierlevel zurückzuführen, dessen energetische Lage und Dichte sich systematisch mit dem Rb-Gehalt erhöhen. Während dieses Signal die DLTS-Messungen der ACIGS-Proben dominiert, ist es in silberfreien CIGS-Proben nicht nachzuweisen. Bei der Untersuchung von ACIGS-Solarzellen wurde jedoch auch ein signifikant unterschiedliches Performance-Verhalten im Vergleich zu (silberfreien) CIGS-Solarzellen beobachtet. Der Grund hierfür liegt in einem geänderten Dotierverhalten und einer parasitären Energiebarriere am CIGS/Puffer Übergang. Auch hier konnten die Effekte durch numerische Simulationen belegt und die Ergebnisse auf weitere Wirkungsgrad Verbesserungen hin untersucht werden.

Diese Ergebnisse zeigen, wie mit Hilfe von numerischen Simulationen und geeigneten Input Daten, digitale Experimente durchgeführt, physikalische Grenzen aufgetan und reale Effekte analysiert werden können. Mit robusten Input Daten können insbesondere die auftretenden Verluste in einer CIGS-Solarzelle bestimmt und somit die experimentelle Forschung und Entwicklung von Dünnschicht Solarzellen unterstützt werden.

Abstract

The global goal of this work was to build an accurate digital model of a Cu(In,Ga)Se_2 (CIGS) solar cell. Therefore, a simulation software was developed which allows to reproduce fundamental characteristics of the heterojunction. Based on the fundamental drift-diffusion equations, the most important physical relations were implemented in the software to describe a CIGS solar cell at the level of semiconductor physics. The material parameters used should be as close as possible to reality. While many parameters are known, a large uncertainty lies in the description of the electrical defects in the CIGS semiconductor. These lead to the most dominant power loss in the solar cell via Shockley-Read-Hall (SRH) recombination. In the CIGS material, these defects can have a variety of possible origins and can occur differently depending on the process or deposition equipment. However, an accurate description in the numerical model is essential to specify the exact loss mechanisms and the magnitude of the single losses.

In order to obtain accurate and comprehensive knowledge about the defects in the CIGS material, CIGS layers from different systems, produced with different types of processes, were investigated. For this purpose, Deep Level Transient Spectroscopy (DLTS) measurements were adapted for the application on CIGS solar cells. DLTS is a very sensitive method to measure defects in semiconductor materials with high accuracy. For accurate and reliable measurements, a special measurement procedure was developed and suitable measurement parameters were identified. With this, finally the characteristic properties defect density, energetic position, capture cross section and type (minority or majority) of the defects in the different samples were determined. The results were then used as input parameters in the software and in this way the defects were reproduced numerically.

A central point of this work was to investigate the influence of rubidium introduced by a rubidium fluoride (RbF)-post-deposition treatment (PDT) step on the defects and their properties by using the developed numerical model. For this purpose, DLTS measurements were performed on simplified CIGS samples which were gradient-free and treated with different single alkali elements in the first step. Thereby, characteristic signatures could be assigned to the individual alkali elements in the DLTS measurements.
On this basis, different series of samples of CIGS solar cells from a production-like inline co-evaporation system were analyzed. In the CIGS material, two significant defects (a minority defect and a majority defect) were identified in the middle of the band gap, which represent potential recombination centers. The minority defect showed a reduction of the defect density by a factor of 3 due to the PDT, while the majority defect was not affected by the PDT. This different behavior could be attributed to the spatial origin of the defects. The defect influenced by the PDT is probably located at grain boundaries, where the Rb mainly segregates. The second defect is homogeneously distributed in the layer. The experimental results were verified by numerical simulations and strategies for further development steps were elaborated.

In (Ag,Cu)(In,Ga)Se_2 (ACIGS) solar cells, where a small amount of copper in CIGS is substituted by silver, similar defects were measured as in CIGS cells, although an influence by a RbF PDT could not be verified directly. This is largely due to a strong signal from a doping level which energetic position and density systematically increase with the Rb content. While this signal dominates

the DLTS measurements of the ACIGS samples, it is not detectable in silver-free CIGS- samples. However, when investigating ACIGS solar cells, a significantly different behavior in performance and defect characteristics in dependence of the Rb amount was observed compared to CIGS solar cells. The reason for this is a change in doping behavior and a detrimental energy barrier at the CIGS / buffer interface. Again, the observed effects were proven by numerical simulations and the results could be investigated for further efficiency improvements.
These results presented in this work demonstrate how numerical simulations and appropriate input data, can be used to perform digital experiments, identify physical limitations, and analyze real-world effects. In particular, by using robust input data, the losses occurring in a CIGS solar cell can be determined, thus supporting experimental research and development.

Preface

Zu allererst möchte ich mich bei Prof. Dr.-Ing. Michael Powalla für die Übernahme der Betreuung meiner Promotion bedanken. Auch vielen Dank an Prof. Dr. rer. nat. Uwe Rau für die Übernahme des Zweitgutachtens.

Vielen Dank an Andreas Bauer und Theresa Magorian Friedlmeier für die direkte Betreuung meiner wissenschaftlichen Arbeit am ZSW. Es war mir immer eine Freude.

Ein ganz spezielles Dankeschön geht an Ana Kanevce für ihre Betreuung, die Klärung unzähliger Fragen zur Halbleiterphysik und nicht zuletzt für die Korrektur meiner Thesis.

Ein sehr großes Dankeschön geht an Mario Zinßer, ohne den die letzten drei Jahre sicherlich ganz anders verlaufen wären. Ich denke, der gegenseitige Austausch hat zu einer extrem produktiven Arbeitsweise von uns beiden geführt und es ist nicht selbstverständlich so einen Kollegen an seiner Seite zu haben.

Vielen Dank auch an das gesamte MAT Team für die Hilfe im Labor, Beantwortung von Fragen und sonstige Unterstützung. Hervorzuheben sind hier Frank Nauerz, der jede meiner Strukturieungsanfragen mitgemacht hat und Tanja Wohnhaas für die Aufnahme der REM Bilder. Danke an Rico und das gesamte CIGS-Präparations Team für die Bearbeitung meiner Experimente.

Ein ganz besonderer Dank geht an meine Familie. An meine Schwester die mich immer unterstützt hat. Und an meine Eltern, ohne deren jahrelange bedingungslose Unterstützung ich nicht an diesen Punkt gekommen wäre.

Zuletzt möchte ich meiner wunderbaren Frau Lisa und meiner genauso wunderbaren Tochter Toni danken, die für mich immer ein Rückzugsort waren und auch die vermeintlich stressigen Zeiten rückblickend sehr schön gemacht haben. Vielen Dank!

Contents

Acronyms and symbols

Acronyms

AAC	Ag/(Ag+Cu)
ACIGS	(Ag,Cu)(In,Ga)Se_2
ACGI	(Ag+Cu)/(Ga+In)
ALD	atomic layer deposition
APT	atom probe tomography
ARC	anti-reflective coating
AZO	aluminum doped zinc oxide
CBD	chemical bath deposition
CBO	conduction band offset
CdS	cadmium sulfide
CGI	Cu/(Ga+In)
CGS	$CuGaSe_2$
CIGS	Cu(In,Ga)Se_2
CIS	$CuInSe_2$
CV	capacitance-voltage
DC	direct current
DFT	density-functional theory
DLTFS	Deep Level Transient Fourier Spectroscopy
DLTS	Deep Level Transient Spectroscopy
DOS	density of states
EMA	effective medium approximation
EQE	external quantum efficiency
FF	fill factor
GB	grain boundary
GDOES	glow discharge optical emission spectroscopy
GGI	Ga/(Ga+In)
GI	grain interior
GUI	graphical user interface
HERA	High Energy Resolution Analysis
IEA	International Energy Agency
IQE	internal quantum efficiency
iZnO	intrinsic zinc oxide
IV	current-voltage
JVT	temperature dependent current-density-voltage
JV	current-density-voltage

KF	potassium fluoride
KIS	$KInSe_2$
MgF_2	magnesium fluoride
MPP	maximum power point
NaF	sodium fluoride
OECD	Organisation for Economic Co-operation and Development
PCE	power conversion efficiency
PDT	post-deposition treatment
PV	photovoltaic
RbF	rubidium fluoride
RDLTS	Reverse DLTS
REF	reverse engineering fitting
RF	radio frequency
RIS	$RbInSe_2$
SCR	space charge region
SE	spectral ellipsometry
SEM	scanning electron microscopy
SLG	soda-lime glass
SNR	signal-to-noise-ratio
SQ	Shockley-Queisser
SRH	Shockley-Read-Hall
SRV	surface recombination velocity
STC	standard testing condition
TCO	transparent conductive oxide
TEM	tunneling electron microscopy
TFPV	thin-film photovoltaic
ToF-SIMS	time of flight secondary ion mass spectroscopy
TMM	transfer-matrix method
VBM	valence band maximum
VRB	van Roosbroeck
ZMO	zinc magnesium oxide
ZnO	zinc oxide
Zn(O,S)	zinc oxide sulfide
ZrO	zirconium oxide
ZSW	Zentrum für Sonnenenergie- und Wasserstoffforschung Baden-Württemberg

Constants

ϵ_0	vacuum permittivity: $8.854\,187\,812\,8{\cdot}10^{-12}\,\mathrm{As/(Vm)}$
h	Planck's constant: $6.626\,070\,15{\cdot}10^{-34}\,\mathrm{Js}$
k_B	Boltzmann constant: $1.38{\cdot}10^{-23}\,\mathrm{m^2Kg/(s^2K)}$

π	Pi: 3.14159...
q	elementary charge: $1.602{\cdot}10^{-19}\,\mathrm{C}$

Latin symbols and variables

A	sample area in m^2
C	capacitance in F
C_n	Auger coefficient electrons in m^6/s
C_p	Auger coefficient holes in m^6/s
C_P	pulse capacitance in F
C_R	reverse capacitance in F
D_n	electron diffusion coefficient in m^2/s
D_p	hole diffusion coefficient in m^2/s
e_n	emission time constants of electrons in $1/\mathrm{s}$
e_p	emission time constants of holes in $1/\mathrm{s}$
E	energy in eV
E_A	acceptor ionization energy in eV
E_D	donor ionization energy in eV
$E_\mathrm{F,n}$	quasi-fermi level electrons in eV
$E_\mathrm{F,p}$	quasi-fermi level holes in eV
E_g	conduction band minimum in eV
E_T	trap energy in eV
E_V	valence band maximum in eV
g_A	acceptor degeneracy factor
g_D	donor degeneracy factor
G	generation rate in $\mathrm{cm}^3\mathrm{s}$
$h_\mathrm{k,l}$	distance between mesh node k and mesh node l in m
I	current in A
I_MPP	maximum power point current in A
I_SC	short circuit current in A
J	current density in A/m^2

J_0	reverse saturation current density in A/m^2
J_{MPP}	current at maximum power point in A/m^2
J_{n}	electron current in A/m^2
J_{p}	hole current in A/m^2
J_{ph}	photocurrent density in A/m^2
J_{SC}	short circuit current density in A/m^2
L_{P}	position of intersection of trap level and fermi level at V_{P} in m
L_{R}	position of intersection of trap level and fermi level at V_{R} in m
m_{e}	effective electron mass in Kg
m_{h}	effective hole mass in Kg
n	electron density in $1/\mathrm{m}^3$
n_{d}	diode ideality factor
n_{D}	donor auxiliary density in $1/\mathrm{m}^3$
n_{ref}	reference electron density in SRH-model in $1/\mathrm{m}^3$
n_{T}	density of traps occupied by electrons in $1/\mathrm{m}^3$
N_{A}^-	acceptor density in $1/\mathrm{m}^3$
N_{C}	conduction band effective density density of states in $1/\mathrm{m}^3$
N_{D}^+	donor density density in $1/\mathrm{m}^3$
N_{IF}	interface trap density in $1/\mathrm{m}^2$
N_{intr}	intrinsic carrier density in $1/\mathrm{m}^3$
N_{T}	trap density in $1/\mathrm{m}^3$
N_{V}	valence band effective density density of states in $1/\mathrm{m}^3$
p	hole density in $1/\mathrm{m}^3$
p_{A}	acceptor auxiliary density in $1/\mathrm{m}^3$
p_{ref}	reference hole density in SRH-model in $1/\mathrm{m}^3$
p_{T}	density of traps occupied by holes in $1/\mathrm{m}^3$
P_{MPP}	power at maximum power point in W
r	recombination coefficient in m^3/s
r_{Auger}	Auger recombination coefficient in m^3/s
r_{rad}	radiative recombination coefficient in m^3/s

r_{SRH}	SRH recombination coefficient in m^3/s
r_{s}	area-normalized series resistance in $\Omega\mathrm{m}^2$
r_{sh}	area-normalized shunt resistance in $\Omega\mathrm{m}^2$
R	recombination rate in $\mathrm{m}^3\mathrm{s}$
R_{Auger}	Auger recombination rate in $\mathrm{m}^3\mathrm{s}$
R_{IF}	interface recombination rate in $\mathrm{m}^3\mathrm{s}$
R_{rad}	radiative recombination rate in $\mathrm{m}^3\mathrm{s}$
R_{SRH}	SRH recombination rate in $\mathrm{m}^3\mathrm{s}$
S_{n}	electron surface/interface recombination velocity in m/s
S_{p}	hole surface/interface recombination velocity in m/s
T	temperature in K
t	time in s
t_0	waiting time in s
t_{P}	pulse width in s
t_{W}	time window in s
U_{T}	thermal voltage in V
V	voltage in V
V_{bi}	built-in potential in V
V_{MPP}	maximum power point voltage in V
V_{OC}	open circuit voltage in V
V_{P}	pulse voltage in V
V_{R}	reverse voltage in V
W	space charge region width in m
W_{R}	space charge region width under reverse bias in m

Greek symbols and variables

ϵ_{r}	dielectric permittivity
μ_{n}	electron mobility in $\mathrm{m}^2/(\mathrm{V}\,\mathrm{s})$
μ_{p}	hole mobility in $\mathrm{m}^2/(\mathrm{V}\,\mathrm{s})$
ν_{n}	electron thermal velocity in m/s

ν_p	hole thermal velocity in $\mathrm{m/s}$
ρ	charge density in $\mathrm{C/m^3}$
σ_e	electron capture cross section in $\mathrm{m^2}$
σ_h	hole capture cross section in $\mathrm{m^2}$
τ_n	electron lifetime in s
τ_p	hole lifetime in s
ϕ_BB	spectral intensity of a black body spectrum in $1/(\mathrm{m^2 s\,eV})$
ϕ_el	electrical potential in V
φ_n	electron quasi-Fermi potential in V
φ_p	hole quasi-Fermi potential in V
ϕ_sun	spectral intensity of the Am1.5G solar spectrum in $1/(\mathrm{m^2 s\,eV})$
χ	chemical potential in eV
ω_k	size of mesh node k in m

1 Introduction

These sentences were written exactly 10 months after Russia started its illegitimate war of aggression against Ukraine. As a result, Europe and a large part of the rest of the world have been pushed from a pandemic crisis into an energy and economic crisis. Prices for heat, electricity, mobility and even food increased massively. It has been once again made clear and called into people's minds what should have long been a social consensus. Namely, that the German, European and worldwide energy industry is still too heavily based on the combustion of fossil fuels. The share of renewable energies in electricity production in the Organisation for Economic Co-operation and Development (OECD) countries was just below $30\,\%$ [1]. In Germany, the share was just under $50\,\%$ [2], which shows that in many other parts of the world the expansion of renewable energies is significantly behind and must be massively accelerated, both in electricity production and in the heat sector. The International Energy Agency (IEA) indicates a global increase in renewables of $3.78\,\mathrm{TW}$ needed over the next five years to meet the NetZero scenario by 2050 [3]. An important pillar in this transition is the expansion of photovoltaic (PV) technologies [4]. Several countries and regions have released programs for the expansion of renewables, with PV playing an essential role, like the U.S. inflation reduction act, China's 14-years plan or the REPowerEU plan [5, 3, 6].

Based on these programs, it is obvious that the expansion of photovoltaics will be pushed forward tremendously. Currently, the predominant technology is silicon wafer-based PV, which accounts for a large part of the installed PV capacity [7]. However, thin-film photovoltaic (TFPV) has several advantages compared to wafer-based silicon PV: First, the use of flexible substrates is possible [8]. In addition, the amount of material used is very low, since the layers are very thin in the µm range. This also means that the energy payback time is very low, which is achieved by using efficient and energy-saving coating methods [9, 10]. An example of such a thin film technology is Cu(In,Ga)Se_2 (CIGS) photovoltaics. This technology has already reached market maturity and various manufacturers are selling CIGS thin film modules commercially [11, 12, 13]. Despite the great progress made in recent years, there is still a great need to further increase efficiencies, production costs and the carbon dioxide footprint of the production to keep pace with silicon photovoltaics. However, before a technology can be applied to a module or production, it must be developed on a smaller scale in the laboratory. One way to accelerate the development, besides experimental work, is the use of numerical simulations. They allow not only to reproduce experimental data, but also to make predictions and simulate experiments on the computer with relatively little effort.

Therefore the main goal of this thesis was to build an accurate numerical model of a CIGS heterojunction in order to support the process development. Herein, the semiconductor properties of the used materials have to be known in detail in order to build up an exact model. Since the numerical simulations show that the recombination of charge carriers at electrical defects is one of the largest losses in CIGS solar cells, the exact knowledge of the defect properties in the CIGS material is of highest importance. With the reproduction of the defects in the numerical simulation it is possible to analyze the recombination mechanisms within the heterojunction precisely, quantify the corresponding losses and to develop strategies to reduce this loss.

For this purpose, a measurement procedure was developed within this thesis to measure the defects in the CIGS material with Deep Level Transient Spectroscopy (DLTS). DLTS is a capacitive method, which allows to measure the defect properties very precisely [14]. Since defects in CIGS can have a variety of origins, CIGS layers from different deposition systems investigated in terms of the inherent defects. In the combination of these DLTS measurements and numerical simulations, dominant defects in the CIGS material can be measured, the influence of a so-called PDT step on these can be shown, and the measurements can be reproduced in the simulation. Furthermore, an outlook on the development could be given, which can be expected for further improvements of the cells.

The work is structured as follows: First, the fundamentals of CIGS solar cells are briefly presented in Chapter 2. An upper efficiency limit is introduced and loss mechanisms in the cell that lead to this limit not being reached are discussed. Strategies used to reduce such losses are also discussed. The chapter also gives a brief overview of the samples used in this thesis and the characterization methods are described. Then, the methodology of the self-written simulation software is presented in Chapter 3 and the allocation of losses in CIGS solar cells is explained. Herein the fundamental problem of the Shockley-Read-Hall (SRH) recombination as dominant loss in CIGS solar cells is addressed. The DLTS method is discussed in an own section in Chapter 4, as it was a central point of this thesis. A detailed example of how to build a simulation model, use the results from DLTS measurements as input data for the simulation and interpret the data is given in Chapter 5. Chapter 6 discusses fundamental DLTS measurements on gradient-free samples with different alkali elements. These measurements can be considered as baseline measurements of the following chapters. In Chapter 7, the influence of a RbF-PDT step on the defects measured by DLTS in a CIGS layer from a fabrication-like system is shown and the results are reproduced in simulation. In Chapter 8, one step further is taken and the effect of RbF-PDT on the ACIGS solar cell is more systematically investigated. Again, the measurements are supported by simulations. Finally, the work and its results are summarized in Chapter 9.

2 Fundamentals of Cu(In,Ga)Se_2 Solar Cells

This chapter gives an overview of the basic physics of Cu(In,Ga)Se_2 (CIGS) solar cells. It starts with the basic operation principle in Section 2.1, introduces a theoretical thermodynamic efficiency limit in Section 2.2 and describes possible loss mechanisms in solar cells in Section 2.3. Section 2.4 summarizes strategies to reduce the corresponding power losses. In Section 2.5, the different sample types, used in this work are described. lastly, in Section 2.6 all used characterization techniques are described.

2.1 Basic Operation Principle of CIGS Solar Cells

CIGS solar cells are a thin film photovoltaic (PV) technology, with an active material containing Cu, Ga, In and Se (sometimes Sulfur) building a chalcopyrite crystal structure [15]. Due to the direct band gap of CIGS, providing a high absorption coefficient, layer thicknesses of 2 to $3\,\mu\mathrm{m}$ are sufficient for the (almost) complete absorption of light. The CIGS layer is deposited on a (commonly) Molybdenum (Mo) coated substrate, which can be glass or a flexible material like polyamide or steel-foil [16, 17]. The Mo layer serves as back contact for the charge extraction. The pn-junction is build with a thin film of a buffer material deposited on top of the CIGS layer. The most common material is CdS, but also Cd-free materials are used, like zinc oxide sulfide (Zn(O,S)) [18]. The layerstack is completed with two subsequent deposited transparent conductive oxide (TCO) layers, shown in Figure 2.1 (A). The intrinsic zinc oxide (iZnO) supports the formation of the pn-heterojunction and is simultaneously a protection against sputter damages due to the subsequent layer of aluminum doped zinc oxide (AZO). The AZO serves as n-contact for the charge extraction.
Since, the n-type doping of cadmium sulfide (CdS) or other buffer materials usually is significantly higher, and the energetic bands are different to the CIGS bands, the junction can be described as a pn^+-heterojunction. The heterointerface between CdS and CIGS reveals a typical spike conduction band offset (CBO), like illustrated in the band diagram in Figure 2.1 (B) for the unbiased and dark case.
Incident photons with energies higher than the band gap energy of the CIGS are absorbed and create electron-hole pairs by exciting an electron from the valence band into the conduction band. From this point the charge carriers will diffuse to regions of lower concentrations (electrons towards the p-doped region and holes towards the n-doped region). Nevertheless, a second force drives the carriers into the opposite direction. Due to the absorption of photons and the corresponding excitation of charge carriers, the electrochemical potentials of electrons and holes have been changed. The gradient of these electrochemical potentials is the driving force of the drift current, separating the charge carries. The superposition of drift and diffusion can be solved exactly using the equations introduced in Chapter 3, resulting in an electrical current flow, which can be extracted from the device.

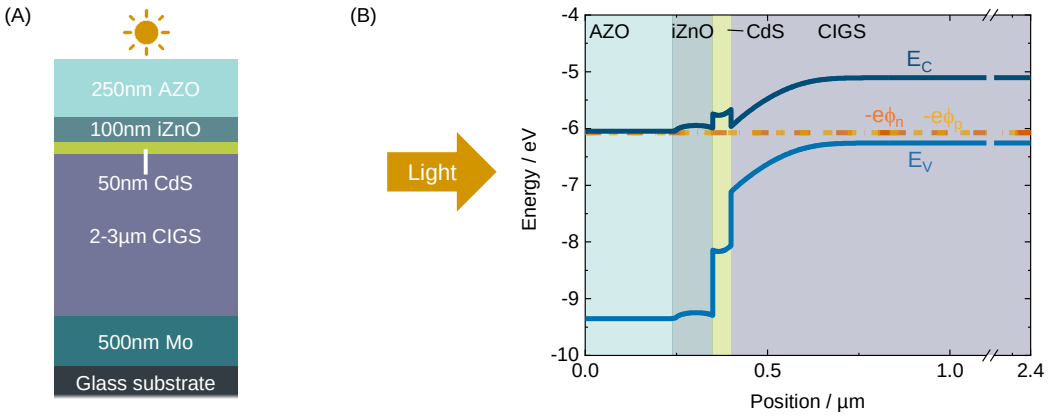

Figure 2.1: (A) Representative layer stack of a CIGS thin film solar cell and (B) the corresponding energy band diagram.

A JV-curve of a solar cell device can be obtained by changing the applied voltage (and therefore the load resistance). The resulting curve can be described (within limits) by the one diode model with following characteristic:

$$J(V) = -J_{\mathrm{ph}} + J_0 \left(exp\left(\frac{q(V - J(V)r_{\mathrm{s}})}{n_{\mathrm{d}} k_{\mathrm{B}} T} \right) - 1 \right) + \frac{V - J(V)r_{\mathrm{s}}}{r_{\mathrm{sh}}} \tag{2.1}$$

with the photocurrent density J_{ph}, the reverse saturation current density J_0, the charge of an electron q, the ideality factor n_{d}, the Boltzmann constant k_{B} and the temperature T. The series resistance r_{s} and the shunt resistance r_{sh} are zero and infinity, respectively, in the ideal case and can be neglected on the material level. With this assumption, the diode equation for the semiconductor pn-junction (without resistive effects) can be obtained:

$$J(V) = -J_{\mathrm{ph}} + J_0 \left(exp\left(\frac{qV}{n_{\mathrm{d}} k_{\mathrm{B}} T} \right) - 1 \right) \tag{2.2}$$

From this characteristic, the prominent solar cell parameters short circuit current density J_{SC}, open circuit voltage V_{OC} and fill factor (FF) can be derived: The J_{SC} is defined as the negative current density at zero voltage. The V_{OC} is defined as the voltage of zero current. The maximum power point (MPP) is defined by the voltage V_{MPP}, where the power (density) gets maximum, defined by the product $P_{\mathrm{MPP}} = V_{\mathrm{MPP}} \cdot J_{\mathrm{MPP}}$. From the MPP the FF is determined the ratio [19, 15]:

$$FF = \frac{V_{\mathrm{MPP}} \cdot J_{\mathrm{MPP}}}{V_{\mathrm{OC}} \cdot J_{\mathrm{SC}}}. \tag{2.3}$$

The power conversion efficiency (PCE) is defined as the ratio between the maximum generated power and the incident radiative power of the AM1.5G solar spectrum at standard testing condition (STC) (P_{In}):

$$PCE = \frac{P_{\mathrm{MPP}}}{P_{\mathrm{In}}} = \frac{V_{\mathrm{MPP}} \cdot I_{\mathrm{MPP}}}{P_{\mathrm{In}}} = \frac{FF \cdot V_{\mathrm{OC}} \cdot I_{\mathrm{SC}}}{P_{\mathrm{In}}} \tag{2.4}$$

A nonuniform elementary composition is a common practice, resulting in a Ga/(Ga+In) (GGI) grading, often in from of a double grading with increasing band gap towards the back contact and

towards the CdS interface. The band gap is dependent on the composition, where an increase of the Gallium fraction (increasing GGI) leads to an increased band gap, like described in literature [20, 21, 22]. This band gap engineering has several advantages like reduced back contact recombination, improved V_{OC} and better band alignments between the CIGS absorber and the buffer layer [23, 21, 24]. Due to the graded band gap a definition of the band gap of the device is not straightforward. Often an approach suggested by Kirchartz et al. is used, by taking the inflection point of the photovoltaic quantum efficiency [25].

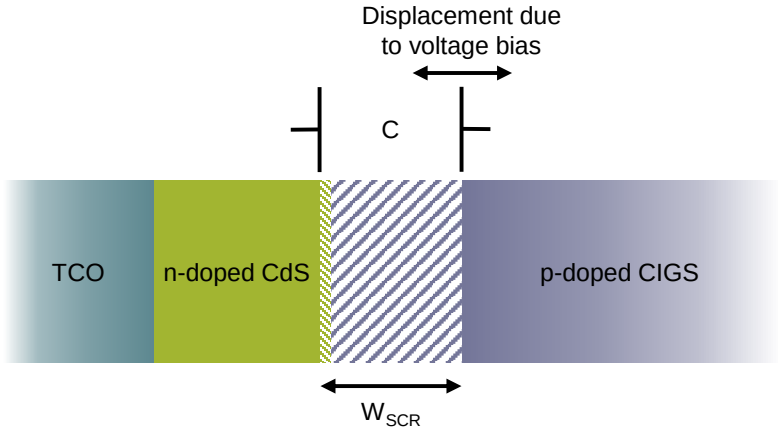

Figure 2.2: Schematic Illustration of the SCR at the heterojunction. The capacitance C can be described by assuming a capacitor with the SCR edges as plates with the distance W_{SCR}. Due to an external bias, the position of the edges are shifting

Besides the current-density-voltage (JV) characteristic of a solar cell or a pn-junction, the capacitance-voltage (CV) characteristic is of great interest in device characterization. In general, the capacitance C of a CIGS solar cell device is defined by the capacitance of the pn-junction and can be described equivalent to the capacitance of a simple plate capacitor, where the edges of the space charge region (SCR) correspond to the plates [26]:

$$C = \frac{\epsilon_0 \epsilon_{\mathrm{r}} A}{W} \tag{2.5}$$

with the dielectric permittivity ϵ_0, the material permittivity ϵ_{r}, the size A of the sample and the width of the space charge region W. The principle idea is illustrated in Figure 2.2. Due to the difference in doping of the highly doped CdS and the moderately doped CIGS layer, the SCR is mainly located in the CIGS layer (indicated by the large shaded region in the CIGS layer and the small shaded region in the CdS layer). The exact location of the SCR edges depent on the doping of both materials and on the external voltage V_{ext}. Therefore the width of the SCR follows:

$$W(V_{\mathrm{ext}}) = \sqrt{\frac{2\epsilon_0 \epsilon_{\mathrm{r}}}{q} \left(\frac{1}{N_{\mathrm{A}}^-} + \frac{1}{N_{\mathrm{D}}^+} \right) \cdot (V_{\mathrm{bi}} - V_{\mathrm{ext}})} \,. \tag{2.6}$$

Herein q is the elementary charge, N_{A}^- and N_{D}^+ are the density of acceptor and donor dopants, respectively an U_{bi} is the build-in potential of the diode [26]. Again, due to the difference in doping of both participating materials, only the SCR edge within the CIGS layer is displaced by an external voltage. This displacement due to a bias voltage, can be used to determine the doping density of the CIGS layer. Therefore, the capacitance of the solar cell is measured for different bias voltages.

By rearranging Equations 2.5 and 2.6 and assume an effective p-doping of the CIGS layer (only N_{A}^{-}), following relation can be obtained [14]:

$$\left(\frac{A}{C}\right)^2 = \frac{2\left(V_{\mathrm{bi}} - V_{\mathrm{ext}}\right)}{q\epsilon_0\epsilon_{\mathrm{r}}N_{\mathrm{A}}^{-}} \tag{2.7}$$

Plotting $(A/C)^2$ against V_{ext} gives a straight line (in the ideal case, without pertubating influence of deep defects or secondary pn-junctions and uniform doping profiles).The slope of the line relates to the doping density N_{A}^{-} and the interception with the voltage axis corresponds to V_{bi}

2.2 Theoretical Efficiency Limit of CIGS Solar Cells

A first approach of a fundamental efficiency limit can be defined by the Shockley-Queisser (SQ) limit, taking into account the unavoidable losses of solar cells. The SQ limit is a thermodynamic limit, predicting the maximum achievable efficiency in dependence of the absorber band gap. Herein following assumption are made [27, 28]:

- Only photons with energies larger than absorber band gap are absorbed, according to a step-like absorption profile with absorptance being 1 above the band gap E_{g} and 0 below.
- For each absorbed photon one electron-hole pair is created.
- Herein only the band gap energy can be used and the excess energy is lost due to thermalization.
- The solar cell with a temperature $300\,\mathrm{K}$ emitts radiation by itself due to radiative recombination, which is the only type of recombination, following Planck's law [29].
- The carrier temperature is equal to the cell and ambient temperature.
- The contacts for charge extraction are perfectly selective, no ohmic losses occur.

From these assumptions, the J_{SC} can be directly calculated via the integral over the photon Eneregy E [25]:

$$J_{\mathrm{SC,SQ}} = q\int_{E_{\mathrm{g}}}^{\infty}\phi_{\mathrm{sun}}(E)dE \tag{2.8}$$

and the dark saturation current is given by the integral over the black body radiation ϕ_{BB}:

$$J_{0,\mathrm{SQ}} = q\int_{E_{\mathrm{g}}}^{\infty}\phi_{\mathrm{BB}}(E, T = 300K)dE \tag{2.9}$$

The Shockley-Queisser current-voltage curve then follows the equation

$$J = J_{0,\mathrm{SQ}}\left(exp\left(\frac{qV}{k_{\mathrm{B}}T}\right) - 1\right) - J_{\mathrm{SC,SQ}} \tag{2.10}$$

The exponential term results from the voltage dependent emission due to radiative recombination within the solar cell. In order to calculate the corresponding PCE, one has to divide the maximum extracted power $P_{\mathrm{max}} = -J(V_{\mathrm{max}})V_{\mathrm{max}}$ by the incoming power density:

$$PCE_{\mathrm{SQ}}(E) = \frac{P_{\max}}{\int_0^\infty E\phi_{\mathrm{sun}}(E)dE} \tag{2.11}$$

The resulting efficiency over the band gap is illustrated in Figure 2.3, revealing a double maximum at $1.2\,\mathrm{eV}$ and $1.4\,\mathrm{eV}$ with efficiencies about $33\,\%$. Additionally, the band gap region of CIGS, which is possible due to adjusting the GGI ratio is shown in green. This region fits very well to the maximum of the SQ curve, showing the potential of CIGS solar cells.

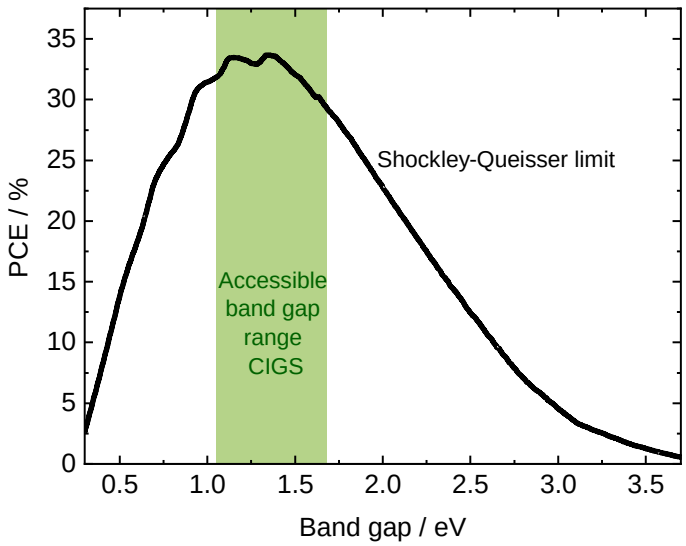

Figure 2.3: Calculated SQ limit in dependence of the band gap for the AM1.5G spectrum.

2.3 Loss Mechanisms in CIGS Solar Cells

In addition to the fundamental and unavoidable losses discussed in the previous section, other technological and avoidable losses occur in thin-film solar cells. This section gives an overview of the most prominent loss mechanisms in CIGS solar cells. Herein the text is limited to those mechanisms which are considered in the numerical simulations, as well. Resistive losses, shading losses due to metallization grids and shunting effects are not considered. Figure 2.4 gives an illustration of the losses, following the path of light. In the following, the occurring losses are divided into optical and electrical losses.

2.3.1 Optical Losses

The optical losses on material level can be divided into three parts: reflectance loss, absorption loss and transmittance loss. The reflectance loss occurs at every material interface with different refractive indices. The resulting reflectance is influenced by the whole layerstack and can be calculated by analytical approaches like the transfer-matrix method (TMM). A common strategy to minimize reflectance losses is the evaporation of an anti-reflective coating (ARC) layer on top of the layer stack, containing of a transparent material with a suitable refractive index. In the CIGS research, a standard ARC material is magnesium fluoride (MgF_2).

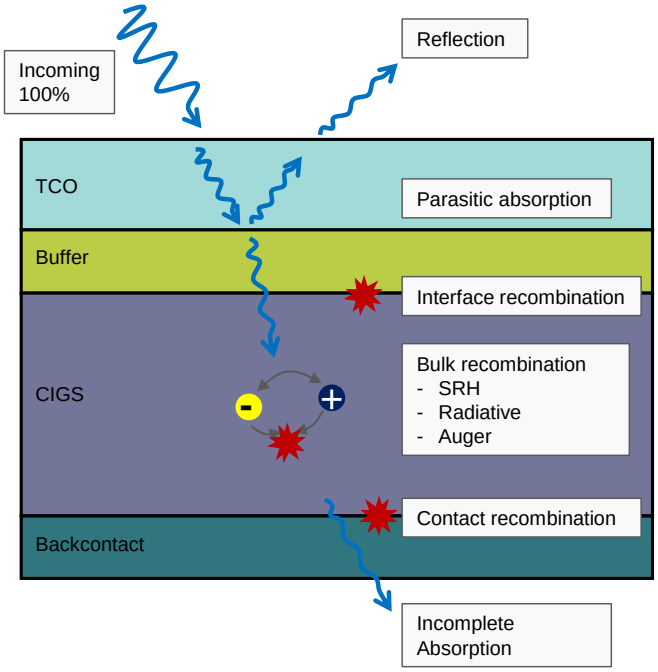

Figure 2.4: Illustrated of possible (and in the simulation considered) losses in CIGS solar cells on the material level.

The (parasitic) absorption takes place in layers before the actual active CIGS layer, absorbing a part of the incident light before it enters the CIGS. This part of the light is lost for the creation of electron hole pairs in the absorber layer. For thick, incoherent layers like glass substrates or encapsulating materials, the absorption loss is calculated via the Lambert-Beer law. For layerstacks, containing of thin layers in the range of the wavelength of the incident light, the absorptance have to be treated with methods like TMM in order to account for thin film interferences.
Lastly, the incomplete absorption or transmittance, denotes that part of light, which is not absorbed by the CIGS. This can be for example, due to an absorber thickness being to small.

2.3.2 Electrical Losses

The electrical losses on the material level are only due to recombination processes. The most prominent loss mechanism herein, is the **Shockley-Read-Hall (SRH) recombination** via defects, resulting in reduced carrier lifetimes and therefore reduced performance. The basic equation of the recombination rate is given by [30]:

$$R_{\mathrm{SRH}} = \frac{np - N_{\mathrm{intr}}^2}{\tau_{\mathrm{p}}(n + n_{\mathrm{ref}}) + \tau_{\mathrm{n}}(p + p_{\mathrm{ref}})} \tag{2.12}$$

and is discussed in more detail within Section 3.2.5 of the numerical implementation of the SRH recombination. The SRH recombination process is a two-step process, where an electron from the conduction band and a hole from the valence band are captured by a defect. Figure 2.5 shows the four possible processes of electron capture (1), electron emission (2), hole capture (3) and hole emission (4). Two capture processes (of an electron and a hole) result in a recombination of the charge carriers [30].

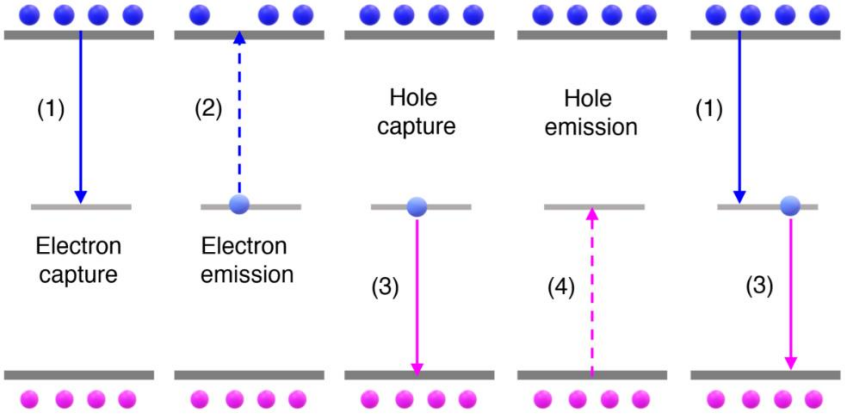

Figure 2.5: Within the SRH statistics four different states are considered. Process (1) is the capture of an electron by a defect state, process (2) the corresponding emission. Process (3) and (4) are hole capture and emission, respectively. A recombination event of an electron and a hole is the combination of two subsequent capture processes, shown on the right. Taken from [30]

The probability for a recombination process, and therefore the recombination rate is depending on the fundamental quantities of a defect: the energetic position within the band gap, the defect density and the capture cross section of electrons and holes. Depending on the energetic position within the band gap of the material, a defect is either defined as a shallow defect or a deep defect. Shallow defects (near the bands $E_\mathrm{T} - E_\mathrm{V} \lesssim k_\mathrm{B}T$) may slow down the carrier transport (by trapping and releasing) or can even contribute to the effective doping. Deep defects ($E_\mathrm{T} - E_\mathrm{V} > k_\mathrm{B}T$) capture carriers from the band and, due to the energetic distance to the bands, the probability for an excitation into the band is fairly low [30, 31].

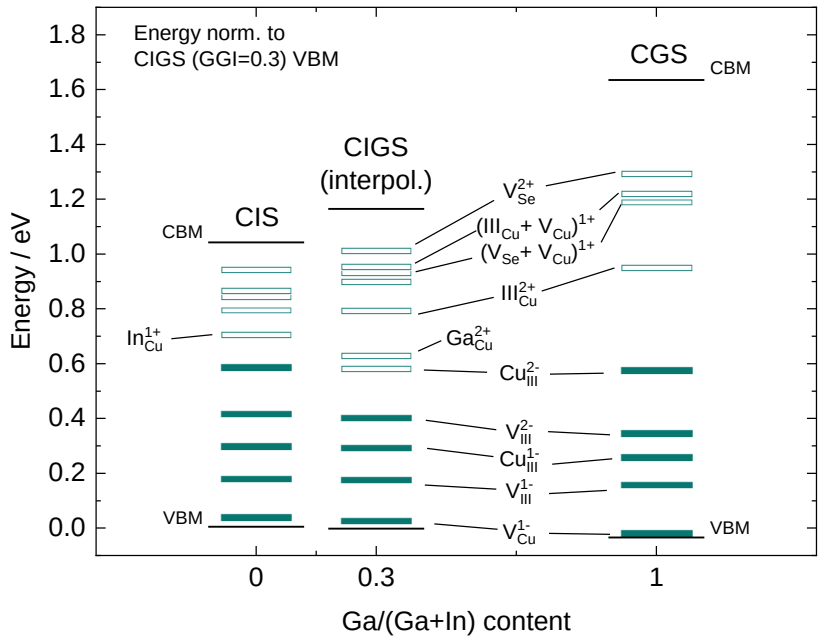

Figure 2.6: Defect levels in $CuInSe_2$ (CIS) and $CuGaSe_2$ (CGS) calculated by density-functional theory (DFT) simulations and interpolated defects levels for CIGS with GGI = 0.3. "III" indicates a group III element with In for CIS, Ga for CGS and either In or Ga for CIGS. The illustration is adapted from [32], data are taken from Wei et al. [33] and Zhang et al. [34]

Defects in CIGS absorber materials can have a variety of origins, due to the polycrystalline nature of the material and the stoichiometric variations[35]. Typical types of defects are vacancies (e.g. Cu vacancies $\mathrm{V_{Cu}}$, which are partly responsible for the p-type doping in CIGS solar cells [36]), interstitial atoms in the host crystal lattice, atom substitutions (e.g. an In atom on a Cu position $\mathrm{In_{Cu}}$ [22]), stacking faults or edge dislocations [26]. Furthermore, in CIGS defect complexes like the $(\mathrm{V_{Se}} + \mathrm{V_{Cu}})$ or $(2\mathrm{V_{Cu}^{-}} + \mathrm{In_{Cu}^{2+}})$ have been observed [37, 38, 34]. Figure 2.6 gives and overview of calculated defects level in CIS and CGS [33, 34]. Additionally the interpolated defect levels of CIGS with a GGI of 0.3 are shown [32].

Further bulk recombination mechanisms are the radiative and the Auger recombination. The **radiative recombination** is a fundamental recombination process. Although it is already considered in the SQ theory, an "extra" radiative recombination takes place due to a radiative recombination coefficient which does not equal the corresponding coefficient of a black body and due to non-step-like absorptance profiles [25].
The **Auger recombination** is getting more important for highly doped semiconductors like in silicon solar cells [39]. The Auger recombination is a three particle process, where an electron in the conduction band gives it's energy to another electron in the conduction band and recombines with a hole in the valance band. The second electron afterwards gets back to the conduction band edge by thermalization [40].

Furthermore, recombination can take place at interfaces and surfaces. The **surface recombination** is often assigned to the recombination due to dangling bonds at semiconductor surfaces. In the numerical modelling of semiconductor devices, the surface recombination is commonly described via the the surface recombination velocity (SRV) of electrons and holes at the contacts of the device and is used as a boundary condition for the simulation [41].
In this thesis, surface and interface recombination are distinguished, where **interface recombination** is defined as a recombination at interfaces within the device and not at terminating surfaces like contacts. The interface recombination can be described by the SRH recombination as well, with the difference, that the trap density is in units of $\mathrm{cm^{-2}}$ instead of $\mathrm{cm^{-3}}$ like for the bulk recombination. Technologically, both, the surface and interface recombination can be reduced by suitable passivation strategies [42].

2.4 Pathways to Improve the Efficiency

This section discusses two main approaches in CIGS deposition to improve the performance. First, the role of alkali elements is discussed. Herein a special focus lies on the effect of alkali-post-deposition treatment (PDT) processes. In the second part the improvements due to the addition of silver to the CIGS alloying are discussed. Next to these strategies, other improvement strategies have been developed within the last decades, like the accurate control of the Ga-content of the CIGS layer and the corresponding development of the so called double grading of the CIGS band gap towards the CdS layer and the back contact. In order to reduce the optical reflection losses of a device, a common improvement strategy is the application of an anti-reflection coatings [15]. Due to the scientific relevance, this section is limited to the discussion of alkali elements in CIGS layers and the alloying with silver.

2.4.1 Alkalis in CIGS

Alkali elements play an important role in CIGS solar cells, since the unintentional incorporation of sodium in the CIGS layer lead to an improvement of the cell performance [43]. This diffusion of Na into the CIGS is nowadays utilized in the preparation of the devices, or is replaced by more controllable methods like a PDT step or a precursor approaches [44]. Independent of the method of introducing Na into the CIGS layer, the sodium in the CIGS increases the hole concentration. Although the exact doping mechanism is still an ongoing discussion, it is assumed, that the formation of $\mathrm{Na_{In}}$ and $\mathrm{Na_{Cu}}$ plays a decisive role [45, 46]. Furthermore, the main part of the incorporated sodium is found at grain boundaries (GB) and interfaces. The amount of sodium in the grain interiors (GIs) and the amount of sodium at the GBs depends strongly on the Cu/(Ga+In) (CGI) ratio of the CIGS [47, 48].
This situation can even change, if some additional alkali elements are introduced into the CIGS layer. In all of the recent world records of CIGS solar cells, a PDT step with alkali-fluorides of heavy alkali elements like potassium, rubidium or cesium have been applied in addition to the Na incorporation [49, 50, 51]. Also the introduction of heavy alkali elements can increase the doping density [52, 53, 54, 55] with a beneficial effect on V_{OC}. Herein, an exchange mechanism with Na atoms plays an important role, where the Na is pushed into the grains or towards the surface. The replacement by the secondary alkali leads to a reduction of the overall sodium concentration in the layer [53, 56, 54, 57]. Since heavier alkalies more unlikely diffuse into the GIs, they rather segregate at the grain boundarys (GBs) [58]. This was confirmed by different experimental measurements like atom probe tomography (APT) [59, 60, 61]. Furthermore, it is assumed that additional alkali elements can reduce the recombination at GBs by the passivation of defects [62, 52, 63, 55, 64]. Again, the exact mechanisms can depend on the stoichiometry of the CIGS.
In addition, PDT steps can induce the formation of secondary phases like $\mathrm{KInSe_2}$ (KIS) or $\mathrm{RbInSe_2}$ (RIS) on the Cu- and Ga-depleted CIGS surface [57, 65, 66, 67, 68]. Theoretical calculations revealed, that the formation enthalpy of a $\mathrm{AInSe_2}$ phase with A = Na, K, Rb and Cs is the lowest for all possible secondary phases [58]. Lepitit et al. suggested following mechanism: the alkali atoms occupy copper vacancies and Cu-sites and push copper into the layer. At the same time, Ga diffuses to the CIGS surface and forms $\mathrm{GaF_3}$, which is washed away afterwards [57]. Regardless of the exact mechanism, the formation itself and the effect of such a secondary phase is strongly discussed in literature.

2.4.2 Silver Alloying in CIGS

The substitution of parts of copper by silver in CIGS solar cells shows an increasing interest in the last years. In the meantime, high efficiency devices have been already demonstrated [69, 70, 71, 72]. There are several reasons to use silver-alloyed CIGS for high efficiency solar cells. It is assumed that silver is reducing or passivating defects in the absorber layer [73, 70, 74]. Yang et al. showed data, where (Ag,Cu)(In,Ga)$\mathrm{Se_2}$ (ACIGS) devices indeed revealed a higher carrier lifetime, compared to CIGS devices. Another point is the reduction of the Urbach energy, reported by different groups [75, 76]. Additionally, silver affects the energetic band configuration of the CIGS absorber. Theoretical calculations revealed, that both, valence and conduction band are shifting downwards with the addition of silver, resulting in higher band gaps and higher chemical potentials [77, 20]. Erslev et al. experimentally confirmed the effect on the band gap [76]. From a technical point of view the use of ACIGS is of high interest, because ACIGS can be grown at lower temperature, compared to CIGS, due to a reduced melting point [78, 79, 70]. Larger grains and smoother surfaces make ACIGS an appropriate bottom cell in tandem devices [70, 78, 80, 81].

Nevertheless, the use of ACIGS instead of a silver-free CIGS absorber results in some new challenges, as well. First, silver enhances the elemental intermixing during the ACIGS growth, resulting in a flattened GGI profile. Therefore, obtaining the well established band gap profile with double grading and notch is more difficult [82, 71]. Additionally, the diffusivity of alkali elements depends on the silver content in CIGS. Aboulfadl et al. showed DFT simulations, which reveal an increasing solubility of alkali elements with increasing silver content. Furthermore, silver affects the surface of the absorber layer. Donzel-Gargand et al. report a highly Cu-depleted ACIGS surface, preconditioning the formation of an Alkali-In-Se phase [83, 84]. Furthermore, the changes in the CIGS surface affect the growth of the subsequent buffer layer [85, 77]. Both, the formation of secondary phases at the ACIGS surface and the influence on the buffer growth can have a large impact on the heterojunction and therefore on the device performance.

2.5 Cells Used in This Work

This section describes the different samples used in this work in order to verify the developed numerical model. Some investigations base on samples from a laboratory evaporation systems like Chapter 6 or Chapter 5. The main investigations are performed on samples from a production-like multi-stage co-evaporation system (Chapters 7 and 8). Table 2.1 gives an overview of the used samples and the corresponding preparation methods. The Sections 2.5, 2.5 and 2.5 give more details on the properties of the three different sample types and the corresponding preparation methods.

Note: The sample preparation was conducted by the MAT-Team at Zentrum für Sonnenenergie- und Wasserstoffforschung Baden-Württemberg (ZSW). The planning of the experiments and the selection of the samples was carried out by the author.

	Research Tool	**High Efficiency Line**	**Industrial Scale**
Method	Static one-stage co-evaporation	Static multistage co-evaporation	Dynamic multistage inline co-evaporation
Substrate	Soda lime glass and ZrO	alkali-aluminosilicate glass	Soda lime glass
Grading	uniform, without band gap grading	pronounced double grading	(smooth) double grading
PDT	without, NaF, KF, RbF	RbF	without, RbF

Table 2.1: Overview of the investigated samples and their corresponding preparation methods.

Uniform Band Gap Samples for Alkali Analysis

Note: The sample preparation was conducted by Alexander Eslam and Roland Würz from the MAT-Team at ZSW.

The samples discussed in Chapter 6 are prepared in a laboratory evaporation system with a single stage process, where the co-evaporation of all elements is conducted at the same time. An accurate control of the system, allows to grow samples with a homogeneous element distribution within the layer depth, with no compositional change. These samples represent a simplified CIGS solar cell. For the investigations on alkali elements, the samples were grown on ceramic zirconium oxide (ZrO) substrates, preventing any diffusion of alkali elements into the deposited layers during the growth. Thus, a separated view on the PDT process, without an influence of the alkali elements from the substrates is possible and the view on the effect of single different alkali elements, as well. In the presented work, following samples on ZrO substrates have been investigated:

- no PDT: a sample with neither alkali elements from the substrate, nor from a PDT step after the CIGS deposition. This sample serves as the alkali-free reference
- NaF-PDT: a CIGS sample, containing Na due to an in-situ PDT step after the CIGS deposition. No other alkali element is present in a significant amount
- KF-PDT: A CIGS sample, containing only K due to an in-situ PDT step after the CIGS deposition. No other alkali element is present in a significant amount
- RbF-PDT: a CIGS sample, containing only Rb due to an in-situ PDT step after the CIGS deposition. No other alkali element is present in a significant amount

The analyzed samples are from two different evaporation batches. Batch I includes the alkali-free sample, the NaF-PDT sample and the KF-PDT sample. Batch II includes the RbF-PDT samples. In both cases an alkali-free sample and a sample on standard soda-lime glass (SLG) were prepared as references. The sample layerstack is the standard CIGS setup with approx. layer thicknesses: Substrate/500nm Mo/2000nm CIGS/50nm CdS/100nm ZnO/250nm AZO. The active area of $0.5\,\mathrm{cm}^2$ was prepared by mechanical scribing.

High Efficiency CIGS Solar Cells

Note: The sample preparation was conducted by Philip Jackson and Stefan Paetel from the MAT-Team at ZSW.

The CIGS sample for the DLTS measurements in Chapter 5 is from the high efficiency line from ZSW, where several world records have been fabricated e.g. [49, 51]. The process is a multi-stage co-evaporation within the static system, depositing a thick CIGS layer of 2.5 to $3\,\mu\mathrm{m}$ with subsequent rubidium fluoride (RbF)-PDT and with a thin CdS layer (30 to $50\,\mathrm{nm}$) on top. The sample uses a reduced CdS thickness compared to the standard layerstack, zinc magnesium oxide (ZMO) instead of iZnO as intrinsic TCO and an increased thickness of the metallization grid. The active area definition was conducted by a lithographical process. Additionally, an ARC layer of MgF_2 was deposited on top in order to minimize reflection losses.

CIGS Solar Cells from an Industrial Scale Co-evaporation System

Note: The sample preparation was conducted by Rico Gutzler, Stefan Paetel and Co-workers from the MAT-Team at ZSW.

Investigation of CIGS samples of Chapter 7 and on ACIGS samples of Chapter 8 are conducted on samples from a fabrication-like inline system for the coating of large area devices and small

modules. The process is a multi-stage co-evaporation process of the elements. In case of ACIGS, silver is deposited parallel to copper. The standard RbF-PDT is performed in-situ in the last chamber of the inline tool with slight Se-background. All samples have been grown on SLG with the standard layerstack SLG/500nm Mo/2000nm (A)CIGS/50nm CdS/100nm ZnO/250nm AZO.

For the CIGS investigation, samples from two different evaporation batches have been used. In both cases the only variation of the samples was the application of a RbF-PDT or not. The samples with and without Rb have been grown in the same CIGS-evaporation. The nominal RbF source temperature was $520\,^{\circ}\mathrm{C}$.

- Batch I: variation with/without RbF-PDT
- Batch II: variation with/without RbF-PDT

For the ACIGS investigations, in summary three different batches have been fabricated, each with a variation of the RbF source temperature. Within each variation, all samples have been grown in the same CIGS evaporation run, and thus except the RbF supply, no parameter was changed. Among the variations, the (Ag+Cu)/(Ga+In) (ACGI) of the samples was changed:

- Variation I: Sample with ACGI = 0.77, variation of the RbF source temperature from $460\,^{\circ}\mathrm{C}$ to $580\,^{\circ}\mathrm{C}$ in steps of $30\,^{\circ}\mathrm{C}$
- Variation II: Sample with ACGI = 0.81, variation of the RbF source temperature from $460\,^{\circ}\mathrm{C}$ to $580\,^{\circ}\mathrm{C}$ in steps of $30\,^{\circ}\mathrm{C}$
- Variation III: Sample with ACGI = 0.88, variation of the RbF source temperature from $450\,^{\circ}\mathrm{C}$ to $570\,^{\circ}\mathrm{C}$ in steps of $30\,^{\circ}\mathrm{C}$

Fabrication Steps to Complete CIGS Solar Cells

This section explains the standard process needed to complete the CIGS solar cells. After the CIGS deposition, the surface is cleaned by a rinsing step with an aqueous solution to wash away the not incorporated Rb, RbF and other residuals from the surface. In a further solution based step, the buffer layer CdS is deposited by a thiourea based chemical bath deposition (CBD) process. A detailed description and a reaction scheme of the process can be found in the literature [86]. Afterwards a layer of high-resistivity zinc oxide (ZnO) or ZMO is deposited by a radio frequency (RF) magnetron sputtering process in an inline sputtering tool. In the same sputtering system, the transparent conductive AZO is sputtered on top by a direct current (DC) process (in case of high efficiency cells RF-process). A metal grid is deposited on top by electron-beam evaporation. The area definition is conducted either by mechanical or by laser scribing.

2.6 Basic Characterization Techniques Used in This Work

This section describes the used characterization techniques for solar cell devices and thin film characterization.

Standard Device Characterization Methods

Current-voltage Measurements Current-voltage (IV) measurements have been performed with a 4-terminal sensing under AM1.5G, one sun, $25\,^{\circ}\mathrm{C}$ STC with a WACOM Class A (IEC-60904-9) solar simulator and with previous light soaking for $10\,\mathrm{min}$ at STC, as well. All currents can be recalculated into the corresponding current densities via the lateral size of the cell.

External Quantum Efficiency Measurements For external quantum efficiency measurements of selected cells a Bentham PVE300 setup was used. The measurements were conducted with white bias light and in a wavelength range from 300 to $1300\,\mathrm{nm}$ in steps of $5\,\mathrm{nm}$. The setup was calibrated with reference silicon (300 to $1100\,\mathrm{nm}$) and germanium (800 to $1600\,\mathrm{nm}$) solar cells prior to the actual measurements.

Capacitance Voltage Measurements for the Determination of Doping Densities

CV measurements have been performed with the cryogenic setup, described in Chapter 4 in more detail, and PhysTech Hera DLTS system [87] in dark, at room temperature and at $200\,\mathrm{K}$ in order to test the sensitivity of the measurements to temperature changes. For all samples only small changes in the measurements and the resulting effective doping are observed, thus calculations using the room temperature value are reasonable. The standard measurements have been conducted in a voltage range between -1 to $0.6\,\mathrm{V}$, with a measurement frequency of $1\,\mathrm{MHz}$ and an effective probing voltage of $100\,\mathrm{meV}$. The value for the doping density was extracted by the slope of a linear regression fit on the undisturbed part of a Mott-Schottky plot.

Time of Flight-Secondary Ion Mass Spectroscopy Measurements for Composition Profiling

time of flight secondary ion mass spectroscopy (ToF-SIMS) measurements were done by a ToF-SIMS^5 from Iontof. The analyzing source is a $30\,\mathrm{keV}$ bismuth (Bi) ion beam; the sputtering source a $2\,\mathrm{keV}$ cesium (Cs) ion beam. The analyzed region had a smaller size than the sputtering crater to avoid crater edge effects, which diminish depth resolution. The matrix elements Ag, Cu, In, Ga, and Se were quantified based on measurement of the Cs-cluster signal (e.g. CsAg+, etc), which is less prone to matrix effects than the direct single-ion signal, and the profile is normalized to agree with the composition determined by X-ray fluorescence spectroscopy. The alkali elements are quantified using a pre-determined factor to account for the effects of the matrix on the ionization probability of the alkali element. The factor is based on measurements of special samples with a defined implantation profile for the alkali ions. More information can be found in [88, 89, 90].

3 Fundamentals of Numerical Simulation of Solar Cells and Building up a Simulation Tool

Herein the electronic Drift-Diffusion Simulation was written by the author, the meshing 2D algorithm was written by Mario Zinßer and the optical simulation in form of the transfer-matrix method (TMM) and the 1D meshing algorithm were written in collaborative work of Mario Zinßer and the author.

This chapter describes the numerical methods used in the presented simulation software on semiconductor level in order to develop a numerical simulation model for Cu(In,Ga)Se_2 (CIGS) solar cells. The aim is to develop a model in order to allocate the occurring loss mechanisms and find the dominant loss paths herein. First, a short overview of the meshing methods is given. After that, the basic set of equations is introduced in 3.2.1, which is adapted for numerical treatment in section 3.2.2. Section 3.2.4 shows further improvements to the basic equations to increase the numerical stability. Afterwards additional implementations are discussed. First, in Section 3.2.3 a detailed look on the implemented recombination processes is made. Second, in Section 3.2.5 all implementations are presented, which are necessary to treat more complex structures like heterojunctions etc. The solving of the whole set of introduced equations is explained in section 3.2.6 and in Section 3.2.7 the possibilities of boundary conditions are presented.
Section 3.3 describes the used optical models.
In the end the applications of the fundamental methods are introduced: Section 3.4 explains the external quantum efficiency (EQE) simulation, Section 3.5 introduces the method of reverse engineering fitting (REF) and Section 3.6 the used loss analysis approach.

3.1 Mesh Generation

In order to perform a numerical simulation of a given geometry, it is necessary to divide simulation domain in finite elements. Each finite element is defined by a node (or mesh point) and a shell (defined by the borders to all neighboring finite elements). The predefined (like values of mobilities, band gaps etc.) and calculated properties (like electrical potential, carrier densities etc.) are assigned to the mesh points. The enclosed area of the finite element has the same properties assigned to the corresponding mesh point and is not changing within this area. In the presented software implementation, the possibilities of using a 1D or a 2D Mesh is implemented. Both possibilities are explained in the following two paragraphs.

1D Quasi-equidistant Mesh

The simplest case of a mesh in one dimension is a mesh of equally distributed mesh points over the whole simulation domain. This would end up with difficulties at the interface between two neighbouring materials or regions. Therefore, the meshing algorithm firstly sets the mesh points directly at geometry defining structures. After this, the rest of the mesh points are added with respect to the initial points. In order to avoid numerical problems, a "quasi-equidistant" approach

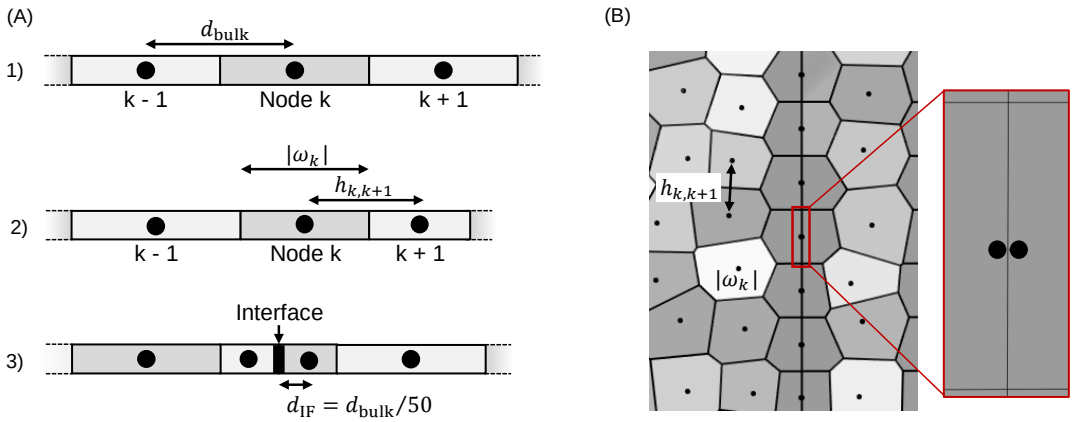

Figure 3.1: Illustration of the resulting (A) 1D and (B) 2D meshes, created with the implemented meshing algorithms.

was used, where the mesh point are first set at equivalent distance to each other and are shifted afterwards by a random factor. Herein the maximum random shift was limited to half the distance of the equidistant mesh d_{bulk}. Figure 3.1 (A) illustrates the basic idea of the "quasi-equidistant" 1D mesh. Part 1) illustrate the equidistant mesh with a constant distance of d_{bulk}. After the random shifting of the points (Part 2)), the distances between two nodes are randomly distributed as well and the value is calculated via the Pythagorean theorem $h_{\mathrm{k,k+1}} = \sqrt{\left((x_{\mathrm{k+1}} - x_{\mathrm{k}})^2 + (y_{\mathrm{k+1}} - y_{\mathrm{k}})^2\right)}$ [91], which is trivial in the 1D case, but can be used and extended in 2D and 3D meshes. The mesh points next to a material interface are placed in a way, that the distance to the interface is a factor of 50 smaller than the distance between two mesh points in the equidistant case.
The control volume of the k-th node is defined by the area of the polygon in 2D and the distance of the node boundaries in 1D: $|\omega_{\mathrm{k}}| = \frac{x_{\mathrm{k}}+x_{\mathrm{k+1}}}{2} - \frac{x_{\mathrm{k-1}}+x_{\mathrm{k}}}{2}$. The node boundaries are defined by the perpendicular bisector of the connection between mesh points x_{k} and $x_{\mathrm{k+1}}$ [92]. This approach can be transferred to the 2D mesh.

2D Delauney-Voronoi Mesh

Figure 3.1 (B) illustrates the situation in a 2D Delaunay-Voronoi mesh, which is used for 2D simulation models. This mesh is build up by triangles (Delaunay mesh) and the corresponding dual graph is called a Voronoi diagram (shown in Figure 3.1 (B)) [93]. As in the 1D case, distances between mesh points ($h_{\mathrm{k,k+1}}$) and control volumes ($|\omega_{\mathrm{k}}|$) can be defined. Furthermore the relation between mesh point borders and the perpendicular bisector between two mesh points is valid. This is achieved by the use of a Delaunay triangulation in combination with a Bower-Watson algorithm [94]. Similar to the 1D case, first all contour patterns are described by a new method of cohesive mirror points, illustrated in the zoomed-in part in Figure 3.1 (B). Afterwards the remaining simulation domain is filled with further mesh points . A detailed description of the meshing algorithm can be found in the PhD-Thesis of Mario Zinßer [95]. The big advantage of the resulting Delaunay-Voronoi mesh is, that current flows between mesh points can be described as perpendicular across the borderlines of the finite elements. This can be utilized in the numerical description of the basic semiconductor equations, introduced in Section 3.2.

3.2 Drift-diffusion Model for the Simulation of Solar Cells

3.2.1 The van Roosbroeck System

The basic set of equation to describe the steady state behavior of a system, called Van Roosbroeck System [96]:

$$\underline{\nabla} \cdot (\epsilon \underline{\nabla} \phi) = -\rho/\epsilon_0 \tag{3.1a}$$
$$\underline{\nabla} \cdot \underline{J}_{\mathrm{n}} = -q(G - R) \tag{3.1b}$$
$$\underline{\nabla} \cdot \underline{J}_{\mathrm{p}} = q(G - R) \tag{3.1c}$$

where Equation 3.1a is called Poisson's equation which can be obtained from the first Maxwell's law [97]. Equations 3.1b and 3.1b are the continuity equations for electrons and holes, respectively. ϵ_{r} is the dielectric permittivity , ϵ_0 is the vacuum permittivity, ϕ is the electrostatic potential, ρ is the local charge density, q is the absolute value of the charge of an electron, G is the generation rate density of electron-hole pairs and R is the corresponding recombination rate density[98]. The current of electrons $\underline{J}_{\mathrm{n}}$ and holes $\underline{J}_{\mathrm{p}}$ can be described by following equations:

$$\underline{J}_{\mathrm{n}} = -q\mu_{\mathrm{n}} n \underline{\nabla}\phi + qD_{\mathrm{n}} \underline{\nabla} n = -q\mu_{\mathrm{n}} n \underline{\nabla}\varphi_{\mathrm{n}} \tag{3.2a}$$
$$\underline{J}_{\mathrm{p}} = -q\mu_{\mathrm{p}} p \underline{\nabla}\phi - qD_{\mathrm{p}} \underline{\nabla} p = -q\mu_{\mathrm{p}} p \underline{\nabla}\varphi_{\mathrm{p}} \tag{3.2b}$$

where n is the electron density, p is the hole density, $\mu_{\mathrm{n,p}}$ are the electron and hole mobilities, respectively and $D_{\mathrm{n,p}}$ are the diffusion coefficients which satisfy the Einstein relation $D_{\mathrm{n,p}} = k_{\mathrm{B}} T \mu_{\mathrm{n,p}}/q$ with the Boltzmann constant k_{B} and the temperature T. The right hand side of equations 3.2a and 3.2b implies, that the negative gradients of the quasi Fermi potentials φ_{n} and φ_{p} are the driving forces of the currents [92]. The local charge density is defined as:

$$\rho = n + p + C \tag{3.3}$$

The Equations 3.1 build a set of coupled nonlinear ordinary differential equations due to the carrier densities dependence on the potentials:

$$n = N_{\mathrm{C}} exp\left(\frac{q(\phi - \varphi_{\mathrm{n}}) - E_{\mathrm{C}}}{k_{\mathrm{B}} T}\right) \tag{3.4a}$$
$$p = N_{\mathrm{V}} exp\left(\frac{q(\varphi_{\mathrm{p}} - \phi) + E_{\mathrm{V}}}{k_{\mathrm{B}} T}\right). \tag{3.4b}$$

Equations 3.4 are written in form of the Boltzmann approximation, which is valid for non-degenerately doped semiconductors. An extension of this approximation is the formalism via the Blakemore approximation or the Fermi-Dirac statistics (see section 3.2.1.1). The value of the doping C in equation 3.3 can be calculated by the difference of positive (donator) and negative (acceptor) charged dopants: $C = N_{\mathrm{D}}^{+} - N_{\mathrm{A}}^{-}$. $E_{\mathrm{C,V}}$ denotes the minimum of the conduction band and the maximum of the valence band, respectively, $N_{\mathrm{C,V}}$ denotes the corresponding effective density of states (DOS) [98, 92].

3.2.1.1 Carrier Statistics beyond the Boltzmann-approximation

In section 3.2.1 the equations 3.4 were introduced to describe the carrier concentration within a semiconductor, depending on the distance of the quasi-fermi level to the corresponding band edge (E_C for φ_n and E_V for φ_p). For high doping values, more accurate statistics have to be used. For the following discussion the terms of η_n and η_p are introduced. They are defined as the argument in the exponential function of equations 3.4:

$$\eta_n = \frac{q(\phi - \varphi_\mathrm{n}) - E_\mathrm{C}}{k_\mathrm{B}T} \tag{3.5a}$$

$$\eta_p = \frac{q(\varphi_\mathrm{p} - \phi) + E_\mathrm{V}}{k_\mathrm{B}T} \tag{3.5b}$$

In case, when differentiation between the electron and hole term is not necessary, η without an index is used. In the following, only equations for electrons are given, while the formulation for holes can be equally derived. Equation 3.5a can be used to describe the electron density as a product of the effective DOS and a distribution function $F(\eta)$:

$$n(\eta) = N_C F(\eta) \tag{3.6}$$

For 3D bulk semiconductors with parabolic energy bands the statistical distribution function for charge carriers is given by the Fermi-Dirac integral, which gives the exact result in the borders of assumption. For reasons of simplification, in terms of computational effort, often approximations of this integral are used. The already mentioned Boltzmann distribution is one possibility, another possibility is the Blakemore-distribution [99]. Herein, the Blakemore-statistic has a larger range of validity compared to the Boltzmann-statistic, but the latter has great computational advantages due to their exponential form. The distribution functions are summarized in Equation 3.7:

$$F(\eta) = \frac{2}{\sqrt{\pi}} \int_0^{\mathrm{inf}} \frac{\xi^{1/2}}{exp(\xi - \eta) + 1} d\xi \tag{3.7a}$$

$$F(\eta) = \frac{1}{exp(-\eta) + 0.27}, \qquad \eta \leq 1.3 \tag{3.7b}$$

$$F(\eta) = exp(\eta), \qquad \eta \leq -2 \tag{3.7c}$$

As indicated in equations 3.7b and 3.7c, both approximations only have a limited range of validity regarding η. While the Blakemore approximation is only valid for η values lower than 1.3, the Boltzmann approximation is valid for values below -2. Figure 3.2 (A) shows the difference of the Fermi-Dirac statistic in comparison to Blakemore and Boltzmann statistic. Graph (B) visualizes the range of validity in relation to the doping density of the semiconductor. It can be seen, that the Boltzmann statistic is valid for values up to approx. $1{\cdot}10^{17}\,\mathrm{cm}^{-3}$. For higher values the error between the approximation and the correct values of Fermi-Dirac is getting larger. The Blakemore approximation can be used for doping values up to $1{\cdot}10^{18}\,\mathrm{cm}^{-3}$. In summary, the Boltzmann approximation can be used in numerical simulation for calculations excluding materials with doping values around $1{\cdot}10^{20}\,\mathrm{cm}^{-3}$ [100]. But for most applications the usage of Boltzmann statistics is reasonable or the error is negligible. The following derivation of discretization and other

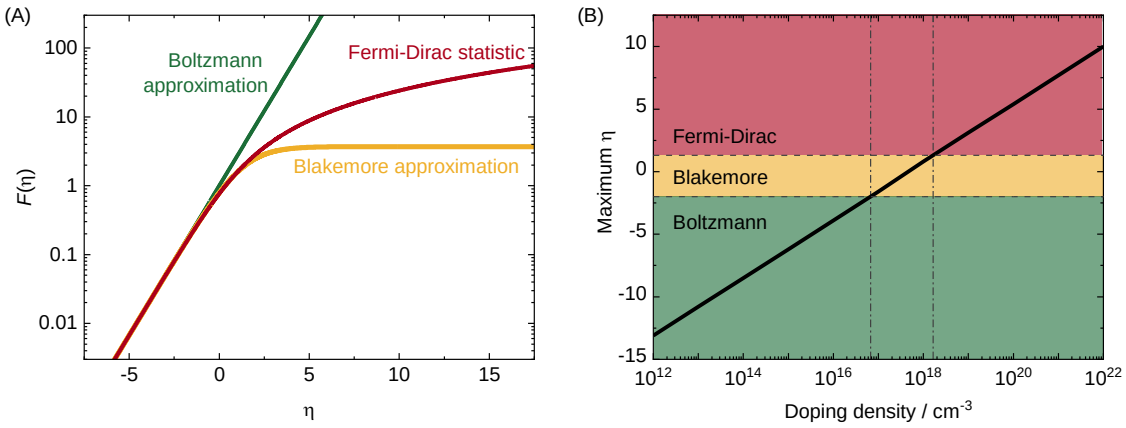

Figure 3.2: (A) Plot of different carrier statistics and approximation in dependence of η and (B) visualization of the corresponding ranges of validity in relation to the doping density.

descriptions like Shockley-Read-Hall (SRH) recombination are only in the scope of the Boltzmann approximation. For the usage of Fermi-Dirac statistics, extra formulations are necessary.

3.2.2 Discretizing the van Roosbroeck System

In order to use the Equations 3.1 for semiconductor simulations, several reformulations have to be applied in form of their discretization. As described in Section 3.1, for the purpose of drift diffusion simulations, a given geometry is divided into nodes x_k with control volumes $|w_\mathrm{k}|$ and distance between neighboring nodes k and k+1 $h_{\mathrm{k,k+1}}$. Via this nodal description , the Fundamental Theorem of Calculus and the method of central finite differences the Poisson's equation can be rewritten in the differential form. Via an integration and the multiplication of a suitable integrating factor, the continuity equations in 3.2 can be rewritten in the form of Scharfetter-Gummel [101]:

$$\underline{j}_{\mathrm{n;k,k+1}} = -\frac{q\mu_\mathrm{n}U_\mathrm{T}}{h_{\mathrm{k,k+1}}}\left[B\left(-\frac{\phi_{\mathrm{k+1}}-\phi_\mathrm{k}}{U_\mathrm{T}}\right)n_\mathrm{k} - B\left(\frac{\phi_{\mathrm{k+1}}-\phi_\mathrm{k}}{U_\mathrm{T}}\right)n_{\mathrm{k+1}}\right] \tag{3.8a}$$

$$\underline{j}_{\mathrm{p;k,k+1}} = \frac{q\mu_\mathrm{p}U_\mathrm{T}}{h_{\mathrm{k,k+1}}}\left[B\left(\frac{\phi_{\mathrm{k+1}}-\phi_\mathrm{k}}{U_\mathrm{T}}\right)p_\mathrm{k} - B\left(-\frac{\phi_{\mathrm{k+1}}-\phi_\mathrm{k}}{U_\mathrm{T}}\right)p_{\mathrm{k+1}}\right] \tag{3.8b}$$

Due to readability, the vector notation is omitted in the following. In the given form, these equations are only valid in the range of the Boltzmann approximation, but there are extension for an arbitrary carrier distribution function.

The function $B(x)$ represents the Bernoulli equation in the form of:

$$B(x) = \frac{x}{e^x - 1} \tag{3.9}$$

Finally, the van Roosbroeck system is obtained in its discrete form in one dimension :

$$0 = \epsilon_0\epsilon_\mathrm{r}\left(\frac{1}{h_{\mathrm{k,k+1}}}\phi_{\mathrm{k+1}} - \left[\frac{1}{h_{\mathrm{k,k+1}}} + \frac{1}{h_{\mathrm{k-1,k}}}\right]\phi_\mathrm{k} + \frac{1}{h_{\mathrm{k-1,k}}}\phi_{\mathrm{k-1}}\right) - q\left(C_\mathrm{k} + p_\mathrm{k} - n_\mathrm{k}\right)|\omega_\mathrm{k}| \tag{3.10a}$$

$$0 = j_{\mathrm{n;k,k+1}} - j_{\mathrm{n;k-1,k}} - q\left(G_\mathrm{k} - R_\mathrm{k}\right)|\omega_\mathrm{k}| \tag{3.10b}$$

$$0 = j_{\mathrm{p;k,k+1}} - j_{\mathrm{p;k-1,k}} - q\left(G_\mathrm{k} - R_\mathrm{k}\right)|\omega_\mathrm{k}| \tag{3.10c}$$

where ϕ_k denotes the electrostatic potential at a node k and $j_{\mathrm{n;k,k+1}}$ the electron current from node k into node k+1 in Scharfetter-Gummel form. This nomenclature can be extended to all other quantities. R_k is the recombination rate in node k, which can be subdivided into different recombination mechanisms (see 3.2.3). G_k gives the generation rate of charge carriers, given by the used optical model (see Section 3.3). Additionally it has to be mentioned that n_k and p_k and R_k can also depend on the potentials ϕ, φ_n and φ_p. The detailed derivation of the discretized equations can be found in literature [92].

For an arbitrary dimension, the following form can be used:

$$0 = \sum_{w_\mathrm{l}\varepsilon\mathscr{N}(\omega_\mathrm{k})}\left(-\epsilon_0\epsilon_\mathrm{r}|\partial\omega_\mathrm{k}\cap\partial\omega_\mathrm{l}|\frac{\phi_\mathrm{l}-\phi_\mathrm{k}}{h_{\mathrm{k,l}}}\right) - q|\omega_\mathrm{k}|\left(C_\mathrm{k} - n_\mathrm{k} + p_\mathrm{k}\right) \tag{3.11a}$$

$$0 = \sum_{w_\mathrm{l}\varepsilon\mathscr{N}(\omega_\mathrm{k})}\left(|\partial\omega_\mathrm{k}\cap\partial\omega_\mathrm{l}|j_{\mathrm{n;k,l}}\right) - q|\omega_\mathrm{k}|\left(G_\mathrm{k} - R_\mathrm{k}\right) \tag{3.11b}$$

$$0 = \sum_{w_\mathrm{l}\varepsilon\mathscr{N}(\omega_\mathrm{k})}\left(|\partial\omega_\mathrm{k}\cap\partial\omega_\mathrm{l}|j_{\mathrm{p;k,l}}\right) + q|\omega_\mathrm{k}|\left(G_\mathrm{k} - R_\mathrm{k}\right) \tag{3.11c}$$

These equations represent a summation of the potential differences (3.11a) and current flows (3.11b, 3.11c) between the node k and all neighbouring elements (ω_l). Herein the term $|\partial\omega_\mathrm{k}\cap\partial\omega_\mathrm{l}|$ is the length of the boundary line segment (between ω_k and ω_l).

3.2.3 Numerical Description of Recombination Processes

The following section will introduce the recombination processes of radiative, SRH and Auger recombination implemented in the software. In general the recombination rate R in Equations 3.11b and 3.11c can be written as:

$$R(n,p) = r(n,p)\left(np - N_\mathrm{intr}^2\right) \tag{3.12}$$

with the intrinsic carrier density N_intr. This equation is only valid in the scope of the Boltzmann statistics. Herein the recombination coefficient $r(n,p)$ can be split up into single recombination rates for each recombination type: $r_\mathrm{radiative}$ as radiative recombination coefficient, r_SRH as SRH recombination coefficient and r_Auger as Auger recombination coefficient:

$$r(n.p) = r_\mathrm{radiative}(n,p) + r_\mathrm{SRH}(n,p) + r_\mathrm{Auger}(n,p) \tag{3.13}$$

The **radiative recombination** rate is a material specific parameter, without any further dependency of the charge carrier densities n and p. For CIGS the value of $r_{\mathrm{radiative}}$ is in the range of $1{\cdot}10^{-10}\,\mathrm{cm}^3/\mathrm{s}$ is used in simulations [102, 103].

In case of the **Auger recombination**, the corresponding coefficient has a dependence on the charge carrier densities, described by [40]:

$$r_{\mathrm{Auger}}(n,p) = C_{\mathrm{n}} n + C_{\mathrm{p}} p \tag{3.14}$$

A typical range for C_{n} and C_{p} is around $1{\cdot}10^{-32}\,\mathrm{cm}^6/\mathrm{s}$ [104].

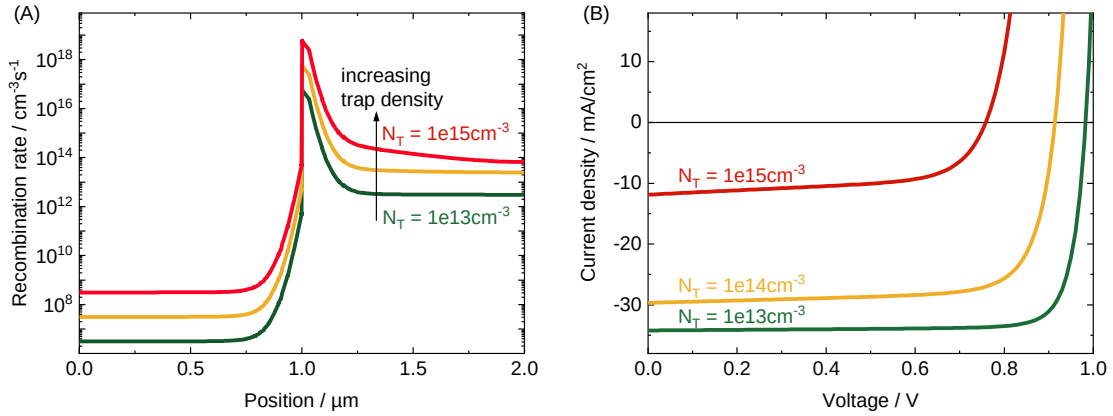

Figure 3.3: Illustration of the influence of changing trap density on the (A) position dependent recombination rate within a pn-junction and (B) the resulting JV-curves.

At last, the **SRH** recombination is the most important recombination type, responsible for a significant power loss in several solar cell technologies [30]. The SRH recombination coefficient can be described by:

$$r_{\mathrm{SRH}}(n,p) = \sum_{i}^{N} \left(\frac{1}{\tau_{\mathrm{p,i}}(n + n_{\mathrm{ref,i}}) + \tau_{\mathrm{n,i}}(p + p_{\mathrm{ref,i}})} \right) \tag{3.15}$$

where the sum over i indicates the summation over multiple single defects N. The reference (or auxiliary) densities $n_{\mathrm{ref,i}}$ and $p_{\mathrm{ref,i}}$ gives the amount of active traps and depends on the energetic position $E_{\mathrm{T,i}}$, with respect to the intrinsic fermi level E_{intr}:

$$n_{\mathrm{ref,i}} = N_{\mathrm{C}} \exp\left(-\frac{E_{\mathrm{C}} - E_{\mathrm{T,i}}}{k_{\mathrm{B}} T} \right) = n \exp\left(\frac{\Delta E_{\mathrm{T,i}}}{k_{\mathrm{B}} T} \right) \tag{3.16a}$$

$$p_{\mathrm{ref,i}} = N_{\mathrm{V}} \exp\left(-\frac{E_{\mathrm{T,i}} - E_{\mathrm{V}}}{k_{\mathrm{B}} T} \right) = p \exp\left(-\frac{\Delta E_{\mathrm{T,i}}}{k_{\mathrm{B}} T} \right) \tag{3.16b}$$

the single electron and hole lifetimes $\tau_{\mathrm{n,p;i}}$ are calculated via

$$\tau_{\mathrm{n,p;i}} = \frac{1}{N_{\mathrm{T,i}} \sigma_{\mathrm{n,p;i}} \nu_{\mathrm{th,n/p;i}}} \tag{3.17}$$

With the trap density $N_{\mathrm{T,i}}$, the capture cross-section $\sigma_{\mathrm{n,p;i}}$ of electrons and holes, respectively and the thermal velocity of both charge types $\nu_{\mathrm{th,n/p;i}}$. The parameters $N_{\mathrm{T,i}}$, $\sigma_{\mathrm{n,p;i}}$ and $E_{\mathrm{T,i}}$ are (partly) experimentally accessible, for example with DLTS or admittance [105, 106].

The effect of a changing trap density on the local recombination rate within a device and the influence on the JV-curve can be seen in Figure 3.3 (A) and (B) for the exemplary case of a pn-junction. For increasing trap densities, the recombination rate increases as well. This results in a reduction of V_{OC}, fill factor (FF) and J_{SC}.

3.2.4 Improvements of the Discretized Equations

Since the van Roosbroeck system is based on highly non-linear differential equations with exponential functions, the numerical stability of the solving algorithm is difficult to ensure. Rewriting of the basic equations, next to other strategies, can help to make the calculations more stable. The following presents two important formulations.

Modification of the Bernoulli equation

One possibility to increase the numerical stability of the simulation is the modification of the Bernoulli function in the form of:

$$B(x) = \begin{cases} B(x) = \frac{x}{e^x - 1}, & \text{if } x > 0. \\ B(-x) = B(x) \cdot e^x, & \text{if } x < 0. \end{cases} \tag{3.18}$$

Modification of the Current Equations

A further improvement of numerical stability, used in the presented method, is the modification of the Scharfetter-Gummel current equations. Equation 3.8a can be modified by the extraction of the term $B(x)n_{\mathrm{k}}$ and some simplifications to:

$$\underline{j}_{\mathrm{n;k,l}} = -\frac{q\mu_{\mathrm{n}}U_{\mathrm{T}}}{h_{\mathrm{k,l}}} B\left(-\frac{\phi_{\mathrm{l}} - \phi_{\mathrm{k}}}{U_{\mathrm{T}}}\right) n_{\mathrm{k}} \left(1 - \frac{N_{\mathrm{C,l}}}{N_{\mathrm{C,k}}} \cdot \exp\left(-\frac{\varphi_{\mathrm{n,l}} - \varphi_{\mathrm{n,k}}}{U_{\mathrm{T}}}\right)\right). \tag{3.19}$$

Equal derivation can be concluded for hole currents. In summary the improvements due to the above introduced modifications can be illustrated by the position dependent current over a simulated device. Figure 3.4 shows the hole and electron current for a simple pn-junction for small external bias of $0.1\,\mathrm{V}$. While Graph (A) shows the results of the calculation with unchanged equations, Graph (B) shows the results after the modification of the Bernoulli function and Graph (C) after the modification of the Scharfetter-Gummel current equations. With each modification a significant improvement in terms of distortions can be achieved.

3.2.5 Additional Numerical Implementations

While the Drift-Diffusion model in the form of the van Roosbroeck system can solve the potential and current distribution of simple devices, additional implementations are necessary for more complex structures or applications. Herein the description of interfaces within the devices is of high importance. Therefore the model for thermionic emission and interface recombination are

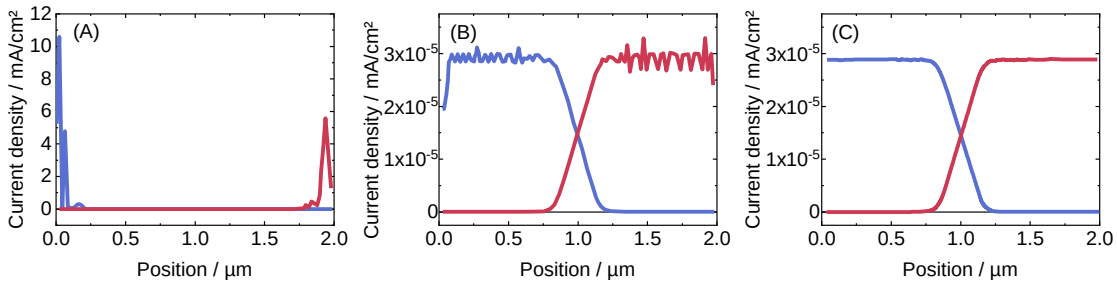

Figure 3.4: Effect of the modification of the basic semiconductor equations on the electron and hole currents over position in a simple pn-junction biased at $0.1\,\mathrm{V}$. Graph (A) shows the result of a simulation withour improvements of the equations. Graph (B) shows the result after the Bernoulli modification and Graph (C) after the Bernoulli and SG-current modification.

described in Section 3.2.5.1. Another important aspect is the temperature dependence of physical quantities, which is discussed in Section 3.2.5.2.

3.2.5.1 Numerical Description of Interface Properties

This section gives an overview of the used physical theories for the description of interfaces in solar cell devices. First, the theory and implementation of thermionic emission at heterojunctions is introduced. Afterwards the recombination at interfaces is explained.

Thermionic Emission

Discontinuities and the resulting barriers in form off "cliffs" or "spikes" in the energetic bands of a solar cell device can strongly influence the current within the device and therefore the whole JV-characteristic [107, 108]. The theory of thermionic emission is based on the assumption that only charge carriers with a sufficient thermal energy can move across the heterojunction. The current over a heterojunction for electrons from mesh node k to node l can be described by [107, 108, 109, 110, 111]

$$j^{TE}_{\mathrm{n;k,l}} = q\nu_{\mathrm{th,n;l}} n_{\mathrm{l}} - q\nu_{\mathrm{th,n;k}} n_{\mathrm{k}} \exp\left(\frac{-\Delta E_{\mathrm{C}}}{U_{\mathrm{T}}}\right) \tag{3.20}$$

and for holes

$$j^{TE}_{\mathrm{p;k,l}} = -q\nu_{\mathrm{th,p;l}} p_{\mathrm{l}} + q\nu_{\mathrm{th,p;k}} p_{\mathrm{k}} \exp\left(\frac{-\Delta E_{\mathrm{V}}}{U_{\mathrm{T}}}\right). \tag{3.21}$$

Nodes k and l represent the adjacent nodes next to the hetero-interface (compare Figure 3.5 (A)), $\nu_{\mathrm{th,n/p}}$ represents the thermal velocity of electrons and holes respectively and n and p are the carrier concentrations of the adjacent nodes. The heights of the band offset ΔE_{C} and ΔE_{V} are determined by the Anderson's rule [112]:

$$\Delta E_{\mathrm{C}} = \chi_{\mathrm{l}} - \chi_{\mathrm{k}} \tag{3.22a}$$

$$\Delta E_{\mathrm{V}} = (\chi_{\mathrm{l}} - E_{\mathrm{g;l}}) - (\chi_{\mathrm{k}} - E_{\mathrm{g;k}}) \tag{3.22b}$$

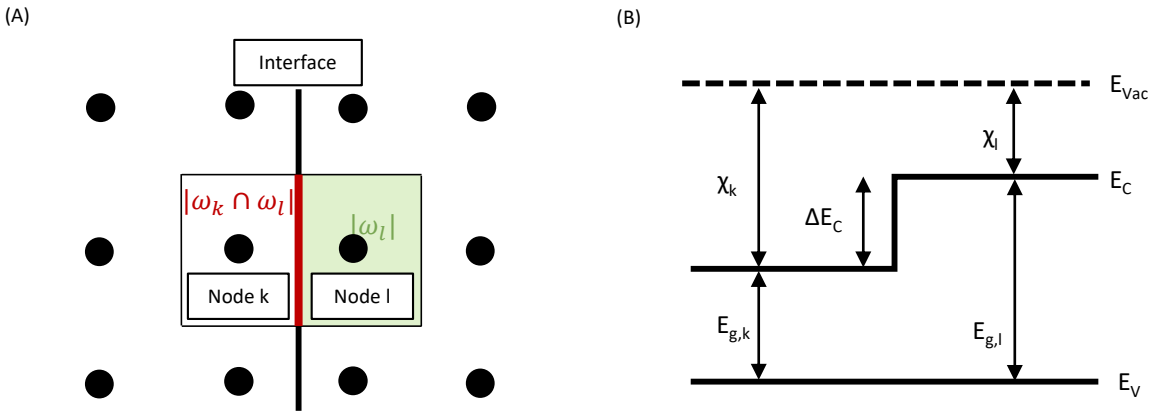

Figure 3.5: Schematic Interface of a TE hetero-interface

The underlying assumptions are that only injection process take place and interface dipols are not affected. Furthermore the above formulation neglects the quantum-mechanical process of tunneling, which is dependent on the width of the barrier. If needed, the given formulation can be extended with a "tunneling" factor, introduced elsewhere [110].

Figure 3.5 (B) illustrates the basic of calculating the band-offsets with an example of a discontinuity in the conduction band. Figure 3.6 (A) shows the effect of the height of E_C on the JV-curves of a simple pn-junction with such a band-offset.

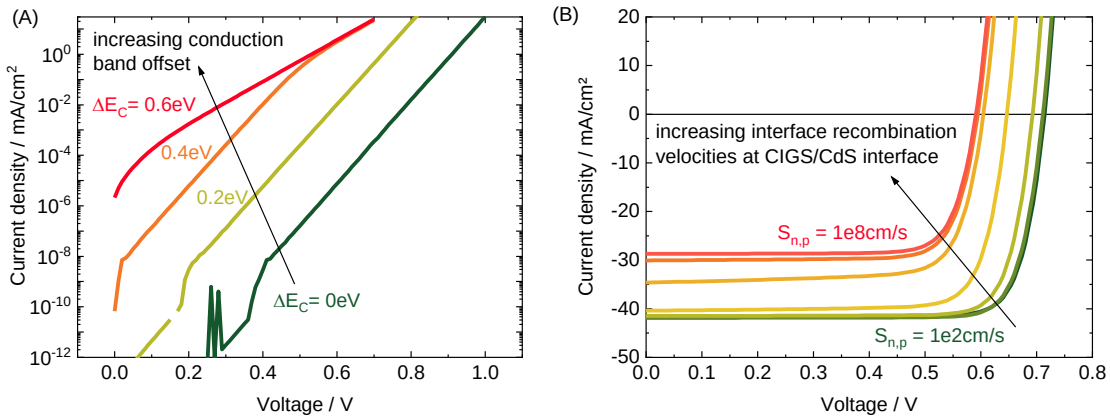

Figure 3.6: (A) Dark JV-curves of a pn-junction with a discontinuity in the conduction band with changing step height. (B) Influence of changing interface recombination velocities at the CdS/CIGS interface on the JV-curves of a CIGS solar cell.

Interface Recombination

Interface recombination is implemented with respect to the publication of Wilhelm et al. [113] as trap assisted recombination at interfaces. Here, both (all in 2D) mesh points , which are located at either side of the junction are treated by this formulation. The interface recombination rate is calculated by:

$$R_{\mathrm{IF}} = \frac{np - N_{\mathrm{intr}}^2}{(n + n_{\mathrm{ref}})/S_{\mathrm{p}} + (p + p_{\mathrm{ref}})/S_{\mathrm{n}}} \tag{3.23}$$

with the intrinsic carrier density (which is calculated by Equation 3.35), the reference densities n_{ref} and p_{ref} and the surface recombination velocities of electrons and holes $S_{\mathrm{n,p}} = \sigma_{\mathrm{n,p}} v_{\mathrm{th}} N_{\mathrm{IF}}$. The reference densities are calculated via:

$$n_{\mathrm{ref}} = N_{\mathrm{intr}} \exp\left(\frac{E_{\mathrm{trap}}}{k_{\mathrm{B}}T}\right) \tag{3.24a}$$

$$p_{\mathrm{ref}} = N_{\mathrm{intr}} \exp\left(\frac{-E_{\mathrm{trap}}}{k_{\mathrm{B}}T}\right) \tag{3.24b}$$

Herein, the characteristic trap parameters trap density N_{IF}, capture cross-section of electrons and hole $\sigma_{\mathrm{n,p}}$ and trap energy E_{trap} are used. In contrast to the bulk trap assisted recombination, the unity the trap density is in cm^{-2}, and describes a surface trap densit at the interfaces.

3.2.5.2 Temperature Dependencies

This section describes the implementation of temperature dependencies in the semiconductor simulation. Since the temperature plays a significant role in all levels of device performance a detailed description is necessary. For an example, the temperature dependence on micro-scale of fundamental material properties influences the operating behavior of a pn-junction and therefore of a whole module installed in open air [114]. Therefore the next two paragraphs dealing with the temperature dependence of the doping density, defined by the quantities N_{A}^{-} and N_{D}^{+}, and of the density of states N_{V} and N_{C}.

Incomplete Ionization

The formalism of incomplete ionization describes the mechanism of effective doping, which is temperature dependent. When a given amount of dopants $N_{\mathrm{D,0}}$ or $N_{\mathrm{A,0}}$ is introduced into a semiconductor, not all of them contribute to the effective doping [115]. The amount of atoms which make a contribution to the free carrier concentration (ionized) is determined by material parameters and by the temperature and defined by following equations [116]:

$$N_{\mathrm{D}}^{+} = \frac{N_{\mathrm{D,0}}}{1 + g_{\mathrm{D}} \exp\left(\frac{E_{\mathrm{F,n}} - E_{\mathrm{D}}}{k_{\mathrm{B}}T}\right)} = \frac{N_{\mathrm{D,0}}}{1 + g_{\mathrm{D}} \frac{n}{n_{\mathrm{D}}}} \tag{3.25a}$$

$$N_{\mathrm{A}}^{-} = \frac{N_{\mathrm{A,0}}}{1 + g_{\mathrm{A}} \exp\left(\frac{E_{\mathrm{A}} - E_{\mathrm{F,p}}}{k_{\mathrm{B}}T}\right)} = \frac{N_{\mathrm{A,0}}}{1 + g_{\mathrm{A}} \frac{p}{p_{\mathrm{A}}}} \tag{3.25b}$$

where the g_{A} and g_{D} are degeneracy factors, which are set to values of 2 and 4, respectively. The energies $E_{\mathrm{F,n}}$ and $E_{\mathrm{F,p}}$ are the quasi-fermi energies of electrons and holes, respectively, and the energies E_{D} and E_{A} are the donor and acceptor ionization energies. The right hand side of the equations represent a simplification in the scope of the Boltzmann statistics, where $n_{\mathrm{D}} = N_{\mathrm{C}} \exp\left(-\frac{\Delta E_{\mathrm{D}}}{k_{\mathrm{B}}T}\right)$ and $p_{\mathrm{A}} = N_{\mathrm{V}} exp\left(-\frac{\Delta E_{\mathrm{A}}}{k_{\mathrm{B}}T}\right)$ are auxiliary densities with the distance of the ionization energy to the corresponding band $\Delta E_{\mathrm{D}} = E_{\mathrm{C}} - E_{\mathrm{D}}$ and $\Delta E_{\mathrm{D}} = E_{\mathrm{A}} - E_{\mathrm{V}}$ [1].

[1] Values of ΔE_{D} and ΔE_{A} are set to $50\,\mathrm{meV}$ for all materials by default.

Density of States

The basic formula of the effective DOS is given by [117]:

$$N_{\mathrm{C,V}} = 2\left(\frac{2\pi m_{\mathrm{e,h}} k_{\mathrm{B}} T}{h^2}\right)^{3/2} \tag{3.26}$$

with the effective masses of electrons and holes $m_{\mathrm{e,h}}$ and Planck's constant h. The temperature dependency of the effective DOS arises from the ratio of the DOS at a given temperature T to the $300\,\mathrm{K}$ reference, resulting in the dependence of the order $3/2$. The temperature dependent effective DOS is therefore calculated via:

$$N_{\mathrm{C,V}}(T) = N_{\mathrm{C,V}}(300K)\left(\frac{T}{300K}\right)^{3/2} \tag{3.27}$$

Herein, $N_{\mathrm{C,V}}(300K)$ is the effective DOS of conduction and valence band at $300\,\mathrm{K}$.

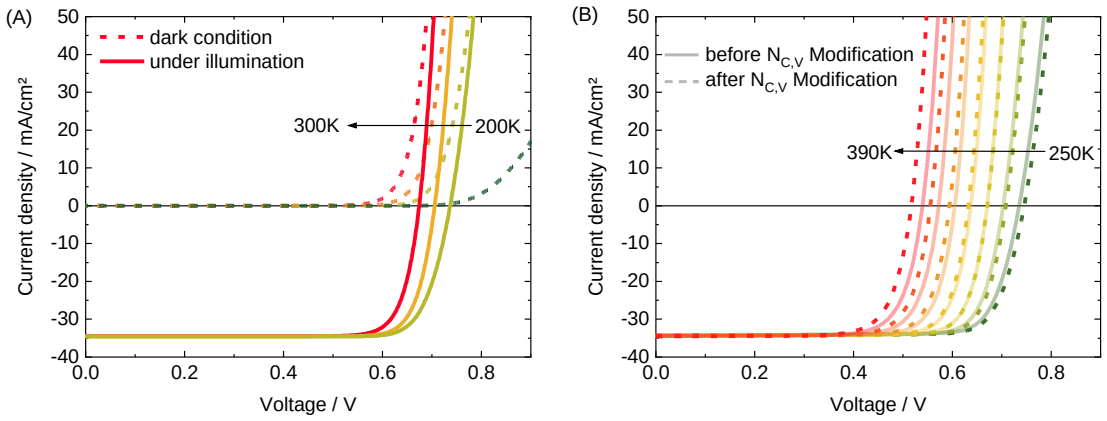

Figure 3.7: (A) Simulated dark and light JV-curves of a CIGS solar cell with a variation of the Temperature. In this example the imcomplete ionization is considered. In Figure (B) the temperature dependency of the DOS is additionally considered. The graph compares the light JV-curves before and after the modification.

Functional Dependence of the Band Gap

In order to reproduce the common property of CIGS solar cells of a band gap grading, a tool was developed to define this grading in a graphical user interface (GUI). Figure 3.8 shows a screenshot of this tool. It allows to assign a band gap grading to an arbitrary layer. The definition is realized via five points, distributed over the normalized layer depth. The position of the first and last point are fixed on the x-axis at the beginning and end of layer (0 and 1), so that only the y-value can be changed. For the remaining three points within the layer, both coordinates, x and y, can be changed. Herein the y-value is a factor, multiplied by the "default" band gap value, defined in the material properties. All five points are used to construct a cubic spline in order to obtain a continuous profile without discontinuities. This allows to define a huge variaty of possible profiles.

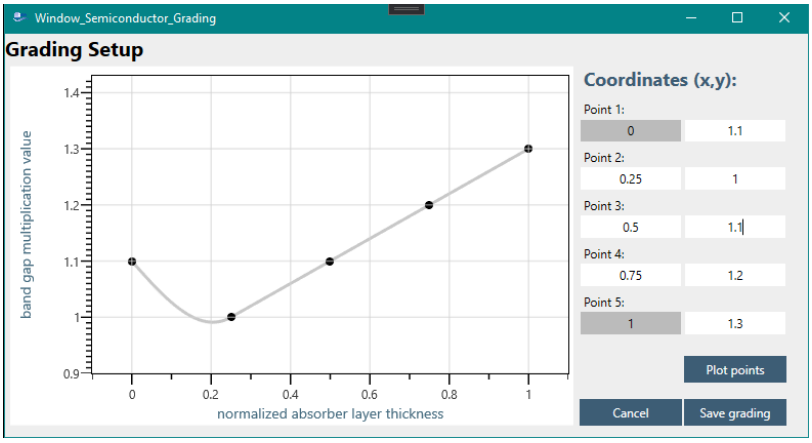

Figure 3.8: Illustration of the "grading" tool within the software for the definition of band gap profiles.

3.2.6 Solving the van Roosbroeck Model

In order to numerically solve the above introduced semiconductor equations, based on the set of nonlinear differential equations (Equations 3.10), an iterative solver in combination with the Newton-Raphson method is used [118] in this work. Therefore, the used physical equations have to be set in a numerically treatable form, namely the residuum function $\underline{F}(\underline{\Phi})$, which is constructed as a vector with $3N$ (N = amount of finite elements) entries:

$$\underline{F}(\underline{\Phi}) = \left(\underline{F_1}, \underline{F_2}, \underline{F_3}\right) = \begin{pmatrix} F_{1,1} \\ \vdots \\ F_{1,N} \\ F_{2,1} \\ \vdots \\ F_{2,N} \\ F_{3,1} \\ \vdots \\ F_{3,N} \end{pmatrix} \tag{3.28}$$

where the subvector $\underline{F_1}$ represents the Poisson equation at every finite element, given by Equation 3.10a and the subvectors $\underline{F_2}$ and $\underline{F_3}$ represent the continuity equations 3.10b and 3.10c, respectively. The vector $\underline{\Phi}$ represents all electrical and quasi-fermi potentials in an one dimensional vector:

$$\underline{\Phi} = \left(\underline{\phi}, \underline{\varphi_n}, \underline{\varphi_p}\right) = \begin{pmatrix} \phi_1 \\ \vdots \\ \phi_N \\ \varphi_{n,1} \\ \vdots \\ \varphi_{n,N} \\ \varphi_{p,1} \\ \vdots \\ \varphi_{p,N} \end{pmatrix} \tag{3.29}$$

The Newton-Raphson algorithm is a root-finding method, which requires the first derivative of the residual function $\underline{F}(\underline{\Phi})$, represented by the Jacobi-matrix $\underline{\underline{J}}(\underline{\Phi})$ with the size of 3N x 3N:

$$\underline{\underline{J}}(\underline{\Phi}) = grad_{\underline{\Phi}}\underline{F}(\underline{\Phi}) \begin{pmatrix} \frac{\partial F_{1,1}}{\partial \phi_1} & \cdots & \frac{\partial F_{1,1}}{\partial \phi_N} & \frac{\partial F_{1,1}}{\partial \varphi_{n,1}} & \cdots & \frac{\partial F_{1,1}}{\partial \varphi_{n,N}} & \frac{\partial F_{1,1}}{\partial \varphi_{p,1}} & \cdots & \frac{\partial F_{1,1}}{\partial \varphi_{p,N}} \\ \vdots & \ddots & \vdots & \vdots & \ddots & \vdots & \vdots & \ddots & \vdots \\ \frac{\partial F_{1,N}}{\partial \phi_1} & \cdots & \frac{\partial F_{1,N}}{\partial \phi_N} & \frac{\partial F_{1,N}}{\partial \varphi_{n,1}} & \cdots & \frac{\partial F_{1,N}}{\partial \varphi_{n,N}} & \frac{\partial F_{1,N}}{\partial \varphi_{p,1}} & \cdots & \frac{\partial F_{1,N}}{\partial \varphi_{p,N}} \\ \frac{\partial F_{2,1}}{\partial \phi_1} & \cdots & \frac{\partial F_{2,1}}{\partial \phi_N} & \frac{\partial F_{2,1}}{\partial \varphi_{n,1}} & \cdots & \frac{\partial F_{2,1}}{\partial \varphi_{n,N}} & \frac{\partial F_{2,1}}{\partial \varphi_{p,1}} & \cdots & \frac{\partial F_{2,1}}{\partial \varphi_{p,N}} \\ \vdots & \ddots & \vdots & \vdots & \ddots & \vdots & \vdots & \ddots & \vdots \\ \frac{\partial F_{2,N}}{\partial \phi_1} & \cdots & \frac{\partial F_{2,N}}{\partial \phi_N} & \frac{\partial F_{2,N}}{\partial \varphi_{n,1}} & \cdots & \frac{\partial F_{2,N}}{\partial \varphi_{n,N}} & \frac{\partial F_{2,N}}{\partial \varphi_{p,1}} & \cdots & \frac{\partial F_{2,N}}{\partial \varphi_{p,N}} \\ \frac{\partial F_{3,1}}{\partial \phi_1} & \cdots & \frac{\partial F_{3,1}}{\partial \phi_N} & \frac{\partial F_{3,1}}{\partial \varphi_{n,1}} & \cdots & \frac{\partial F_{3,1}}{\partial \varphi_{n,N}} & \frac{\partial F_{3,1}}{\partial \varphi_{p,1}} & \cdots & \frac{\partial F_{3,1}}{\partial \varphi_{p,N}} \\ \vdots & \ddots & \vdots & \vdots & \ddots & \vdots & \vdots & \ddots & \vdots \\ \frac{\partial F_{3,N}}{\partial \phi_1} & \cdots & \frac{\partial F_{3,N}}{\partial \phi_N} & \frac{\partial F_{3,N}}{\partial \varphi_{n,1}} & \cdots & \frac{\partial F_{3,N}}{\partial \varphi_{n,N}} & \frac{\partial F_{3,N}}{\partial \varphi_{p,1}} & \cdots & \frac{\partial F_{3,N}}{\partial \varphi_{p,N}} \end{pmatrix} \tag{3.30}$$

With $\underline{\underline{J}}(\underline{\Phi})$ as first derivative, the residual $\underline{F}(\underline{\Phi})$ can be approximated by a first order Taylor series around the vector $\underline{\Phi_i}$ [119]:

$$\underline{F}(\underline{\Phi}) = \underline{\underline{J}}(\underline{\Phi_i}) \cdot \underline{\Phi} + \underline{F}(\underline{\Phi_i}) - \underline{\underline{J}}(\underline{\Phi_i}) \cdot \underline{\Phi_i} \tag{3.31}$$

$\underline{F}(\underline{\Phi})$ can be set to zero, because we are interested in its root. The equation can be solved for $\underline{\Phi}$, which is the next approximation $\underline{\Phi}_{\mathrm{i+1}}$ for the actual root:

$$\underline{\Phi}_{\mathrm{i+1}} = \underline{\Phi}_{\mathrm{i}} - \underline{\underline{J}}^{-1}(\underline{\Phi}_{\mathrm{i}}) \cdot \underline{F}(\underline{\Phi}_{\mathrm{i}}) \tag{3.32}$$

Since the numerical handling of inverse matrices ($\underline{\underline{J}}^{-1}$) is a great effort, the following equation is solved by an iterative method:

$$\underline{\underline{J}}(\underline{\Phi_i}) \cdot (\underline{\Phi_i} - \underline{\Phi_{i+1}}) = \underline{\underline{J}}(\underline{\Phi_i}) \cdot \Delta\Phi = \underline{F}(\underline{\Phi_i}) \tag{3.33}$$

In the presented method, a biconjugate gradient method with an incomplete LU decomposition as preconditioner is used [120]. To start the Newton's method a suitable initial guess $\underline{\Phi_0}$ as a starting point has to be set. As presented in Section 3.2.8 in more detail, first the Poisson problem (only electrical potential, not quasi-fermi potentials) is solved. Therefore the initial guess for the electrical potential $\underline{\phi}$ is determined by the so called local charge neutrality condition [92]:

$$\underline{\phi_0} = \frac{E_\mathrm{C} + E_\mathrm{V}}{2q} - \frac{1}{2} U_\mathrm{T}\, log\left(\frac{N_\mathrm{C}}{N_\mathrm{V}}\right) + U_\mathrm{T}\, arcsinh\left(\frac{C}{2N_\mathrm{intr}}\right) \tag{3.34}$$

with the former introduced intrinsic carrier density N_intr, which can be calculated via:

$$N_\mathrm{intr} = \sqrt{N_\mathrm{C} N_\mathrm{V} \exp\left(-\frac{E_\mathrm{C} - E_\mathrm{V}}{k_\mathrm{B} T}\right)} \tag{3.35}$$

and the thermal voltage U_T

$$U_\mathrm{T} = \frac{k_\mathrm{B} T}{q} \tag{3.36}$$

After solving the Poisson problem, the whole van Roosbroeck system is solved. The initial guess for this set of equations results from the solution of the Poisson $\underline{\phi}_\mathrm{Poisson}$ and both quasi-fermi potentials set to zero:

$$\underline{\Phi}_\mathrm{VRB} = (\underline{\phi}_\mathrm{Poisson}, \underline{0}, \underline{0}) \tag{3.37}$$

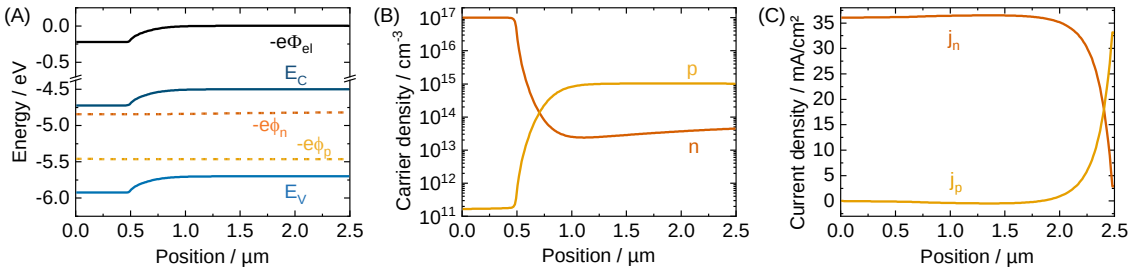

Figure 3.9: Example of an unbiased, illuminated simple pn-junction. (A) Energy bands are shifted to set the maximum of the electrical potential to zero. From the three potentials, all other quantities like (B) carrier densities or (C) currents can be calculated.

For a more intuitive handling of the independent variables and a better presentability of the final data, a transition of the energy bands is performed by shifting all potentials down by the amount of the minimum of the initial guess of the electrical potential. This ends up in an energy diagram, which has a maximum of the electrical potential at $y = 0$. This is visualized in Figure 3.9. From this point on the workflow described in Section 3.2.8 is applied. All other properties like carrier densities or local currents can be derived from the three potentials, like illustrated in Figures 3.9 (B) and (C).

Finally, the last part which is required to solve the system, is the supply of boundary conditions. This is the topic of the next section.

3.2.7 Boundary Conditions

Boundary conditions in the scope of the drift-diffusion equations describe the properties of the electrical contacts of the simulation domain. Depending on the type of contact, there are different formulations. In this presented method different types of electrical boundary conditions are implemented: as Ohmic contacts in form of Dirichlet boundary conditions and in the form of the SRV formalism. Finally, the effect of contact barriers leading to a Schottky contact is discussed.
Electrical boundary conditions are applied on all the finite elements with intended electrical contact, like ground, operating voltage or another additional voltage. In the presented studies, only configurations with one geometrical part on ground (most of the times one end of a layerstack) and one part on the actual applied voltage (the other side of the layerstack) are considered, resulting in a potential difference between two voltages. The following equations are given for this type of configurations.

Ohmic Contact in From of Dirichlet Conditions

The ohmic contact in form of Dirichlet conditions can be described by following equations [92]:

$$\phi^{ground} = \phi_0^{ground} \qquad \phi^{op} = \phi_0^{op} + V_{\mathrm{op}}, \tag{3.38a}$$

$$\varphi_{\mathrm{n}}^{ground} = \varphi_{\mathrm{n;0}}^{ground}, \qquad \varphi_{\mathrm{n}}^{op} = \varphi_{\mathrm{n;0}}^{op}, \tag{3.38b}$$

$$\varphi_{\mathrm{p}}^{ground} = \varphi_{\mathrm{p;0}}^{ground}, \qquad \varphi_{\mathrm{p}}^{op} = \varphi_{\mathrm{p;0}}^{op}. \tag{3.38c}$$

Herein the superscripts "ground" and "op" indicate all finite elements with the corresponding boundary conditions of ground and operating voltage and ϕ_0 is calculated via the local charge neutrality 3.34. The quasi-fermi potentials $\varphi_{\mathrm{n;0}}$ and $\varphi_{\mathrm{p;0}}$ are defined by the initial guess of the van Roosbroeck (VRB) system (equation 3.37) and a potential energy shifting.

Ohmic Contact in SRV Formalism

A more descriptive method is the formalism of Ohmic contacts over the surface recombination velocity (SRV), which models the current over the boundary interfaces and not directly the independent variables φ_{n} and φ_{p} [41, 121]:

$$\phi^{ground} = \phi_0^{ground} \qquad \phi^{op} = \phi_0^{op} + V_{\mathrm{op}}, \tag{3.39a}$$

$$j_{\mathrm{n}}^{ground} = qS_{\mathrm{n}}^{ground}\left(n^{ground} - n_0^{ground}\right), \qquad j_{\mathrm{n}}^{ground} = -qS_{\mathrm{n}}^{op}\left(n^{op} - n_0^{op}\right), \tag{3.39b}$$

$$j_{\mathrm{p}}^{ground} = qS_{\mathrm{p}}^{ground}\left(p^{ground} - p_0^{ground}\right), \qquad j_{\mathrm{p}}^{ground} = -qS_{\mathrm{p}}^{op}\left(p^{op} - p_0^{op}\right). \tag{3.39c}$$

S_{n} and S_{p} are the surface recombination velocities of electrons and holes, respectively. n_0 and p_0 are the equilibrium carrier densities of electrons and holes at the points of interest.

Schottky Contact at Metal-semiconductor Barriers

In case of a contact barrier, which can occur for example at a metal/semiconductor contact with non-optimal band alignment (often due to a not suitable metal work function), Equations 3.39 have to be adapted. Therefore, the barrier height ϕ_{B} is added to Equation 3.39a:

$$\phi^{ground} = \phi_0^{ground} - \phi_{\mathrm{B}}, \qquad \phi^{op} = \phi_0^{op} + V_{\mathrm{op}} - \phi_{\mathrm{B}} \tag{3.40}$$

Herein the barrier height can be calculated via the difference of metal work function ϕ_{M} and the semiconductor equilibrium fermi potential. Figure 3.10 shows the effect of an increasing potential barrier at the CIGS/Mo interface on the current-density-voltage (JV) characteristic in the case of a (A) low doping and (B) high doping of the CIGS layer.

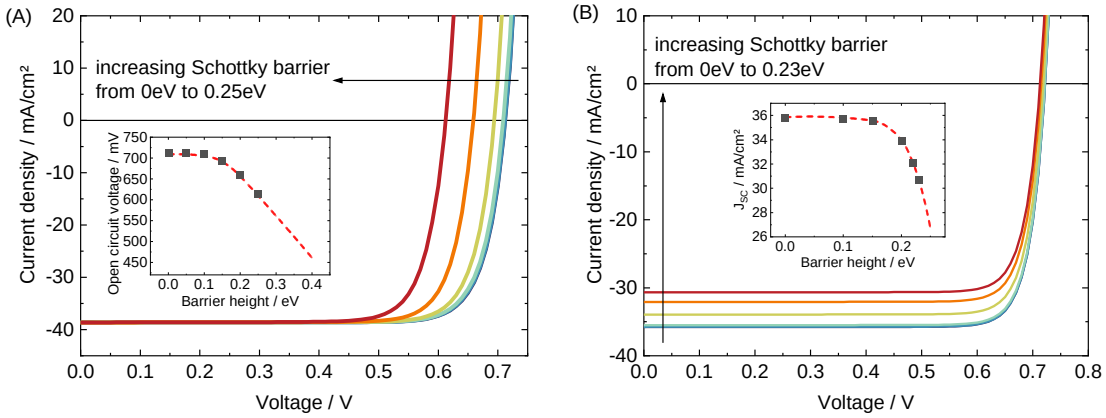

Figure 3.10: Influence of contact barrier at the CIGS/Mo interface on the JV-characteristic of a CIGS solar cell. Depending on the doping of the CIGS layer, the barrier influences either (A) the V_{OC} in case of low doping of $1{\cdot}10^{15}\ \mathrm{cm}^{-3}$ or (B) J_{SC} in case of high doping of $1{\cdot}10^{17}\ \mathrm{cm}^{-3}$

3.2.8 Principle of Program Flow

In this section, the basic idea behind the presented software and the general workflow of a semiconductor simulation is presented. The basic program flow is illustrated in Figure 3.12. Before starting a simulation, the geometry of the device of interest has to be defined. Therefore we developed a "Designer" to create the geometry of semiconductor devices over a GUI. Figure 3.11 shows a screenshot of the Designer for 1D layerstacks. The 2D designer works equivalently by defining areas. Via the designer, the user can define an actual semiconductor layerstack, which is simulated electrically and optically (pale green layers). For layers which are electrically insulating, but optically shall be taken into account, there is a possibility to define coherent layers (pale blue), like anti-reflective coating (ARC) which are simulated within the TMM calculation, and incoherent layers (dark green), like glass or encapsulating materials, which are treated by the Lambert-Beer law. The first and last row define the adjacent materials after the layerstack and the electrical boundary conditions. The material parameters have to be defined in advance in n extra ".txt" files, containing all information of semiconductor properties (band gaps, DOS, mobilities, defects, . . .), electrical properties (sheet resistances, . . .) and optical properties (refractive data, Lambert-Beer attenuation factor,. . .).

Figure 3.11: 1D Designer for the definition of semiconductor layerstacks.

The program starts a simulation with collecting the necessary input information: the geometry of the device (defined in a ".txt" file), the electrical boundary conditions, the approximate number of mesh points, the type of optic calculation and types of recombination which have to be considered. This can be seen on the left side of Figure 3.13, showing a screenshot of the program GUI. After collecting all these information, a mesh is generated, depending on the given geometry (Point 2 in flow chart). Afterwards, the local charge neutrality for each mesh point is calculated (compare Equation 3.34) and set as an initial guess for the Poisson Problem (only electrical potential, Point 3). With the initial guess, the actual calculation of the Poisson problem can be conducted. In the next step, the program takes into account, whether the device is simulated under dark conditions or under illumination. In case of dark conditions, the program skips directly to the solving of the van Roosbroeck system. In case of illumination, the program conducts all calculations which are necessary for the simulation of the illuminated case, even the actual optical calculation (mostly via TMM).

With the generation rate from the optical simulation and the Poisson solution as starting values, the whole van Roosbroeck system can be solved. Therefore, first the generation rate is ramped up in factor 10 steps. After reaching the correct generation rate, the external bias is ramped up in steps of $0.01\,\mathrm{V}$. In each step, the electrical and the quasi-fermi potentials are calculated for the new boundary conditions and with the solution of the previous step as starting value. These ramping mechanisms are needed to ensure numerical stability. Jumping directly from zero to the value of interest could cause numerical problems. Nevertheless, the ramping up of the generation rate can probably be avoided by a "scaling scheme" applied to the equations [122, 123, 124], which was not implemented in the presented program. The ramping of the external voltage can be avoided as well by clever setting of the initial guess, but when simulating photovoltaic devices, one is interested in JV-curves, most of the time. By ramping up the voltage and taking the current at the contacts, the JV-curve can be directly obtained. Finally, the last step is the processing and plotting of the calculated data. See Figure 3.13 for an example of a calculated CIGS band diagram at $0.71\,\mathrm{V}$ bias (upper graph) and the corresponding IV-curve with power curve and Schockley-Queisser IV-curve as reference (lower graph). On the right side, the results of the fitting of the data with an one diode equation are displayed (the used fitting algorithm is described in [125]).

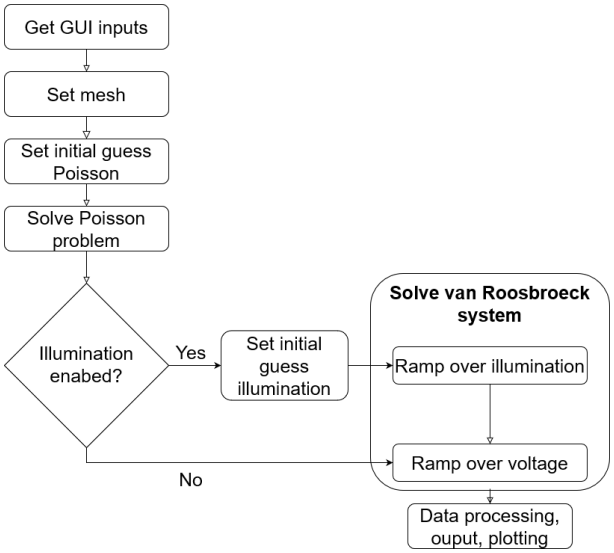

Figure 3.12: Flow diagram of the presented semiconductor simulation tool.

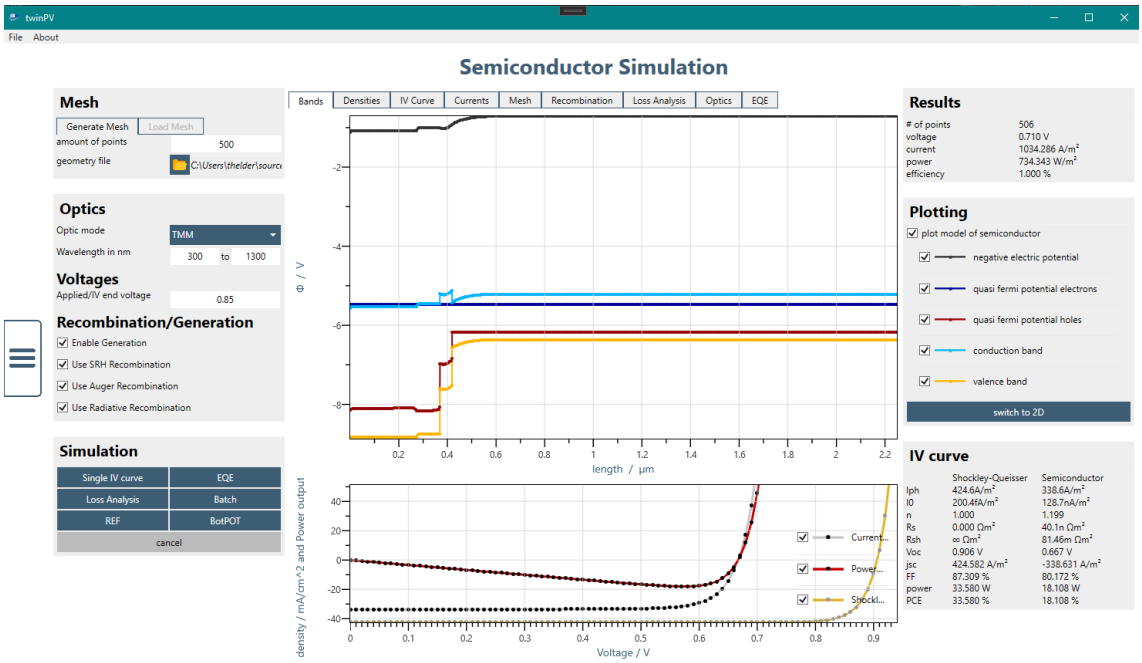

Figure 3.13: GUI of the presented semiconductor simulation tool.

3.3 Optical Modelling

This section describes the methods to calculate the optical properties such as absorptance, reflectance and transmittance of a semiconductor device. Herein the TMM serves as as the standard method, implemented in the software (compare section 3.3.1). Furthermore, the Lambert-Beer method, used to describe large (incoherent) layers which cannot be handled with the TMM, is introduced in Section 3.3.2.

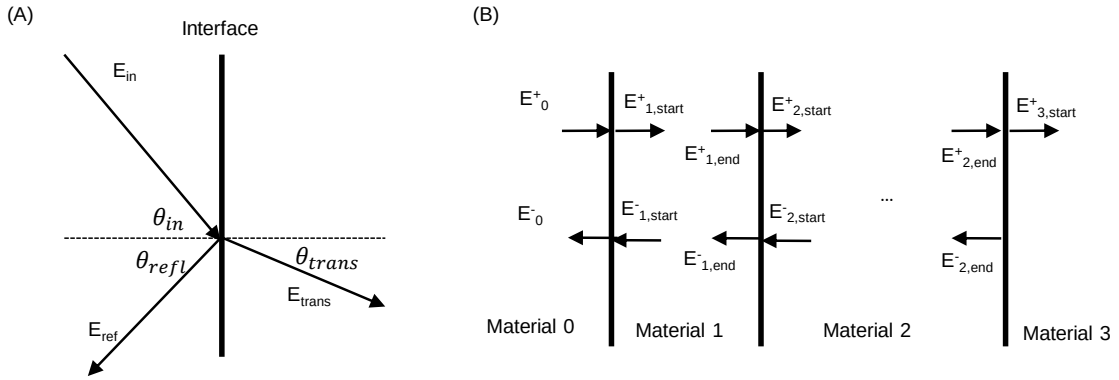

Figure 3.14: (A) Definition of angles and incoming, reflected and transmitted electric fields at a material interface. (B) Principle idea of electric field for the derivation of the TMM.

3.3.1 Transfer-matrix Method

The content of this section has been developed and implemented in collaborative work with Mario Zinßer.

In thin film optics, the so called transfer-matrix method is a common method to calculate the reflected, transmitted and absorbed part of a given spectrum [126]. In the case of thin film photovoltaics it is one way to determine the quantities and derive a generation profile, which can be used as an input for a semiconductor simulation.

The method is based on the well-known Fresnel equations [126], which give the part of light that is reflected (r_s and r_p) or transmitted (t_s and t_p) at an interface between two layers (compare Figure 3.14 (A)):

$$r_\mathrm{s} = \frac{n_1 cos\theta_1 - n_2 cos\theta_2}{n_1 cos\theta_1 + n_2 cos\theta_2} \tag{3.41a}$$

$$r_\mathrm{p} = \frac{n_2 cos\theta_1 - n_1 cos\theta_2}{n_2 cos\theta_1 + n_1 cos\theta_2} \tag{3.41b}$$

$$t_\mathrm{s} = \frac{2 n_1 cos\theta_1}{n_1 cos\theta_1 + n_2 cos\theta_2} \tag{3.41c}$$

$$t_\mathrm{p} = \frac{2 n_1 cos\theta_1}{n_2 cos\theta_1 + n_1 cos\theta_2} \tag{3.41d}$$

Herein, the indices "s" and "p" stand for the polarization direction perpendicular to the incident plane (s) and parallel to the incident plane (p). If the angle of incidence is known, the reflected angle is trivial $\theta_\mathrm{in} = \theta_\mathrm{refl}$ and the transmittance angle (θ_2 in Equations 3.41) can be determined by Snell's law [127]: $n_1 sin\theta_\mathrm{in} = n_2 sin\theta_\mathrm{trans}$. In case of not perfectly smooth surfaces, modified Fresnel coefficients can be used, which derivation can be found elsewhere [128]. It is important to note, that the refractive indices, the angles and the electrical fields, introduced in this section are all complex and wavelength dependent quantities. Therefore the implementation of the presented optical methods in the program is realized with a for-loop over all wavelength of interest. For readability, the identifiers of complex quantities and the wavelength dependencies have been omitted.

For a layerstack containing more than one interface, multiple reflections, where the single reflection paths can interfere with each other, occur. Figure 3.14 (B) illustrates the situation of multiple interfaces in the case of perpendicular light incidence. The incoming light can be reflected or transmitted at the first interface. The transmitted part of the light has the same two possibilities at the second interface, and so on. Between two reflection events, the light is propagating through a medium and it might be absorbed (depending on the refractive indices). This results in a situation which can be described by only the forward components at the beginning $E^{+}_{\mathrm{i,start}}$ and at the end $E^{+}_{\mathrm{i,end}}$ of a layer "i" and the backward components $E^{-}_{\mathrm{i,start}}$ and $E^{-}_{\mathrm{i,end}}$, respectively. In this case, forward means in the direction of the incident light. The idea of the TMM is to connect the electric fields with each other only by events of refraction or propagation, mathematically described with a matrix formalism. A refraction event between materials i and i+1 can then be written as the connection of the electrical fields on the left-hand side of an interface with the ones on the right-hand side by (both, forward and backward direction have to be taken into account) [129, 126]:

$$\begin{pmatrix} E^{+}_{\mathrm{i,end}} \\ E^{-}_{\mathrm{i,end}} \end{pmatrix} = \mathbf{D}_{\mathrm{i}}^{-1}\mathbf{D}_{\mathrm{i+1}} \begin{pmatrix} E^{+}_{\mathrm{i+1,start}} \\ E^{-}_{\mathrm{i+1,start}} \end{pmatrix} = \frac{1}{t_{\mathrm{i,i+1}}} \begin{pmatrix} 1 & r_{\mathrm{i,i+1}} \\ r_{\mathrm{i,i+1}} & 1 \end{pmatrix} \begin{pmatrix} E^{+}_{\mathrm{i+1,start}} \\ E^{-}_{\mathrm{i+1,start}} \end{pmatrix} \tag{3.42}$$

where t and r are the Fresnel coefficients (valid for both polarization directions) and $\mathbf{D}_{\mathrm{i}}^{-1}$ accounts for the inverse of the matrix $\mathbf{D}_{\mathrm{i}}$. A propagation of light through the i-th layer can be described by the connection of the electric fields on the right-hand side of the left interface (beginning of layer i) with the electric fields on the left-hand side of the right interface (end of layer i) via a propagation matrix $\mathbf{P}_{\mathrm{i}}$:

$$\begin{pmatrix} E^{+}_{\mathrm{i,start}} \\ E^{-}_{\mathrm{i,start}} \end{pmatrix} = \mathbf{P}_{\mathrm{i}} \begin{pmatrix} E^{+}_{\mathrm{i,end}} \\ E^{-}_{\mathrm{i,end}} \end{pmatrix} = \begin{pmatrix} exp(-i\frac{2\pi n_{\mathrm{i}}}{\lambda}cos(\theta_{\mathrm{i}})z) & 0 \\ 0 & exp(i\frac{2\pi n_{\mathrm{i}}}{\lambda}cos(\theta_{\mathrm{i}})z) \end{pmatrix} \begin{pmatrix} E^{+}_{\mathrm{i,end}} \\ E^{-}_{\mathrm{i,end}} \end{pmatrix} \tag{3.43}$$

The total transfer matrix of light passing through a layerstack can be described by the multiplication of all the corresponding diffraction and propagation matrices. In the end, the problem only depends on the electric fields of the incoming light, the reflected ratio and the transmitted electrical fields. Therefore, the whole situation can be described by one 2x2 matrix ($\mathbf{M}$) [129]:

$$\begin{pmatrix} E^{+}_{0} \\ E^{-}_{0} \end{pmatrix} = \mathbf{D}_{0}^{-1} \left(\prod_{\mathrm{i}=1}^{N} \mathbf{D}_{\mathrm{m}}\mathbf{P}_{\mathrm{m}}\mathbf{D}_{\mathrm{m}}^{-1} \right) \mathbf{D}_{\mathrm{N+1}} \begin{pmatrix} E^{+}_{\mathrm{N+1,start}} \\ E^{-}_{\mathrm{N+1,start}} \end{pmatrix} = \mathbf{M} \begin{pmatrix} E^{+}_{\mathrm{N+1,start}} \\ E^{-}_{\mathrm{N+1,start}} \end{pmatrix} \tag{3.44}$$

Herein no incoming light from the back of the layerstack is assumed. With the resulting information about the electrical fields at every interface in the layerstack, it is possible to calculate the electrical field at any point within the stack. In order to calculate the energy density (for absorption calculations) one has to calculate the Poynting vector $\underline{S} \cdot \hat{z}$ at a given point z [126]:

$$s - polarization: \qquad \underline{S} \cdot \hat{z} = \frac{Re\left(n \cdot cos(\theta)(E^{+*} + E^{-*})(E^{+} - E^{-})\right)}{Re\left(n_0 \cdot cos(\theta_0)\right)} \tag{3.45a}$$

$$p - polarization: \qquad \underline{S} \cdot \hat{z} = \frac{Re\left(n \cdot cos(\theta^{*})(E^{+} + E^{-})(E^{+*} - E^{-*})\right)}{Re\left(n_0 \cdot cos(\theta_0^{*})\right)} \tag{3.45b}$$

where the superscript $*$ indicates the complex conjugate of the belonging quantity. With the Poynting vector, the ratio of absorbed light in a layer can be calculated (by simply taking the difference between the Poynting vector at the beginning and end of the layer) or a local absorption rate $a(z)$ at a position z can be calculated via the derivative of $\underline{S}$:

$$s-polarization: \qquad a(z) = \frac{|E_\mathrm{f} + E_\mathrm{b}|^2 Im(n \cdot cos(\theta) \cdot k_\mathrm{z})}{Re(n_0 \cdot cos(\theta_0))} \tag{3.46a}$$

$$p-polarization: \qquad a(z) = \frac{Im(n \cdot cos(\theta^*)(k_\mathrm{z}|E_\mathrm{f} - E_\mathrm{b}|^2 - k_\mathrm{z}^*|E_\mathrm{f} + E_\mathrm{b}|^2))}{Re(n_0 \cdot cos(\theta_0^*))} \tag{3.46b}$$

When talking about optical generation of charge carriers in the context of semiconductor simulations, one has to distinguish between absorption rate and generation rate. While the absorption rate is defined over a given wavelength range, the generation rate in semiconductors is only different from zero if the photon energy is larger than the band gap of the semiconductor $h\nu > E_\mathrm{g}$. Only photons which fulfill this requirement, can be taken into account when calculating the generation rate.

3.3.2 Lambert-Beer Attenuation

The Lambert-Beer attenuation is a simple way to describe the absorption in semiconductor materials. Although effects like interferences and reflection cannot be taken into account with this method, it is a helpful way to perform fast and approximated absorption calculations. Moreover, it can be used to describe incoherent layers in layerstack, which cannot be described by the TMM method (incoherent layers). The basic equation of the Lambert-Beer law is based on an exponentially decay of the light intensity [130, 131]:

$$I(z) = I_0 exp\left(-\frac{4\pi k z}{\lambda}\right) = I_0 exp\left(-\alpha(\lambda) z\right) \tag{3.47}$$

with the attenuation coefficient $\alpha(\lambda)$, which is connected to the refractive index of the material. In order to calculate a local absorption rate $a(z)$, the spatial derivative can be used:

$$a(z) = \frac{\partial I(z)}{\partial z} = \alpha(\lambda) \cdot I_0 exp(-\alpha(\lambda) z). \tag{3.48}$$

3.4 Simulation of External Quantum Efficiency Characteristics

For the simulation of EQE characteristics, the principle simulation methods explained above are used as well. The difference is, that the given spectrum is divided into multiple small sub-spectra. For each of these spectra a single optical (TMM) simulation and a subsequent drift-diffusion simulation is performed. With the simulated current $J_\mathrm{calculated}$ at the contacts of the device and the reference current J_ref, the EQE can be calculated for each sub-spectrum according:

$$EQE(\Delta\lambda) = \frac{J_\mathrm{calculated}}{J_\mathrm{ref}} \tag{3.49}$$

Where the referent current can be calculated over the amount of photons in the sub-spectrum:

$$J_{\mathrm{ref}} = \cdot \int_{\lambda_{\mathrm{end}}}^{\lambda_{\mathrm{start}}} \frac{I(\lambda) \cdot \lambda}{hc} d\lambda \tag{3.50}$$

Where $I(\lambda)$ is the wavelength dependent intensity density of the given spectrum and λ_{start} and λ_{end} are the start and end wavelength of the sub-spectrum. Since the EQE connects both levels of semiconductor and optical simulation over a wavelength dependent approach, electical effects can be observed can be observed in the EQE as well. It is important to note that in order to simulate realistic EQE curves, one has to set the electrical parameters carefully.

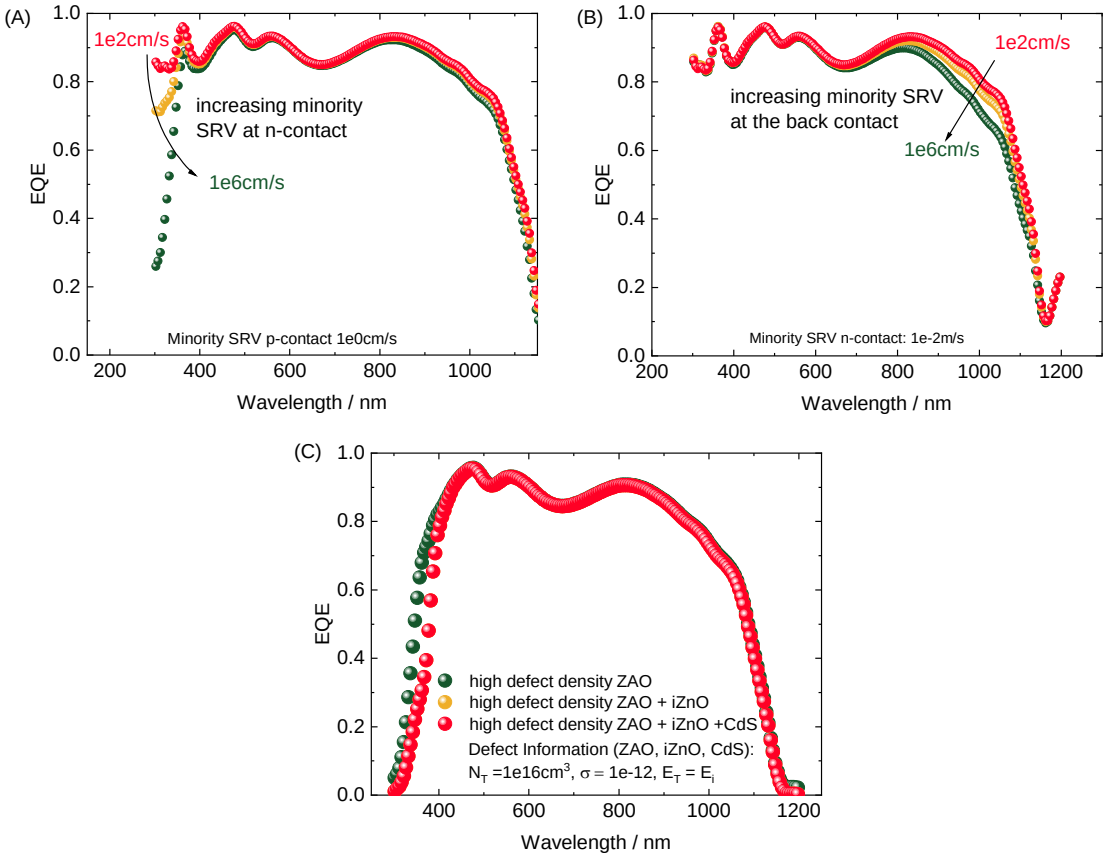

Figure 3.15: Simulated EQE curves with effect of the (A) minority SRV at the n-contact, (B) minority SRV at the p-contact and (C) bulk SRH recombination in different layers on top of the CIGS.

Figure 3.15 (A) and (B) show examples of simulated EQE curves of a CIGS solar cell with a variation of the front and back contact SRV, respectively. Even for high SRV values of $1{\cdot}10^6\,\mathrm{cm/s}$, the EQE does not drop to zero for small wavelengths. The change of the minority SRV at the front contact influences the EQE for small wavelength below $400\,\mathrm{nm}$ because in this wavelength range the penetration depth of the corresponding photons is small. Most of these high energy photons are absorbed in the transparent conductive oxide (TCO) layers already. In contrast long wavelength photons above approx. $1000\,\mathrm{nm}$ are absorbed in deeper regions of the cell, near to the back contact. Therefore, the minority SRV mainly influences the long wavelength region of the EQE. In this simulation no or a very low bulk recombination rate in the TCO and buffer layers was assumed. Only if a high SRH recombination is assumed in these layers, the EQE shows a realistic behavior

in the short wavelength range (compare Figure 3.15 (C)). This means, that the carrier generation in these layers could contribute to the current density, but it does not happen due to recombination processes like SRH or interface recombination.

3.5 Parameter Determination by Reverse Engineering Fitting

This method and the underlying algorithm was developed by Mario Zinßer within the scope of his doctoral study. A detailed description can be found in his thesis [95] or in the following publications: [132, 114]

The reverse engineering fitting (REF) is a special kind of fitting procedure, used for the parameter determination from experimental data. The method is based on a gradient-free procedure, since the calculation of derivatives is not possible in the treated cases. Within this approach a downhill simplex algorithm was used. The final goal is to match an experimentally obtained JV-curve with a simulated JV-curve by adjusting fundamental semiconductor properties (like mobilities, trap densities,...). Since JV-curves of real devices include lateral current transport losses in grid and TCO, a first REF has to be performed to exclude the resistive losses and obtain the internal material JV-curve of the actual semiconductor junction. Within the 2D electrical Poisson solver a parameter set of the material pn-junction (identifier:mat) (j_{ph}^{mat}, j_0^{mat}, n_d^{mat}, r_s^{mat}, r_{sh}^{mat}) is obtained from the initial parameter set (j_{ph}^{exp}, j_0^{exp}, n_d^{exp}, r_s^{exp}, r_{sh}^{exp}) via the REF (compare dissertation Mario Zinßer [95] or publications [132, 133, 114]).
In a second REF step, the simulated semiconductor JV-curve is matched with this material parameter set. Herein the set of the pn-junction JV data, which is given by n voltage current pairs (V_i^{mat} , I_i^{mat}) is compared with the simulated I-V curve with also n voltage-current pairs (V_i^{mat}, $I^{sim}(V_i^{mat})$). In each step of the optimization, the semiconductor properties are varied in order to find a better set of parameter values. The final loss function for the optimization is the mean squared error [134]:

$$\chi = \frac{1}{\sum_{i=0}^{n-1} w_i} \cdot \sum_{i=0}^{n-1} w_i \cdot \left(I_i^{mat} - I^{sim}(V_i^{mat}\right)^2 \tag{3.51}$$

with the weights w_i, which consider non-equidistant voltage steps and an exponential current-voltage dependence [114]. The parameters are varied until a certain accuracy of the loss function is reached. In order to ensure reasonable runtimes and good convergence, the amount of parameters was limited to 4 to 6, depending on the application. The reliability of this method is demonstrated in [132].

To determine the quality of the fit, the ratio of the sum of all residual squares with respect to the sum of all total squares are calculated. The exact calculation is given as

$$R^2 = 1 - \frac{\sum_{i=0}^{N-1}(y_i - p_i)^2}{\sum_{i=0}^{N-1}(y_i - \bar{y})^2} \tag{3.52}$$

with all N measured values y_i, their mean value $\bar{y} = \frac{1}{N}\sum_{i=0}^{N-1} y_i$, and the corresponding predicted value p_i [114].

3.6 Methodology of Loss Analysis

To obtain knowledge about the dominant loss paths in a CIGS solar cell and to determine the magnitude of these losses, a loss analysis can be performed. Herein optical, and electrical losses are considered. The optical loss in thick “incoherent“ layers is calculated via the Lamber-Beer law, introduced in Section 3.3.2. The coherent layerstack is calculated via the TMM. The TMM directly gives the part of reflected light (R) of the layerstack, the absorbtance (A_i) in each single layer i and the amount of transmitted light (T) into the substrate (incomplete absorption). These quantities are directly calculated into current and therefore power losses.

Since every optical loss, results in a reduction of the J_{SC} of the solar cell, a reduction of the V_{OC} occurs as well. This loss in V_{OC} (due to the loss in J_{SC}) is taken as an extra loss in the analysis.

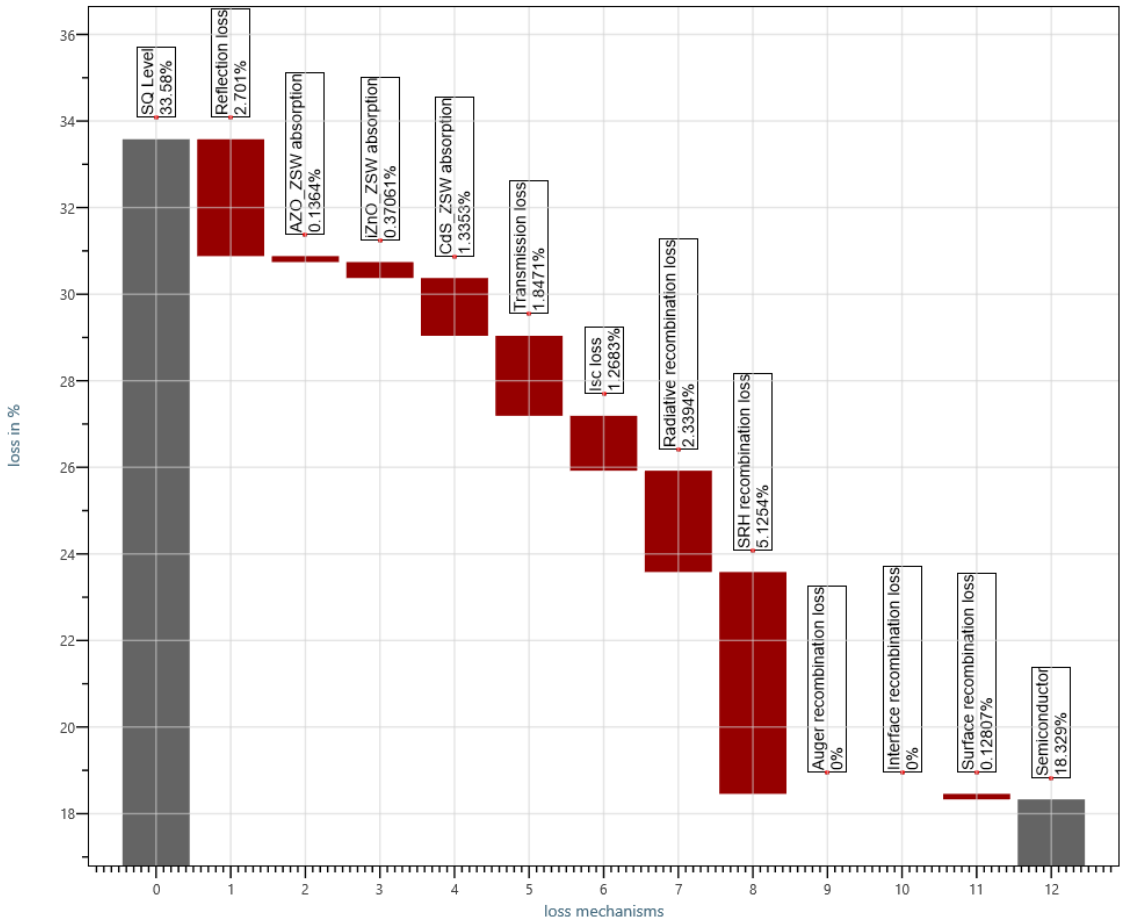

Figure 3.16: Representative example of the illustration of a loss analysis in the presented software.

After the determination of the optical losses, the electrical losses are calculated by performing drift diffusion simulations of the illuminated device. Since the single recombination mechanisms are not independent from each other, a defined calculation protocol must be followed. The idea behind the protocol is to switch on the different recombination mechanism after each other and perform a semiconductor simulation each time. The difference in power of two subsequent simulations corresponds to the power loss of the last recombination mechanism.

The first simulation is performed with only the radiative recombination activated, since it represents the most fundamental recombination type.

At this point it must be mentioned that the described procedure represents an estimation for the upper limit of the power loss due to radiative recombination based on the assumption that the emitted photons are entirely lost. In fact, these photons can take the following paths within the cell: either they reach an adjacent layer and are absorbed there, or they leave the solar cell completely and are thus not available for current generation. However, it is also possible for photons emitted by radiative recombination to be absorbed in the CIGS and can thus generate new free charge carriers. This case is known as photon recycling, as described in reference [135]. Photon recycling was not considered in this simulation - it is assumed that every photon produced by radiative recombination leaves the CIGS absorber and is therefore counted as a loss. More detailed calculations regarding the radiative recombination loss can be found in literature [136].

The further order of considered recombination mechanisms follows the way of charge carriers within the device: the next mechanism after the radiative recombination is the SRH recombination, followed by the Auger recombination. Afterwards optional interface recombination is taken into account. At last the power loss due to recombination of minority charge carriers at contacts is calculated.
All calculated power losses are plotted together with the SQ efficiency and the resulting efficiency of the device. Figure 3.16 illustrates the results of an exemplary loss analysis of a CIGS solar cell, displayed in the GUI of the software. Like commonly assumed in literature, the result of loss analysis of a CIGS solar cells reveals that the non-radiative SRH recombination is the largest loss mechanism in the semiconductor layerstack.

3.7 Quasi-three Dimensional FEM Poisson Solver for the Calculation of Lateral Electrical Transport

The quasi-three-dimensional Poisson solver was written by Mario Zinßer and was used by the author within this work. For further readings see following publications [132, 137, 133, 114] or the dissertation of Mario Zinßer [95].

For the actual simulation of laterally extended devices, an electrical calculation on top of the semiconductor simulation is necessary to account for the lateral current transport (in TCO and Grid etc.). Herein a quasi-three dimensional FEM Poisson solver was used. It is based on resistive connection of neighboring finite elements and calculates the spatially resolved potential distribution within a solar device. From this, all other properties like currents can be calculated. Figure 3.17 shows a typical simulation result of a back and front potential distribution of a typical $0.5\,\mathrm{mm}^2$ CIGS solar cell. For further information the reader is referred to the references in the introduction of this section.

The following nomenclature is used within this thesis: A device simulation always refers to a simulation of a laterally expanded solar cell using the quasi-3D Poisson solver. In contrast, a semiconductor simulation denotes the simulation of a semiconductor layerstack on material level with the methods introduced in Section 3.2 and Section 3.3, based on the Drift-Diffusion equations. The result of the semiconductor simulation can then be used as input for lateral current simulation.

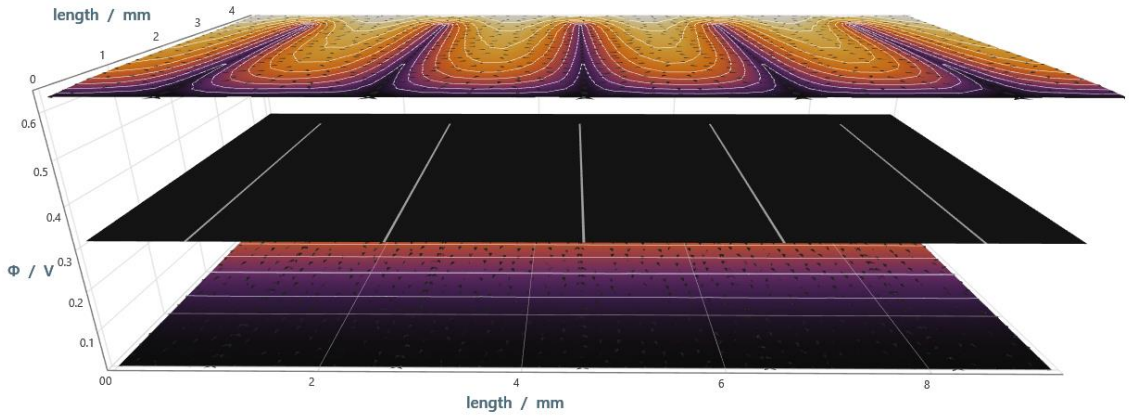

Figure 3.17: Representative simulation result of a potential distribution of the back and the front potential of a CIGS solar cell.

Conclusion

This chapter shows the numerical basics for the simulation of CIGS cells. Starting from fundamental equations like the Poisson's and continuity equation, a simulation tool is developed. With the implementation of interface effects, temperature dependencies and exact modelling of SRH recombination, it is possible to describe complex simulation models like heterojunctions of CIGS solar cells. The optical modelling was realized by TMM and Lambert-Beer calculations. Due to the detailed simulation model, it is possible to allocate and quantify all losses, occurring in a CIGS semiconductor layerstack. Herein, the loss analysis reveals, that the SRH recombiantion of charge carriers via defects is the major loss path in CIGS solar cells. Therefore the exact knowledge of the defect properties is crucial for a reliable simulation. This topic is addressed in the next chapter.

4 Basic Physics of Deep Level Transient Spectroscopy and Experimental Realization

As the last Chapter reveals, the Shockley-Read-Hall (SRH) recombination of charge carriers via defects is the dominant loss factor in Cu(In,Ga)Se_2 (CIGS) solar cells. In order to conduct numerical investigations on the influence of inherent defects in CIGS, it is inevitable to have detailed information of the characteristic properties of the defects. Only with reliable data on the defects, a robust numerical modelling of a CIGS solar cell is possible. For the determination of the defect properties of the investigated CIGS material, a method called Deep Level Transient Spectroscopy (DLTS) was used in this thesis. Since the measurement technique of DLTS plays an important role in the presented work, the experimental setup, the fundamental physics and the used methods are explained in detail in this chapter.

The principle of DLTS measurements is based on the trapping and releasing of carriers by electrical active defects in a semiconductor material. Due to a voltage pulse, free charge carriers (comparable to light induced free charge carriers) are created. Parts of them are trapped by defects and are only released after some time after the pulse. The interaction of the charge carries with the defects is observed by the change of the capacitance of the sample. From the exact behavior of the capacitance with time, it is then possible to derive the properties of the defects and thereby determine the dimension of the related loss.

In Section 4.1 the actual DLTS technique is explained along the original technique and with an overview of some enhancements and modifications of this technique in Section 4.1.4. Section 4.2 describes the used measurements setup and explains the basic hardware components of the setup. Section 4.3 gives an overview of the sample preparation.

4.1 Defect Characterization in Semiconductor Materials Using DLTS Measurements

This section describes the principle of DLTS measurements: from the formation of a capacitance transient (Section 4.1.1) over the creation of the DLTS signal (Section 4.1.2) to the evaluation of the defect properties (Section 4.1.3). Finally some advanced DLTS techniques, used in this work, are described (Section 4.1.4).

4.1.1 Formation of a Capacitance Transient

The principle operation mechanism is based on applying of voltage pulses to the sample by the pulse generator and the subsequent recording of a changing capacitance with time (called a transient). The measurement of the capacitance is performed by the Boonton Capacitance Meter.

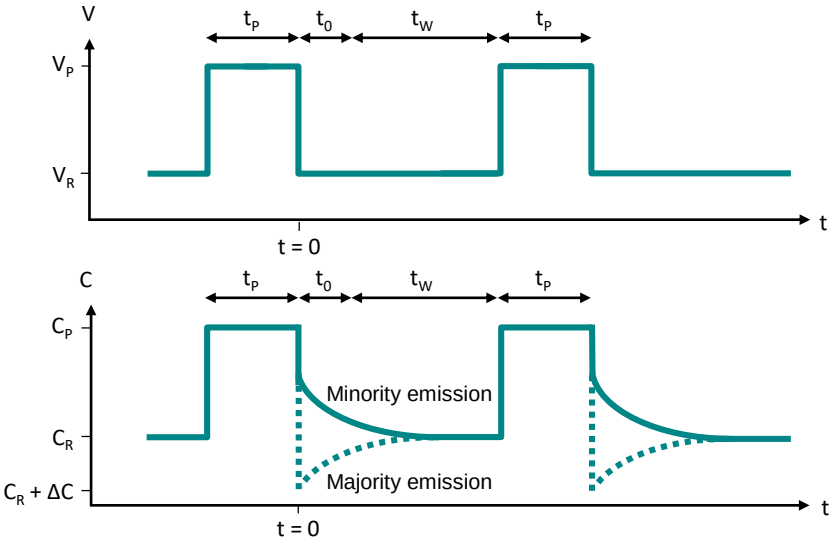

Figure 4.1: Principle of the DLTS operation with applying pulses and measuring and recording capacitance transients.

Figure 4.1 shows a schematic illustration of the applied voltage and the response of the capacitance during a DLTS measurement. As a starting point, a reverse voltage V_R is applied to the sample and a reverse capacitance C_R can be assigned to this state. If a pulse voltage V_P with a pulse width t_P is applied, this capacitance changes according to Equation 2.5 to the pulse capacitance C_P. After the pulse, the charge carriers in the bands can follow the electric field fast enough, but charge carriers trapped in defects are released by a thermal and therefore slower process. Right after the end of the pulse, the amount of free charge carriers is therefore different to the amount before the pulse. This changes the effective doping and thus leads to a difference between the equilibrium capacitance and the capacitance right after the pulse ΔC. Only when the trapped charge carriers are emitted, the capacitance returns to the initial value C_R. The change of the capacitance in time is called a capacitance transient $C(t)$ and is the fundamental measurement of the DLTS techniques.
Depending of which type of carriers is involved in the trapping and detrapping process, the transient occurs as a minority transient (decreasing capacitance) or a majority transient (increasing capacitance) (see Figure 4.1). A detailed description of the capacitance transient can be found in the next paragraph. Regarding the measurement technique, the time between two pulses contains of a waiting time t_0 and the time window t_W. The recording of the transient happens during the time period of t_W. The waiting time t_0 is necessary to avoid over-swing or other interfering signals after the pulse. This procedure of pulse, waiting time and time window is repeated several times to use a mean transient and reduce the signal-to-noise-ratio (SNR) [14].

The capacitance transient for a p-doped material like CIGS can be described (in case of a single defect state) via an exponential decay [26]:

$$C(t) = C_\mathrm{R}\left(1 - \frac{p_\mathrm{T}(t=0)}{2N_\mathrm{A}} exp\left(-\frac{t}{\tau_\mathrm{p}}\right)\right) = C_\mathrm{R} + \Delta C exp\left(-\frac{t}{\tau_\mathrm{p}}\right) \tag{4.1}$$

with the density of occupied traps at the end of the pulse $p_\mathrm{T}(t=0)$, the time constant of the emission process $\tau_\mathrm{p} = 1/e_\mathrm{p}$ and the capacitance at reverse bias

$$C_{\mathrm{R}} = A\sqrt{\frac{q\epsilon_0\epsilon_{\mathrm{r}}N_{\mathrm{A}}}{2(U_{\mathrm{bi}} - U_{\mathrm{R}})}}. \tag{4.2}$$

Herein A is the area of the sample and U_{bi} is the build-in voltage of the pn-junction. The capacitance difference ΔC is then defined for a majority carrier emission by [26]:

$$\Delta C = -C_{\mathrm{R}}\frac{p_{\mathrm{T}}(t=0)}{2N_{\mathrm{A}}}, \tag{4.3}$$

for a minority carrier emission by:

$$\Delta C = C_{\mathrm{R}}\frac{n_{\mathrm{T}}(t=0)}{2N_{\mathrm{A}}}. \tag{4.4}$$

This description of the capacitance transient is the basic principle for the DLTS measurement. In real devices, the emission processes of multiple defect states superimpose each other.

4.1.2 From Capacitance Transient to the DLTS Signal

As already mentioned, the emission of charge carriers from defects, is a thermally activated process and therefore depends on the temperature of the sample. Hence, the capacitance transient changes when changing the temperature of the sample [14]. This effect is utilized in DLTS measurements. Figure 4.2 (A) shows how the capacitance of a representative CIGS sample changes with increasing temperature due to the change in carrier emission. The resulting DLTS signal (Figure 4.2 (B)) can be created by translating each capacitance transient in a scalar value. In the simplest case, which is the original method introduced by Lang et al. [105], the transients are evaluated via a double boxcar-function. This means the transients are evaluated at two points in time by taking the difference in the capacitance:

$$\Delta C = C(t_2) - C(t_1) = \frac{p_{\mathrm{T}}(0)}{2N_{\mathrm{A}}}C_0\left(exp(\left(-\frac{t_2}{\tau_{\mathrm{p}}}\right) - exp(\left(-\frac{t_1}{\tau_{\mathrm{p}}}\right)\right) \tag{4.5}$$

Due to the low emission rates at low temperatures, the capacitance transient is flat, and the corresponding DLTS signal is low (see violet data points). On the other hand, at high temperatures the emission process can happen very fast, so that the main capacitance drop of the transients takes place before t_1 (compare red data points). In between, there is a temperature where the capacitance drop between the two times t_1 and t_2 becomes maximal/minimal and therefore a maximum/minimum occurs in the DLTS signal. Within the presented work, signals of majority defects occur as maxima in the DLTS temperature scan, while signals of minority defects occur as minima. The temperature $T_{\mathrm{max/min}}$ at which this maximum/minimum occurs depends strongly on the exact values of t_1 and t_2 and on the value of the time window t_{w}. Both dependencies are used in the following step of the DLTS evaluation, discussed in the following section.

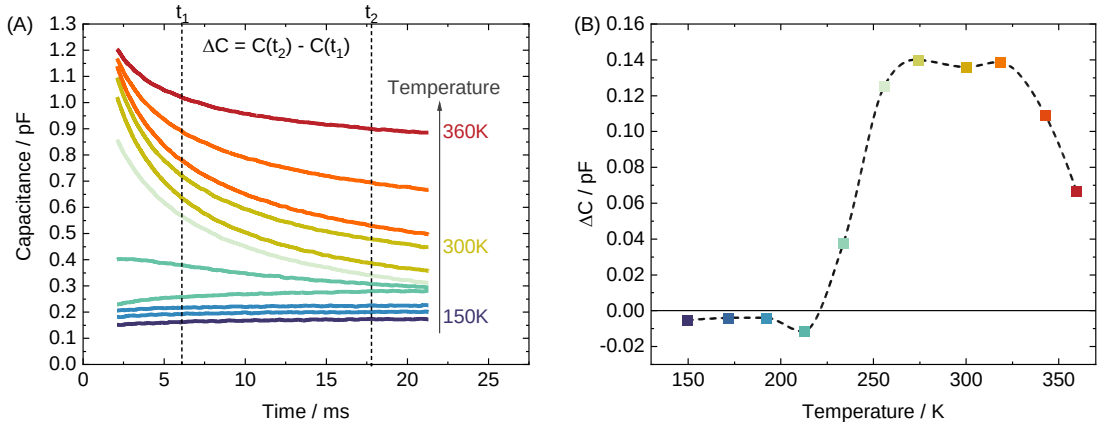

Figure 4.2: (A) Temperature dependence of capacitance transients of a CIGS solar cell. The transients are shifted for sake of readability. (B) Resulting DLTS signal.

4.1.3 Determination of Characteristic Defect Properties

The actual evaluation of the fundamental defect properties is conducted via an Arrhenius plot, created from the DLTS-Signal. Therefore, a maximum or minimum in the temperature scan is assigned to an emission rate or time constant. For the boxcar-DLTS the emission rate can be calculated analytically by taking the derivation of Equation 4.5 and setting it to zero. The corresponding emission time constant is:

$$\tau_{\mathrm{p,max}} = \frac{1}{e_{\mathrm{p,max}}} = \frac{t_2 - t_1}{ln(t_2/t_1)} \tag{4.6}$$

Based on the thermal emission rate e_{p} (inverse of the time constant) of trapped carriers:

$$e_{\mathrm{p}} = N_{\mathrm{V}} \nu_{\mathrm{th}} \sigma_{\mathrm{h}} exp\left(-\frac{E_{\mathrm{T}}}{k_{\mathrm{B}} T}\right) \tag{4.7}$$

an Arrhenius plot can be constructed. The found emission time constants / rates ($e_{\mathrm{p,max}}$ or $\tau_{\mathrm{p,max}}$ at the temperature scan extremum) can be plotted as one data point in a $ln(N_{\mathrm{V}} \nu_{\mathrm{th}} \tau_{\mathrm{p}})$ over $1/T$ plot. By varying the time window t_{W}, the evaluation points t_1 and t_2 or their ratio t_2/t_1, a shifting of the extremum on the T-axis is induced. Thus, for each constellation of the evaluation times, a new data point in the Arrhenius plot is obtained. Figure 4.3 (A) shows a schematic shifting of a maximum in the DLTS temperature scan due to t_{W} or $t_{1,2}$ variations. For each of these curves a corresponding data point in the Arrhenius graph (B) can be calculated (labeled by colors). Herein, increasing time windows are shifting the maximum in the temperature scan to lower temperatures. The corresponding data points in the Arrhenius plot occur on the right side, due to the inverse temperature axis.

The energetic position of the underlying defect can be determined via the slope $(E_{\mathrm{T}} - E_{\mathrm{V}})/k_{\mathrm{B}}$ of a linear regression. The y-axis intersect is linked with the capture cross section over $ln(N_{\mathrm{V}} \nu_{\mathrm{th}} \tau_{\mathrm{p}} \sigma_{\mathrm{p}})$. Nevertheless, the determination of the capture cross section via the Arrhenius plot method is very error-prone [138] due to the logarithmic y-axis. For a more accurate determination one has to perform a pulse width variation [139].

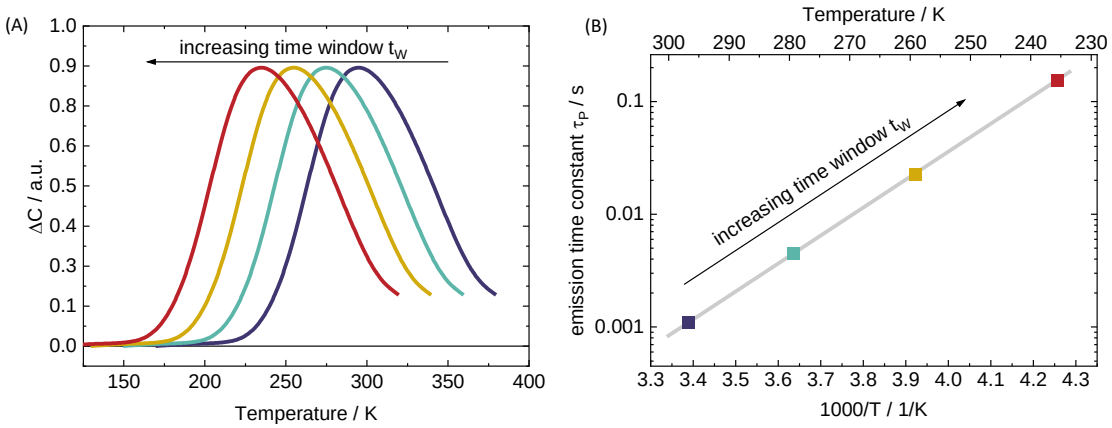

Figure 4.3: (A) Shifting of the DLTS maximum due to t_{W} or $t_{1,2}$ variation and (B) resulting Arrhenius graph.

The defect density cannot be calculated from the Arrhenius plot, but via the amplitude of the capacitance transient ΔC. With Equations 4.3 and 4.4 the defect density N_{T} is [87]:

$$N_{\mathrm{T}} = \Delta C \frac{2N_{\mathrm{A}}}{C_{\mathrm{R}}} \frac{W_{\mathrm{R}}^2}{L_{\mathrm{R}}^2 - L_{\mathrm{P}}^2} \tag{4.8}$$

Herein, W_{R} is the width of the space charge region (SCR) under reverse bias, L_{R} and L_{P} are the positions of the intersections of the trap level and Fermi level at reverse bias and pulse voltage, respectively.

4.1.4 Advanced DLTS Techniques

While the previous section described the basic method of DLTS, several modifications and extensions are available within the used DLTS system from PhysTech. The most important points for this thesis are discussed in this section.

Correlation Functions

In order to generate a higher number of data points in the Arrhenius plot, the used software of PhysTech evaluates the recorded capacitance transients not only with the classical Boxcar method, furthermore so called "correlation function" or "weighting functions" $w(t)$ are used. Instead of evaluating the transients at two single points in time, the transients are weighted according to:

$$\Delta C = 1/t_{\mathrm{W}} \int_{t_0}^{t_0+t_{\mathrm{W}}} w(t)C(t)dt. \tag{4.9}$$

Typical weighting functions are sine, cosine or step-functions. With this method, different regions of the transient can be taken more into account than other and signals can be separated. Figure 4.4 gives an example of the standard boxcar weighting function (A) and the sinus (b1) weighting function (B) which is the standard function of the used software. In case of a non-Boxcar correlation function, Equation 4.6 for the calculation of the emission time constant at the DLTS maximum doesn't hold anymore and $\tau_{\mathrm{p,max}}$ has to be calculated numerically by the software. The

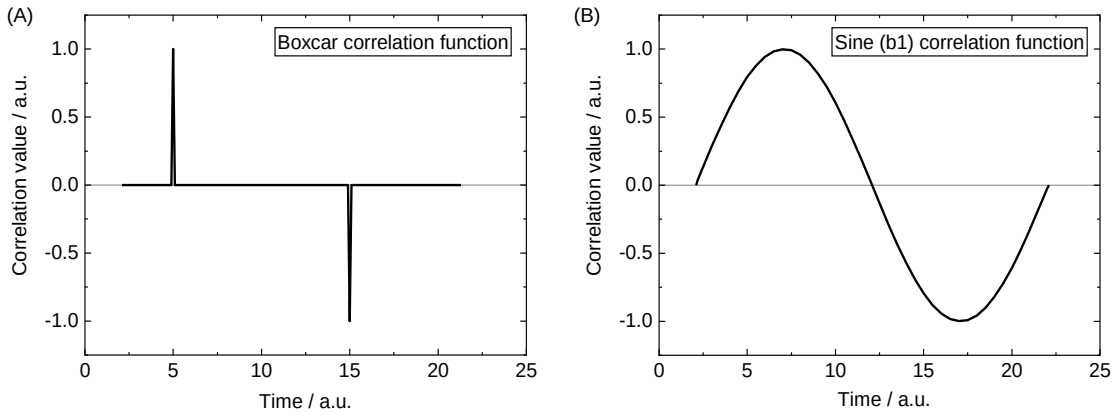

Figure 4.4: Examples of correlation functions used by the PhysTech Software. Graph (A) illutrates the classical double-Boxcar correlation function and Graph (B) the "b1" sinus correlation function.

determination of $\tau_{\mathrm{p,max}}$ is again realized by calculating the derivative of Equation 4.9 and finding the root by setting it to zero [140].

Reverse Deep Level Transient Spectroscopy (RDLTS

In a Reverse Deep Level Transient Spectroscopy RDLTS measurement, in contrast to the DLTS measurement, the pulses are applied in the reverse direction; i.e. the negative voltage is increased to U_{P} during the pulse starting from the initial voltage U_{R}. Since with the increase of negative voltage the width of the SCR increases, the charge carriers are emitted during the pulse. After the end of the pulse, a trapping of the charge carriers is measured and the sign of the capacitance transient is reversed. Hence, in a RDLTS measurement, majority pulses appear as minimum and minority pulses appear as maximum in the DLTS signal. Figure 4.5 illustrates this relation between peak polarity a pulse direction schematically. An advantage of the Reverse DLTS (RDLTS) method is, that it is very sensitive to minority defects [141].

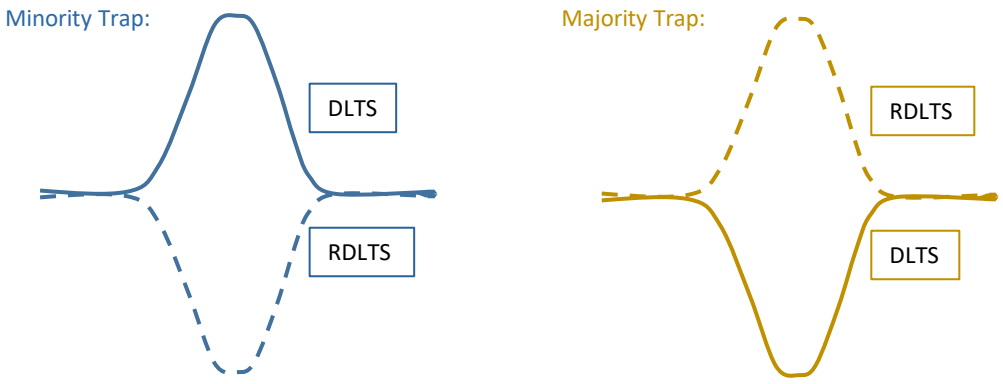

Figure 4.5: Relation between pulse direction (DLTS or RDLTS) and the peak polarity in the resulting temperature scan.

Deep Level Transient Fourier Spectroscopy (DLTFS)

In the Deep Level Transient Fourier Spectroscopy (DLTFS) method, the Fourier coefficients are obtained from the transients by using discrete Fourier transforms. From them, the emission time constants τ_{e} and τ_{p} and the amplitudes of the transients can be calculated [142]. From the tome

constants, analogous to the procedure in the classical DLTS method, the energetic position of the trap in relation to the valence band $E_{\mathrm{T}} - E_{\mathrm{V}}$, the trapping cross section σ_{n} or σ_{p}, and the defect density N_{T} can be determined. The advantage of this evaluation method is, besides the high resolution in determining the defect levels, that it can be done completely automatically.

High Energy Resolution Analysis - Deep Level Transient Spectroscopy

Another possibility to obtain the emission time constants τ_{e} and τ_{p} directly from the transients is the evaluation by means of so-called High Energy Resolution Analysis (HERA). The term HERA covers different evaluation methods, in which various mathematical methods such as Fourier transform, Laplace transform, exponential fitting or convolution are applied. In this work a direct evaluation of the transients by means of inverse Laplace transformation was used, as well as an evaluation method, which combines inverse Laplace transformation and a multi-exponential fitting of the transients. The advantage of these evaluation methods is that they can be fully automated. Defect levels can also be determined with a very high resolution of overlapping emission processes. More information can be found elsewhere [87].

4.2 Cryostate Setup for Temperature Dependent Measurements and electrical Hardware

Both measurements, DLTS and capacitance-voltage (CV) are conducted in a cryostate setup which offers the possibility for a variety of electrical characterizations tools (DLTS, CV, IV, C(f), etc.) and the possibility to perform temperature dependent measurements due to a cooling system with liquid nitrogen as cooling agent. Within this work the setup was used for DLTS, CV and temperature dependent current-density-voltage (JVT) measurements. Figure 4.6 shows a schematic illustration of the used setup. It shows the electronic hardware for DLTS and CV measurements. For JVT measurements, the "DLTS System" part of the hardware is replaced by a Keithley source measure unit. The chamber of the cryostate can be evacuated below values of $1{\cdot}10^{-6}\,\mathrm{mbar}$. The vacuum

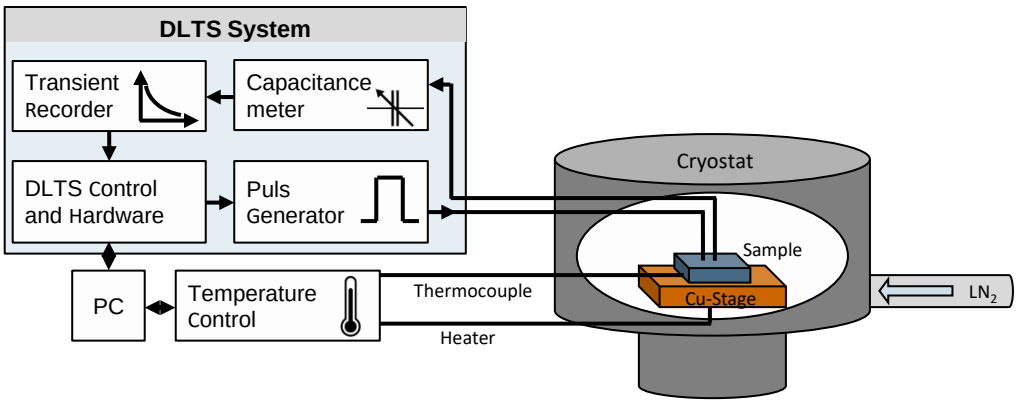

Figure 4.6: Schematic illustration of the used cryostate setup used for DLTS and CV measurements.

is necessary to prevent the condensation of water inside, when the Cu-Stage is cooled with liquid nitrogen, which results in temperatures around and slightly below $80\,\mathrm{K}$. The nitrogen is supplied through a Coaxial transfer line with multiple insulation shields from a cryogenic dewar and can be controlled manually via a shield flow mechanism. The temperature control is realized by a temperature controller by Lakeshore Modell 335, two single thermocouples and a heater. The heater is located below the stage and is working against the cooling of the liquid nitrogen. One of the thermocouples is mounted directly on the copper stage, the second one is soldered on the sample in order to have the exact temperature of the device. While the stage sensor is used for the controlling of the temperature, the value of the second one is used as sample temperature. The thermal contact between stage and sample was realized by a double-sided adhesive copper tape, which enabled sufficient thermal conductivity under vacuum conditions. Nevertheless, due to a non-perfect thermal contact, temperature differences between stage and sample of $10\,\mathrm{K}$ or more can occur. The electrical contact is established with contacting tips mounted on a micro-manipulator for accurate contacting, even on small contacting areas. The electrical signal is transferred with coaxial cables to the measurement units.

Electrical hardware

Within this work a Hera DLTS System from PhysTech was used. The DLTS system uses the in Section 4.2 explained cryogenic setup. The measurement system itself contains the following hardware components: The DLTS control hardware, a Boonton capacitance meter [143] and a pulse generator. In the used setup for this work, a special fast pulse generator was used, which enables pulses down to $1{\cdot}10^{-5}\,\mathrm{s}$.

The principle operation mechanism is based on applying voltage pulses to the sample by the pulse generator and the subsequent recording of a changing capacitance with time (called a transient). The measurement of the capacitance is performed by the Boonton Capacitance Meter. From the transients, the characteristic properties of involved defects can be determined as described in Section 4.1.3. While the original way of evaluation is the boxcar-car approach with a linear regression in the Arrhenius plot, some advanced techniques are developed in the last decades.

4.3 Sample Preparation

Due to the specification of the Booton Capacitance meter and to ensure high sensitivity, the capacitance of the samples has to be below $4\,\mathrm{nF}$. The capacitance of standard CIGS solar cells, used in this work, lies in the range of $100\,\mathrm{nF}$ for an area of $0.5\,\mathrm{cm}^2$. Therefore the active area was reduced down to $1\,\mathrm{mm}^2$ to provide a suitable capacitance for DLTS measurements. With regard to an optimal electrical contact, the area was defined by a square with $1\,\mathrm{mm}$ edge length around the metal contacting pad of the metallization grid by mechanical scribing. Figure 4.7 (A) shows an optical microscopy image of the defined area around the metal pad. This method serves good results, but for measurements with low noise and optimum contact properties (low leakage current) the definition of the area has to be improved. The most prominent issue of the mechanical scribing are the frayed edges leading to shunting currents due to local short circuits.
To avoid this an area definition method by a lithography process was introduced. The area is defined between the metal grid fingers within the former active area of the solar cell. With four laser patterned lines the new area is defined by removal of the top transparent conductive oxide (TCO) layer (compare Figure 4.7 (B)). This method can also lead to some problems due to high contact resistances between measurement tip and sample and electrical shunts due to scratching of the tips

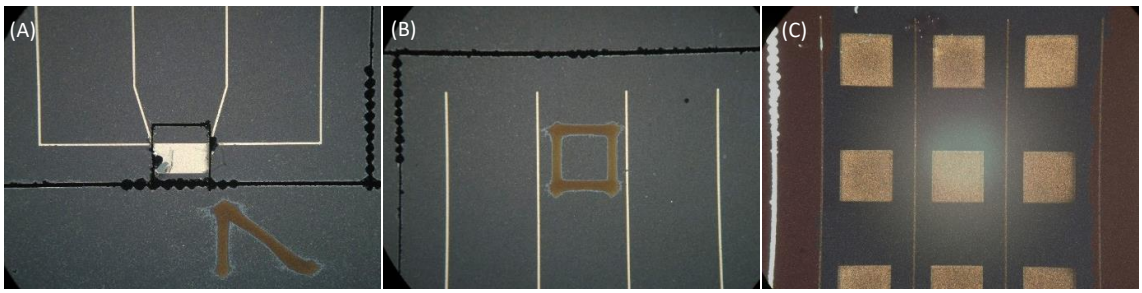

Figure 4.7: Different methods of area definition for DLTS measurements. (A) mechanical scribing around the pad of the grid metallization, (B) lithographic definition within the active cell area between two gridfingers and (C) additional metallization pads with etched aluminum doped zinc oxide (AZO).

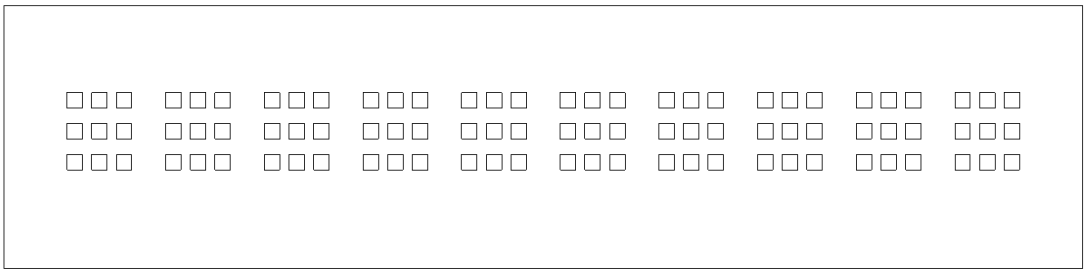

Figure 4.8: CAD drawing of the used mask for the evaporation of additional metallization pads.

through the thin TCO layer.

To avoid this, a second method was invented, where in the first step a new metal pad is deposited on to the sample with the desired area. In a second step, the TCO around the pad is removed by a wet chemical etching step in order to electrically isolate the sample from the rest of the cell. Figure 4.7 (C) shows an optical microscopy image of an additionally deposited metal pads. Regions without AZO occur more bluish, regions with AZO occur reddish. The etching of the TCO of these parts was prevented by a coating of acid proof photoresist.
For the correct alignment of the pad between the grid fingers, a special evaporation mask was designed, which orientates to the original cell geometry. Figure 4.8 shows a CAD drawing of the used mask. This method enables measurements with low leakage current, small contact resistances and therefore high quality signals.

4.3.1 Standard measurement procedure and measurement parameters

This section gives an summary of the applied measurement procedure and standard measurement parameters for the DLTS measurements of CIGS solar cells.
In order to ensure that all samples were measured in a stable state, they were left to relax in the dark in the cryostat system for at least 30 minutes before the start of the measurement. After this relaxation step, some basic measurements have been conducted. Herein the quality of the contact was tested in terms of leakage current and capacitance compensation. Furthermore the doping density of the sample was measured via a CV measurement and a subsequent Mott-Schottky evaluation, as described in Section 2.6.
The standard procedure of the DLTS measurement consists of a measurement in forward pulse direction during the cooling of the sample down to liquid nitrogen temperature and a subsequent

measurement in reverse pulse direction during the heating of the sample.
The measurement parameters of both directions have been the same and have been set in order to cover a large range by using a 3 different time windows along with two different pulse widths (resulting in a 3x2 matrix): the time window t_{W} was set to 1, 10 and $100\,\mathrm{ms}$ and was adapted if need in later measurements. The pulse width was selected to be in the order of 1 and $10\,\mathrm{ms}$ and was also adapted if needed. For example, short pulse widths of $0.1\,\mathrm{ms}$ often result in measurements with good peak separation but a low SNR. The values of the voltage parameters V_{P} and V_{R} were set for an optimum ratio of peak amplitude (larger pulses result in a larger scan depth and therefore more participating defects) and peak resolution (often lower pulse voltages result in better peak resolution). For V_{P} values of between 0 and $0.1\,\mathrm{V}$ and for V_{R} values between -2 and $-0.5\,\mathrm{V}$ were used. After the measurements, the evaluation was conducted by an manual maximum analysis and for promising samples and measurements an DLTFS and Hera evaluation was conducted (see sections above).

Conclusion

In summary, the method of DLTS provides the possibility of the exact determination of defect properties like energetic position, defect density, capture cross section and defect type (majority or minority trap). These parameters can be directly used as input parameters for the semiconductor simulation and enables the reproduction of the underlying defects. Therefore the shape of a capacitance transient, caused by a delayed emission of charge carries from defects, is analyzed. In the classical technique of DLTS, from the temperature dependence of the capacitance transients a DLTS signal is obtained, followed by an evaluation via an Arrhenius plot. In advanced methods, the capacitance transients are directly evaluated over Fourier or Laplace transformations in order to resolve superimposing emission processes. The whole measurement is conducted in a cryostate setup with liquid nitrogen cooling in order to enable the temperature dependent measurement.

5 Setting up a Device Model for a High Efficiency CIGS Solar Cell

In this chapter the process of setting up and defining a semiconductor model is described in detail. For this purpose, a high efficiency (and a former world record from 2016) solar cell from the high efficiency line at Zentrum für Sonnenenergie- und Wasserstoffforschung Baden-Württemberg (ZSW) with $\mathrm{PCE} = 22.6\,\%$ is used as the experimental counterpart. Within this section, the simulation model is built up from parameters obtained by measurements of capacitance-voltage (CV), Deep Level Transient Spectroscopy (DLTS) and time of flight secondary ion mass spectroscopy (ToF-SIMS) and reproducing the basic measurements of IV characteristic and external quantum efficiency (EQE). Herein, DLTS measurements have been performed not on the record cell itself, but on a similar device. This chapter serves as a verification and an example of a semiconductor simulation with all belonging steps and therefore serves as a reference for the following chapters, where the building up of a semiconductor model is not described in detail for every single problem. First, the collection of the needed inputs for a detailed simulation is explained. Afterwards, the simulations results are compared with the experimental findings.

5.1 Finding the Right Inputs

This section illustrates the gathering of the most important input quantities for the simulation. First, determination of suitable parameters and the determination of layer thicknesses is discussed. Afterwards, the modelling of the band gap profile of the Cu(In,Ga)Se_2 (CIGS) layer via a multi-layer approach is explained. In the end, DLTS measurements on a high efficiency CIGS solar cell are shown, which results are used as input for the semiconductor simulation of the record cell.

5.1.1 Setting the Baseline Parameters

Some of the most important parameters are the layer thicknesses, influencing both, the optical and electrical calculations. Figure 5.1 shows a schematic layerstack of the sample indicating an absorber layer with $2700\,\mathrm{nm}$, a thin cadmium sulfide (CdS) layer with $30\,\mathrm{nm}$ and a transparent conductive oxide (TCO) combination of zinc magnesium oxide (ZMO) and aluminum doped zinc oxide (AZO) with $50\,\mathrm{nm}$ and $200\,\mathrm{nm}$, respectively. The thickness values are obtained from scanning electron microscopy (SEM) cross-sections and from optical transmittance measurements. On top of, a $110\,\mathrm{nm}$ thick layer of magnesium fluoride (MgF_2) is deposited as an anti-reflective coating.

For the basic semiconductor parameters, not all quantities are experimentally accessible or only hard to acquire. Whenever possible, semiconductor parameters were based on the in-house measurements. Otherwise, values from literature were included. Table 5.1 gives an overview of the used simulation parameters for all materials which have been taken into account electrically (for example MgF_2 is only considered optically). The table is based on the baseline parameters, which are specified in Table A.2 in Section A.1. The bold numbers indicate values which have been

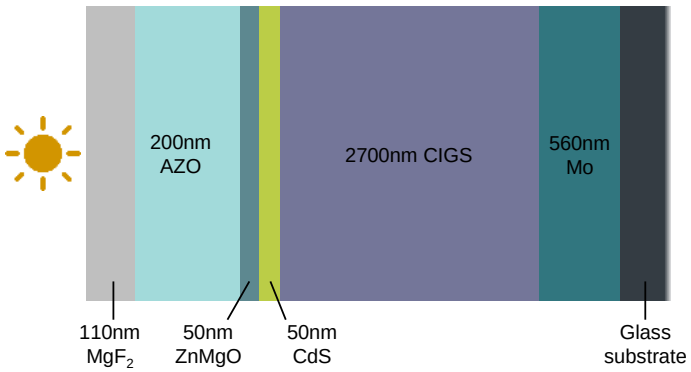

Figure 5.1: Schematic illustration of the layerstack of the high efficiency CIGS solar cell.

determined experimentally.
Information about energy bands and mobilities have been taken from the baseline model by Gloeckler et al. [144]. The minimum value of the band gap profile of the CIGS layer was determined to be $1.08\,\mathrm{eV}$ from EQE measurements. The exact implemented band gap profile of CIGS is discussed in Section 5.1.2.
For doping densities, typical values from in-house measurements or literature values have been used. The doping density of the CIGS layer, determined via CV measurements, reveals a value of approx. $2{\cdot}10^{16}\,\mathrm{cm}^{-3}$. Within the presented simulation, the Boltzmann statistic is valid. Therefore the TCO layers of AZO and ZMO the values have been set to $1{\cdot}10^{18}\,\mathrm{cm}^{-3}$ and $1{\cdot}10^{15}\,\mathrm{cm}^{-3}$, respectively For the defect properties of CIGS, the results from DLTS measurements have been used, which are discussed in Section 5.1.3. For all other materials, a mid-gap defect with high density is assumed in order to match the simulated EQE curve with the experimentally obtained one (problem discussed in Section 3.4).
The surface recombination velocity (SRV) of minorities at the contact was set to $1\,\mathrm{cm/s}$ of majorities to $1{\cdot}10^{7}\,\mathrm{cm/s}$. These values have been selected to match the V_{OC} of the experimentally obtained device characteristic. Nevertheless, the change of the minority SRV has only a minor influence on the device performance for devices with graded band gaps towards the back contact [146]. The radiative recombination coefficient for CIGS was set to $4{\cdot}10^{-11}\,\mathrm{cm}^3/\mathrm{s}$ according to Yamaguchi et al. [103]. The radiative coefficients of all other layers were set according to the reference [145]. The Auger recombination was not taken into account in this model. Therefore the coefficients were set to zero.
Optical Data for CIGS are taken from Minoura et al. [147]. Refractive data for all other layers have been measured in-house on the corresponding layers by spectral ellipsometry (SE).

5.1.2 Reproduction of the Band Gap Profiles in Numerical Simulations

Furthermore, ToF-SIMS measurements have been used to model the band gap profile of the solar cell. Figure 5.2 (A) shows the profiles of the GGI and CGI within the absorber layer and the resulting band gap gradient, calculated with two different formulas from Witte et al. [21] and Boyle et al. [20]. Figure (B) illustrates the band gap modelling for the simulation model in comparison to the band gap profile according to Boyle et al. The dashed light gray line indicates the approximated minimum band gap of $1.08\,\mathrm{eV}$ extracted from EQE, already indicating a difference to the calculated band gap profile minimum of $1.13\,\mathrm{eV}$. Therefore the band gap profile was modelled by shifting the profile downwards, until the minimum of the profile corresponds to the EQE value. Due

			CIGS	CdS	ZMO	AZO
Thickness		d / nm	**2700**	**30**	**50**	**200**
Band gap		E_g/eV	**1.08***	2.4	3.3	3.3
Chemical potential		χ/eV	-4.5	-4.2	-4.45	-4.45
Relative permittivity		ϵ_r	12.9	10	9	9
Effective DOS cond. band at 300K		$N_\mathrm{C}/\frac{1}{cm^3}$	2.2e18	2.2e18	2.2e18	2.2e18
Effective DOS val. band at 300K		$N_\mathrm{V}/\frac{1}{cm^3}$	1.8e19	1.8e19	1.8e19	1.8e19
Donor density		$N_\mathrm{D}/\frac{1}{cm^3}$	1e6	1e17	1e15	1e18
Acceptor density		$N_\mathrm{A}/\frac{1}{cm^3}$	**2e16**	1e6	1e6	1e6
Electron mobility		$\mu_\mathrm{e}/\frac{cm}{Vs}$	100	100	100	100
Hole mobility		$\mu_\mathrm{h}/\frac{cm}{Vs}$	25	25	25	25
Radiative recombination coeff.		$r_\mathrm{rad}/\frac{cm^3}{s}$	1e-11‡	1.7e-10	1.7e-10	1.7e-10
Auger coefficient electrons		$C_\mathrm{n}/\frac{cm^6}{s}$	0	0	0	0
Auger coefficient holes		$C_\mathrm{p}/\frac{cm^6}{s}$	0	0	0	0
Thermal velocity electrons		$\nu_\mathrm{th,e}/\frac{cm}{s}$	1e7	1e7	1e7	1e7
Thermal velocity holes		$\nu_\mathrm{th,h}/\frac{cm}{s}$	1e7	1e7	1e7	1e7
Deep defect	Energetic position†	E_T/meV	**450**	1200	1650	1650
	Trap density	$N_\mathrm{T}/\frac{1}{cm^3}$	**1e13**	1e20	1e18	1e20
	Capt. cross sect. electrons	σ_n/cm^2	**1e-12**	1e-14	1e-14	1e-14
	Capt. cross sect. holes	σ_p/cm^2	**1e-12**	1e-14	1e-14	1e-14

Table 5.1: Summary of the used semiconductor parameter within this chapter. The bold numbers are experimentally obtained values, all others are taken from literature [144, 121, 145, 103]. * indicates a graded band gap as given in the text. † energetic positions of defects are given with respect to the valence band maximum E_V. ‡ The value for the radiative recombination coefficient of CIGS was set according to [103].

to a missing coupling of optical and electrical calculations within layers with changing material parameters, a multi-layer approach had to be used. Therefore the CIGS layer was divided into 22 (sub-)layers. The first two layers have a thickness of $300\,\mathrm{nm}$ and $400\,\mathrm{nm}$, respectively and model the notch at the front of the CIGS layer. The remaining 20 layers have a thickness of $100\,\mathrm{nm}$ and build a linear grading towards the back contact. The optical data for the single layers are taken from the publication of Minoura et al. [147], providing GGI-dependent refractive data of CIGS. Due to the minor differences between the refractive data of the single sublayers, the error in the TMM calculation due to the multi-layer approch is neglectable. The electrical counterpart of the band gap profile was modelled by piece-wise introducing a grading via the a spline formalism (like explained in Section 3.2.5.2) resulting in a continuous function throughout the whole layer. Thus the treatment of the interfaces by thermionic emission is avoided.

5.1.3 DLTS Measurements on High Efficiency CIGS Solar Cells

DLTS measurements, in DLTS and Reverse DLTS (RDLTS) pulse direction, have been performed on a similar high efficiency cell, comparable with the record cell. The results of the DLTS measurements are shown in Figure 5.3 (A). Compared to the RDLTS measurements, the DLTS measurements show a better quality of the temperature scan itself and the corresponding evaluation

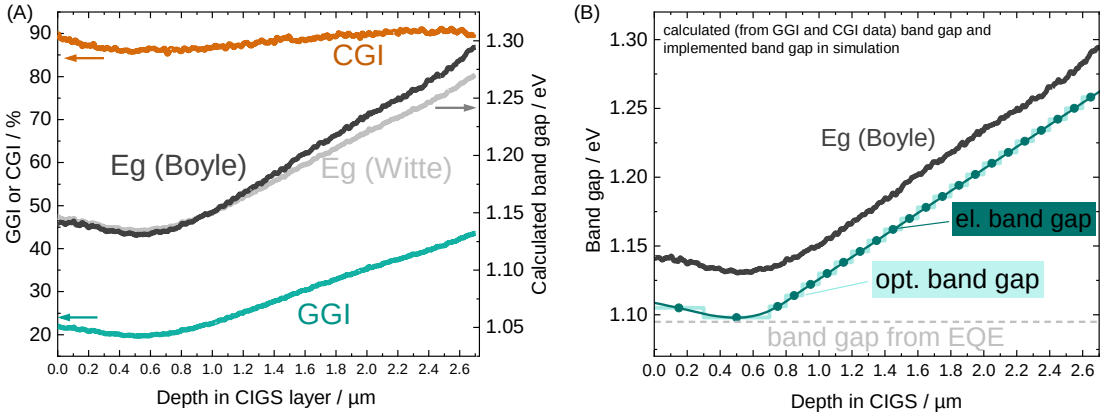

Figure 5.2: (A) depth profiles of Cu/(Ga+In) (CGI) (orange) and Ga/(Ga+In) (GGI) (blue) ratios within the CIGS layer of the high efficiency cell. The resulting band gap profiles are plotted in black (calculation according to Boyle et al. [20] and in grey (according to Witte et al. [21]). Graph (B) shows the modelling of the band gap profile in pale and dark blue in comparison to the calculated band gap by following Boyle et al.

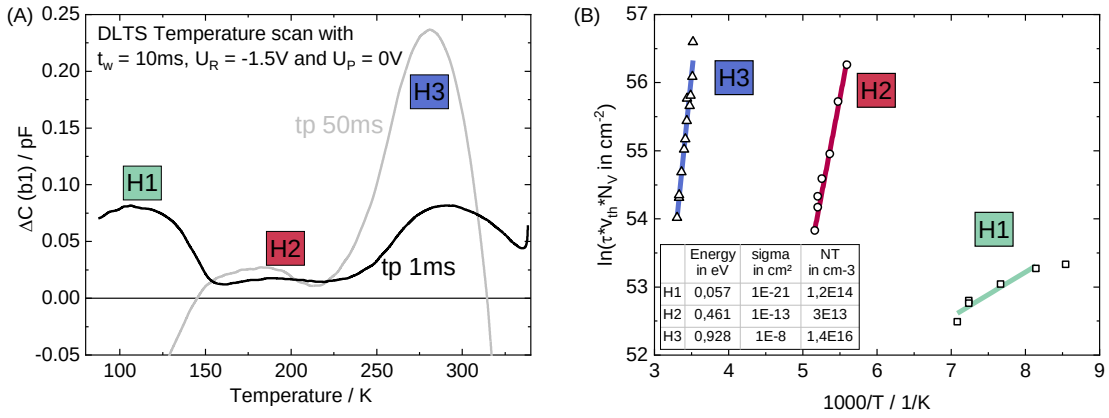

Figure 5.3: (A) DLTS measurement of a high efficiency solar cell with showing three majority trap levels H1, H2, H3. Graph (B) shwos the corresponding Arrhenius plots of the maximum evaluation.

of the extrema. This might be due to the fact, that the observed peaks “H1“, “H2“ and “H3“ have all majority traps as origin and RDLTS measurements are preferentially sensitive to minority traps. The temperature scans of two measurements with two different pulse widths are shown. While the $1\,\mathrm{ms}$ measurement reveals all three peaks, the $50\,\mathrm{ms}$ measurements shows rapidly decreasing signals for high and low temperatures, superimposing the peaks H1 and H3 such as H1 is not observed anymore and the peak position of H3 is affected (peak position should be independent of the pulse width). Especially for the evaluation of H3 this is a significant source of error, even for the short pulse measurement. Figure 5.3 (B) shows the corresponding Arrhenius plot of the three peaks, including a table with the defect properties. The H1 peak revealed an energetic position of only $57\,\mathrm{meV}$, representing rather a shallow defect level which might contribute to the effective doping. The H2 peak can be assigned to a defect at $460\,\mathrm{meV}$ above E_V and a defect density of $3{\cdot}10^{13}\,\mathrm{cm}^{-3}$. The third peak at $300\,\mathrm{K}$ exhibits unreasonable defect properties, although the data points in the Arrhenius plot revealed a very good linear behavior. The energetic position is evaluated to be $930\,\mathrm{meV}$ above E_V, which could be realistic, but a capture cross section of $1{\cdot}10^{-8}\,\mathrm{cm}^2$ is not. Also the trap density of more than $1{\cdot}10^{16}\,\mathrm{cm}^{-3}$ seems unreasonable and gives an indication, that this peak is influenced by metastabilities or other distorting effects. Therefore only the H2 defect was implemented in the simulation model. Nevertheless, during the simulation study the

value of the H2 trap density had to be reduced slightly to fit the result to the experimental data from $3{\cdot}10^{13}\,\mathrm{cm}^{-3}$ to $1{\cdot}10^{12}\,\mathrm{cm}^{-3}$ (see Table 5.1). This adaption is regularly necessary, because the value of the capture cross section from the Arrhenius plot is strongly error-prone and can only be used as a rough estimation of the order of magnitude.

5.2 Simulation Results

With the 1D simulation model from the last section, JV and EQE simulations can be performed. The results are shown in Figure 5.4 (A) and (B). Figure (A) shows the JV curves of the experimental measurements, the semiconductor simulation and a combination of the semiconductor simulation with a subsequent electrical simulation via the Poisson solver. The inserted table gives the characteristic quantities of the corresponding JV curves. The semiconductor simulation shows a similar V_{OC} as the experimental result with $743\,\mathrm{mV}$ instead of $741\,\mathrm{mV}$. But the fill factor (FF) is with $3\,\%$ higher than the experimentally obtained one of $80.6\,\%$ and the current is only slightly $0.2\,\mathrm{mA/cm}^2$ higher.

The slight differences between a model and an experiments are unavoidable, as different aspects and loss mechanisms appearing in experiments are not considered in the semiconductor simulation. For example, the shading of the metal grids has a small influence on the J_{SC}. In this case, the influence is small because most of the metallization was prepared outside the active area. A comparison with the results of the device simulation shows that the shading is responsible for a J_{SC} loss of $0.4\,\mathrm{mA/cm}^2$, which corresponds to a relative loss of only $1\,\%$, showing a good agreement.

The lateral current transport through the TCO and grid has a much larger influence on the device performance. The resistive losses mainly have an influence on the FF. It is reduced by $1.5\,\%$ from $83.6\,\%$ to $82.1\,\%$. This value is still $1.5\,\%$ higher than the experimental value, which shows that the model can be further refined and some parameters have to be adjusted to achieve an even better fit. One possibility would be to use the reverse engineering fitting (REF) method introduced in Section 3.5. This is illustrated elsewhere in Section A.2.2 on the basis of another example. Nevertheless, the V_{OC} value fits very well to the experimental result, even for the device simulation. In summary the calculated efficiency is $22.8\,\%$, and thus very near to the actual value of $22.6\,\%$.

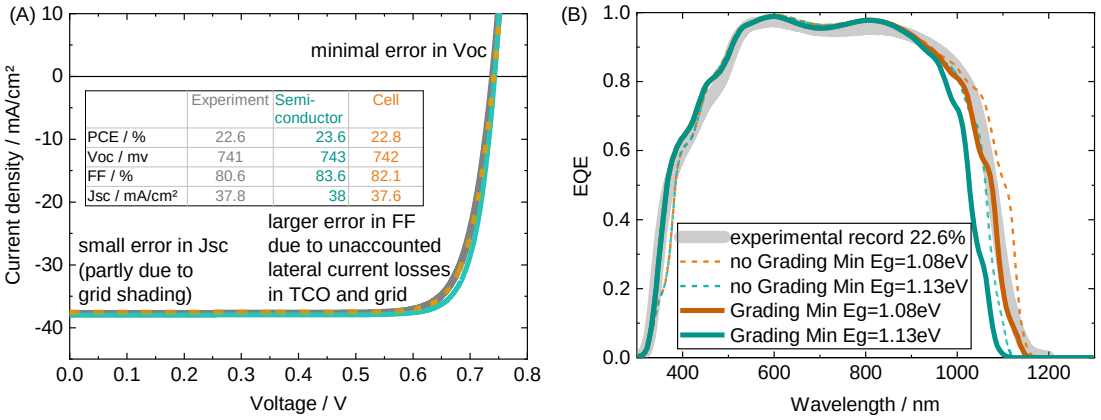

Figure 5.4: Results of numerical simulations and comparison to the experimental data. (A) shows the IV curves together with the characteristic data. Graph (B) shows the experimental obtained EQE as thick gray line together with simulated EQE plots from different simulation models.

Furthermore, the EQE was simulated on semiconductor level. Figure (B) shows the experimentally measured EQE in light gray together with different simulated EQE curves. Again, the problem of the exact band gap, as discussed in the previous section, is addressed. The simulated curves show a comparison between the band gap calculated according to Boyle et al. ($1.13\,\mathrm{eV}$) and the band gap extracted from the experimental EQE ($1.08\,\mathrm{eV}$). In both cases, the simulation was performed without grading and with grading as illustrated in Figure 5.2 (B). For the graded case, the determined band gap values were used as minimum values. It can be seen that without grading, the experimental EQE is one time underestimated in the long wavelength region and one time overestimated. For the case with grading, the EQE is significantly underestimated for a minimum value of $1.13\,\mathrm{eV}$. However, for a value of $1.08\,\mathrm{eV}$ there is a clear agreement with the experimental curve. This is also true for the short wavelength region, where the EQE curves with grading show a significantly higher agreement. In general, the simulated curve shows a good agreement with the experimentally obtained curve. This is true for the large part of the curve. Only single regions show a small deviation. This shows that the chosen modeling of the bandgap makes sense and is reasonable and the model incorporates enough details for meaningful simulations.

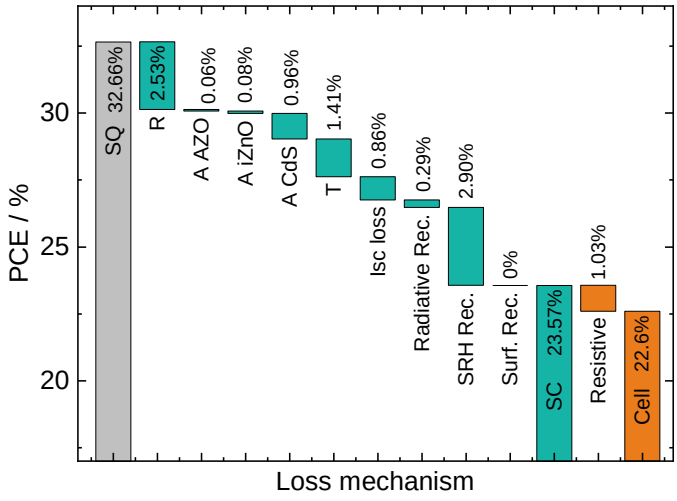

Figure 5.5: Loss analysis of the high efficiency record cell.

Additionally a loss analysis was performed on the model to identify the largest loss mechanisms of the device with the assumed parameters. The result is shown in Figure 5.5. The main optical loss is still the reflectance loss although an anti-reflective coating (ARC) layer was already applied to the layerstack. The calculated loss of $2.53\,\%$ is in good agreement with the experimental value of $3\,\%$, which was obtained by the weighted integral reflectance in the wavelength region from $300\,\mathrm{nm}$ to the wavelength of the band gap $\lambda_{gap} = 1150\,\mathrm{nm}$. The main electrical loss is the loss due to Shockley-Read-Hall (SRH) recombination.

A complete elimination of the SRH recombination would lead to a semiconductor efficiency of $26.5\,\%$ and a device performance of $25.68\,\%$, showing that the SRH is a very significant loss, and the potential of further improvements with decreased SRH recombination.

Conclusion

In summary, the build up of a simulation model was shown in detail. Herein experimental results from CV, DLTS and ToF-SIMS measurements have been used as inputs. The calculated EQE shows a good agreement with the experimental curve. The JV curve was reproduced with a combination of a semiconductor simulation and an electrical quasi-3D Poisson solver. Therefore, this chapter serves as an example for the following chapters.

6 Defects in grading-free CIGS solar cells with different alkali treatments

The following DLTS measurements and evaluations were conducted by Laura Friedl under guidance of the author and the results reflect the main findings of her Bachelor Thesis [148]. The samples have been fabricated by Roland Würz and the CIGS preparation team at Zentrum für Sonnenenergie- und Wasserstoffforschung Baden-Württemberg (ZSW).

This chapter analyses the effect and the electronic fingerprints of alkali metals in CIGS solar cells. The focus lies on the characterization of Cu(In,Ga)Se_2 (CIGS) solar cells with capacitance-voltage (CV) and Deep Level Transient Spectroscopy (DLTS) measurements and the investigation of effects of controllable alkali amounts due to post-deposition treatment (PDT) steps. Hence the CIGS samples are grown in a laboratory evaporation system (compare Section 2.5) on Na-containing glass substrate and alkali-free zirconium oxide (ZrO) substrates. The ZrO substrates are used to eliminate the diffusion of Na into the CIGS during the growth of the layer. A subsequent PDT step can be applied and it's corresponding effect can be investigated without influence of other alkali elements. Herein PDT processes with different alkali elements like Na, K and Rb are are discussed and compared.

6.1 Properties of Investigated Samples

The CIGS layer of the samples presented in this chapter were deposited using the laboratory equipment in a single-stage process. Table 6.1 gives an overview of the investigated samples and Figure 6.3 shows representative IV-curves. The sample preparation was divided into two runs. The first run investigates the effect of a sodium fluoride (NaF) and a potassium fluoride (KF)-PDT, the second run the effect of rubidium fluoride (RbF). For both runs, reference devices have been

Sample	**PDT**	**Substrate**	**PCE** (%)	$\mathbf{V_{OC}}$ (mV)	**FF** (%)	$\mathbf{J_{SC}}$ ($\mathrm{mA/cm^2}$)	$\mathbf{N_A}$ ($\mathrm{cm^{-3}}$)
R1_ZrO_w/o	without	ZrO	9.85	553	58.3	29.9	1.09e14
R1_ZrO_NaF	NaF	ZrO	16.38	683	77.9	30.8	4.00e15
R1_ZrO_KF	KF	ZrO	13.38	599	73.6	30.4	2.70e15
R1_SOL_w/o	without	SOL	16.05	686	78.4	29.8	2.89e15
R2_ZrO_w/o	without	ZrO	10.35	552	64.1	29.2	1.07e14
R2_ZrO_RbF	RbF	ZrO	14.46	657	75.4	29.2	5.20e15
R2_SOL_w/o	without	SOL	15.92	665	78.4	30.5	-

Table 6.1: Summary of the characteristic values of the single stage, gradient-free samples. The single horizontal line divides the rows into samples from same deposition runs.

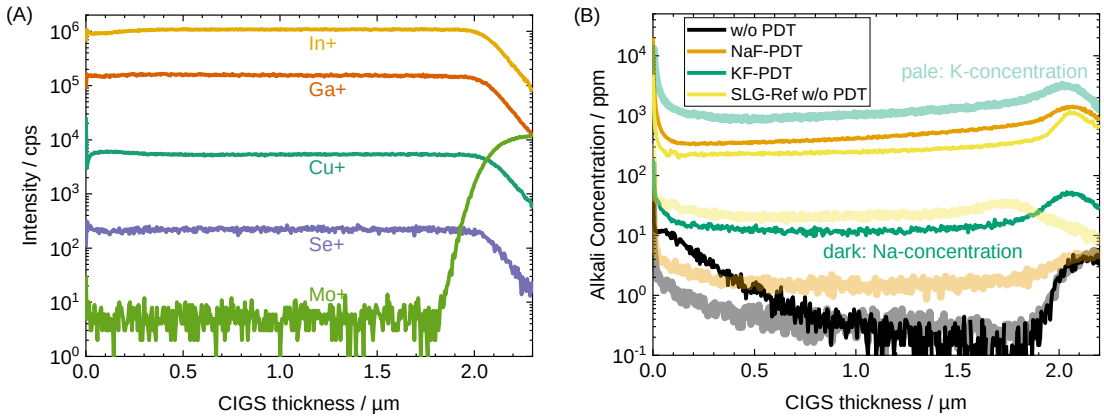

Figure 6.1: time of flight secondary ion mass spectroscopy (ToF-SIMS) measurements of single stage, gradient-free CIGS solar cells with different alkali treatments. Graph A shows the composition of the samples, graph B the alkali element content.

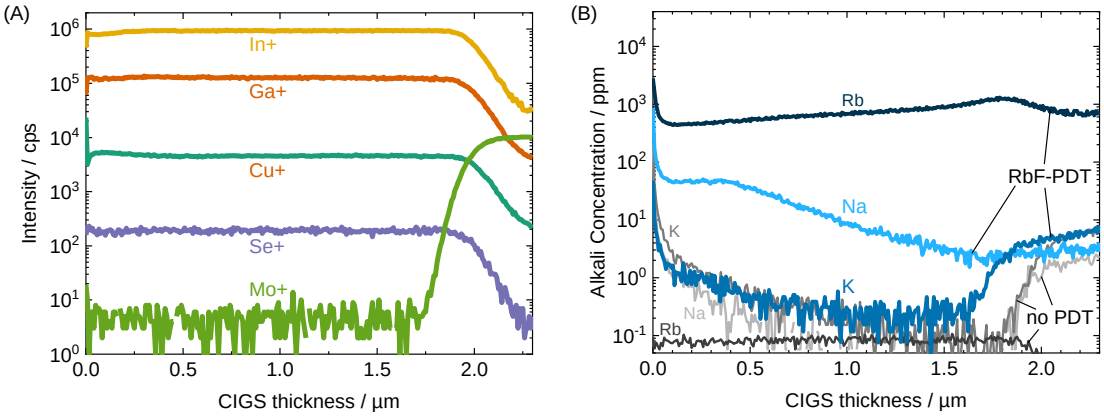

Figure 6.2: ToF-SIMS measurements of single stage, gradient-free CIGS solar cells with and without RbF-PDT. Graph A shows the composition of the samples, graph B the alkali element content.

fabricated with an alkali-free sample on ZrO and a sample grown on standard soda-lime glass (SOL). The actual samples with an applied PDT were grown on ZrO, as well. This ensures that the samples contain only alkali elements from the PDT.
The type of substrate (ZrO or SOL), the type of treatment (without, NaF, KF or RbF) and the number of the run (R1 or R2) are taken into account in the names of the devices. For the devices $\mathrm{R1\_ZrO\_NaF}$ or $\mathrm{R1\_ZrO\_KF}$ grown on ZrO, a PDT process was performed with NaF or KF, respectively. For the reference samples $\mathrm{R1_{ZrO_w}/o}$ and $\mathrm{R1_{SOL}\_w/o}$ no PDT was performed. Therefore, the $\mathrm{R1_{ZrO_w}/o}$ sample contains no alkali elements and the SOL-sample contains only alkali elements, which diffused from the substrate during the layer growth (compare next paragraph). The CIGS layers of these samples were prepared in the same evaporation process. In a second process, samples RbF-PDT have been fabricated. Again, the reference samples $\mathrm{R2_{ZrO}\_w/o}$ and $\mathrm{(R2_{SOL}\_w/o)}$ without further alkali treatment have been fabricated. The sample with RbF-PDT $\mathrm{(R2_{ZrO}\_RbF)}$ was also grown on ZrO.

Another characteristic of the samples is the homogeneity in depth. In contrast to the widely used Ga/(Ga+In) (GGI)-profiles [23, 149], the used samples have a constant distribution of elements over the depth of the absorber layer, which excludes the influence of the gallium gradient and other changing properties on the defects. Figure 6.1 shows the composition profiles of the CIGS matrix elements (A) and the alkali elements Na and K (B) for the samples of the first run. Figure 6.2

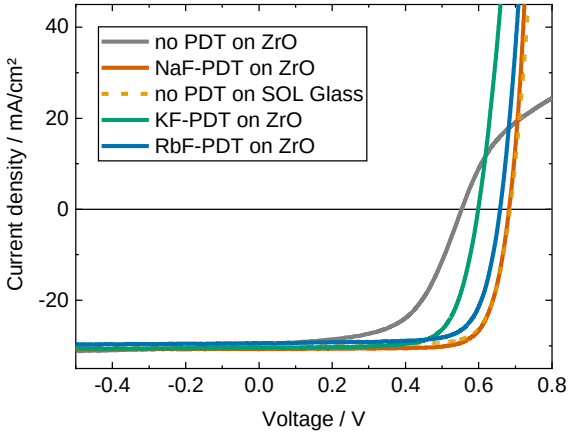

Figure 6.3: IV curves of the investigated one stage gradient free samples.

shows the matrix element profiles in Graph (A) and the profiles of Na, K and Rb in Graph (B) for the second run. In both cases, the flat profiles of the matrix elements (Cu^+,Ga^+,In^+,Se^+) can be clearly seen. Due to the elemental diffusion during the absorber growth, the depth profiles of Na, K and Rb were not uniform. A higher concentration towards the CdS and the back contact was observed. While the average alkali concentration in the CIGS layer for the untreated sample is almost zero ($\leq 1\,\mathrm{ppm}$), the values significantly increase after a PDT step. After the NaF-PDT, the average Na concentration increases to $450\,\mathrm{ppm}$, after the RbF-PDT, the Rb concentration increases to $700\,\mathrm{ppm}$. For a KF-PDT the value is even higher up to a K concentration of $1100\,\mathrm{ppm}$. In comparison, the alkali concentration of the sample, grown on glass are: $260\,\mathrm{ppm}$ sodium and $22\,\mathrm{ppm}$ potassium.

Table 6.1 shows an overview of the mean values (over a test strip with 10 cells) of the IV parameters of the samples. For the subsequent DLTS measurement, a cell with an efficiency close to the mean value (an average performing cell) was selected. A significant improvement in efficiency, V_{OC} and fill factor (FF) of the cells with alkali elements in the CIGS absorber can be seen, compared to the devices without PDT. Here, the strongest increase is seen due to the NaF-PDT, which can increase the efficiency from almost $10\,\%$ to over $16\,\%$. Comparing across all treatments, the KF-PDT is the one with the smallest effect, with an increase of just $3\,\%$. It is also interesting to note that the samples on glass substrates with no NaF-PDT have almost the same cell parameters as the ZrO samples with NaF-PDT. This suggests that the effect of sodium is similar whether it is present during film growth, or only afterwards. This trend can also be seen in Figure 6.3. The IV-curve of the untreated solar cells shows a strong S-shape behavior. By applying a PDT step, S-shape behavior vanishes and a significant increase in V_{OC} and FF can be observed. Although these improvement in V_{OC} and FF is valid for all types of the PDT, the strength of this beneficial effect strongly depends on the used alkali element. Herein, the KF-PDT shows the smallest effect, followed by RbF, and NaF with the strongest effect. Since the samples with RbF and NaF are from different deposition batches, a comparison is only possible within limits.

Figure 6.4 shows the DLTS and Reverse DLTS (RDLTS) measurement of the above introduced samples on ZrO substrates for no PDT (A), NaF (B), KF (C) and RbF-PDT (D). For every sample, a significant difference in the DLTS measurements can be observed. While the untreated sample shows a very distinctive peak at $180\,\mathrm{K}$, all other samples show peaks with increased width, indicating an overlapping of peaks from different trap levels or peaks originating from traps with distributed energy values (like Gaussian, etc.). Furthermore, the temperature, at which the peaks occur differ between the samples. For NaF-treated cells, the main peak occurs at temperatures below $200\,\mathrm{K}$.

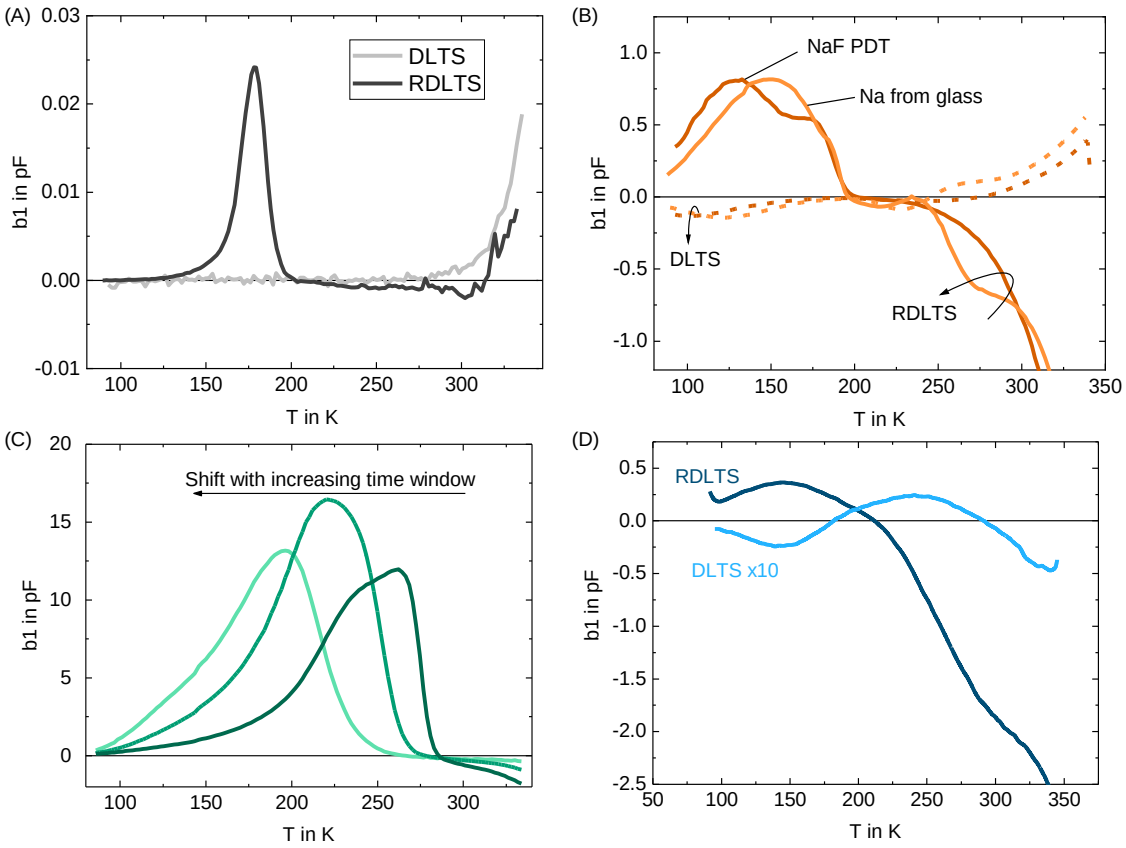

Figure 6.4: DLTS measurements of single stage, gradient-free CIGS solar cells with different alkali treatments.

For KF-treated samples, a the maximum in the RDLTS occurs for temperatures higher than 200 K. In the case of RbF, a peak at low temperatures, as well as for higher temperatures is present. If not stated otherwise, the standard measurement parameter of the shown DLTS and RDLTS measurements are: $t_\mathrm{P} = 1$ and 50 ms and $t_\mathrm{W} = 1,\ 10$ and 100 ms with a pulse height of 2 V. In DLTS configuration, the reverse bias is set on -2 V, in RDLTS configuration on 0 V. In the following sections, the investigations are discussed in detail.

6.2 DLTS Measurements on an Alkali-free Reference

In the following, the analysis of the prominent minority peak of the untreated cell is performed in a detailed way, in order to give an exemplary DLTS evaluation workflow. Afterwards the results will be compared with results of samples with different alkali treatments.

As already depicted in Figure 6.4 (A), the untreated sample reveals one prominent peak "H0". This is only the case for RDLTS measurements. For standard DLTS no peak can be observed, regardless of the used measurement parameters. Only an increasing signal at high temperatures above 300 K is present, as well as for the RDLTS measurement. Since the signal does not change the direction (above or below the x-axis) when changing the pulse direction, it is probably not connected with a defect related process in the classical sense of the DLTS measurement. Nevertheless, within the scope of the used parameters of the RDLTS measurements, no further peak can be observed. The response of the peak on changes in t_W and t_P is depicted in Figure 6.5 (A). With a variation of t_W from 1 ms, over 10 ms to 100 ms and t_P values of 1 and 50 ms, a huge part of the parameter-space is

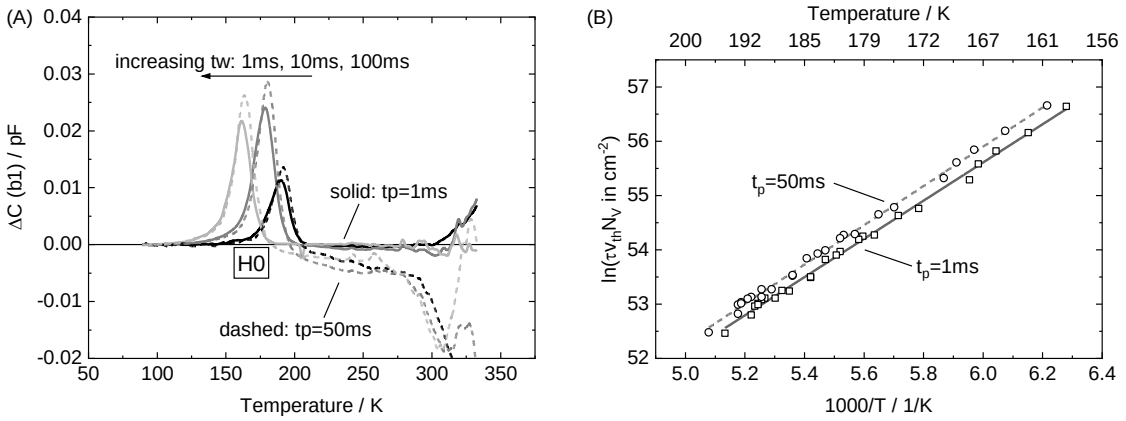

Figure 6.5: DLTS measurements of single stage, gradient-free CIGS solar cells without any alkali treatment and without alkali from the substrate. Graph (B) shows the corresponding Arrhenius plot of the manual evaluation.

scanned. Within this range following effects on the DLTS signal can be observed: First, the position of the peak shifts to lower temperatures when increasing the time window t_{W}. This observation follows the theory as introduced in Section 4.1 and leads to the Graph 6.5 (B). The Arrhenius plots of the manual evaluation of both t_{P} measurements are shown. The linear regression plots show comparable slopes with a slight offset in y-direction. Therefore, both evaluations result in similar energetic levels, with a mean of $(305\pm10)\,\mathrm{meV}$ above the E_{V}. Table 6.2 lists the evaluation data of the defect peak H0, obtained with different evaluation methods, introduced in Section 4.1.4 for both pulse widths. The offset in y-direction leads to a deviation in the resulting capture cross section, which is a known problem of this evaluation method [138]. Czudek et al. reported similar results on samples grown on glass substrates with a sodium diffusion barrier. They obtained an energy level of 300 to $350\,\mathrm{meV}$ and assigned this defect to be located at grain boundaries. Also they could observe this peak only for samples without sodium [150].

The second feature is, that for increasing the pulse width from $1\,\mathrm{ms}$ to $50\,\mathrm{ms}$, the peak is increasing in height by around $20\,\%$, indicating, that pulses of $1\,\mathrm{ms}$ do not fill all traps and the peak amplitude is not yet in saturation. This point can be discussed in detail, by taking the evaluation results of this trap into account, as well. For each evaluation method, the trap density of the $50\,\mathrm{ms}$ measurement is higher, compared with the $1\,\mathrm{ms}$ measurement. This leads to the conclusion, that the mean value of $1.02{\cdot}10^{12}\,\mathrm{cm}^{-3}$ is slightly underestimating the real value.

In conclusion, DLTS measurements have been performed on alkali-free CIGS samples. Within the used measurement parameters, only one defect peak was detected which can be assigned to a "solo CIGS" defect. According to the energetic level, the chemical origin of this defect may be a copper on indium $\mathrm{Cu_{In}}$ or copper on gallium $\mathrm{Cu_{Ga}}$ site, which theoretical energetic position for $CuInSe_2$ (CIS) or $CuGaSe_2$ (CGS) is $290\,\mathrm{meV}$ above valance band maximum. Since the CIGS layer is grown rather Cu-poor (typical CGI values approx. 0.8 to 0.9) than Cu-rich this interpretation seems not to be very reasonable [141]. Nevertheless, the measured samples are an alloy of CIS and CGS, and therefore an influence of the mixture of elements on the energetic position of defect levels cannot be excluded.

	Maximum evaluation		Hera evaluation		DLTFS		**Mean**	**Standard Deviation**
puls width t_p / ms	1	50	1	50	1	50		
Energy $E_T - E_V$ / meV	286	312	299	312	309	311	**305**	**10**
Trap density N_T / $1{\cdot}10^{12}\,cm^{-3}$	0.99	1.23	0.84	1.23	0.76	1.05	**1.02**	**0.20**
capture cross section σ / $1{\cdot}10^{-15}\,cm^2$	0.35	1.46	0.82	1.46	1.05	1.69	**1.14**	**0.5**

Table 6.2: Summary of the characteristic values of the single stage, gradient-free samples without alkali treatment, obtained with different types of evaluation.

6.3 DLTS Signatures of Different Alkali Elements in CIGS Solar Cells

With introducing alkali elements into the CIGS layer, the situation completely changes. This was already observed in Figure 6.4. Different alkali PDTs introduce different peaks in the DLTS measurement and at different temperatures. For all investigated types of PDT, much broader peaks compared to the untreated sample are recorded. For this reason, the following evaluations are not as straight forward as the one for the untreated samples and exhibit higher systematic errors compared to the ones for the untreated samples.

NaF-treated sample

The RDLTS measurements of the NaF sample in Figure 6.6 (A) shows a broad maximum between $100\,K$ and $200\,K$. A higher resolution of this peak was achieved by reducing the pulse voltage step (difference between reverse and pulse voltage) from $2\,V$ to $0.5\,V$, revealing at least two defect levels contributing to this peak. This two defect levels are marked as "Na1" and "Na2" in Figure 6.6 (A). As a consequence of the smaller pulse height, a smaller region of the absorber layer is scanned, resulting in a lower peak amplitude, but at the same time the measurement is less blurred.

Graph 6.7 shows the calculated space charge region (SCR)-width in dependence on the applied bias, based on the measured doping densities. In case of the NaF, the SCR width of the unbiased sample is approximately $540\,nm$. For a $2\,V$ pulse in reverse direction, it increases to approx. $1\,\mu m$. In comparison, for the smaller $0.5\,V$ pulse, the SCR width only changes to $690\,nm$. This shows, that the accessible region is significantly larger with the $2\,V$ pulse and therefore the probability for blurring and widening of the peak is higher. Nevertheless, the two underlying peaks are not completely separated (maybe due to similar activation energies or chemical origins) making the evaluation more complicated and error-prone. A separated evaluation of the two constituents of this peak is possible, but difficult. On possibility is the usage of automated evaluation methods like a Hera-evaluation or Deep Level Transient Fourier Spectroscopy (DLTFS). In contrast, the DLTS measurements in Graph (B) reveal no double peak shape at the corresponding temperatures, even for the small voltage pulse. This could be either due to a lower resolution in the DLTS configuration, or a weaker response of the "Na2" constituent. Furthermore, the peak amplitude of the DLTS measurement is one order of magnitude smaller than the RDLTS peak (compare y-axis of Graph

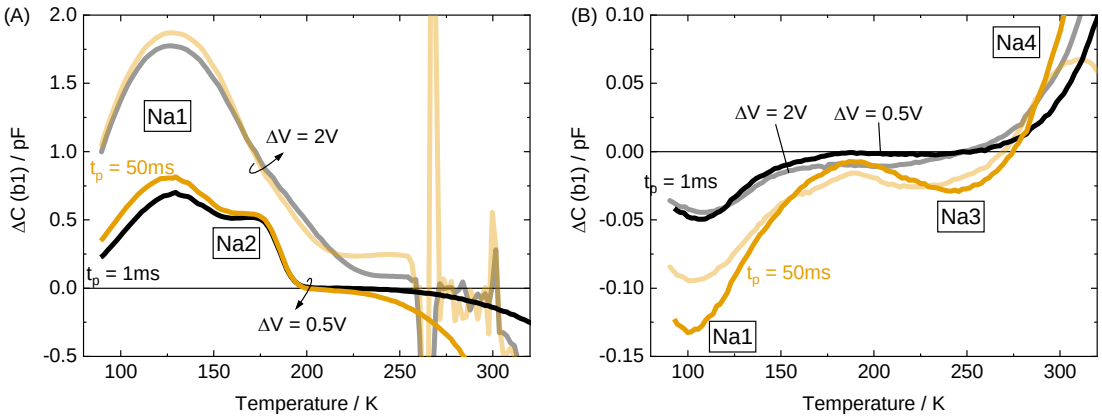

Figure 6.6: RDLTS (A) and DLTS (B) measurements of single stage, gradient-free CIGS solar cells grown on ZrO substrate with a NaF-PDT with different DLTS measurement voltages.

	Na1	**Na2**	**Na3**	**Na4**
$E_\mathrm{T} - E_\mathrm{V}$ /meV	75±7	215±15	337±90	712±90
N_T / $1{\cdot}10^{14}\,\mathrm{cm}^{-3}$	2.91±0.97	1.66±0.61	0.16±0.03	0.48±0.13
σ / cm^2	$1{\cdot}10^{-20}$	$2{\cdot}10^{-17}$	$4{\cdot}10^{-17}$	$5{\cdot}10^{-14}$

Table 6.3: Summary of the results from DLTS measurements on the NaF treated sample. For the capture cross section σ no error is given due to the high deviation of the values.

(A) and (B)) and some additional peaks can be observed compared to the RDLTS measurement. At approximately 250 K a further minority peak "Na3" can be observed and at approximately 300 K a majority peak "Na4" occurs in several measurements. The rapidly increasing signal amplitude at high temperatures sometimes overwhelms the 300K and 250k peaks.

The peaks of Na3 and Na4 are not present in the RDLTS measurements or are superimposed by large noise for temperatures above 250 K.

The energetic position of the four identified defect levels, corresponds to the temperatures at which the peaks occur in the DLTS measurements. Peaks at low temperatures in the DLTS scan can be assigned to defect levels with low energetic positions. "Na1" reveals the lowest activation energy of $(75{\pm}7)\,\mathrm{meV}$ and can be therefore assumed to be a shallow doping level. With a trap density of $(2.91{\pm}0.97){\cdot}10^{14}\,\mathrm{cm}^{-3}$, the contribution to the netto doping ($4{\cdot}10^{15}\,\mathrm{cm}^{-3}$) is rather low. peak "Na2" corresponds to a minority trap level at $(215{\pm}15)\,\mathrm{meV}$ and a trap density of $(1.66{\pm}0.61){\cdot}10^{14}\,\mathrm{cm}^{-3}$. The energetic position is too high to assign this peak to a shallow dopant. Furthermore, defect signals in DLTS measurements on CIGS solar cells in the temperature range of "Na1" and "Na2" are often assigned to a so called "N1" signal [151, 152]. Zabierwoski et al. suggest a $\mathrm{In_{Cu}}$-related origin and show that the sample preconditioning has a huge influence on the position and shape of the peak [152]. Although an influence of unintentional ambient light soaking etc. can not be excluded, the presented measurements are comparable with each other, due to the applied relaxation procedure in dark and vacuum, lasting at least 1 hour before the DLTS measurement. Furthermore, a set of measurements have been performed on each sample on different days with different measurement parameters. The given energetic positions and trap densities reflect the resulting average values with standard deviation. Such significant variations like Zabierowksi et al. cannot be reported. The high temperature peaks can be evaluated to energetic positions of $(337{\pm}90)\,\mathrm{meV}$ and $(712{\pm}90)\,\mathrm{meV}$ for "Na3" and "Na4", respectively. According

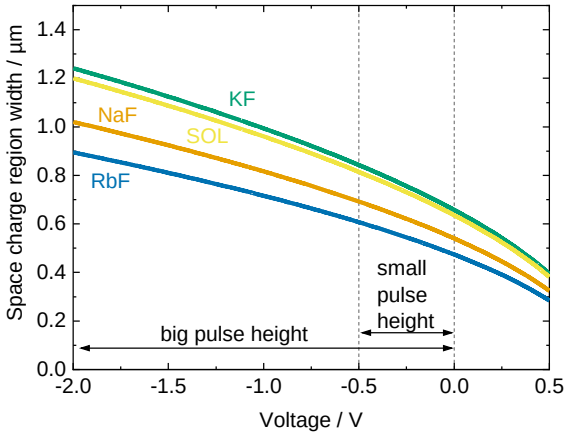

Figure 6.7: Calculated SCR width of the investigated sample in dependence of the external bias As a reference vertical lines at $-0.5\,\mathrm{V}$ and $0\,\mathrm{V}$ are given.

to the smaller peak amplitudes, the resulting trap densities are lower than those of "Na1" and "Na2" with $(1.66\pm0.32)\cdot10^{13}\,\mathrm{cm}^{-3}$ and $(4.8\pm1.3)\cdot10^{13}\,\mathrm{cm}^{-3}$. In summary, four different defect levels have been identified with DLTS in NaF-treated CIGS. Two of them have shallower energetic positions $\leq 250\,\mathrm{meV}$ and two have positions deeper within the band gap. The latter are likely SRH recombination candidates and could have an impact on cell performance. All results are summarized in Table 6.3 The values of capture cross sections are given without standard deviation due to the high variance in the results.

KF-treated sample

By replacing the NaF by KF, the DLTS results completely change. As Figure 6.8 indicates, these measurements show a huge variation. Graph (A) shows the measurement with a pulse step height of $2\,\mathrm{V}$, Graph (B) with a height of only $0.5\,\mathrm{V}$, in both cases for DLTS and RDLTS configuration. All other parameters are the same. For the large pulse minority peaks in RDLTS configuration occur at temperatures between 200 and $270\,\mathrm{K}$, in contrast, for the small pulse the peaks occur at lower temperatures between 120 and $200\,\mathrm{K}$. The DLTS measurements change as well. While for the $2\,\mathrm{V}$ pulse, only a minimum is observed at $300\,\mathrm{K}$, for the small pulse a peak at temperatures around $120\,\mathrm{K}$ occurs. These variations can maybe be related to the before mentioned "N1" behavior reported by Zabierowski et al. [152]. Moreover, this sample was experimentally difficult to measure, because the electrical contact was not sufficient, which can lead to parasitic behavior in the DLTS measurement. Another explanation, but less probable, is that the defect properties change with depth in the CIGS layer. With the $2\,\mathrm{V}$ pulse, the scanned range is much wider, and could reach defects with changed properties or different defect levels. This is not very probable because the samples have a very constant composition profile, as well as the alkali elements.

A further challenge is the extreme width of the peaks, ranging from $100\,\mathrm{K}$ to $280\,\mathrm{K}$, covering nearly the whole measurement range. The blurring or the superimposing of multiple defect levels is a major challenge for the further evaluation. Although the peaks in the RDLTS measurements obviously containing signals from multiple defect levels or from an energetic distribution, only representative values of the local maximum are evaluated. The results are summarized in Table 6.4. The evaluation of level "K1.1" result in energy levels ranging from 380 to $440\,\mathrm{meV}$. In contrast, the values for "K1.2" of the small pulse measurement lie significantly lower between

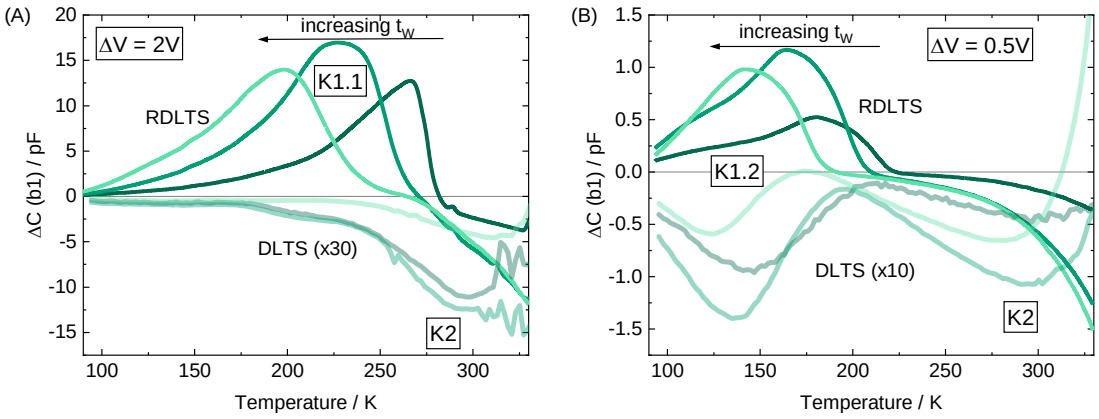

Figure 6.8: RDLTS and DLTS measurements of single stage, gradient-free CIGS solar cells grown on ZrO substrate with a KF-PDT with different pulse voltage steps (difference between reverse and pulse voltage) of (A) 2 V and (B) 0.5 V.

	K1.1	**K1.2**	**K2**
$E_T - E_V$ /meV	427±88	224±31	497±78
N_T / $1{\cdot}10^{14}\,cm^{-3}$	35.6±14.8	7.27±2.77	2.12±0.22
σ / cm^2	$6{\cdot}10^{-14}$	$3{\cdot}10^{-16}$	$6{\cdot}10^{-17}$

Table 6.4: Summary of the results from DLTS measurements on the KF treated sample. For the capture cross section σ no error is given due to the high deviation of the values.

180 to 250 meV. The mean values are (224±31) meV and (427±88) meV. Level "K2" has an energetic position of approx. 500 meV. Compared to the results of the NaF sample, two main points show significant differences: The KF-treated devices reveal higher trap densities N_T in the range of $1{\cdot}10^{15}\,cm^{-3}$, which fits to the concentration of K in the CIGS layer (100 ppm), which is significantly higher than the Na concentration in the NaF-sample (450 ppm). Second, for the KF-sample no doping level with energies below 100 meV was found. The presence of deep defects could be connected to the device performance: the KF sample show worse performance, compared to the NaF sample. A main difference is present in the V_{OC}, maybe caused by increased Shockley-Read-Hall (SRH) recombination.
In conclusion, the data reveal, that KF, introduces defect levels in the CIGS, which are measurable with DLTS. With the evaluated defect properties, it is possible, that these defects are electrically active and play a role for the device performance.

RbF-treated sample

At last, the RbF sample shows again, differences in the temperature scan, compared to the other samples. Figure 6.9 shows the DLTS and RDLTS characteristic of a RbF-treated CIGS sample on ZrO. Graph (A) shows the results for a long pulse of 10 ms, Graph (B) for a short filling pulses of 0.1 ms. Here, as well, broad peaks are dominating the temperature scans. In general, three different peaks can be identified: a minority peak "Rb1" at low temperatures around 150 K, a majority peak "Rb2" at 200 K, which is only present in the DLTS measurements for small pulses, and a majority peak "Rb3" at high temperatures of 300 K. Table 6.5 summarizes the results of the corresponding evaluations. Again, mean values with standard deviation are given. "Rb1"

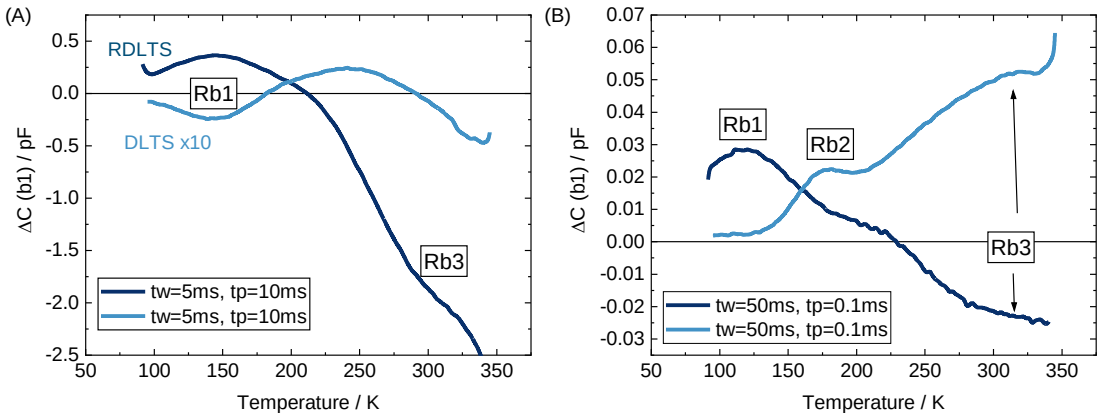

Figure 6.9: RDLTS and DLTS measurements of single stage, gradient-free CIGS solar cells grown on ZrO substrate with a RbF-PDT with different pulse widths of (A) 10 ms and (B) 0.1 ms. the DLTS curve in Graph (A) is increased by factor 10 to ensure readability of the plot.

	Rb1	**Rb2**	**Rb3**
$E_T - E_V$ /meV	130±47	255±8	490±43
N_T / $1{\cdot}10^{13}\,cm^{-3}$	3.96±3.11	1.58±1.03	3.79±3.06
σ / cm^2	$1{\cdot}10^{-18}$	$1{\cdot}10^{-17}$	$3{\cdot}10^{-17}$

Table 6.5: Summary of the results from DLTS measurements on the RbF treated sample. For the capture cross section σ no error is given due to the high deviation of the values.

and "Rb2" show energetic positions near the valence band with 130 and 255 meV, respectively. The high temperature peak reveals an energetic position near the middle of the band gap with 490 meV. In general, the trap density is low, compared to the KF and NaF samples (in the order of $1{\cdot}10^{13}\,cm^{-3}$, compared to $1{\cdot}10^{14}$ to $1{\cdot}10^{15}\,cm^{-3}$). And also the capture cross sections show lower values, ranging from $1{\cdot}10^{-18}\,cm^2$ to $1{\cdot}10^{-17}\,cm^2$. This could already indicate, that a RbF-PDT introduces fewer detrimental defect levels in the absorber. This assumption cannot be verified with the cell parameter of the samples because the RbF samples show a worse performance than the NaF-treated sample. Also the RbF sample has not been fabricated in the same batch like the NaF and KF samples. But it fits to the trend in the past CIGS development, to go from light alkali to heavy alkali PDT processes to achieve higher lifetimes and V_{OC} values [153].

6.4 On the Origin of Alkali Elements

The last section of this chapter deals with the origin of the alkali elements and the influence on the DLTS measurements. While the usage of ZrO substrates enables the growth of CIGS layers without the presence of alkali elements, this is not the case when growing the CIGS layer on glass substrates. Due to the high process temperatures, alkali elements like potassium and sodium can diffuse from glass, through the molybdenum into the CIGS layer. As the IV characteristics and the corresponding data in section 6.1 show, the presence of alkali elements during the growth of CIGS has a significant influence on the solar cell performance. Herein, the increase of the doping plays an important role. In order to investigate the influence on the defect properties, DLTS measurements have been performed on the above introduced CIGS sample on soda-lime glass (without PDT). The results are shown in Figure 6.10, in light blue the DLTS measurement

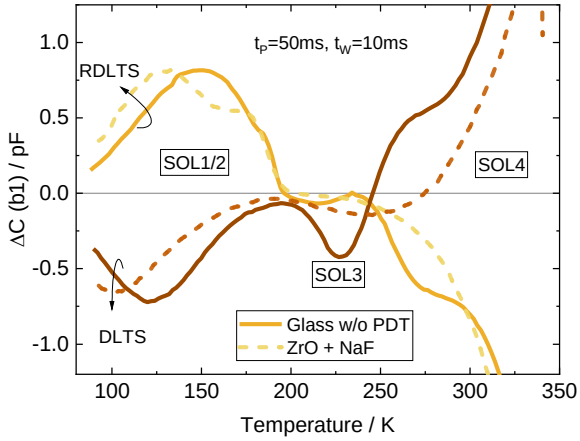

Figure 6.10: DLTS and RDLTS measurements of single stage, gradient-free CIGS solar cells grown on ZrO substrate with a NaF-PDT (dashed) and grown on glass substrate (sodium diffusion into the CIGS) without additional alkali treatment.

and in black the corresponding RDLTS measurement. In comparison the measurements on the NaF-treated sample on ZrO is plotted in the same graph. Obviously, the measurements agree with each other and reveal the same features with slight differences in absolute values. For example, the double peak between 100 and $200\,\mathrm{K}$ cannot be separated, although adapted parameters with a lower pulse height for a better resolution of peaks have been used, as well. Nevertheless, the two samples show not only nearly the same IV characteristics, but also very similar DLTS results. A detailed evaluation of the identified peaks was not possible. But the general energetic levels are as following: the low temperature peak "SOL1/2" corresponds to energies between 130 and $270\,\mathrm{meV}$ with a trap density in the range of $1{\cdot}10^{14}\,\mathrm{cm}^{-3}$ and therefore are comparable to the results from the NaF-treated sample. Defect level "SOL3" corresponds to an energetic position of $580\,\mathrm{meV}$ and a trap density of $1{\cdot}10^{13}\,\mathrm{cm}^{-3}$. The energetic position is relatively high, compared to the energy of "Na3" of the NaF-treated sample. It is possible, that the strong increase at high temperatures influences the peak position of "SOL3" and thus results in a wrong evaluation. Also for "SOL4" it was not possible to perform a reasonable evaluation, most likely due to the strong increase for high temperatures, as well, superimposing the actual peak. A reason for the significantly more difficult evaluation of the measurements of the glass sample cannot be given. One possibility is, that in contrast to the NaF-sample, two kind of alkali elements are present in the CIGS layer. As the ToF-SIMS measurements in Section 6.1 reveal, the glass sample contains $258\,\mathrm{ppm}$ sodium (approx. factor 2 less than in the NaF-sample) and $22\,\mathrm{ppm}$ potassium (factor 15 more than in the NaF-sample, but factor 50 less than in the KF-sample).

Conclusion

This chapter reveals the individual signatures of single alkali elements in DLTS measurements on simplified CIGS samples and how that they introduce defect levels in the absorber material. Although each alkali treatment shows different features in the DLTS measurements, some similarities are present as well. Each treatment introduces (almost) shallow defect levels ($E_\mathrm{T} \leq 100\,\mathrm{meV}$) or defect level with a low distance (approx. $200\,\mathrm{meV}$) to the valance band maximum. These levels occur in RDLTS measurements as a broad maximum around $150\,\mathrm{K}$. Furthermore, in each case a majority peak at $300\,\mathrm{K}$ occurs, corresponding to defect level from 500 to $700\,\mathrm{meV}$. The exact energy level depends on the applied alkali fluoride treatment. Some additional peaks are present,

depending on the sample. In comparison to the untreated sample, one can conclude, that the alkali treatments (which are intended to passivate defect levels in order to enhance the charge carrier lifetime [154]) introduce defect levels.

Figure 6.11 relates all experimentally determined defect levels to the theoretical calculations of Wei et al. and Zhang et al., introduced in Figure 2.6 in Section 2.3. Herein the figure shows the theoretical (interpolated) defect levels for a CIGS material with GGI=0.3 on the left hand side together with the measurement of the alkali-free sample. The energetic level of the H0 peak corresponds to the theoretical value of a Cu_{III}^{1-} defect, as already discussed in the text above. The right hand side shows the alkali induced defect levels of the corresponding alkali containing samples. The major part of the defect levels is located in the lower part of the band gap. The defect levels, which occur as peaks at low temperatures in the DLTS measurement have energetic positions near to the valence band maximum (VBM). For each of three PDT samples, also a defect level near the middle of the band gap is observed (Na4, K2 and Rb3). Since the theoretical defect levels on the left hand side are calculated without considering alkali elements, a comparison with the alkali-induced defect levels has to be done carefully.

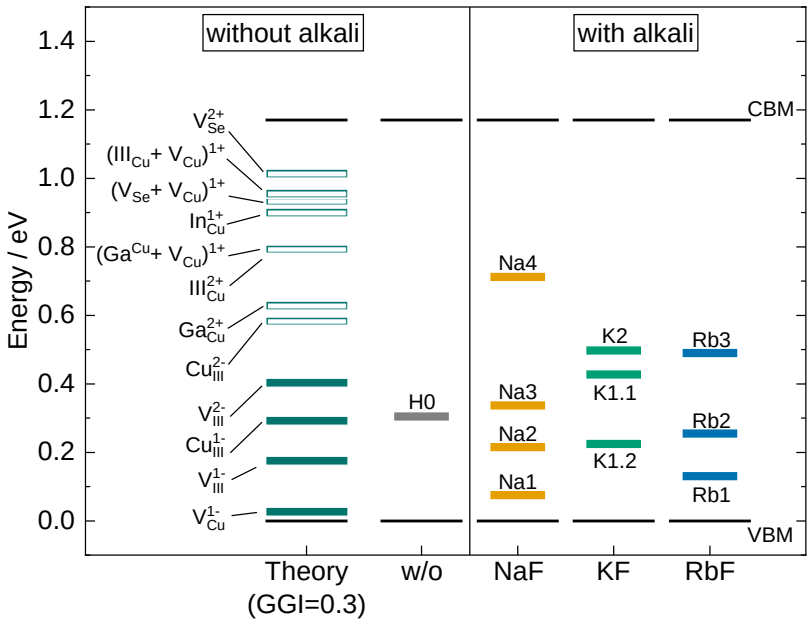

Figure 6.11: Theoretical defect levels for a GGI=0.3 CIGS material (on the most left side) in comparision to the H0 defect level observed in RDLTS measurement as only defect in the alkali-free sample. The right hand side shows the determined defect levels with DLTS of CIGS samples with different types of PDTs (NaF, Kf, RbF).

Malitckaya et al. and Oikkonen et al. showed density-functional theory (DFT) calculation which reveal, that alkali elements in the CIS lattice can produce defects with transition levels in the band gap, but do not give exact values for the energetic positions [58, 155]. Herein, all alkali metals prefer to accumulate on the Cu sublattice and the formation energy of point defects increases with increasing atom weight of the alkali metal (Li, Na, K, Rb, Cs). This is a possible explanation for the lower observed defect density for the Rb induced defects in comparison to the Na and K induced ones. Furthermore, the lighter alkali elements tend to diffuse into grain interiors, whereas

the heavier ones favor the formation of secondary phases and the segregation at grain boundaries [58].

These results have to kept in mind, when analyzing samples with multiple types of alkali elements, intermixing within the CIGS layer, like in Chapters 7 and 8. It can be noted, that as soon as alkali elements are introduced into the CIGS layer, the evaluation and interpretation of DLTS is getting significantly more complicated.

7 Influence of RbF PDT on the Defect Characteristic of CIGS Samples from a Production Like Inline Evaporation System

The results of this section have been published in parts in the publication "DLTS Investigations on CIGS Solar Cells from an Inline Co-evaporation System with RbF Post-deposition Treatment" [156].

With the basic measurements on the effect of single Alkali treatments on the Deep Level Transient Spectroscopy (DLTS) characteristics in Chapter 6, further investigations on post-deposition treatment (PDT) effects in Cu(In,Ga)Se_2 (CIGS) are discussed in this chapter. In the following the effect of rubidium fluoride (RbF)-PDT on CIGS samples from a production-like multi-stage co-evaporation system (like described in Section 2.5) is discussed. Therefore, the study is based on sample which are comparable to module-CIGS and thus industrially relevant. This chapter starts with introducing the measured sample and describing the most important properties. After that, the DLTS measurements are analyzed and related to the sample properties. Lastly, the found results are set into a global relationship by performing numerical simulations. Herein, strategies for the improvements of the solar cells are discussed.

7.1 Investigated Samples

On the way to a higher market share of CIGS modules, detailed knowledge about the absorber from inline co-evaporation processes is getting more important and is essential for further development. Herein, in order to identify paths of power loss the knowledge of defects in the material is of great interest. Therefore, this chapter is based on samples from two similar deposition series from a production-like co-evaporation CIGS system, denoted as "Series I" and "Series II". Based on the

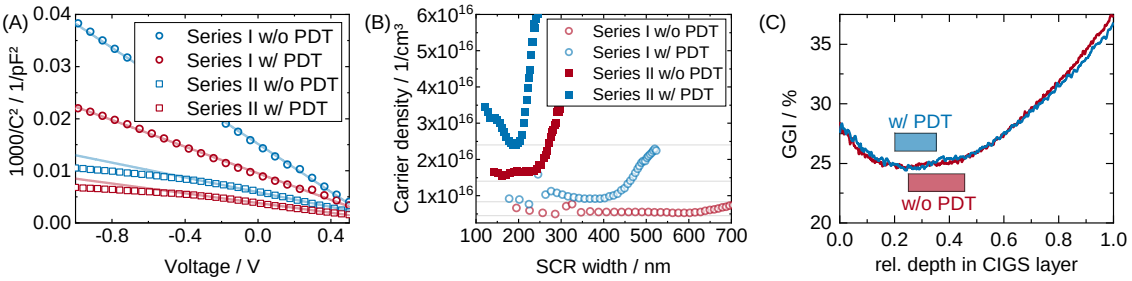

Figure 7.1: Results from capacitance-voltage (CV) measurements for two sets of CIGS solar cells with and without RbF-PDT. (A) Mott-Schottky plots for doping density determination. (B) Carrier density depth profiles resulting from the CV measurements. The gray lines correspond to the results from linear regression in graph (A). Graph (C) shows the depth profile of the Ga/(Ga+In) (GGI) for both samples from sample set I with the measurement range of the DLTS measurements.

same CIGS deposition, for each series, sample with and without RbF-PDT have been fabricated. Except for the PDT step, all other preparation steps are the same. Multiple groups have observed (See the literature review in Chapter 2.4), that the treatment of CIGS samples with alkali elements improves the V_{OC} and fill factor (FF), which might be related to the passivation of defects and the increase of effective doping [154, 52]. The improvement in V_{OC} of the investigated samples is $7\,\mathrm{mV}$ and $23\,\mathrm{mV}$ for Series I and Series II, respectively. The FF in Series II remains unchanged, while the FF of Series I increases by $2\,\%$ absolute. The exact V_{OC} and FF values are listed in Table 7.1. The doping densities determined by CV measurements reveal, that an increase of the density by factor 1.6 to 1.8 is obtained by the alkali treatment. The exact values are listed in Table 7.1, as well. Figure 7.1 shows the corresponding CV measurements. Figure (A) shows the Mott-Schottky plot with the according linear fit for the determination of the doping density. The values from the Mott-Schottky evaluation are added as gray lines in Graph (B). They correspond well with the minima of the well known "U"-shaped N_{A} over W_{SCR} plot of the CIGS devices. Additionally, Graph (C) shows the GGI profiles from glow discharge optical emission spectroscopy (GDOES) measurements of samples from Series I, with the depth, which is accessible by the DLTS measurements with reverse voltage of $-2\,\mathrm{V}$ and a pulse voltage of $0\,\mathrm{V}$, is marked with blue and red rectangles.

7.2 Influence of RbF-PDT on the Defect Characteristics Measured with DLTS

For the majority of the investigated samples without RbF-PDT, the temperature scan is dominated by a significant negative peak around $220\,\mathrm{K}$. Only for higher temperatures an increase in the DLTS signal is observed. This peak, denoted as "E1" can be assigned to a minority trap, due to the negative polarity of the peak. Figure 7.3 shows its movement to lower temperatures with increasing time window t_{W}. Additionally, it is interesting to note, that in contrast to the observations in Chapter 6, no broad peak at low temperatures is observed, although the sample was grown on alkali-containing soda lime glass as well and alkali elements definitely diffused into the CIGS layer. The evaluation of "E1" peak results in an energetic position of $(425\pm25)\,\mathrm{meV}$, which is approximately $150\,\mathrm{meV}$ away from the middle of the minimal band gap of the used CIGS. In this

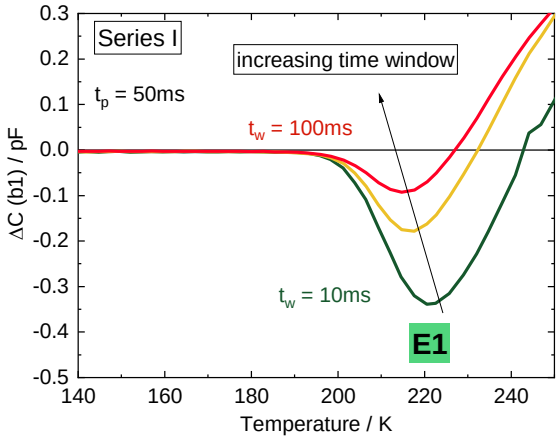

Figure 7.2: Representative measurement of the minority trap E1, which occurs in most of the DLTS measurements, performed on CIGS from the inline evaporation system.

investigation, different evaluation methods have been used to determine the trap properties (manual maximum analysis and DLTFS evaluations). Therefore an average and standard deviation is given for trap energies and trap densities.

	Treatment	Doping cm^{-3}	Voc mV	FF %	Type	Energy E_T meV	$\sigma_\mathrm{n,p}$ cm^2	Trap Density N_T cm^{-3}
Series I	w/o PDT	$4.5{\cdot}10^{15}$	709	75.8	E1	425±25	$1.2{\cdot}10^{-15}$	$(6.0{\pm}3.0){\cdot}10^{13}$
	w/ PDT	$8.3{\cdot}10^{15}$	716	77.6	E1	418±22	$4.2{\cdot}10^{-12}$	$(1.6{\pm}0.5){\cdot}10^{13}$
					H1	198±22	$1.4{\cdot}10^{-17}$	$(1.2{\pm}0.3){\cdot}10^{13}$
Series II	w/o PDT	$1.4{\cdot}10^{16}$	687	71.9	E1	451±32	$1.5{\cdot}10^{-14}$	$(2.3{\pm}0.3){\cdot}10^{13}$
					H2	608±8	$1.2{\cdot}10^{-15}$	$(2.5{\pm}1.5){\cdot}10^{13}$
	w/ PDT	$2.3{\cdot}10^{16}$	710	71.9	E1	459±11	$4.7{\cdot}10^{-13}$	$(7.8{\pm}2.3){\cdot}10^{12}$
					H2	641±16	$2.1{\cdot}10^{-14}$	$(3.1{\pm}0.9){\cdot}10^{13}$

Table 7.1: Summary of the calculated defect properties for all investigated samples.

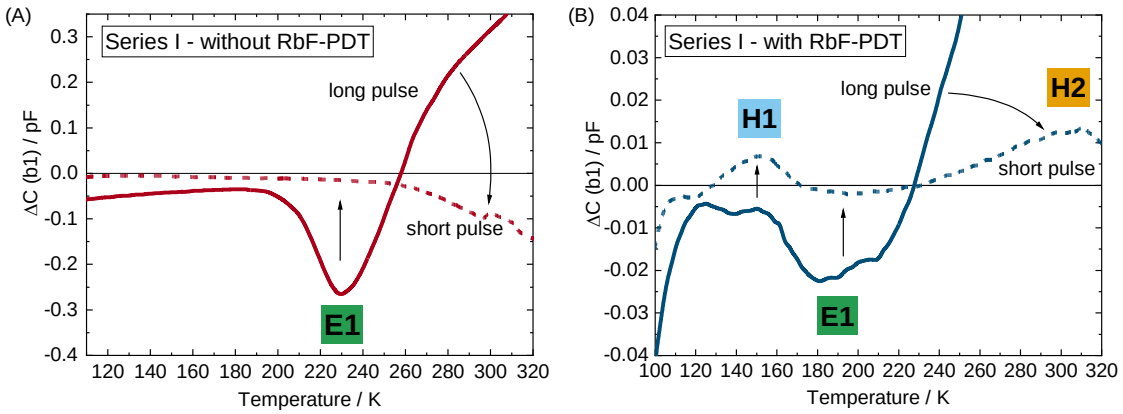

Figure 7.3: Comparison of DLTS measurements of CIGS solar cells (A) with and (B) without PDT from sample set I. For both samples the measurements with a long filling pulse of 50 ms and short filling pulse of 1 ms are shown.

For the corresponding sample with RbF-PDT (same CIGS deposition) a similar temperature scan is recorded. Around 200 K a minimum can be observed and for higher temperatures the signal amplitude increases strongly. Additionally Figure 7.3 compares the short and long filling pulses of CIGS samples (A) without RbF-PDT treatment and (B) with PDT. Long filling pulses of 50 ms are indicated by solid lines and measurements with short filling pulses of 1 ms by dashed lines. Herein, the long pulse measurement in Graph (A) corresponds to the $t_\mathrm{w} = 10\,\mathrm{ms}$ measurement from Figure 7.2. Although the E1 peak of the PDT-sample shows a disturbed shape, it could be fitted and the corresponding energy level was calculated to $(418{\pm}22)\,\mathrm{meV}$, which lies within the errors of the "without PDT" result. Hence both peaks can be assigned to the same origin. Nevertheless, it cannot be excluded, that a second signal is superimposing the E1 peak, resulting in a distorted peak shape.

The large difference between the two measurements is the amplitude of the E1 peak. These differ from each other by an order of magnitude (compare the y-axes). This can be either attributed to a reduced emission process or a significantly reduced trap density. The evaluation data in Table 7.1 reveal a trap density of $(6\pm3)\cdot10^{13}\,\mathrm{cm}^{-3}$ for the sample without PDT and $(1.6\pm0.5)\cdot10^{13}\,\mathrm{cm}^{-3}$ for the sample with PDT. This is equivalent to a reduction in trap density by a factor of 3.8 for the E1 trap and might indicate a passivation of defects in the PDT samples and could be one reason for the improvement in V_{OC}. Nevertheless, the doping density of the CIGS layer influences the V_{OC} strongly, as well [52]. By using the ideal diode following approximation confirms this [157]:

$$\Delta V_{\mathrm{OC}} = \frac{kT}{q}\ln(\frac{N_{\mathrm{A,wPDT}}}{N_{\mathrm{A,w/oPDT}}}) \tag{7.1}$$

By taking the carrier concentrations in Table 7.1 into account, an increase of around 13 to $16\,\mathrm{mV}$ be calculated. In comparison, the experimental differences are $7\,\mathrm{mV}$ and $23\,\mathrm{mV}$, respectively. Therefore, one can assume, that the main part of the V_{OC} increase can be explained by the increase of the carrier concentration and only a minor part is due to the changed trap density.
When applying a short filling pulse of $1\,\mathrm{ms}$ the measurements of both samples with and without PDT, the DLTS signal changes significantly. For both the increasing signal at temperatures above $250\,\mathrm{K}$ reduces strongly. Furthermore, no peak at $200\,\mathrm{K}$ is observed anymore, but for the PDT sample, some new features occur: two majority peaks (due to the positive polarity of the peaks) at $150\,\mathrm{K}$ (“H1“) and $300\,\mathrm{K}$ (“H2“). The low temperature peak can be assigned to a trap state $200\,\mathrm{meV}$ above the valence band edge and with a trap density of $(1.2\pm0.3)\cdot10^{13}\,\mathrm{cm}^{-3}$. Due to it’s properties, it can be assumed not to be a relevant recombination center. For the high temperature peak it was not possible to perform a reasonable evaluation, due to insufficient data quality in this temperature range. This will be topic of the next section.

The second part of this section deals with the DLTS measurements on the samples of Series II. Figure 7.4 (A) shows the temperature scans of the samples with and without PDT. These measurements reveal similar behavior like the first sample series. Again, “E1“-like peak at $220\,\mathrm{K}$ is observed which almost vanishes for the measurement of the corresponding sample with PDT. Additionally, the “H2“ peak at $300\,\mathrm{K}$ is observed in these samples, as well. A maximum analysis of both peaks in both measurements (with and without PDT) results in the Arrhenius plot in Figure 7.4 (B). The results of linear regressions are plotted in yellow (H2 peak) and green (E1 peak) and following trap levels have been evaluated: the E1 minority peaks reveal energy levels of $E_{\mathrm{T,E1,w/oPDT}} = (451\pm32)\,\mathrm{meV}$ and $E_{\mathrm{T,E1,PDT}} = (459\pm11)\,\mathrm{meV}$, the H2 majority peaks in $E_{\mathrm{T,H2,w/oPDT}} = (608\pm8)\,\mathrm{meV}$ and $E_{\mathrm{T,H2,PDT}} = (641\pm16)\,\mathrm{meV}$. Thereby the energy of the E1 trap of Series II agrees with the results from Series I within the errors. Again the energy values represent the mean and standard deviation of different evaluation methods. It should be mentioned, that the two peaks (E1 and H2) do not appear clearly separated from an each other. This superposition might be a possible source of error, even if the magnitude of this uncertainty can not be measured. In detail, this uncertainty is especially related to the peak amplitudes and therefore to the trap densities. This might result in larger errors of the trap densities as specified in Table 7.1. As the amplitudes already imply, the defect density of E1 is significantly reduced by factor 3 from $(2.3\pm0.3)\cdot10^{13}\,\mathrm{cm}^{-3}$ to $(7.8\pm2.3)\cdot10^{12}\,\mathrm{cm}^{-3}$ due to the PDT step and thus, shows an equivalent behavior like in Series I. In contrast, the majority trap H2 shows no significant reduction of the trap density. All values are also listed in Table 7.1 in row “Series II“ and illustrated in Figure 7.5.

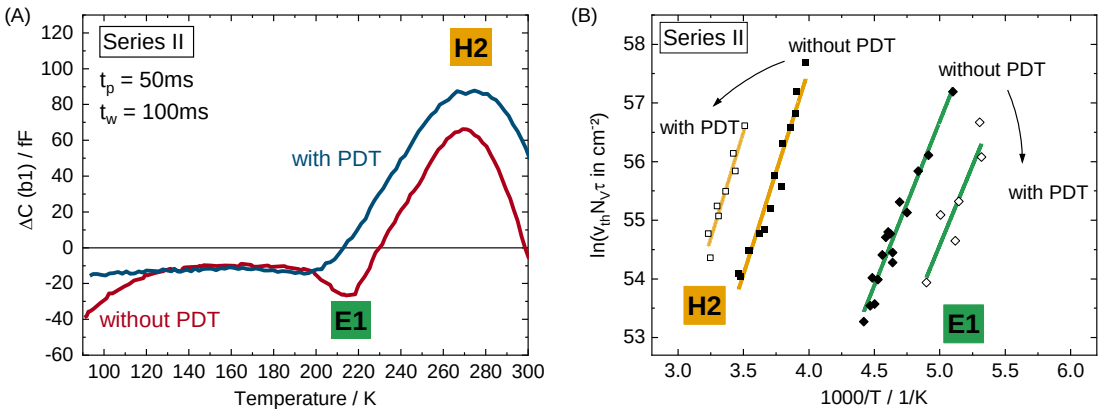

Figure 7.4: (A) DLTS temperature scans for sample set II with minority trap E1 and majority trap H2. Graph (B) shows the Arrhenius plots of the maximum analysis for both traps with and without PDT.

Since the energetic position of both traps, E1 and H2, are located near the middle of the band gap of the used CIGS ($E_{\mathrm{g,CIGS}} \approx 1.15\,\mathrm{eV}$) and show reasonably high cross-sections and trap densities, both are likely candidates to be detrimental recombination centers influencing the device performance. Compare Figure 7.5 (B) for the exact energetic position of the trap levels in the CIGS band constellation. A reduction of the trap density of E1 could therefore be beneficial for the device performance. The underlying mechanism might be a passivation process. In the next paragraph, the presented results will be set in the context of literature:

Karki et al. also reported a strong peak at high temperatures in DLTS measurements. They assign this peak to an energy level of $570\,\mathrm{meV}$ above E_{V}, which is comparable with the H2 peak in this study [52]. Equivalent to the presented results they do not observe an effect of PDT on the trap density, as well. Furthermore, Deitz et al report a trap level in (Ag,Cu)(In,Ga)Se_2 (ACIGS) with an energetic position of $560\,\mathrm{meV}$. They assign this trap state to a $\mathrm{Cu_{In/Ga}}$ substitutional defects as the most likely source [158]. This can be confirmed by density-functional theory (DFT) measurements by Zhang er al., which predict an energy of $580\,\mathrm{meV}$ for $\mathrm{Cu_{In}}$ traps in $CuInSe_2$ (CIS).
Also in the energy range of the E1 peak, similar results can be found in literature. Theoretical calculations reveal an energy level at $410\,\mathrm{meV}$ for indium vacancies V_{In}, which is in the energy range of the observed E1 peak. Experimentally Kerr et al. identified a minority peak around $220\,\mathrm{K}$ with a corresponding energy level of $520\,\mathrm{meV}$ beyond the conduction band edge in CIS [159]. This results in an energetic position of $520\,\mathrm{meV}$ above E_{V} for a band gap of $E_{\mathrm{g,CIS}} \approx 1.04\,\mathrm{eV}$ which is slightly higher than the energies measured in this study [21].
In conclusion, both identified trap levels show different behaviors due to the treatment with Rb. The trap density of E1 is reduced due to the PDT, eventually due to a passivation process, the trap density of H2 is not. This might be connected with the spatial location of the underlying defects. Atom probe tomography (APT) measurements already revealed, that alkali elements like Rb segregate preferably at grain boundaries and interfaces [61, 160]. In combination with the reulst of this study, that E1 is affected by the PDT, leads to the conclusion, that E1 is a defect located at grain boundaries and not in the grain interiors. Results from Paul et al. can confirm this finding [161]. They performed nano-DLTS on a grain boundary area in CIGS and found a similar level to the E1 level with an energy level of $470\,\mathrm{meV}$ above E_{V}.
In contrast, the H2 defect is a defect not exclusively located at grain boundaries. The already mentioned findings of Deitz et el. revealed that the $560\,\mathrm{meV}$ defect has no preferential location, but is distributed through the absorber layer and located in the grain interiors as well [158]. The Rb atoms, segregating at the grain boundaries and therefore, are not able to occupy and passivate this

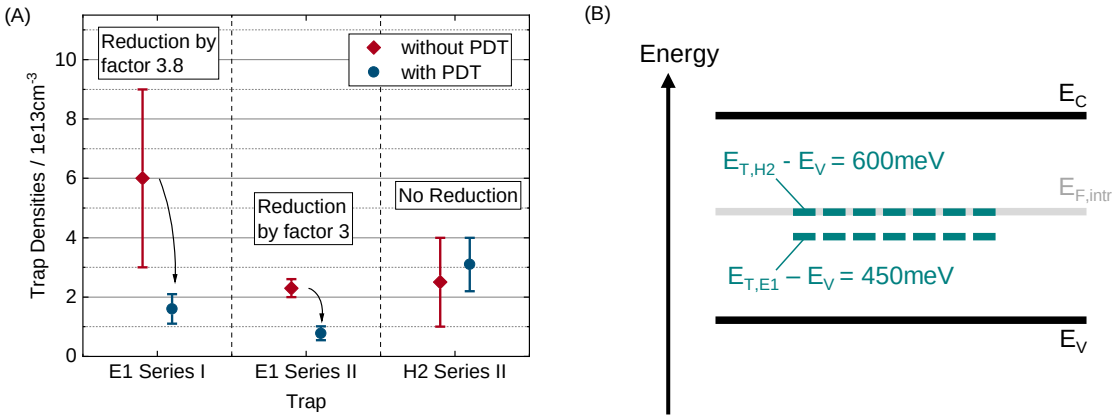

Figure 7.5: (A) Illustration of the trap densities of trap E1 and H2 and the the effect of the RbF-PDT. While a reduction of trap density of E1 can be observed for both sample sets, this is not the case for trap H2. (B) shows the position of the found defects E1 and H2 within the bands of CIGS (minimum band gap).

defect. However, more evidence is needed to proof this theory and to distinguish between different spatial locations (point and extended defects). One possibility might be for example by performing pulse variation measurements like introduced elsewhere [162, 163].

Another point, that can be observed, is that in Chapter 6 similar temperature scans have been recorded for the sample with sodium fluoride (NaF)-PDT. Here the a minority level (Na3) at 250 K and a majority level at 300 K have been identified, which are comparable to peaks E1 and H2 of this investigation. The energetic positions show some differences, but due to their large errors, the assignment of E1 to Na3 and H2 to Na4 is possible. Since this chapter deals with a CIGS absorber from a completely different evaporation process, some differences in the temperature scans and the corresponding defects can be assumed. Nevertheless, the possibility, that E1 (and maybe H2 as well) is a Na induced defect level fits in to the model of the well-known Rb-Na exchange mechanism [66, 59, 88]. This mechanism proposes, that the Na atoms, segregated at grain boundaries during the CIGS growth, are pushed into the grain interiors and towards the interfaces.
With this in mind, the following theory belonging the DLTS measurements could be derived: E1 is a sodium induced defect. By applying a RbF-PDT, the rubidium atoms partly replace the sodium atoms at grain boundaries. Therefore the Na-induced defect signal in the DLTS reduces. The Rb atoms at grain boundaries may induce defects as well, but as showed in the previous Chapter 6, Rb seems to have a less strong defect inducing effect, compared to sodium or potassium. In the case of H2 these findings cannot be concluded, because H2 seems to be 1. homogeneously distributed through the CIGS and 2. the results of Chapter 6 show, that Rb induces a high temperature peak as well.

A key result of this study is the reduction of the trap density of the minority E1 trap by a factor of approximately 3 to 3.8 due to the alkali treatment. Because of the energy level of E1 and H2, and the high trap densities of $\approx 1{\cdot}10^{13}\,\mathrm{cm}^{-3}$, the traps are both likely candidates to have an effect on the cell performance. Despite this significant reduction of the E1 trap density, an effect on cell performance due to the reduced Shockley-Read-Hall (SRH) recombination is not clearly determinable, because a major part of the improvement can be assigned to the increase of the CIGS charge density.
Therefore, the results are reproduced and analyzed by numerical simulations in the next section.

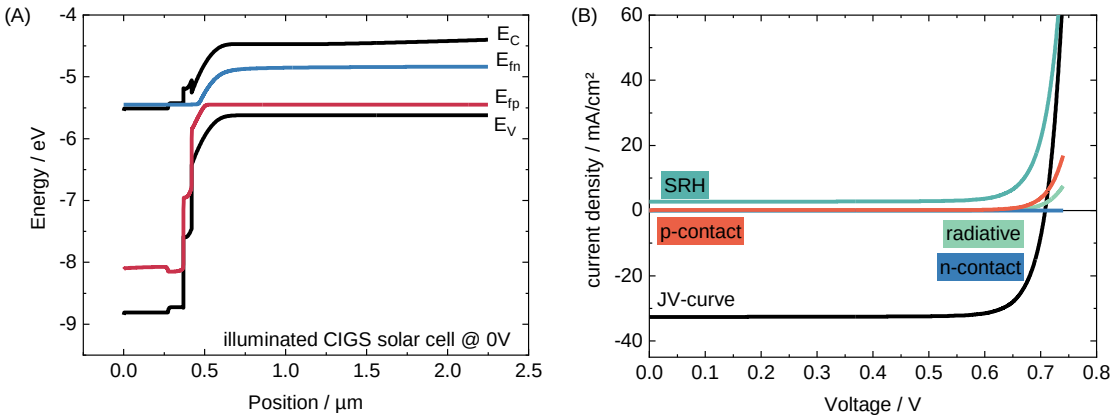

Figure 7.6: (A) Band diagram of the illuminated CIGS solar cell at 0 V bias, used as numerical model for the 1D semiconductor simulations. (B) Resulting current-density-voltage (JV)-curve and corresponding loss curves for SRH recombination, radiative recombination and minority surface recombination at the contacts.

7.3 Reproduction of Experimental Results by Numerical Simulations

This section will discuss the influence of the defect density of both experimentally measured traps (E1 and H2) and the PDT induced changes in doping on the performance of the solar cells. Therefore a numerical 1D model was build up in order to reproduce the experimental findings. Herein the defect properties resulting from DLTS measurements and the doping values from CV measurements are used as inputs. Furthermore, the band gap grading was modelled according to the GDOES measurements shown in Figure 7.1 (C). All other material parameters are set on the default values as defined in A.1. Afterwards, the values of the minority surface recombination velocity (SRV) at the contacts have been set in order to match the V_{OC} value of the PDT-sample from Series II ($710\,\mathrm{mV}$. The resulting band diagram can be seen in Figure 7.6 (A) for the illuminated, unbiased case. In Graph (B), the resulting JV-curve is shown along with the loss curves of SRH recombination, radiative recombination and minority surface recombination at p-and n-contact. With the defect properties from the DLTS measurements, the SRH recombination is the major loss mechanism in this model, which is even effecting the J_{SC}. Nevertheless, the resulting JV-curve shows a slightly higher FF and J_{SC} values ($81\,\%$ and $32.69\,\mathrm{mA/cm^2}$) than the experimental results. The reason for the overestimated current is the unconsidered metal grid shading. One reason for the high FF is definitely the limitation of the 1D semiconductor simulation, not taking into account the electrical losses in the transparent conductive oxide (TCO) and grid.

Since we are mainly interested in the V_{OC} and the changes in the characteristic parameters, the further simulations have been conducted with the semiconductor JV-curve. Figure 7.7 (A) shows the influence of the doping density of the CIGS layer and the trap density of the E1 defect on the V_{OC}. The defect density of the H2 defect was kept constant. The black circles indicate the positions of the experimental samples from Series II with and without PDT. The arrow indicates the change due to the PDT step (lower E1 density and higher doping). The simulations indicate a V_{OC} improvement of $17\,\mathrm{mV}$, which is slightly lower than the experimentally obtained value ($23\,\mathrm{mV}$). The beneficial effect due to the doping density increase is only $10\,\mathrm{mV}$, resulting in a V_{OC} improvement due to the E1 passivation of $7\,\mathrm{mV}$. A further reduction of the E1 density would have only a minor effect (indicated by the almost horizontal iso-V_{OC} lines for low trap densities). One possible reason is, that the recombination at H2 (higher density than E1) is still happening, so that the reduced recombination over E1 is only a small part of the total recombination rate.

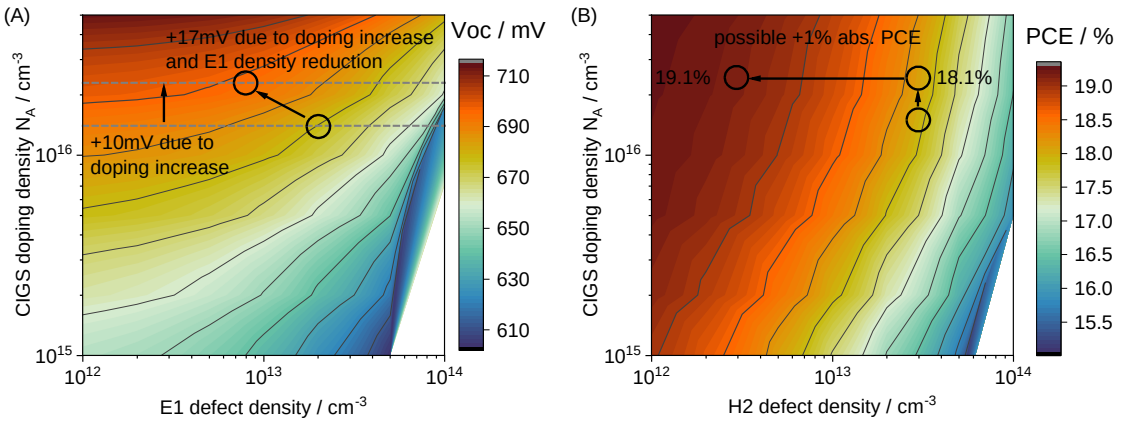

Figure 7.7: Results of a 1D semiconductor simulation with parameter variation. In Graph (A), the doping density of CIGS and the defect density of the E1 defect on the V_{OC} is varied. In (B) doping density and the trap density of H2 is varied.

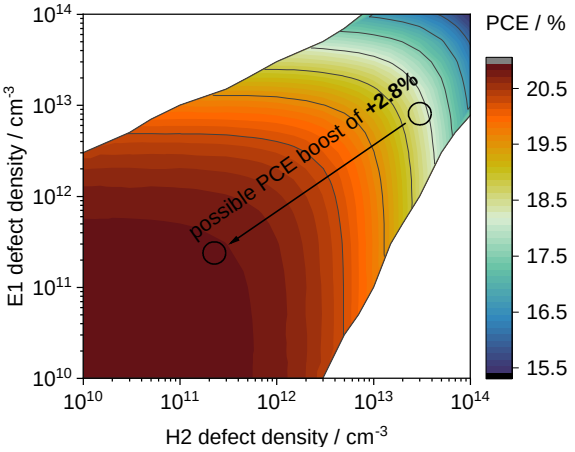

Figure 7.8: Simulation results of a simultaneous reduction of E1 and H2 trap density. The arrow indicates the possible PCE gain from the simulation reference (measured trap densities) to the maximum value.

Therefore, the change of the H2 defect density has a higher impact on the simulated cell performance than a change of the E1 density. Figure 7.7 (B) shows an imaginary reduction of the H2 density and a simultaneous variation of the doping density like in Figure (A). This graph shows the stronger dependence on the H2 trap density. An imaginary reduction of the H2 density by one order of magnitude, indicated by the horizontal arrow, could lead to approx. $1\,\%$ absolute power conversion efficiency (PCE) gain compared to the reference (experimental values of the PDT sample from Series II as inputs, resulting in $18.1\,\%$ simulated efficiency). As well for H2, a further reduction results only in limited improvements because a plateau region is reached.

Indeed, both traps have to be reduced to obtain a higher efficiency boost. The simulations in Figure 7.8 show, that a rigorous reduction of both trap densities of E1 and H2 below $5{\cdot}10^{11}\,\mathrm{cm}^{-3}$ could lead to an efficiency of almost $21\,\%$, which corresponds to a gain of $2.8\,\%$ absolute, with respect to the simulated reference. Both configurations are indicated again by black circles and a connecting arrow.

Figure 7.9 (A) shows the resulting JV-curve of a device with trap densities of $1{\cdot}10^{11}\,\mathrm{cm}^{-3}$ or E1 and H2. Still, the SRH recombination is present, reducing the J_{SC}, but this can be assigned to recombination within the other layers of aluminum doped zinc oxide (AZO), intrinsic zinc

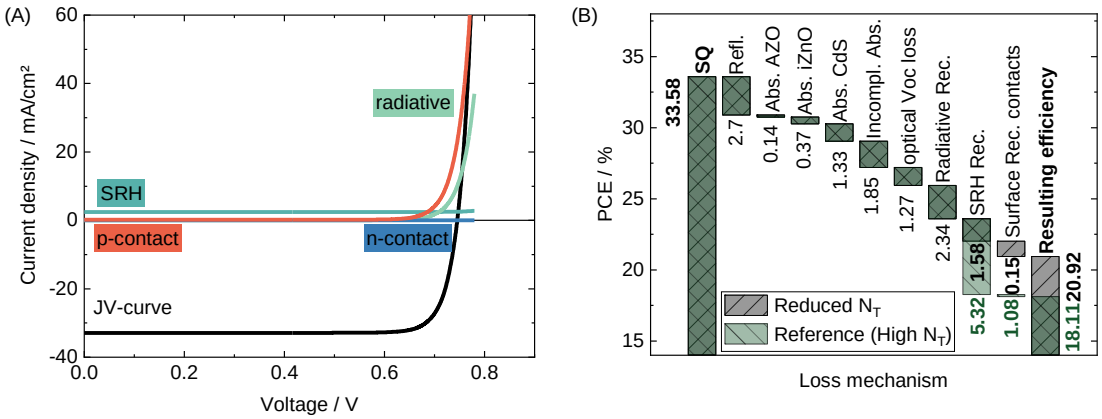

Figure 7.9: (A) Simulated JV curve of a CIGS solar cell with significantly reduced trap densities of E1 and H2 together with the corresponding loss curves. Graph (B) shows a loss Analysis of this device in comparison with the reference model including the actual measured trap densities.

oxide (iZnO) and cadmium sulfide (CdS). The main loss mechanism, reducing V_{OC} and FF is the recombination of minority carriers at the contact (red) and the radiative recombination (green). As fewer carriers are lost due to SRH, the surface recombination becomes a more significant loss mechanism. This is illustrated in Figure 7.9 (B), where all loss mechanisms from Shockley-Queisser (SQ) down to the simulated efficiency are visualized. Since the same optical model was used for the reference model and the model with reduced defect densities, the optical losses (reflectance, parasitic absorptance, incomplete absorptance and V_{OC} loss due to J_{SC} loss) are the same. Due to the methodology of the loss analysis, even the loss due to the radiative recombination is the same (treatment as the fundamental recombination mechanism including device imperfections like band alignments or finite mobilities). But for the remaining recombination mechanisms, the amount of the PCE losses change significantly. The PCE loss due to the SRH recombination reduces from $5.32\,\%$ to $1.57\,\%$. On the other hand, the loss due to minority carrier surface recombination increases from $0.15\,\%$ to $1.08\,\%$. This results in the mentioned effective PCE gain of absolute $2.8\,\%$.

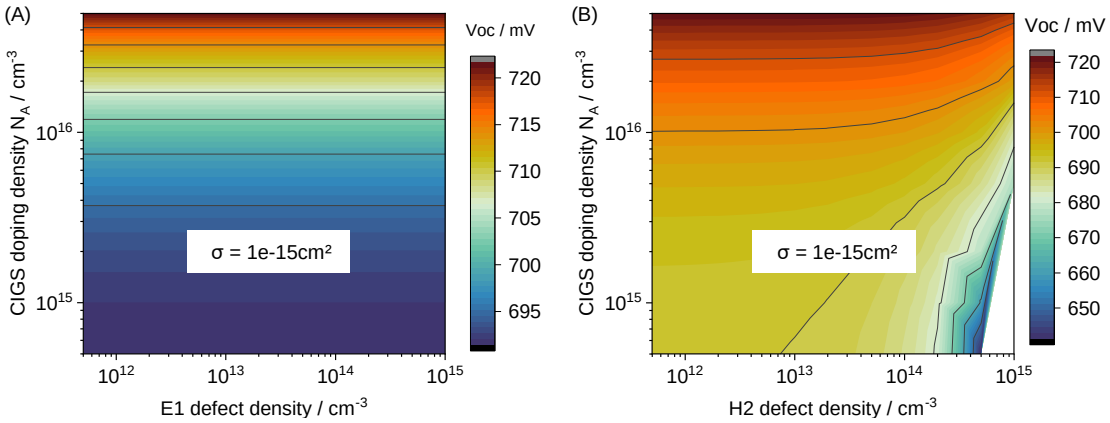

Figure 7.10: Parameter variation of doping density and (A) E1 trap density and (B) H2 trap density with reduced capture cross sections of $1{\cdot}10^{-15}\,\mathrm{cm}^2$.

Another point which has to be taken into account: the effects of E1 and H2 density in the parameter variations depends strongly on the assumed capture cross section of the defects. Since the capture cross section values from DLTS measurements are relatively error-prone, exact statements from

simulations can not be made, until the capture cross sections are not known in detail. Figure 7.10 shows again parameter variations of the doping density and (A) E1 density and (B) H2 density, here with capture cross sections of $1{\cdot}10^{-15}\,\mathrm{cm}^2$ instead of $1{\cdot}10^{-13}\,\mathrm{cm}^2$ (used in above parameter variations). Obviously the dependence of the V_{OC} on the defect densities reduces drastically. The change of the E1 density shows almost no influence anymore and also the change in the H2 density shows a strongly reduced effect.

Conclusion

Within this chapter the successful investigation of CIGS samples from a fabrication-like inline system with DLTS was shown. The characteristic peaks in the temperature scans have been identified and the corresponding defect properties have been evaluated. Two prominent defect features have been found: one minority trap E1 at approx. $450\,\mathrm{meV}$ above E_{V} and one majority level H2 at approx. $600\,\mathrm{meV}$. Furthermore, it was shown that the process step of a RbF-PDT influences the defect characteristic of the DLTS measurement. By applying a PDT, the defect density of the defect E1 is reduced by factor 3 to 3.8. In contrast, the density of the H2 defect is not affected due to the PDT.
Although the increase of the doping density is one major part for the V_{OC} and PCE boost, numerical simulations can show, that also the reduction of the E1 defect density can play a role. This effect nevertheless, depends strongly on the assumed capture cross sections. Additionally simulations have been conducted to estimate the potential of further defect passivation on the efficiency. Herein an efficiency boost of $2.8\,\%$ is predicted for a significant passivation of both traps, E1 and H2.

8 Systematic investigation of the effects of RbF PDT in silver alloyed CIGS solar cells and the reproduction in numerical simulation

The results of this section have been published in parts in the publication "How Small Changes Make a Difference: Influence of Low Silver Contents on the Effect of rubidium fluoride (RbF)-post-deposition treatment (PDT) in CIGS Solar Cells" [90]. (License number: 5444700409395)

The interest on the partial substitution of copper with silver in Cu(In,Ga)Se_2 (CIGS) solar cells increased within the last years [160, 158, 77, 82]. The growth of smooth layers with large grains is of great advantage in tandem architectures with other thin-film technologies like perovskite solar cells [78, 70]. Furthermore, results with efficiencies above $20\,\%$ of Ag containing CIGS solar cells have been already reported [71, 69]. Nevertheless, the performances are still lagging behind the record efficiencies of silver-free samples [49, 50]. As well in (Ag,Cu)(In,Ga)Se_2 (ACIGS) solar cells, like it was already the case for CIGS, the established process step of an alkali PDT plays an important role in reaching higher efficiencies [49, 164, 60]. Although it is known, that a PDT step with alkali fluorides leads to increased doping densities and passivated grain boundaries resulting in longer carrier lifetimes and in a performance gain, several questions remain unsolved [52, 154]. These include for example a precise understanding of the observed sodium rubidium exchange mechanism [88]. In the case of silver alloyed CIGS solar cells, additionally the stoichiometric and morphological conditions change. Herein, a deeper understanding of the role of alkali elements in ACIGS is crucial for the further development.

Therefore, this chapter focuses on the role of RbF-PDT in silver alloyed CIGS (ACIGS). ACIGS solar cells with varying Rb content are investigated systematically. Again these samples have been fabricated in a fabrication-like inline co-evaporation system, like the samples in Chapter 7. The characterization includes optoelectronical measurements of JV and external quantum efficiency (EQE), compositional investigations with time of flight secondary ion mass spectroscopy (ToF-SIMS) and an analysis with capacitative methods of capacitance-voltage (CV) and Deep Level Transient Spectroscopy (DLTS). In addition, a numerical model is build up to support the interpretations.

8.1 ACIGS Solar Cells with a Variation of the RbF Source Temperature

This investigation is based on a batch of ACIGS solar cells from an inline co-evaporation system with a variation of the RbF-PDT source temperature. Starting from $460\,^{\circ}\mathrm{C}$ the source temperature was increased in steps of $30\,^{\circ}\mathrm{C}$ with a maximum value of $580\,^{\circ}\mathrm{C}$. Every step in temperature corresponds to an increase of an approximately factor two of the RbF evaporation rate. The devices show a decrease of the device performance for an increase of the PDT source temperature, even for

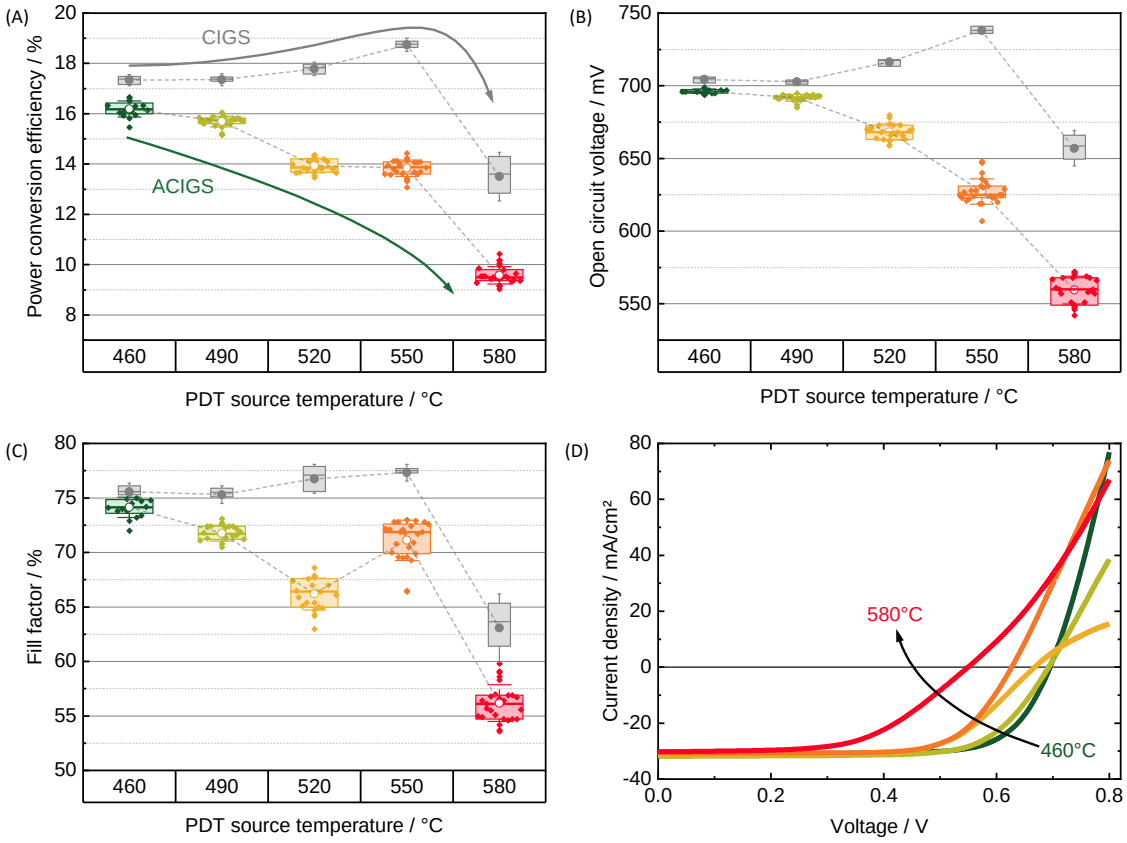

Figure 8.1: IV data of all cells from the investigations showing the behavior of a) power conversion efficiency (PCE), b) V_{OC} and c) fill factor (FF) with increasing RbF source temperature. In addition, data for a comparable CIGS process (without silver) from the same system are shown in gray. The shown IV curves correspond to the samples which were used for CV and DLTS measurements.

small amounts of Rb. Figure 8.1 a) shows the PCE data of this measurement series. The boxplots in Figure 8.1 b) and c) show a significant trend of decreasing V_{OC} and FF, respectively, resulting in a decreasing efficiency with increasing PDT source temperature. This trends can be seen in the representative IV curves in Figure 8.1 d), as well. For the representative IV curves and all following characterizations of the samples, cells with slightly higher PCE and V_{OC} than average have been used . The devices with low Rb show a good diode behavior. As the RbF source temperature increases, a FF and a V_{OC} loss increases as well. The decrease of the FF results in a distorted IV curve in the maximum power point (MPP) region of the $580\,°C$ sample. Only the FF values for a temperature of $550\,°C$ do not fit into the behavior and show significantly increased values compared to the temperature steps before and after. However, an explanation for this outlier could not be found within this investigation. Furthermore, for the IV curves of samples 460, 490 and $520\,°C$ a roll-over effect can be observed with an increasing strength. This trend vanishes for both samples with higher PDT source temperatures. Despite of these features, the trend in decreasing V_{OC} can be clearly seen, which is the dominant parameter and mainly responsible for the decrease of the PCE.

The effect of RbF in ACIGS solar cells is up to now not investigated in detail. Most groups work on potassium fluoride (KF) treatments [84, 69, 165, 85]. Although, there are some investigations on RbF in ACIGS [166, 71, 167], such effects of RbF have not been reported in literature yet, with exception of the study of Kaczynski et al. [168]. However, this study was performed on

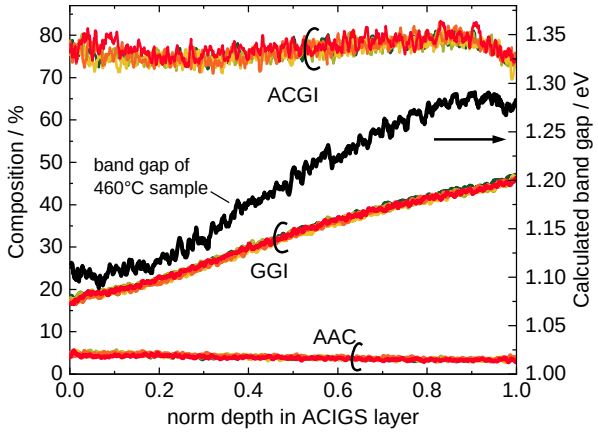

Figure 8.2: Representative composition profiles from ToF-SIMS measurements for one sample for each PDT temperature step. The AAC ratio has a mean value of $\approx 5\,\%$. The GGI shows a grading ranging from $20\,\%$ at the front to $45\,\%$ at the back interface. The ACGI is in the range around 72 to $82\,\%$.

stainless steel substrates and is therefore only in parts comparable to the presented study. A further example of Yang et al. show that a RbF-PDT can have a beneficial effect in ACIGS solar cells [71]. They combine a sodium fluoride (NaF)-PDT with a subsequent RbF-PDT and work with sodium barriers, deposited on the glass substrate. Furthermore, some investigations are published on high band gap ACIGS, which are also not comparable with the investigated samples of this study [166, 77]. In summary, there is no publication available, which shows a beneficial effect of a RbF-PDT in low band gap ACIGS on glass substrates .
But there are also examples, which show a detrimental effect of KF-PDT on the cell characteristic. Valdes et al. show that the beneficial effect of potassium in CIGS and $CuInSe_2$ (CIS) solar cells switches to a detrimental effect after the substitution of parts of Cu by Ag [85].

In general, the behavior of decreasing efficiency without any maximum stands in strong contrast to the common behavior of silver-free devices of a comparable fabrication. Representative data of a RbF variation on CIGS from the same system, shown in gray in Figure 8.1 a)-c), reveal a maximum in efficiency at a PDT source temperature of around 520 to $550\,^{\circ}\mathrm{C}$. The only differences between the CIGS and ACIGS series are the partial substitution of copper by silver and the reduced maximum substrate temperature of below $500\,^{\circ}\mathrm{C}$ during the deposition of ACIGS in comparison with CIGS which is deposited at a temperature above $600\,^{\circ}\mathrm{C}$. The performance gain in CIGS is obtained due to an increased V_{OC} and FF, which can be explained by an increase of the free carrier concentration and a reduction of the trap density [52, 63, 53]. However, in the investigated sample set a rapid decrease of the characteristic quantities V_{OC}, FF and consequently in PCE, is observed.

In order to examine, whether differences in the ACIGS composition could have an influence on the behavior of the cell performance, ToF-SIMS measurements have been performed. Figure 8.2 shows the (Ag+Cu)/(Ga+In) (ACGI), Ga/(Ga+In) (GGI) and Ag/(Ag+Cu) (AAC) depth profiles within the ACIGS layer, which are comparable for all five PDT variations. The GGI reveals a nearly linear trend from $20\,\%$ at the CdS/ACIGS interface to $45\,\%$ at the Mo/CIGS interface. The mean value of the ACGI is $77\,\%$ and the value AAC of is $5\,\%$, which equates to the specified amount of silver that is be substituted. The calculated (from measured AAC, Cu/(Ga+In) (CGI) and GGI) band gap profile in Figure 8.2 shows no clear notch, but regions with smaller slopes in the vicinity of the interfaces [20]. The CGI value of the CIGS reference batch from Figure 8.1 is slightly higher

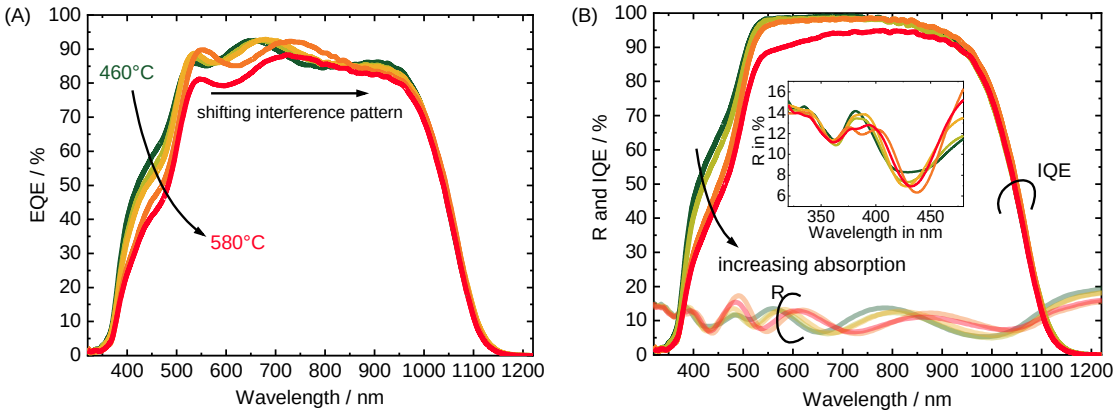

Figure 8.3: a) EQE measurements showing an increasing absorption in the wavelength range around $400\,\mathrm{nm}$ with increasing Rb content. Graph b) shows the corresponding internal quantum efficiency (IQE) and reflectance measurements.

with $82\,\%$, compared to the ACIGS batch. The influence of the ACGI value will be discussed in Section 8.4.

In addition EQE and reflectance measurements have been performed on all variations. Figure 8.3 (A) shows the results of the EQE measurements, Graph (B) shows the reflectance measurements and the resulting IQE curves. Additionally, the reflectance in the wavelength region from 320 to $480\,\mathrm{nm}$ is shown in an inset in Graph (B).
In the EQE, as well as in the reflectance curves, a slight shifting of the interference pattern can be observed, indicating a change of a layer thickness. Also the increased parasitic absorptance in the wavelength range of 400 to $900\,\mathrm{nm}$ is a further hint for a change in layer thickness. With scanning electron microscopy (SEM) cross section images, it can be confirmed, that the cadmium sulfide (CdS) layers show an increasing thickness with increasing RbF source temperature from $50\,\mathrm{nm}$ CdS for the $460\,^{\circ}\mathrm{C}$ sample, up to $70\,\mathrm{nm}$ for the $580\,^{\circ}\mathrm{C}$ sample. Figure 8.4 shows a representative SEM cross-section of the $580\,^{\circ}\mathrm{C}$ sample, revealing well defined CdS, intrinsic zinc oxide (iZnO) and aluminum doped zinc oxide (AZO) layers on top of the smooth ACIGS surface. Next to the increase of the CdS, the formation of a $RbInSe_2$ (RIS) layer is a possible explanation for changing interference patterns and increased absorption. The changing interference maximum in the inlet in Figure 8.3 (B) shows a changing shape from a single to a double maximum with increasing RbF temperature, indicating an additional thin layer. The formation of alkali-indium-selenium compounds on the copper depleted CIGS surfaces is already reported in literature for RIS [53, 66, 67, 56] and $KInSe_2$ (KIS) [169, 65]. Herein Lopes et al. showed results from numerical simulations, which reveal a decreasing FF with increasing KIS layer thickness, resulting in a similar performance behavior as observed in the presented study. Such a RIS layer might be a part of an explanation for the decreasing FF of this study, as well. Both observations, the indication for an increasing CdS layer thickness and for the formation of a RIS layer show that the surface composition and the subsequent growth of CdS is affected by the amount of Rb offered by the PDT step.

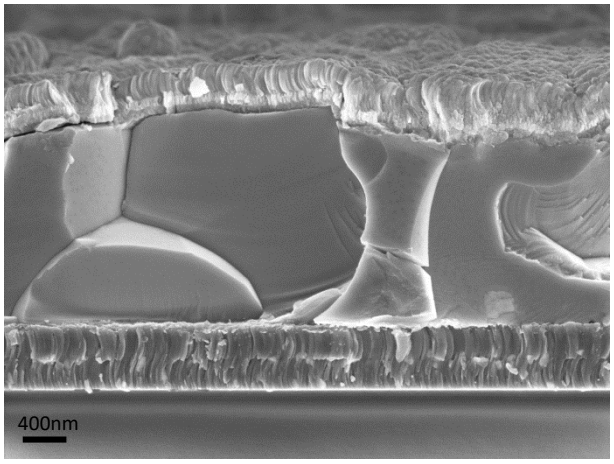

Figure 8.4: SEM cross section of an ACIGS solar cell with 580 °C PDT source temperature from this study. The image was taken with a Zeiss Crossbeam 550 FIB-SEM and an accelerating voltage of 5 kV.

8.2 Determination of Deep Defects in ACIGS solar cells with Capacitative Techniques

As already mentioned, the V_{OC} of an ACIGS solar cell strongly depends on the doping density of the ACIGS layer itself [157]. Therefore, CV measurements have been performed on the sample variation, resulting in a doping profile graph in Figure 8.5 (A). The well-known "U"-shape of the curves are commonly seen for CIGS solar cell devices [170, 171]. The extracted doping densities from linear regression of the corresponding Mott-Schottky plots are shown in Figure 8.5 (B). Herein, the minima of the doping profiles correspond to the doping values from Mott-Schottky evaluation. Both graphs reveal, that the doping densities of the samples are decreasing with increasing amount of Rb, explaining the behavior of V_{OC}, which is in contrast to the behavior expected from silver-free CIGS. The data of the CIGS reference batch from Section 8.1 are shown in gray, revealing a first increase of the doping density with a subsequent decrease. This trend can be directly seen in the V_{OC}.

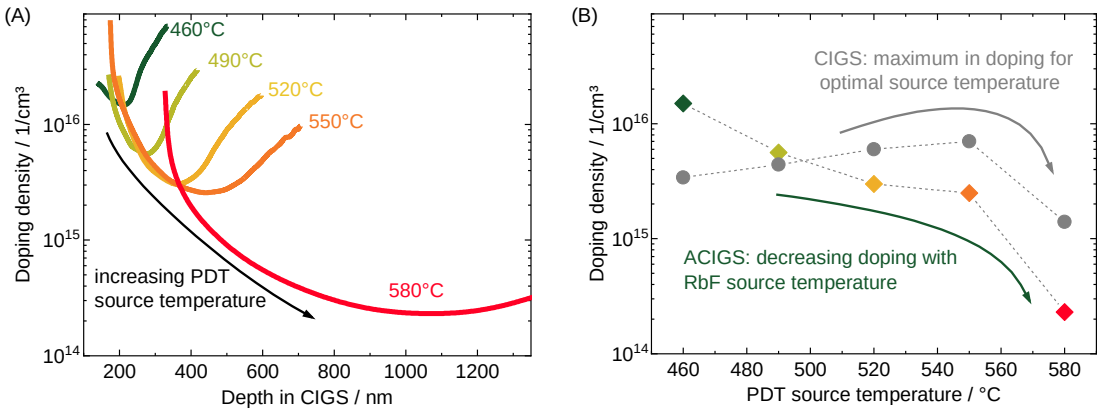

Figure 8.5: a) Doping density over the sample depth calculated from CV measurements. For higher PDT source temperatures the curves are shifting to lower doping values. Graph b) shows the apparent doping extracted from Mott-Schottky plots, again in comparison to the CIGS reference batch in gray.

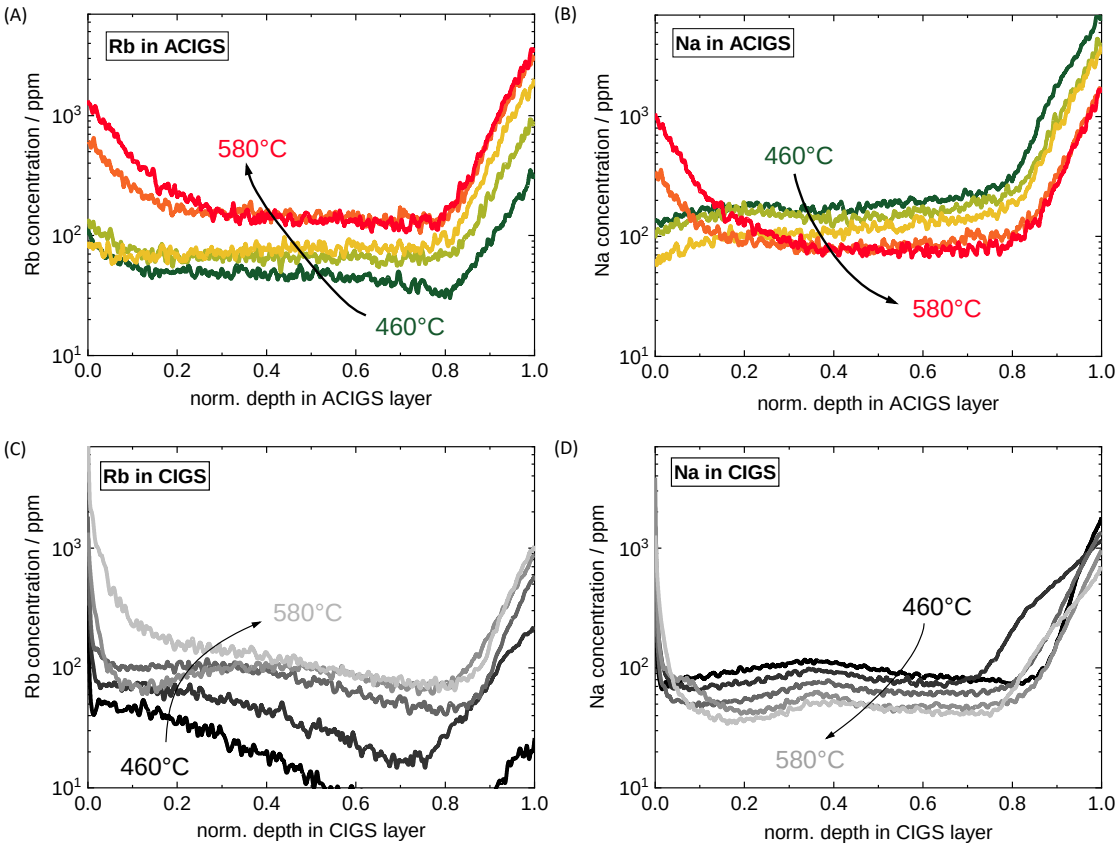

Figure 8.6: Distribution of alkali elements (A) Rb and (B) Na over the ACIGS layer depth determined with ToF-SIMS. Here, 0 represents the interface to CdS and 1 the interface towards the molybdenum back contact. Graph (C) and (D) show the corresponding measurements of the CIGS references.

Again, the value of the 550 °C sample of the ACIGS series does not fit perfectly in the behavior of the rest of the data and shows a value comparable with the 520 °C sample which might be one aspect that leads to the above mentioned higher FF values of these samples. Nevertheless, the trend of decreasing doping density is clearly visible revealing a difference between the doping values of the 460 °C and the 580 °C samples of almost two orders of magnitude.

Despite this high reduction, doping can be assumed to be only a partial explanation for the decrease of V_{OC}. By using the ideal diode equation, an approximated change in V_{OC} of

$$\Delta V_{\mathrm{OC}} \leq \frac{k_{\mathrm{B}}T}{q} \ln \frac{N_{\mathrm{A},460\,^{\circ}\mathrm{C}}}{N_{\mathrm{A},580\,^{\circ}\mathrm{C}}} = 105\,\mathrm{mV} \tag{8.1}$$

can be expected [53]. Experimentally a difference of 140 mV is observed, indicating that other mechanisms, such as a barrier caused by the aforementioned RIS layer can be assumed to be responsible for this discrepancy. But the question why such a fundamentally different behavior of ACIGS compared with CIGS and no V_{OC} enhancement is observed, is still not answered. Since the doping density and therefore the V_{OC} is closely linked with the alkali elements within the (A)CIGS layer, ToF-SIMS measurements have been performed to investigate the alkali concentrations with spatial resolution in depth. Figure 8.6 shows the depth profiles of Rb ((A) and (C)) and Na ((B) and (D)) of the ACIGS and CIGS samples. It is clearly visible for both, CIGS and ACIGS, that the amount of rubidium within the layer is increasing with the RbF source temperature, while the

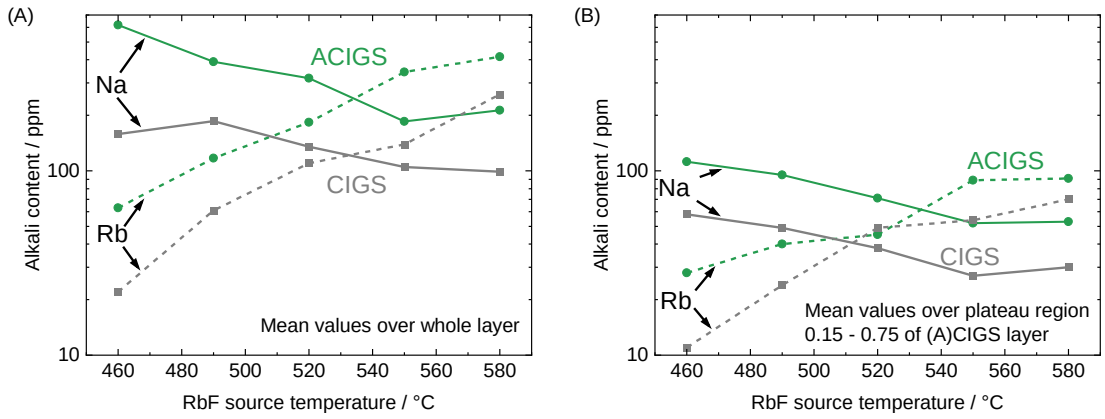

Figure 8.7: Mean Rb and Na contents within the CIGS and ACIGS layer in the whole layer (A) and for the plateau region from 0.15 to 0.75 of the normalized layer thickness.

amount of sodium is decreasing. That is an indication the Rb-Na exchange mechanism, where Rb pushes Na in the grain interior (GI) and towards the surface of the layer (and is later washed away) [88].

Nevertheless, small differences in the absolute values of the alkali concentrations, indicate that **more** Rb is incorporated into ACIGS, compared to CIGS, although the conditions of the PDT process and the amount of the Rb supply during the PDT process was the same. The change in alkali concentration with increasing RbF source temperature is illustrated in Figure 8.7. For ACIGS (in green) and CIGS (in gray) the concentrations of Rb and Na are plotted over the PDT temperature. Figure (A) shows the integral values of the whole layer, and Figure (B) shows the integral values in the plateau region between 0.15 and 0.75 of the normalized (A) CIGS layer, in order to exclude the effect of the increasing alkali concentrations at the interfaces. Both graphs, (A) and (B), show similar results with differences in the absolute values, but only small differences in the general trend. Overall, the alkali amounts in ACIGS are higher compared to CIGS. This observation might be explained with the increasing solubility of alkali elements in ACIGS with increasing silver content, as reported by Aboulfadl et al. [160].

But in principle a similar range of concentrations is covered. The overall amount of Rb in CIGS is in the range of 20 to $300\,\mathrm{ppm}$, for ACIGS in the range of 60 to $400\,\mathrm{ppm}$. Therefore, it can be excluded, that significantly different amounts of Rb in CIGS and ACIGS are responsible for the different behavior in performance. This can bee seen as well in Figure 8.8, where PCE, V_{OC}, FF and doping density are plotted over the averaged amount of Rb in the CIGS and ACIGS layer, respectively. Although the differences in the incorporated amount of Rb are clearly visible, the experimentally realized amounts of Rb in the CIGS and ACIGS layers span over a similar range. The Rb amount for optimal performance in CIGS is approx. realized in the ACIGS, as well.

For the amount of Na, the situation is slightly different. While the amount of Na in CIGS is in the range of 100 to $200\,\mathrm{ppm}$, the amount in ACIGS is in the range of 200 to $600\,\mathrm{ppm}$. Although Na is displaced by Rb, the amounts of Na in ACIGS are higher. One reason is, that already for RbF source temperatures of $460\,^{\circ}\mathrm{C}$, the amounts are significantly higher. This difference in the Na content might be one aspect in the explanation of the different behavior of CIGS and ACIGS. A higher amount of Na in the ACIGS layer might result in a higher amount of $\mathrm{Na_{Cu}}$ like Malitckaya et al. proposed [58]. This can change the doping mechanism by copper vacancies $\mathrm{V_{Cu}}$ and the formation of $\mathrm{Rb_{Cu}}$ sites, and therefore the effective doping. In conclusion, a significant difference

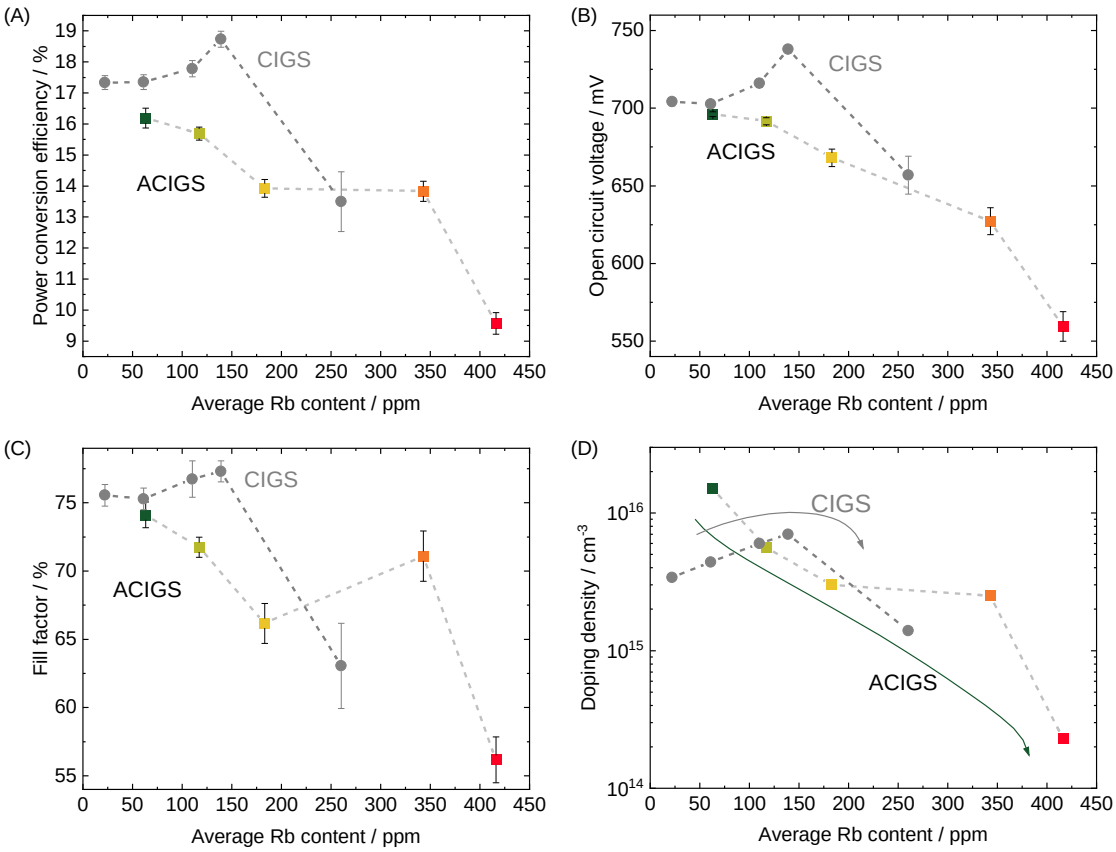

Figure 8.8: Characteristic IV data (A) PCE, (B) Voc, (C) FF and (D) doping density of CIGS and ACIGS solar cells.

in the Rb content cannot be observed for ACIGS and CIGS, excluding an influence of the integral Rb content on the performance behavior. But the significant differences in the Na content might be a part of an explanation.

Furthermore, silver affects the morphology of CIGS layers, because larger grains and therefore fewer grain boundaries are observed for silver alloyed CIGS [70]. Since grain boundaries are the structural features, where alkali, especially Rb segregate, a less strong effect of Rb on doping density and V_{OC} enhancement might be observed [59]. In the presented ACIGS study, only a detrimental effect of RbF on V_{OC} is observed. One possible explanation could be that the doping mechanism is changed due to the substitution of copper by silver. Kodalle et al. showed, that the effect of a RbF-PDT in CIGS (positive or negative) is correlated to the CGI value and the amount of copper vacancies V_{Cu} [66]. As silver addition could affect both the CGI value and the V_{Cu}, changing the doping mechanism, and shifting the CGI in a range where the effect of PDT on V_{OC} is negative.

Another parameter, influencing the V_{OC} of ACIGS solar cells, is the presence of deep defects within the absorber layer causing detrimental Shockley-Read-Hall (SRH) recombination and therefore reduced carrier lifetimes. The effect of RbF-PDT on deep defects in CIGS (without silver) has been investigated by DLTS and other capacitative techniques already in the last years, revealing a passivating effect of Rb and an increasing carrier lifetime [52, 156, 56].
Therefore DLTS measurements have been performed on the presented batch of ACIGS solar cells in standard DLTS and RDLTS direction. Figure 8.9 (A) shows the resulting RDLTS temperature scans of all RbF variations with a pulse width of $10\,\mathrm{ms}$ and a time window of $5\,\mathrm{ms}$. In principle,

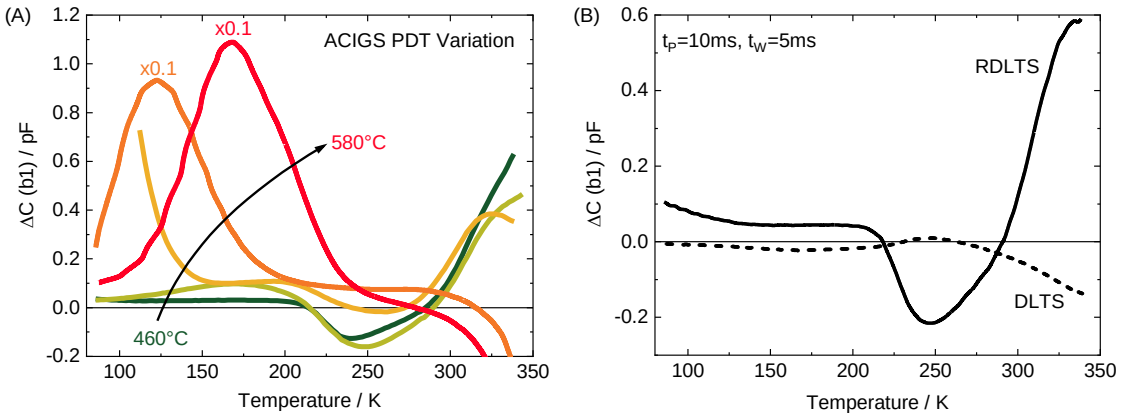

Figure 8.9: a) Reverse DLTS (RDLTS) measurements of the PDT series. For low PDT source temperatures, a broad minimum around 250K can be observed, corresponding to a majority trap level. For higher temperatures, this minimum vanishes and a pronounced maximum (minority trap) occurs, the position of which on the PDT source temperature. In order to improve the readability of the plot, the data in the curves of the 550 °C and the 580 °C samples are divided by factor of ten. Graph (B) shows a comparison of a DLTS and RDLTS of the 460 °C sample with same measurement conditions (except the pulse direction).

the temperature scan shows three significant features: one majority peak at 250 K, a large minority peak for temperatures below 200 K and one minority peak at 330 K. The amplitude of the 550 and 580 °C samples are reduced by factor of ten to make the peaks for all five measurements visible in the same graph.

Since in this measurement series, the RDLTS measurements throughout revealed a superior resolution of the peaks, compared to the DLTS measurements, the following discussion is only based on RDLTS measurements [172, 35]. Figure 8.9 (B) compares the DLTS measurement of the 460 °C sample with the corresponding RDLTS measurement. Both measurements have been conducted with t_W=5 ms, t_P=10 ms and a pulse from -1 V to 0.1 V for DLTS configuration and vice versa for the RDLTS configuration. Similar temperature scans are obtained for DLTS and RDLTS measurements, mirrored at the x-axis due to the opposed pulse direction. The differences lies in the peak amplitude, which is larger by a factor of ten for the RDLTS measurement, resulting in a better signal-to-noise-ratio (SNR) and therefore a more accurate evaluation.

First, the 460 °C and 490 °C DLTS spectra are discussed, and after the higher PDT temperature ones.

Investigating the Majority Peak at 250K

The majority peak at 250 K can be observed only for the lowest PDT source temperatures of 460 °C and 490 °C (dark and light green). Figure 8.10 (A) shows both temperature scans in more detail. Next to the majority peak "AH1", two minority peaks can be observed as well: A minority peak "AE1" at 200 K and a minority peak "AE2" at 330 K. The AH1 peak is a feature which can be observed in most of our ACIGS samples and vanishes for higher PDT temperatures. The vanishing of this peak with increasing Rb supply could indicate a passivation of this defect. But a superimposing of a second signal could be a possible explanation as well. However, since a decrease of efficiency and PCE is observed, it is likely that the effect of possible passivation does not have a significant influence on the performance or is counteracted by other effects. The energetic position of the corresponding defect is located at approx. (650 ± 60) meV above the valence band maximum. The large statistical error (standard deviation) comes from a large uncertainty in the evaluations of the different measurements. Figure 8.10 (B) shows the Arrhenius plots with linear regression lines of the AH1 peak in both measurements (460 °C open symbols and dark green and 490 °C filled

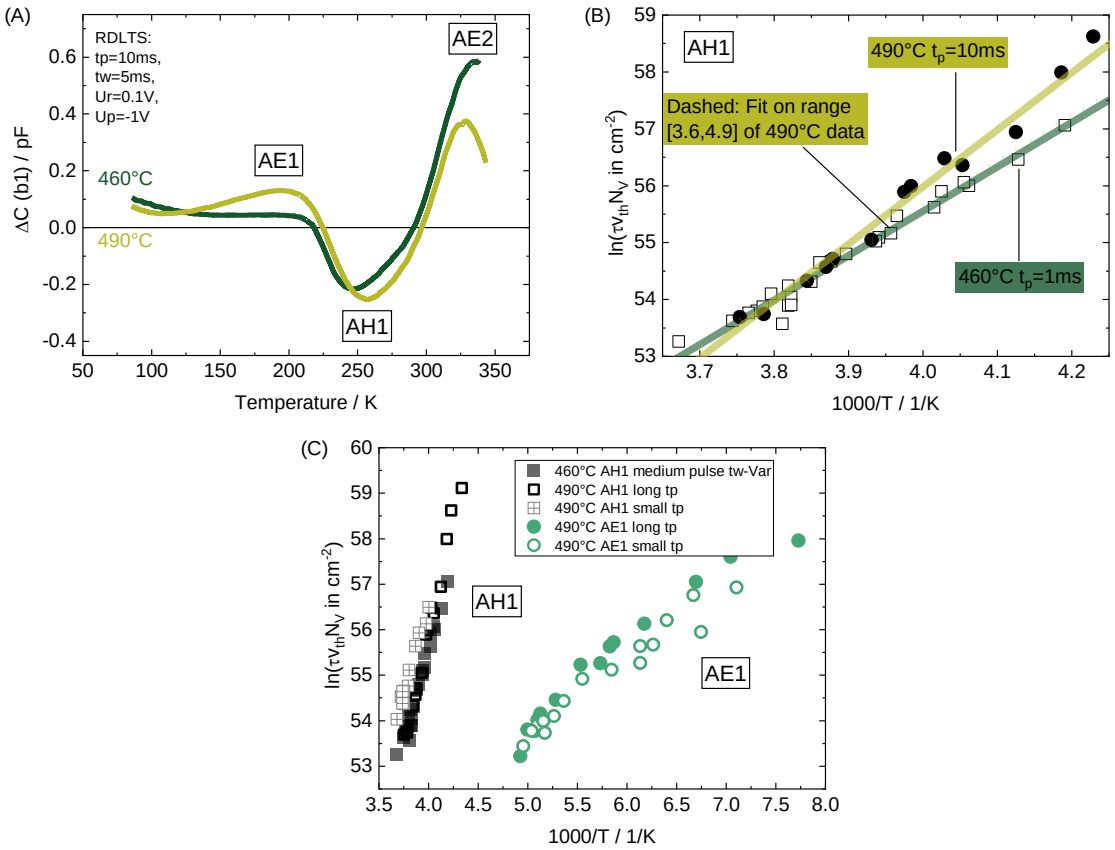

Figure 8.10: Arrhenius plots of the high temperature signals AH1 and AE2 (A). Graph (B) shows the evaluation of AH1 in more detail. Graph (C) shows a summary of the evaluations of both levels, AH1 and AE1.

symbols and light green). The linear regression line of the $490\,°\mathrm{C}$ sample shows a significantly steeper slope than the $460\,°\mathrm{C}$ sample, resulting in energies above $900\,\mathrm{meV}$ instead of the $650\,\mathrm{meV}$. This comes from the deviation for low temperatures (right side of the $1000/T$ plot). A drift of the data points for low temperatures could be assigned to an erroneous temperature measurement due to an imperfect thermal contact of the sample or the thermocouple. An overestimated temperature would lead to the observed effect, shifting the data points upwards (actually shifted to the left). If only the "high" temperature data points for $1000/T \leq 3.95\,1/\mathrm{K}$ are taken into account for the linear regression, an energy of $680\,\mathrm{meV}$ is obtained, which lies within the error of the other evaluation values. This evaluation is indicated by a dashed light green line, which shows almost the same slope as the regression of the $460\,°\mathrm{C}$ evaluation. Furthermore, the energetic position is in a comparable energetic range like the H2 defect, identified in CIGS from Chapter 7. It is likely that the two peaks have the same chemical origin. The reported minority level around $450\,\mathrm{meV}$ (E1) from the same study, which shows a sensitivity to a PDT could not be observed in ACIGS in the present study [156]. The corresponding trap densities of the AH1 peak are in the same range for the $460\,°\mathrm{C}$ and $490\,°\mathrm{C}$ sample with $2{\cdot}10^{13}$ to $3.5{\cdot}10^{13}\,\mathrm{cm}^{-3}$. A passivation of the underlying defect due to the step in source temperature can therefore not be confirmed.

The energy of the AE1 peak can be evaluated to an energetic position of $(150{\pm}30)\,\mathrm{meV}$. Figure 8.10 (C) shows the Arrhenius plots together with the evaluations of the AH1 peak in green. Also in these evaluations a non-linear effect is observed. Due to the small slopes and therefore corresponding low energy values, the error of this effect is rather small. An evaluation of the AE2 peak was not possible within this study and on the recorded measurements. This is on the one hand due to the position of AE2 at the edge of the temperature range and due to a superimposing effect,

leading to highly non-linear Arrhenius data.

Investigating the Low Temperature Peak

Moreover the minority peak “AE0“ at low temperatures is dominating the DLTS measurements of the 550 and 580 °C samples, and is even observable for the 520 °C sample. Figure 8.11 (A) shows the temperature scans of this three samples in more detail for measurements with small pulse duration of 0.1 ms. In contrast to the measurements with long filling pulse in Figure 8.9 (A), the strongly decreasing signal for temperatures beyond 270 K is vanishing. Only the minority peak can be observed, with a varying position, depending on the RbF source temperature. The peak of the 520 °C sample is cut off due to the limited temperature range of the nitrogen cooling. For the sample with increasing Rb (orange and red), the peak shifts to temperatures of 160 and 210 K, respectively. The shifting of the position already indicates a change in the energetic position of the corresponding trap state, which is confirmed by following evaluations. Figure 8.11 (B) shows the Arrhenius plot of the AE0 peak of the DLTS measurements in Graph (A). The changing slope of the linear regressions lines revealing a change in energetic position from 25 meV above the E_V for the 520 °C sample, over 60 meV and 160 meV for the 550 °C and 580 °C samples, respectively.

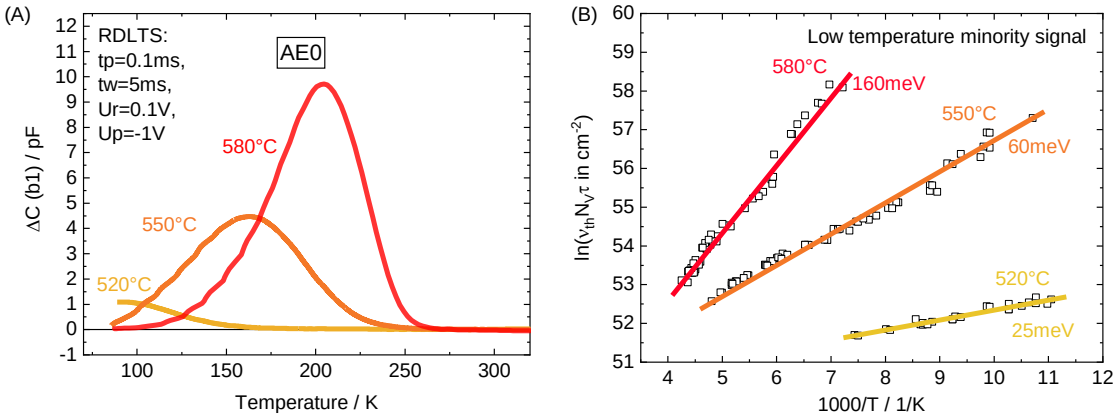

Figure 8.11: Temperature scans of the RbF variation on ACIGS. Graph (A) shows the measurements of the low temperature signal with a smaller pulse width of 0.1 ms, Graph (B) shows the temperature scans of the 460 and 490 °C samples with a long pulse. The discussed defect signals are indicated with abbreviations “AEx“ for minority signals and “AHx“ for majority signals.

Additionally, the trap density is increasing with increasing Rb content, which is already indicated by the increasing amplitude of the AE0 peak. Both quantities, the energetic position in relation to E_V and the trap density are plotted in Figure 8.13 (A) revealing the systematic increase with increasing Rb content. The increase in trap density might be explained with the fact, that AE0 is a Rb-correlated defect and the trap density is obviously directly correlated with the amount of supplied Rb. Nevertheless, its chemical origin and the reason for the changing energetic position is beyond the scope of this study. But the systematic behavior of the signals shows the need for further investigations. Weiss et al. show some similar investigations on CIGS solar cells with a variation of the PDT source temperature. They report a "N1" related defect, measured by admittance measurements, with an activation energy depending on the PDT source temperature [56]. They assign this defect to the formation of a current barrier due to a layer of RIS.

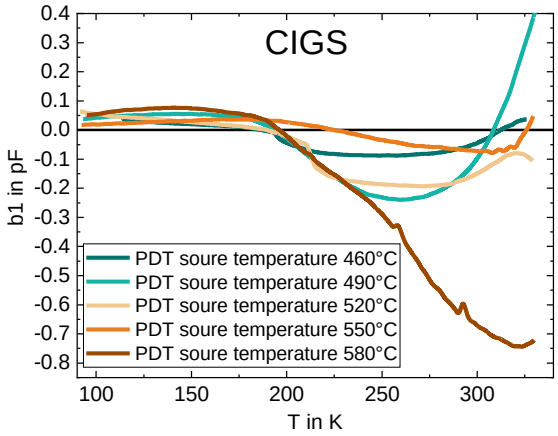

Figure 8.12: DLTS measurements of the samples of the silver-free CIGS reference batch.

For silver-free CIGS sample, no comparable results can be reported. Although a strong increase of the DLTS signal for low temperatures below 100 K can often be observed, similar to the 520 °C sample of the ACIGS series, no such distinctive peak occurs. In the reference batch without silver, no such low temperature signal or peak can be observed. Figure 8.12 reveals a broad peak around 200 K, but without systematic behavior with the supplied Rb. Due to bad signal quality, further evaluations were not possible. But from the position in the temperature scan it seems reasonable, that the peak ihas the same origin like the H2 peak from Chapter 7 and the AH1 peak of the ACIGS series from this Chapter. The fact that the peak is observable for high Rb contents as well, strengthens this assumption even more, as for the H2 peak in Chapter 7 no reduction was observed with the PDT as well.

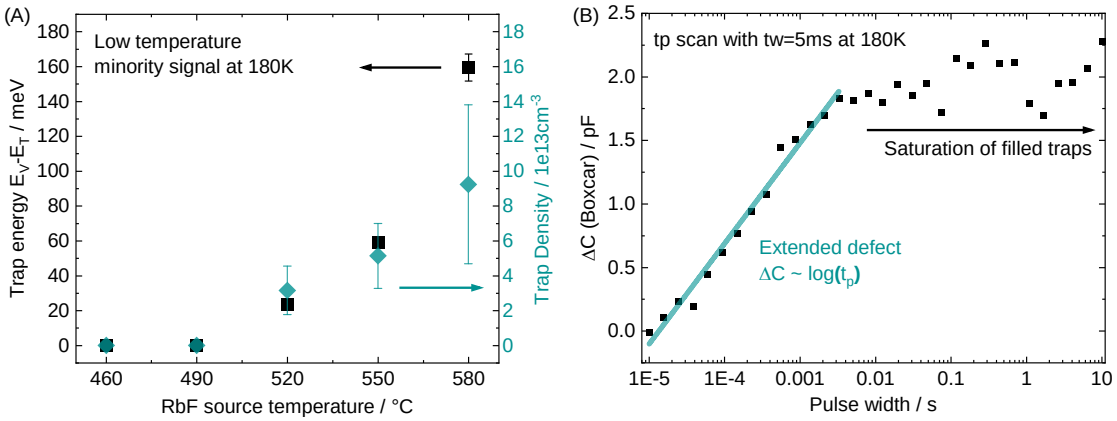

Figure 8.13: a) Trap energy levels and trap density from evaluations of the RDLTS temperature scans showing an increasing behavior with the PDT source temperature. Graph b) shows results of a pulse width variation at 180K of the 580 °C samples.

In order to get more information about the origin of this signal, pulse-width-dependent DLTS measurements have been conducted on the 580 °C sample. Figure 8.13 (B) shows a variation of the pulse width at 180 K (which corresponds to the temperature, where the maximum in the temperature scan occurs) with a time window of 10 ms. These pulse-width-dependent measurements can reveal the origin of the observed low temperature peak, whether is is an extended or a point defect. Extended defects can be located at grain boundaries or interfaces, point defects describe defects

distributed in the material. These two types of defects can be distinguished by the behavior of the corresponding capacitance difference ΔC from the DLTS measurements in dependence of the pulse width. Point defects follow the relation [173, 174, 175, 163]:

$$\ln\left(\frac{C_\infty - \Delta C}{C_\infty}\right) \propto t_\mathrm{p} \tag{8.2}$$

Where C_∞ is the reverse capacitance value at the sleceted temperature, ΔC is the height of the DLTS signal and t_p is the pulse width. For extended defects, the DLTS signal ΔC is proportional to the natural logarithm of the width of filling pulse [173, 174, 175, 163]:

$$\Delta C \propto \ln t_\mathrm{p} \tag{8.3}$$

Figure 8.13 (B) shows the evaluation of the data for extended defects (Equation 8.3). From $1{\cdot}10^{-5}$ to $1{\cdot}10^{-2}\,\mathrm{s}$ the data exhibit a very good linearity, thus the defect can be defined as an extended one. For pulse widths higher than $1{\cdot}10^{-2}\,\mathrm{s}$, the capacitance difference reaches a saturation plateau, because all traps are filled.
As described above, the location of such an extended defect can be for example at grain boundaries or interfaces. In the classical model of DLTS, no interface defects are in the scope of the measurement, since the measurement depth is defined by the displacement of the space charge region (SCR) depletion edge within the CIGS layer. Hence, the spatial origin of this trap is probably the grain boundaries within the ACIGS layer. Nevertheless, a possible source for errors is the application of the ideal model of moving only one border of the SCR, which is only true for an ideal pn^+-junction. For example, a secondary or disturbed pn-junction could contribute to the signal and could be responsible for the extended-defect-like behavior. Since these pulse width variations were performed on the $580\,^\circ\mathrm{C}$ sample with the lowest doping density of this series of $2.5{\cdot}10^{14}\,\mathrm{cm}^{-3}$, the pn^+-junction is likely fulfilled, but the interfaces can still have an influence due to charged defects, secondary barriers or similar. Even though some indication for the formation of an additional RIS layer and an associated barrier have been observed, an attribution to the observed defect is not possible in this work. The evaluation of the corresponding capture cross section of the low temperature signal leads to a value in the range of $1{\cdot}10^{-18}$ to $1{\cdot}10^{-17}\,\mathrm{cm}^2$. With this small value of σ and the energetic position with a distance $< 200\,\mathrm{meV}$ to E_V, the defect can be assumed not to be a strong recombination center for SRH recombination. However, for the $550\,^\circ\mathrm{C}$ sample the energetic position of the defect is already three times $k_\mathrm{B}T$ and seven times for the $580\,^\circ\mathrm{C}$ sample, indicating a change of the ionization and an effect on doping or other electrical properties of the layer. For the $580\,^\circ\mathrm{C}$ sample the values of the trap density ($N_{\mathrm{T},580\,^\circ\mathrm{C}} = 1{\cdot}10^{14}\,\mathrm{cm}^{-3}$) is in the same order of magnitude as the doping density ($N_{\mathrm{A},580\,^\circ\mathrm{C}} = 2.4{\cdot}10^{14}\,\mathrm{cm}^{-3}$) thus an effect of this defect on the doping is possible. Additionally, it has to be considered, that the observation of the level is only possible for high PDT source temperatures $> 520\,^\circ\mathrm{C}$ and therfore high Rb contents in the ACIGS layer. Nevertheless, due to the systematic behavior of the measurements and the devices, further investigations may reveal insights into the mechanisms of alkali elements in ACIGS solar cells.

In the last two sections the effect of Rb PDT in ACIGS solar cells was presented. The Rb content introduced by the PDT was varied by changing the RbF source temperature leading to a decreasing performance of the solar cells and contrary behavior to, what is expected for silver-free CIGS solar cells. The reason for the decreasing performance is a step-wise reduction of the V_OC and of the FF as well. A strong decrease of the doping density is mainly responsible for the decrease of the V_OC. Within DLTS measurements a strong defect signal at low temperatures can be observed, which shows a very systematical increase of the energetic position and trap density with the amount of

offered Rb. A pulse variation revealed that the origin of this signal might be an extended defect. It is probably located at grain boundaries and interfaces, which fits into the image of Rb segregation at these structural features in CIGS. Due to its energetic position it is no deep defect and only a low SRH recombination rate can be expected. Therefore, the corresponding defect does not explain the decrease in V_{OC}. Nevertheless, this defect can have an influence on other electrical properties like the doping density. A majority level, similar to the H2 peak from Chapter 7 was identified as well, but the effect of the PDT on this peak could not definitely be clarified. With an energy of $650\,\mathrm{meV}$, it could be a candidate for high SRH recombination.
The decrease in FF can probably be attributed to the formation of an additional layer on top of the ACIGS like RIS which induces a barrier for the photocurrent at the ACIGS/CdS interface due to a band-offset. The formation of such a RIS layer and the reproduction in numerical simulations will be the topic of the next section.

8.3 Simulation Study on $RbInSe_2$ Layers

Alkali compounds like RIS or KIS on CIGS surfaces are strongly discussed in literature. The formation and the effect on the cell performance is not yet fully understood, because contradicting results are reported [53, 66, 67, 56, 169, 65]. Nevertheless, tunneling electron microscopy (TEM) measurements already revealed the presence of such a phase at the CIGS-CdS interface in RbF treated devices [176]. Also in the presented study, there are indication for the formation of such a layer. First, the mentioned changes of the reflectance interferences with increasing Rb content and second, the FF loss occurring for high RbF source temperatures. Furthermore, ToF-SIMS measurements with high resolution at the ACIGS/CdS interface reveal some further indications. Figure 8.14 (A) shows the CIGS region near the CdS interface, analyzed with the Cs-cluster method, introduced in Section 2.6. Intensity ratios of the cesium clusters CsIn, CsGa and CsSe to the CsCu cluster are shown for the $460\,^{\circ}\mathrm{C}$ and the $580\,^{\circ}\mathrm{C}$ samples. The data reveal a significant increase of the CsIn/CsCu and CsSe/CsCu ratios in the first $100\,\mathrm{nm}$ for the $580\,^{\circ}\mathrm{C}$ measurement. The ratio of CsGa/CsCu remains more or less unchanged. Furthermore an accumulation of alkali elements (Rb, Na, K) at the CIGS surface can be observed in Figure 8.14 (B) (like already in Section 8.1). The fact, that the stoichiometric ratio shifts to a copper-depleted and In-, Se-rich composition with no effect on the gallium with a simultaneous Rb and Na increase, is a strong indication for a RIS layer. Therefore, this section is intended to have a detailed look on the effects of a possible RIS layer on the cell characteristics.

A numerical model is built up for the batch of ACIGS solar cells. Herein the experimental values of layer thicknesses from SEM cross sections, band gap profiles from ToF-SIMS measurements, doping densities from CV measurements and defect properties of AH1 and AE1 from DLTS measurements are used as input parameters for the simulation. The numerical simulations are based on the assumption, that the RIS layer introduces a new layer between the CIGS and the CdS with the thickness d. Figure 8.15 (A) illustrates the band diagram of an ACIGS solar cell. Depending on the chemical potential and band gap of the RIS, band discontinuities are introduced in the conduction band (ΔE_{C}) and in the valance band (ΔE_{V}). The shown band diagram is based on a chemical potential of RIS of $\chi_{\mathrm{RIS}} = 4.2\,\mathrm{eV}$ and a band gap of $E_{\mathrm{g,RIS}} = 2.8\,\mathrm{eV}$. Depending on the thickness of the RIS layer, a significant influence on the JV-curve can be observed. Figure 8.15 (B) shows the resulting curves for a thickness variation from 1 to $30\,\mathrm{nm}$. For high thicknesses, strongly disturbed JV-curves similar to the experimental ones are obtained, resulting in low FF values. Nevertheless, the V_{OC} remains unaffected. By simultaneously varying the doping density

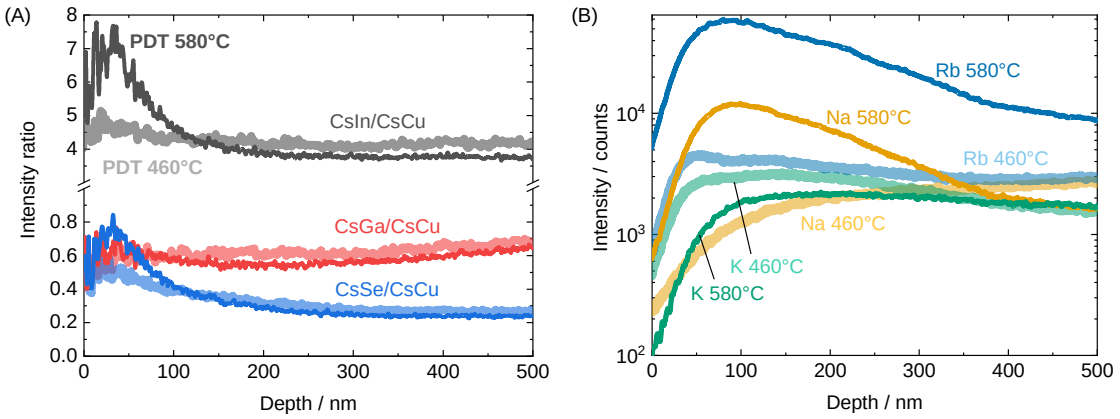

Figure 8.14: ToF-SIMS profiles of the CIGS/CdS interface with high resolution. Graph (A) shows the ratios of the Cs-cluster CsIn, CsGa and CsSe to the CsCu cluster and Graph (B) shows the intensity of the alkali elements Rb, K and Na. Both graphs compare the samples with lowest (460 °C) and highest Rb amount (580 °C).

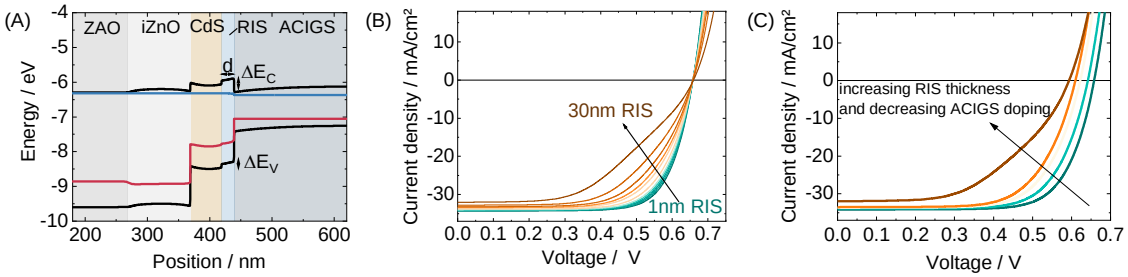

Figure 8.15: (A) Band diagram of a RbF treated ACIGS solar cell with RIS layer on the ACIGS layer used as simulation model. (B) corresponding IV curves of simulations with variation of the RIS thickness. Graph (C) shows the resulting IV curves, taking increased RIS thickness and decreasing doping density into account.

values, according to the experimental results in Section 8.2, the JV curves in Figure 8.15 (C) are obtained. The general behavior of FF and V_{OC} corresponds qualitatively well to the experimental data, although the experimental JV-curves include additional features like roll-overs and series resistance effects, which are not considered in the presented model.

Herein the thickness of the RIS layer was estimated via a parameter variation, shown in Figure 8.16 (A) and (B). Figure (A) shows the dependency of the PCE of the RIS thickness and ACIGS doping density. Figure (B) shows the dependency of the FF. Since the values of the doping densities of the ACIGS layers and the corresponding FF values are known, an estimation of the RIS thickness is possible, as indicated by gray circles in Figure (A). These estimations were used as inputs for the JV-curve simulations of Figure 8.15. Of course, this behavior is strongly dependent on the exact band configuration, more precisely, the conduction band offset at the ACIGS/RIS interface. Figure 8.17 (A) shows the influence of the conduction band offset and the RIS band gap (directly influencing the valence band offset). The influence on the PCE reveals that changing the RIS band gap doesn't affect the efficiency within the investigated range. Changing the electron affinity of the RIS layer and therefore the conduction band offset, has no effect for offset values below $0.35\,\mathrm{eV}$. For higher values, the efficiency strongly decreases. This implies that small changes in the band offset have a large effect on the device performance.

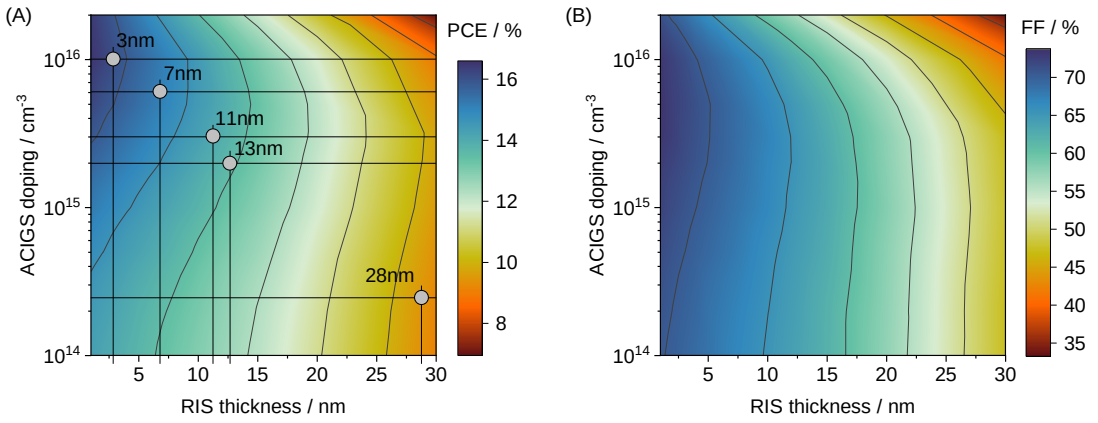

Figure 8.16: Contour plots of (A) PCE and (B) FF depending on the RIS thickness and the ACIGS doping density. Graph (A) shows the approximation of the RIS thickness.

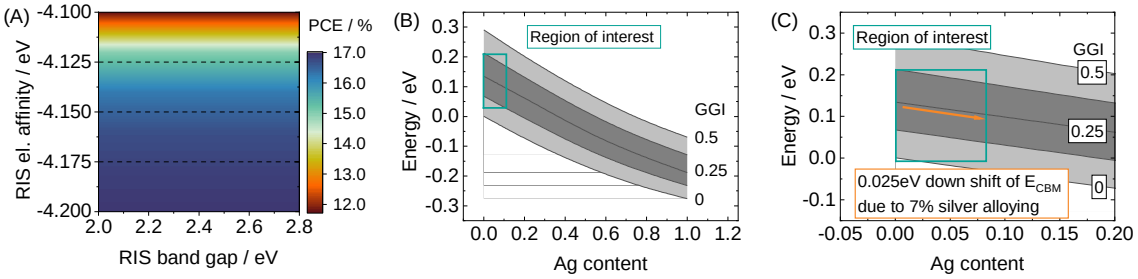

Figure 8.17: (A) Contour plot of the influence of RIS chemical potential and RIS band gap on the efficiency of the devices. (B) shows the results from first principle calculations of the conduction band minimum depending on the silver and gallium content, with respect to the conduction band minimum of CIS. Data were taken from [77]. (C) Zoom in of the interesting part of graph (B).

Herein, a lowering of the ACIGS bands would have a similar effect as shifting the RIS conduction band upwards. density-functional theory (DFT) simulations by Keller et al. on ACIGS have shown, that the band structure (E_C and E_V) of silver alloyed CIGS depends on the silver content [77]. Figure 8.17 (B) shows the results for the conduction band minimum, extracted from the publications of Keller et al. [77]. The influence of the silver content for different GGI values is shown, revealing a decrease of E_C with increasing silver content. The region of interest (GGI and AAC values of the investigated samples) is shown in Figure (C) in more detail. These data reveal, that addition of 6 to 7 % silver could lead to a lowering of E_C by $0.025\,\mathrm{eV}$. Such a shifting of the conduction band could increase the band offset at the CIGS/RIS layer as well and, depending on the exact values, lead to a decrease in efficiency. The horizontal dashed lines in Figure 8.17 (A) have exactly the distance $0.025\,\mathrm{eV}$ from each other, illustrating a possible change in the conduction band. This is one possible explanation, why the behavior of the investigated ACIGS solar cells stands in such a significant difference to the behavior of the silver-free devices. Due to the lowering of the conduction band minimum, induced by the silver, the band offset at the CIGS/RIS interface becomes higher, compared with the situation in silver-free CIGS. This increase of the band offset could lead to a significant increase of the FF-loss. Nevertheless, further investigations are needed to confirm this theory.

8.4 Variation of the ACGI Value

As already mentioned above and already reported by Kodalle et al. the effect of the PDT process is strongly correlated with the CGI value of the CIGS material. Kodalle et al. showed, that the critical value for the CGI, where the effect of a RbF-PDT process changes from a detrimental to a beneficial effect, is around 0.8 for silver-free CIGS [66]. This value is slightly higher than the 0.77 ACGI of the ACIGS batch from Section 8.1 and Section 8.2. However, the value belongs to silver-free CIGS and can change in the presence of silver. Therefore this section studies the influence of the ACGI in ACIGS solar cells on the effect of an applied PDT.

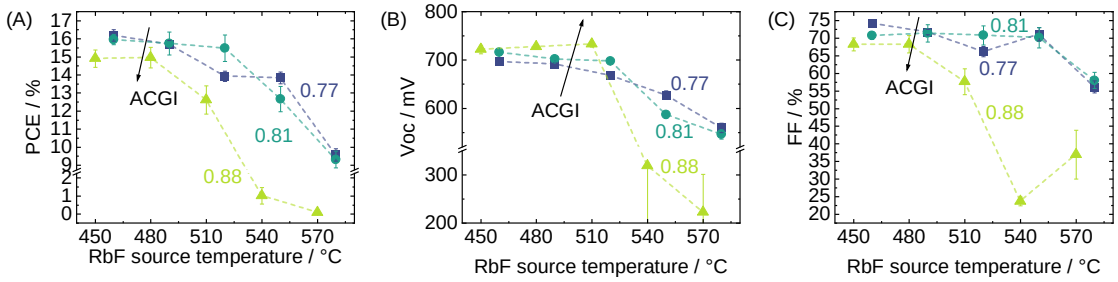

Figure 8.18: Influence of the ACGI value on the effect of the RbF-PDT on (A) PCE, (B) Voc and (C) FF in dependence of the RbF source temperature.

To study the impact of the ACGI, two additional batches of ACIGS solar cells are fabricated with higher ACGI of 0.81 and 88. Taking account the batch of Section 8.2, a 3x5 matrix of three different ACGI values each for five different RbF source temperatures is obtained. For the high ACGI batch, the PDT source temperatures have been reduced by $10\,°\mathrm{C}$ each. Figure 8.18 shows the resulting data of PCE in Graph (A), V_{OC} in Graph (B) and FF in Graph (C). Figure 8.19 (A)-(C) shows the same plots, but in dependence of the integrated Rb content in the ACIGS layer, revealing no significant correlation between ACGI and Rb content. While the trend of PCE with increasing PDT temperature is similar of the 0.77 and 0.81 series, the 0.88 series shows a strong decrease in efficiency. The main reason for this trend is the behavior of the FF with increasing RbF source temperature.

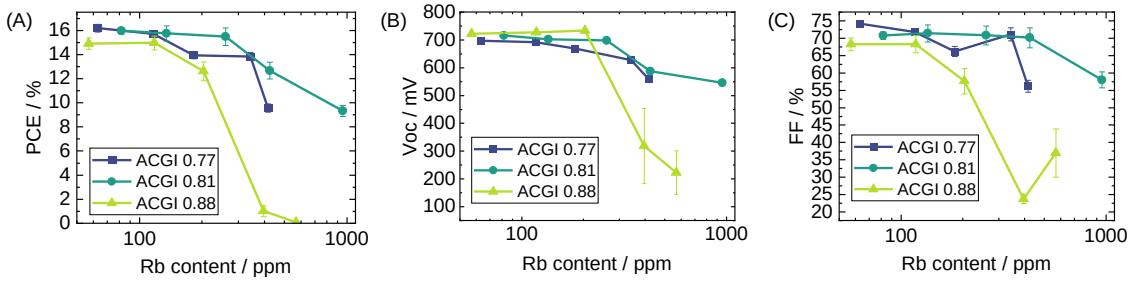

Figure 8.19: Influence of the ACGI value on the effect of the RbF-PDt on (A) PCE, (B) Voc and (C) FF in dependence of the Rb content within the ACIGS layer.

Nevertheless, the V_{OC} shows a different trend. For the first three PDT steps, the effect is changing from detrimental over quasi neutral to slightly beneficial, with increasing ACGI. Indeed, only for the high ACGI value (0.88) the V_{OC} shows an increasing behavior, similar to what is expected for silver-free CIGS. Although the amount of the V_{OC} increases by $10\,\mathrm{mV}$ between $450\,°\mathrm{C}$ and $510\,°\mathrm{C}$,

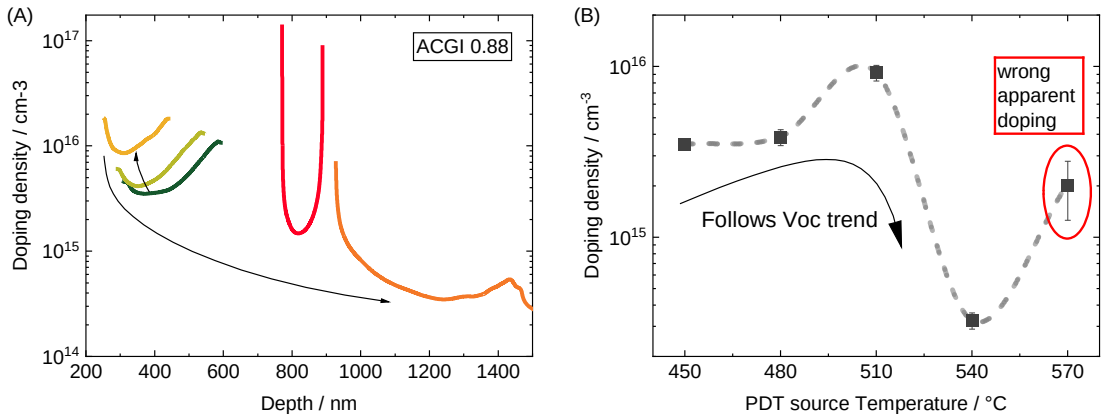

Figure 8.20: (A) Doping profiles of the high ACGI (0.88) ACIGS series and (B) corresponding apparent doping densities.

the increase is significantly lower than what is expected for silver-free CIGS (around $30\,\mathrm{mV}$). The improvement of the V_{OC} can also be connected to the doping density. Figure 8.20 shows the CV measurements of the high ACGI batch.

The doping densities (corresponding to the minima of the U-shaped curves) first increased with increasing PDT source temperatures up to $510\,^{\circ}\mathrm{C}$. For higher values, the doping density is reducing drastically. The same behavior can be observed for the V_{OC}. Herein, the CV measurement of the $570\,^{\circ}\mathrm{C}$ sample is strongly affected by defects, metastabilities or other effects and therefore the interpretation CV results is unreliable . This is confirmed by the V_{OC} of this sample, which decreases further in comparison with the $540\,^{\circ}\mathrm{C}$. But this improvement in V_{OC} for the lower PDT temperatures is superimposed by the detrimental effect of the FF, resulting in a nearly constant PCE for the $480\,^{\circ}\mathrm{C}$ PDT step with a subsequent strong decrease.
From the data presented above, it can be concluded:
1. For low ACGI values, the V_{OC} shows a decreasing behavior and the FF is only moderately affected.
2. For high ACGI values, the V_{OC} shows a slight improvement, but the FF shows strong decrease.
For both cases only a minimal or no improvement in the performance is observed with increasing Rb amount. For higher source temperatures a deterioration in the PCE is observed for all ACGI configurations.
This behavior seems to be different to silver-free CIGS. When looking on literature with KF-PDT, Edoff et al. showed, that the amount of KF for ACIGS has to be reduced down to $10\,\%$, compared to the optimum value of CIGS [69]. This already indicates that the optimum of the alkali content in the ACIGS layer lies in general at lower values.

Conclusion

In this chapter different mechanisms have been identified in ACIGS solar cells which occur due to the treatment with RbF. The comparison with silver-free CIGS revealed some similarities and some differences as well. The low temperature defect was already investigated by Weiss et al. by admittance measurements [56]. Also the assumed RIS layer is an ongoing topic of discussions in literature [53, 66, 67, 56, 166]. In this study a RIS layer is assumed to be responsible for the strong decrease in the FF. Numerical simulations have been used to strengthen this argument.
Only the decrease in doping and in V_{OC} represents a significant difference between silver-free CIGS and the investigated ACIGS. The decrease in doping is the dominant factor that decisively

influences the V_{OC} and thus the device performance. Although the well-known Rb-Na exchange mechanism is observed, it might be possible, that the doping mechanism of Rb in ACIGS is significantly different than for CIGS due to the change in stoichiometry and morphology. This behavior is even more interesting, when taking into account, that only a small amount of 5 to $7\,\%$ of copper is replaced by silver. Nevertheless, the behavior of doping density, V_{OC} and PCE changes considerably. By changing the ACGI ratio of the ACIGS layer, the strong detrimental effect of Rb is attenuated. For high ACGI values of 0.88 even an increasing V_{OC} with increasing Rb amount is observed. However, a strong decrease in FF compensates this beneficial effect. This seems to be a further difference between CIGS and ACIGS: the detrimental effect of the RIS layer might be stronger in ACIGS than in CIGS, caused by a worse band alignment at the CIGS/RIS interface.
Another point which has to be mentioned is that this study is testing only a small region of a larger parameter space of the PDT process. It cannot be excluded that an adjustment of parameters such as PDT duration or substrate temperature or others may lead to a more significant beneficial effect. Nevertheless, the presented results give an insight in the mechanisms of alkali elements in ACIGS solar cells and reveal the need for further investigations.

9 Summary

This thesis demonstrates the development and application of a simulation method, combined with defect measurements on real Cu(In,Ga)Se_2 (CIGS) solar cells. Herein a self written simulation tool was developed from scratch, based on the fundamental drift diffusion equations. In order to determine the most important material properties, a measurement procedure has been developed to investigate inherent electrical defects in the CIGS material with a high accuracy by Deep Level Transient Spectroscopy (DLTS). A special focus of this thesis was set on the role of alkali elements, introduced into the semiconductor device by post-deposition treatment (PDT) steps, which is an important method to reach high efficiency CIGS solar cells.

Therefore, in the first part of this work, all necessary methods were introduced. These methods build a fundamental part of this thesis and the development of them was a main part of the scientific work.
In order to create an accurate numerical model of the CIGS heterojunction, a simulation software was developed. The method is based on the fundamental drift-diffusion equations, namely the Poisson and two continuity equations. All further physical relations are introduced, which were additionally implemented to describe a CIGS solar cell in a sophisticated way. This includes the correct description of the recombination at defects via the Shockley-Read-Hall (SRH) theory, the description of the current transport via band discontinuities using thermionic emission and the implementation of temperature dependencies of certain quantities like the doping or the density of states. This method allows to allocate most of the optical and electrical losses, occurring within the CIGS heterojunction. Herein, it was found, that the SRH recombination over electrical defects represents the dominant loss path in the CIGS device. For the exact reproduction of the defects within the numerical simulation, detailed knowledge of the defect properties and the recombination mechanisms is undeniable.

Nevertheless, the exact recombination mechanisms in the CIGS semiconductor depend strongly on the deposition technique of the layer and can have different chemical origins. Therefore defects and their properties have been characterized in CIGS layers from different deposition systems with DLTS measurements. Herein, the method of DLTS was introduced and the developed measurement routine was explained. It was shown how to get from a capacitance transient to a DLTS signal and from an Arrhenius plot finally to the defect properties. Besides some complementary characterization methods, the development of a measurement method using an existing DLTS setup was the main part of the experimental work. For this purpose, on the one hand, the preparation of the samples was optimized in order to obtain the best possible measurement results. On the other hand, the parameter space of the measurement parameters was adapted to be able to measure defects in the CIGS material in the best possible way. The challenge was to select the parameters pulse duration t_P, time window t_W, reverse voltage V_R and pulse voltage V_P to detect the defect signals with the highest possible resolution. Furthermore, different advanced evaluation methods like Reverse DLTS (RDLTS) or Deep Level Transient Fourier Spectroscopy (DLTFS) were used to characterize the defects in the CIGS semiconductor.

For the application and verification of the simulation methodology, the simulation model was adapted to a real CIGS solar cell. Therefore a high efficiency CIGS solar cell with a PCE of $22.6\,\%$

was reproduced numerically including defect properties from DLTS measurements. The simulation results were compared with the experimentally measured ones. It was found that the external quantum efficiency (EQE) of the cell could be reproduced very well using the semiconductor simulation. For the simulation of the JV curve, the combination of semiconductor simulation and electrical Poisson simulation for vertical current transport was used. The semiconductor simulation alone is not sufficient to reproduce the experimental curve. Only when the lateral current transport in the transparent conductive oxide (TCO) and in the grid is included, a good agreement can be achieved. This example, shows the relevance of multi-level simulation approaches.

A special focus of this thesis was set on the influence of a rubidium fluoride (RbF)-PDT on the defect characteristics of CIGS solar cells. For this purpose, basic DLTS measurements are performed on gradient free CIGS samples. These simplified samples were selected for initial DLTS measurements, since effects due to composition changes in the device can be excluded. In addition, the influence of different alkali (Na, K, Rb) elements on the DLTS measurement was investigated within these series of measurements. The use of zirconium oxide (ZrO) substrates prevents the diffusion of alkali elements from the substrate into the layer. Thus alkali elements can be selectively introduced into the layer by alkali fluoride PDT steps. The measurements revealed that each alkali element (Na, K, Rb) has its own signature in the DLTS measurement and induces different defect levels. Although the PDT step is intended to improve the device performance, defect levels are introduced which are partly deep in the band and cannot be considered as doping levels but may act as recombination centers.

With these results from measurements on the gradient-free CIGS samples as basis, the influence of Rb on the defects in CIGS and ACIGS from a production-like co-evaporation system was investigated. DLTS measurements on CIGS samples with RbF showed a dependence of the characteristic on the treatment of the samples. A minority defect level (E1) was identified in the middle of the bandgap, showing a reduction in defect density by a factor of about 3 after PDT. A second (majority) defect (H2), also near the band center, was found to be unaffected by the PDT. These results may be related to the spatial origin of these defects. With further results from the literature, it can be assumed that the E1 defect is located at grain boundaries, unlike the H2 defect. Moreover, the measurements on the gradient-free CIGS samples with sodium as the only alkali element indicate that the E1 defect is induced by sodium at the grain boundaries. The displacement of sodium by rubidium decreases the defect density, which is observed in the DLTS. Using the data from the DLTS measurements as input values for numerical simulations, the results revealed that the reduction in trap density is responsible for only a small part of the V_{OC} gain due to the PDT. Indeed, both traps must be reduced in density to achieve a significant V_{OC} improvement and a performance enhancement.

A second study on samples from inline co-evaporation was performed on RbF variation on (Ag,Cu)(In,Ga)Se_2 (ACIGS) samples. The RbF content was systematically changed from very low to very high values by changing the temperature of the RbF source. Unlike for CIGS, no maximum in efficiency could be found. The reasons for a completely different performance behavior were investigated. It was shown that an altered or disturbed doping mechanism is responsible for the reduction of V_{OC} with increasing Rb content. Although similarities to DLTS measurements on silver-free CIGS could be identified, it can be assumed that no defect-induced loss mechanism is the reason. In addition, several indications of a secondary phase such as a RIS layer were found, which could be responsible for the attenuation in FF. The interplay of doping and energetic barrier due to a secondary phase was reproduced by numerical simulations supporting the explanations.

These studies demonstrate the need for simulation in PV research and development to assign the important loss mechanisms. In the context of electrical defects and PDT processes in CIGS solar cells fundamental physical limitations were investigated and real-world effects were analyzed. Furthermore, for CIGS and ACIGS samples, an outlook on further improvements and the main limitations for higher efficiencies were given.

Nevertheless, there are several aspects that need to be further investigated. On the one hand, the semiconductor simulation reveals much space for further improvements and further implementations. For example, the implementation of the Fermi-Dirac statistics would enable a more sophisticated simulation of perovskite solar cells. In combination with a description of tunneling interfaces, the simulation of tandem devices might be possible as well. In more general, the stability and performance of the software could be further improved by suitable scaling schemes of the variables or similar. On the other hand, for the DLTS method, further techniques can be developed, like pulse width-dependent measurements for more accurate determination of capture cross-sections or other advanced methods.

A Appendix

A.1 CIGS solar cell standard parameter semiconductor simulation

Table A.2 gives an overview of the used baseline semiconductor parameter, which have been used if no other information is given.

			CIGS	CdS	i-ZnO	AZO
Thickness		d / nm	2000	50	90	250
Band gap		E_{g}/eV	1.15	2.4	3.3	3.3
Chemical potential		χ/eV	-4.5	-4.2	-4.45	-4.45
Relative permittivity		ϵ_{r}	12.9	10	9	9
Effective DOS cond. band at 300K		$N_{\mathrm{C}}/\frac{1}{cm^3}$	2.2e18	2.2e18	2.2e18	2.2e18
Effective DOS val. band at 300K		$N_{\mathrm{V}}/\frac{1}{cm^3}$	1.8e19	1.8e19	1.8e19	1.8e19
Donor density		$N_{\mathrm{D}}/\frac{1}{cm^3}$	1e6	1e17	1e15	1e18
Acceptor density		$N_{\mathrm{A}}/\frac{1}{cm^3}$	1e16	1e6	1e6	1e6
Electron mobility		$\mu_{\mathrm{e}}/\frac{cm}{Vs}$	100	100	100	100
Hole mobility		$\mu_{\mathrm{h}}/\frac{cm}{Vs}$	25	25	25	25
Radiative recombination coeff.		$r_{\mathrm{rad}}/\frac{cm^3}{s}$	4e-11	1.7e-10	1.7e-10	1.7e-10
Auger coefficient electrons		$C_{\mathrm{n}}/\frac{cm^6}{s}$	0	0	0	0
Auger coefficient holes		$C_{\mathrm{p}}/\frac{cm^6}{s}$	0	0	0	0
Thermal velocity electrons		$\nu_{\mathrm{th,e}}/\frac{cm}{s}$	1e7	1e7	1e7	1e7
Thermal velocity holes		$\nu_{\mathrm{th,h}}/\frac{cm}{s}$	1e7	1e7	1e7	1e7
Deep defect	Energetic position†	E_{T}/meV	575	1200	1650	1650
	Trap density	$N_{\mathrm{T}}/\frac{1}{cm^3}$	1e13	1e20	1e18	1e20
	Capt. cross sect. electrons	σ_{n}/cm^2	1e-12	1e-14	1e-14	1e-14
	Capt. cross sect. holes	σ_{p}/cm^2	1e-12	1e-14	1e-14	1e-14

Table A.1: Summary of the baseline semiconductor parameter taken from literature [121, 145, 103]. † energetic positions of defects are given with respect to the valence maximum E_{V}

			CIGS	CdS	i-ZnO	AZO
Thickness		d / nm	2000	50	90	250
Band gap		E_{g}/eV	1.15	2.4	3.3	3.3
Chemical potential		χ/eV	-4.5	-4.2	-4.45	-4.45
Relative permittivity		ϵ_{r}	12.9	10	9	9
Effective DOS cond. band at 300K		$N_{\mathrm{C}}/\frac{1}{cm^3}$	2.2e18	2.2e18	2.2e18	2.2e18
Effective DOS val. band at 300K		$N_{\mathrm{V}}/\frac{1}{cm^3}$	1.8e19	1.8e19	1.8e19	1.8e19
Donor density		$N_{\mathrm{D}}/\frac{1}{cm^3}$	1e6	1e17	1e15	1e18
Acceptor density		$N_{\mathrm{A}}/\frac{1}{cm^3}$	1.5e16	1e6	1e6	1e6
Electron mobility		$\mu_{\mathrm{e}}/\frac{cm}{Vs}$	100	100	100	100
Hole mobility		$\mu_{\mathrm{h}}/\frac{cm}{Vs}$	25	25	25	25
Radiative recombination coeff.		$r_{\mathrm{rad}}/\frac{cm^3}{s}$	1e-10	1.7e-10	1.7e-10	1.7e-10
Auger coefficient electrons		$C_{\mathrm{n}}/\frac{cm^6}{s}$	0	0	0	0
Auger coefficient holes		$C_{\mathrm{p}}/\frac{cm^6}{s}$	0	0	0	0
Thermal velocity electrons		$\nu_{\mathrm{th,e}}/\frac{cm}{s}$	1e7	1e7	1e7	1e7
Thermal velocity holes		$\nu_{\mathrm{th,h}}/\frac{cm}{s}$	1e7	1e7	1e7	1e7
Deep defect	Energetic position†	E_{T}/meV	575	1200	1650	1650
	Trap density	$N_{\mathrm{T}}/\frac{1}{cm^3}$	5e13	1e20	1e18	1e20
	Capt. cross sect. electrons	σ_{n}/cm^2	1e-14	1e-14	1e-14	1e-14
	Capt. cross sect. holes	σ_{p}/cm^2	1e-14	1e-14	1e-14	1e-14

Table A.2: Summary of the baseline semiconductor parameter taken from literature [121, 145, 103]. † energetic positions of defects are given with respect to the valence maximum E_{V}

A.2 Further Application and Verification of Numerical Simulations for the Modelling of CIGS Solar Cells

This Section describes the results which were obtained with the already mentioned self-written simulation software and shows the applicability of this software. Additionally it can be seen as a verification of the simulation methods. Again, it has to be clarified that the electronic drift-diffusion simulation was written by the author, the electric part of the device simulation, the meshing algorithm and the reverse engineering fitting (REF) algorithm was written by Mario Zinßer and the optical simulation in form of the transfer-matrix method (TMM) was written in collaborative work of Mario Zinßer and the author.

This chapter gives different examples of application of the presented simulation program. First the optical simulation via the TMM is verified by the comparison of simulated and measured reflectance curves. Afterwards, the application of the REF is shown for the example of a CIGS module. Lastly, the multi-level approach of the simulation program is presented within a layer thickness optimization.

A.2.1 Optical Simulations of CIGS Solar Cells via the Transfer-matrix Method

Optical simulations are a fundamental part of the simulation of illuminated solar cell devices. Herein a reasonable optical calculation in order to get a correct generation rate is essential. Therefore this section shortly illustrates the possibility of the TMM for optical calculations within the simulation of CIGS solar cells. Figure A.1 (A) shows a representative layerstack of a CIGS solar cell with the corresponding reflectance curves, simulated (black) and measured (gray) in Graph (B). Obviously, the position of the simulated interference maxima fits very well to the experimental measurement. Nevertheless, the amplitudes of the simulation strongly overestimate the measurement. This is due to the assumption of smooth surface, which is made within the TMM calculation, but not corresponding to a real CIGS solar cell. This effect of overestimated interference amplitudes can be reduced by the use of modified Fresnel coefficients [128] or the description of rough interfaces by an effective medium approximation (EMA) [177]. But for cases like CIGS solar cells, where the roughness of the CIGS is much larger than the thickness of the subsequent layer (mostly CdS) even these approaches might be problematic. Nevertheless, for integral values over a large enough wavelength region the error is small. The high amplitudes in reflectance might explain for example the small deviations in the simulated EQE in Chapter 5. Furthermore, Figure A.1 (B) show a deviation for wavelengths above $1000\,\mathrm{nm}$. This might be due to incorrect refractive data of one layer.
This shows, that the TMM is capable to simulate the optical behavior of CIGS solar cell layerstacks. Nevertheless some inaccuracies occur due to surface roughness of real films or incorrect refractive data.

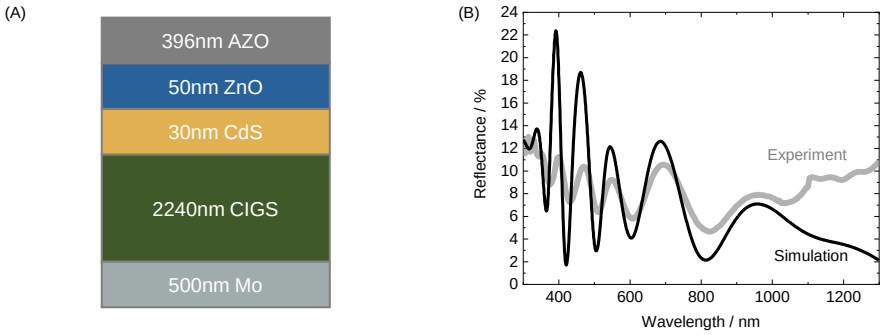

Figure A.1: Measured and simulated reflectance of a CIGS layerstack.

A.2.2 Reverse Engineering Fitting for the Determination of Fundamental Semiconductor Parameter

Parts of this section are published in the following publication by Zinßer et al.: [114]

The method of REF allows to derive the values of parameters, which are normally inaccessible. This section shows how this method can be used on different simulation levels to find the fundamental properties of a CIGS material, with only the JV curve of a module known. Herein, the focus lies on the application of the REF within the semiconductor level.

Figure A.2 illustrates the procedure with the corresponding JV curves (A) and a schematic flow diagram (B). From the module IV characteristic (black) a REF on the electrical level (Poisson

solver) can be applied to calculate the semiconductor characteristic, shown in orange. Herein the optical simulation of the layerstack was only considered in the electrical simulation. In the semiconductor simulation no optical losses are assumed, explaining the high J_{SC} value of the semiconductor curves. A further REF step on the semiconductor level afterwards can be used to obtain fundamental semiconductor parameter values. In this study, six different parameters on semiconductor simulation level have been fitted, selected after a sensitivity analysis the electron mobilities in CIGS and CdS, the acceptor density in CIGS, the donor density in CdS, the trap density of a deep defect in CIGS and the surface recombination velocity (SRV) of electrons at the Mo/CIGS back contact. Table A.3 gives an overview over the parameter values, used as starting values and the values obtained by the REF.

Parameter	Starting values	Output REF
μ_{n} CIGS	$100\,\mathrm{cm}^2/\mathrm{Vs}$	$200\,\mathrm{cm}^2/\mathrm{Vs}$
N_{A}^- CIGS	$1{\cdot}10^{16}\,\mathrm{cm}^{-3}$	$3{\cdot}10^{15}\,\mathrm{cm}^{-3}$
N_{T} CIGS	$3{\cdot}10^{13}\,\mathrm{cm}^{-3}$	$1.5{\cdot}10^{13}\,\mathrm{cm}^{-3}$
S_{n} Mo|CIGS	$1{\cdot}10^{5}\,\mathrm{cm/s}$	$1{\cdot}10^{5}\,\mathrm{cm/s}$
N_{D}^+ CdS	$1{\cdot}10^{17}\,\mathrm{cm}^{-3}$	$1{\cdot}10^{17}\,\mathrm{cm}^{-3}$
μ_{n} CdS	$100\,\mathrm{cm}^2/\mathrm{Vs}$	$100\,\mathrm{cm}^2/\mathrm{Vs}$

Table A.3: Summary of semiconductor parameters used as starting values for the REF and the resulting values.

Some parameters show a change in their value. The CIGS acceptor density is reduced from the starting value of $1{\cdot}10^{16}\,\mathrm{cm}^{-3}$ to $3{\cdot}10^{15}\,\mathrm{cm}^{-3}$. The CIGS mobility in contrast is increased by factor two to $200\,\mathrm{cm}^2/\mathrm{Vs}$. The trap density of the assumed deep defect reduces to the half to $1.5{\cdot}10^{13}\,\mathrm{cm}^{-3}$. On the other hand, some values don't show a change in their values. This is true for the back contact SRV and the cadmium sulfide (CdS) parameters electron mobility and donor density. The resulting curve after fitting the material parameters on semiconductor level is shown as dashed brown curve, showing a very good agreement with the orange one.

The REF approach can be made backwards by performing the simulations on the different levels. First the semiconductor simulation with applying the optical simulation and the geometry properties on the semiconductor characteristic is performed and the blue curve is obtained. A further electrical simulation of the actual module configuration results in the dashed gray line, showing a very good agreement with the actual starting point of the module measurement. These results have been used in further simulations for temperature dependent calculations on semiconductor level and subsequent time-dependent yield calculations with real meteorological data. Also these calculations show a very good agreement with the experimental measurements (see [114]).

In conclusion, this section shows the methodology of the REF to determine parameter values which are otherwise inaccessible. The method can be applied on different levels of the simulation. On semiconductor level it allows to estimate fundamental semiconductor parameters of the materials.

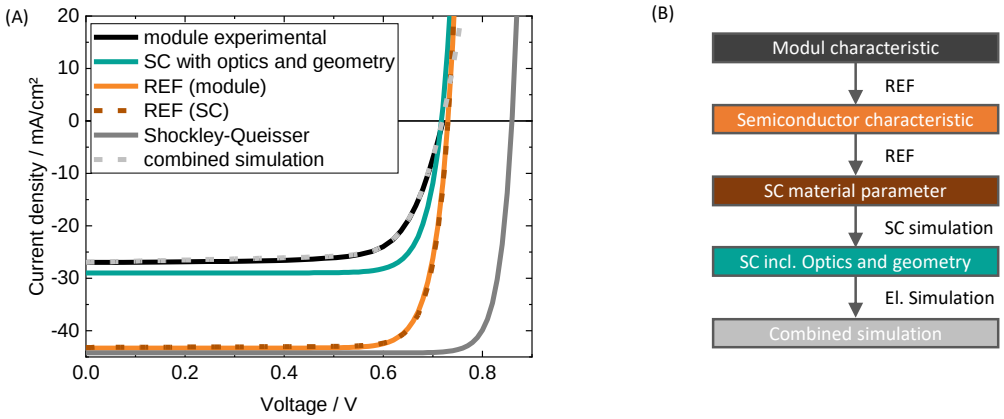

Figure A.2: IV curves of the REF process from module to semiconductor level.

A.2.3 Multi-level Simulations for Layer Thickness Optimization

The last example of simulation application, shows again the combination of the semiconductor simulation together with the electrical device simulation. The problem includes the simultaneous optimization of three different layer thicknesses. For a given CIGS layer the optimum thickness of the buffer layer (CdS), the intrinsic TCO (ZMO) and the doped TCO (AZO) shall be determined. One scientific question was, how thin the buffer layer CdS can be made, when the intrinsic TCO is deposited by atomic layer deposition (ALD), which prevents damage of the underlying layers and accurate deposition of thin layers in the nanometer range.

Therefore four different thicknesses of the CdS layer were selected: 0, 5, 30 and $50\,\mathrm{nm}$. The value of $50\,\mathrm{nm}$ is the standard value, but can be reduced for high efficiency cells with PDT to $30\,\mathrm{nm}$ due to changed growth of the CdS layer. The thicknesses of $0\,\mathrm{nm}$ and $5\,\mathrm{nm}$ are used to test very thin CdS layers. For each of these values, a 2D parameter variation was performed by variation of the ZMO and AZO thickness. The results of the 1D semiconductor simulation are shown in Figure A.3 in the left column. For each CdS thickness, the optimum of the efficiency is located for small thickness values of both, the ZMO and the AZO layer. For these parameter combinations, the absorption of the corresponding layers is small and therefore the current of the device high. But the results are not only defined by optical properties, but by the semiconductor properties as well. This can be seen for the $5\,\mathrm{nm}$ simulation (second row), where increasing the ZMO thickness leads to a strong decrease of the efficiency.
But neither the lateral current transport within the AZO, nor a possible grid shading is considered within the semiconductor simulation. Therefore, the set of IV curves from the semiconductor simulation was used as an input for the electrical Poisson solver calculation, taking into account the correct AZO thickness. The result is shown in the right column of Figure A.3. All eight single graphs are plotted in the same color code shown on the right. Thus, it can be directly seen, that the overall efficiency of the devices is significantly lower compared to the semiconductor data. This is due to the considered grid shading as well as due to the ohmic losses in the TCO and metallization grid. Another important aspect is, that the former efficiency optima for thin layer thicknesses vanished. The maxima shifted towards higher AZO and ZMO thicknesses. The higher AZO layer thickness provides a good enough current transport without to high FF losses. These data show again the big advantage of the combined simulation of semiconductor level and device level.

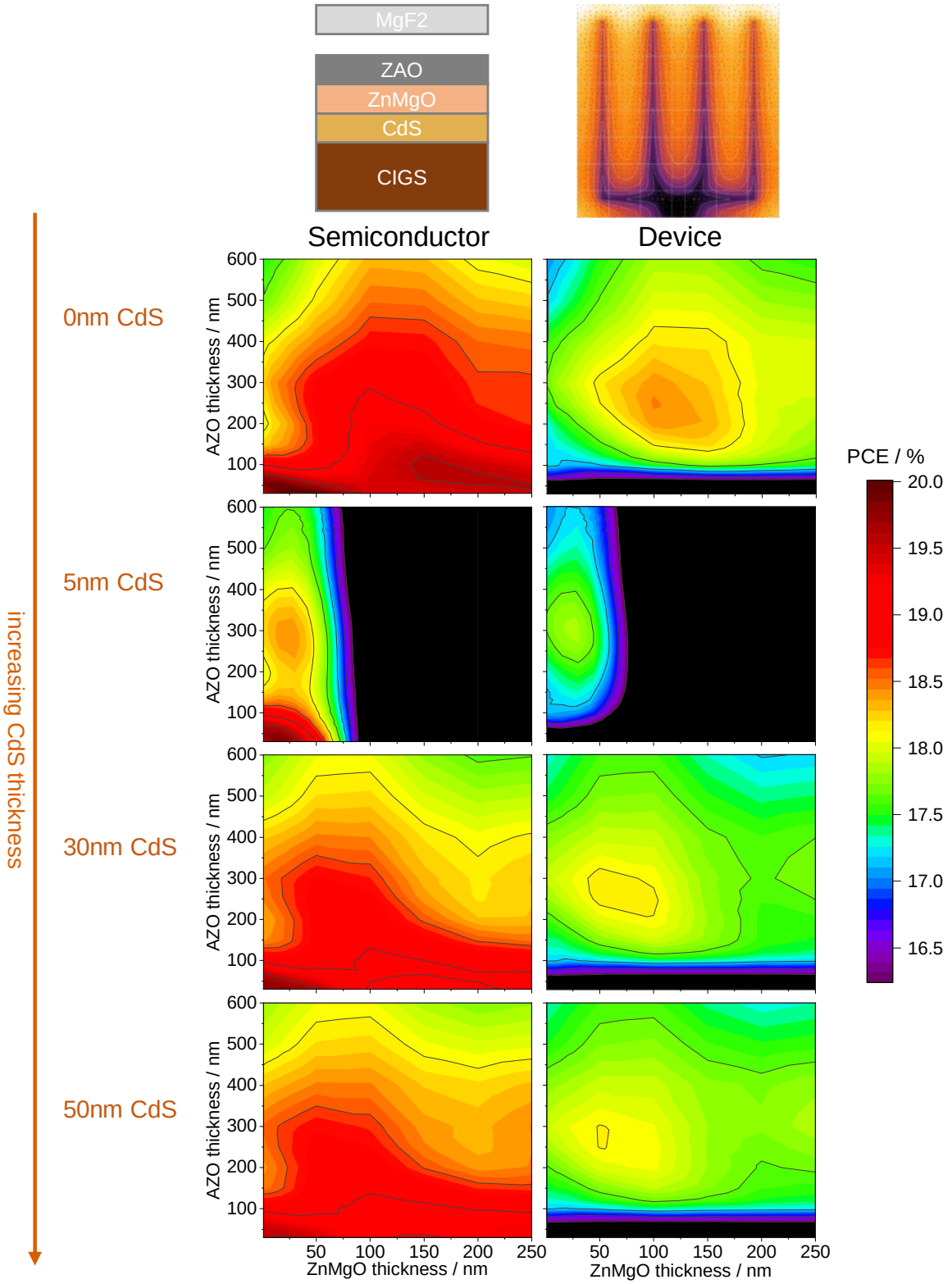

Figure A.3: Simulation of semiconductor pn-junction and device efficiency depending on aluminum doped zinc oxide (AZO) and zinc magnesium oxide (ZMO) thickness for four different CdS thicknesses. The left column gives the the efficinecy on the semiconductor level. The rgight column gives the efficiencies of the $0.5\,\mathrm{cm}^2$ solar cell, where the results from the left column serves as input for the device simulation.

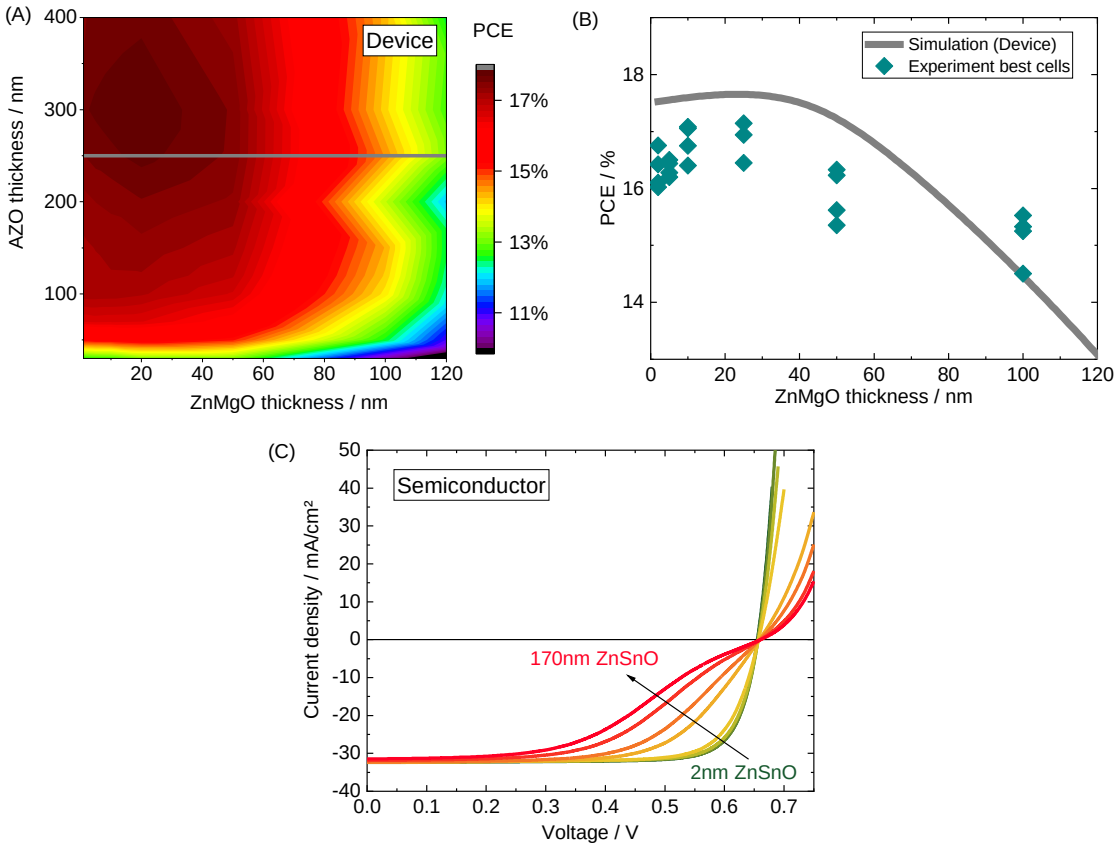

Figure A.4: (A) Zoom in of parameter variation from Figure A.3 of the device simulation with $5\,\mathrm{nm}$ of CdS. (B) comparison of experimental and simulated values for a ZMO thickness variation with an AZO thickness of $250\,\mathrm{nm}$. Graph (C) shows the corresponding simulated JV-curves from the semiconductor simulation to the simulation data from Graph (B).

In the next step, a part of the simulated results are compared with available experimental data. Figure A.4 (A) shows a selected part of the $5\,\mathrm{nm}$ CdS thickness variation on device level, revealing a maximum efficiency of $17.8\,\%$ for $300\,\mathrm{nm}$ AZO and $20\,\mathrm{nm}$ of ZMO. A strong decrease in efficiency is observed for larger ZMO thicknesses over the whole tested range of AZO thickness. The reason for this PCE reduction is a strong roll-over behavior of the JV curves from semiconductor simulation with increasing ZMO thickness, illustrated in Figure A.4 (C). Taking into account the electrical losses, a reduction of the FF and J_{SC} is observed, but the actual shape of the contour plots do not change (compare Figure A.3). Figure (B) shows a comparison of the simulated and experimental values of the best cells of a ZMO thickness variation, for an AZO thickness of $250\,\mathrm{nm}$. In general, the simulations reproduce the behavior of the experimental data. For small ZMO thicknesses, the influence on the efficiency is small, for an increasing ZMO thickness the efficiency decrease. Herein the experimental values show a less reduction compared to the simulation results. Hence, the model has to be redefined, but it is in general capable to simulate such problems.
In conclusion, this section shows, how layer thickness optimizations can be performed with the presented multi-level simulation approach. Herein, experimental data of a thickness variation can be qualitatively reproduced and it is important to use all levels of the multi-level approach needed to obtain reasonable results.

List of Figures

List of Tables

List of Publications

Journal articles

[1] Tim Helder, Ana Kanevce, Andreas Bauer, Mario Zinßer, Stefan Paetel, Theresa Magorian Friedlmeier, and Michael Powalla. DLTS investigations on CIGS solar cells from an inline co-evaporation system with RbF post-deposition treatment. *EPJ Photovoltaics*, 13:7, 2022.

[2] Tim Helder, Ana Kanevce, Mario Zinßer, Rico Gutzler, Stefan Paetel, Wolfram Hempel, Theresa Magorian Friedlmeier, and Michael Powalla. How small changes make a difference: Influence of low silver contents on the effect of RbF–PDT in CIGS solar cells. *Progress in Photovoltaics: Research and Applications*, 2022. ISSN 1062-7995. doi: 10.1002/pip.3628.

[3] Mario Zinßer, Benedikt Braun, Tim Helder, Theresa Magorian Friedlmeier, Bart Pieters, Alexander Heinlein, Martin Denk, Dominik Göddeke, and Michael Powalla. Irradiation-dependent topology optimization of metallization grid patterns and variation of contact layer thickness used for latitude-based yield gain of thin-film solar modules. *MRS Advances*, 7(30): 706–712, 2022.

[4] Mario Zinßer, Tim Helder, Andreas Bauer, Theresa Magorian Friedlmeier, Julia Zillner, Jan-Philipp Becker, and Michael Powalla. Optical and Electrical Loss Analysis of Thin-film Solar Cells combining the Methods of Transfer-Matrix and Finite Elements. *IEEE Journal of Photovoltaics*, 12(5):1154–1161, 2022.

[5] Mario Zinßer, Tim Helder, Theresa Magorian Friedlmeier, Andreas Bauer, Thomas Kirchartz, Uwe Rau, Rolf Wächter, and Michael Powalla. Holistic yield modeling, top-down loss analysis, and efficiency potential study of thin-film solar modules. *Submitted to Communications Physics*, 2022.

[6] Mario Zinßer, Moritz Loy, Tim Helder, Andreas Bauer, Theresa Magorian Friedlmeier, and Michael Powalla. Finite Element Simulation of Electrical Intradevice Physics of Thin-Film Solar Cells and Its Implications on the Efficiency. *IEEE Journal of Photovoltaics*, 12(2): 483–492, 2022.

Conference contributions

[1] Tim Helder, Ana Kanevce, Andreas Bauer, Mario Zinßer, Stefan Paetel, Theresa Magorian Friedlmeier, and Michael Powalla. DLTS investigations on CIGS solar cells from an inline co-evaporation system with RbF post-deposition treatment. Poster presented at the 38th European Photovoltaic Solar Energy Conference and Exhibition, online, 2021.

[2] Tim Helder, Ana Kanevce, Mario Zinßer, Rico Gutzler, Stefan Paetel, Wolfram Hempel, Theresa Magorian Friedlmeier, and Michael Powalla. Investigations on the impact of RbF-PDT in ACIGS solar cells. Oral presentation at the 8th World Conference on Photovoltaic Energy Conversion (WCPEC-8), Milano, Italy, 2022.

[3] Mario Zinßer, Moritz Loy, Tim Helder, Andreas Bauer, Theresa Magorian Friedlmeier, and Michael Powalla. Electrical FEM Simulations of Physics in Thin-Film Solar Cells. Poster presented at the 38th European Photovoltaic Solar Energy Conference and Exhibition, online, 2021.

[4] Mario Zinßer, Tim Helder, Andreas Bauer, Theresa Magorian Friedlmeier, Julia Zillner, Jan-Philipp Becker, and Michael Powalla. Optical and Electrical Loss Analysis of Thin-film Solar Cells combining the Methods of Transfer-Matrix and Finite Elements. Poster presented at the MRS Spring Meeting & Exhibit, 2022.

Bibliography

[1] IEA monthly electricity statistics, howpublished = https://www.iea.org/data-and-statistics/data-tools/monthly-electricity-statistics, note = Accessed: 2022-12-26.

[2] ZSW Press release December 16, 2022, howpublished = https://www.zsw-bw.de/presse/aktuelles/detailansicht/news/detail/news/erneuerbare-energien-deckten-2022-fast-die-haelfte-des-stromverbrauchs.html, note = Accessed: 2022-12-26.

[3] IEA renewable electricity statistics, howpublished = https://www.iea.org/reports/renewables-2022/renewable-electricity, note = Accessed: 2022-12-26.

[4] Fraunhofer ISE Aktuelle Fakten zur Photovoltaik in Deutschland, howpublished = https://www.ise.fraunhofer.de/content/dam/ise/de/documents/publications/studies/photovoltaics-report.pdf, note = Accessed: 2022-12-26.

[5] U.S. Department of Energy - Inflation Reduction Act, howpublished = https://www.energy.gov/lpo/inflation-reduction-act-2022, note = Accessed: 2022-12-26.

[6] EU comission REPowerEU, howpublished = https://commission.europa.eu/strategy-and-policy/priorities-2019-2024/european-green-deal/repowereu-affordable-secure-and-sustainable-energy-europe_de, note = Accessed: 2022-12-26.

[7] Fraunhofer ISE Photovoltaics Report, howpublished = https://www.ise.fraunhofer.de/content/dam/ise/de/documents/publications/studies/aktuelle-fakten-zur-photovoltaik-in-deutschland.pdf, note = Accessed: 2022-12-26.

[8] Vesselinka Petrova-koch. *High-Efficient Low-Cost Photovoltaics*, volume 140 of *Springer Series in Optical Sciences*. Springer International Publishing, Cham, 2020.

[9] Alessandro Martulli, Neethi Rajagopalan, Fabrizio Gota, Toby Meyer, Ulrich W. Paetzold, Steven Claes, Alberto Salone, Jordy Verboven, Robert Malina, Bart Vermang, and Sebastien Lizin. Towards market commercialization: Lifecycle economic and environmental evaluation of scalable perovskite solar cells. *Progress in Photovoltaics: Research and Applications*, 2022.

[10] CIGS White Paper 2019, howpublished = https://cigs-pv.net/wortpresse/wp-content/uploads/2019/04/cigs_white_paper_2019_online.pdf, note = Accessed: 2022-12-28.

[11] Avancis website, howpublished = https://www.avancis.de/, note = Accessed: 2022-12-28.

[12] Flisom website, howpublished = https://www.flisom.com/de/, note = Accessed: 2022-12-28.

[13] Ascent Solar website, howpublished = https://ascentsolar.com/, note = Accessed: 2022-12-28.

[14] A. R. Peaker, V. P. Markevich, and J. Coutinho. Tutorial: Junction spectroscopy techniques and deep-level defects in semiconductors. *Journal of Applied Physics*, 123(16):161559, 2018.

[15] Roland Scheer. *Chalcogenide photovoltaics: Physics, technologies, and thin film devices*. Wiley Online Library. Wiley-VCH, Weinheim, online-ausg edition, 2011.

[16] Patrick Reinhard, Adrian Chirila, Patrick Blosch, Fabian Pianezzi, Shiro Nishiwaki, Stephan Buechelers, and Ayodhya N. Tiwari. Review of progress toward 20% efficiency flexible cigs solar cells and manufacturing issues of solar modules. In Patrick Reinhard, A. Chirilă, Patrick Blösch, Fabian Pianezzi, Shiro Nishiwaki, Stephan Buecheler, and Ayodhya N. Tiwari, editors, *Review of Progress Toward 20% Efficiency Flexible CIGS Solar Cells and Manufacturing Issues of Solar Modules*, pages 1–9. IEEE, 2012.

[17] Michael Powalla, Wolfram Witte, Philip Jackson, Stefan Paetel, Erwin Lotter, Roland Wuerz, Friedrich Kessler, Carsten Tschamber, Wolfram Hempel, Dimitrios Hariskos, Richard Menner, Andreas Bauer, Stefanie Spiering, Erik Ahlswede, Theresa Magorian Friedlmeier, David Blazquez-Sanchez, Ines Klugius, and Wiltraud Wischmann. Cigs cells and modules with high efficiency on glass and flexible substrates. *IEEE Journal of Photovoltaics*, 4(1):440–446, 2014.

[18] Michael Powalla, Stefan Paetel, Erik Ahlswede, Roland Wuerz, Cordula D. Wessendorf, and Theresa Magorian Friedlmeier. Thin–film solar cells exceeding 22% solar cell efficiency: An overview on cdte-, cu(in,ga)se _2 -, and perovskite-based materials. *Applied Physics Reviews*, 5(4):041602, 2018.

[19] Steven S. Hegedus and William N. Shafarman. Thin-film solar cells: device measurements and analysis. *Progress in Photovoltaics: Research and Applications*, 12(23):155–176, 2004.

[20] J. H. Boyle, B. E. McCandless, W. N. Shafarman, and R. W. Birkmire. Structural and optical properties of (Ag,Cu)(In,Ga)Se 2 polycrystalline thin film alloys. *Journal of Applied Physics*, 115(22):223504, 2014.

[21] Wolfram Witte, Daniel Abou-Ras, Karsten Albe, Gottfried H. Bauer, Frank Bertram, Christian Boit, Rudolf Brüggemann, Jürgen Christen, Jens Dietrich, Axel Eicke, Dimitrios Hariskos, Matthias Maiberg, Roland Mainz, Max Meessen, Mathias Müller, Oliver Neumann, Thomas Orgis, Stefan Paetel, Johan Pohl, Humberto Rodriguez-Alvarez, Roland Scheer, Hans-Werner Schock, Thomas Unold, Alfons Weber, and Michael Powalla. Gallium gradients in Cu(In,Ga)Se2 thin-film solar cells. *Progress in Photovoltaics: Research and Applications*, 23(6):717–733, 2015.

[22] Su-Huai Wei and Alex Zunger. Band offsets and optical bowings of chalcopyrites and Zn–based II–VI alloys. *Journal of Applied Physics*, 78(6):3846–3856, 1995.

[23] Marko Topič, Franc Smole, and Jože Furlan. Band–gap engineering in CdS/Cu(In,Ga)Se 2 solar cells. *Journal of Applied Physics*, 79(11):8537–8540, 1996.

[24] Mohit Raghuwanshi, Manjusha Chugh, Giovanna Sozzi, Ana Kanevce, Thomas D. Kühne, Hossein Mirhosseini, Roland Würz, and Oana Cojocaru-Mirédin. Fingerprints Indicating Superior Properties of Internal Interfaces in Cu(In,Ga)Se2 Thin-Film Solar Cells. *Advanced Materials*, page e2203954, 2022.

[25] Thomas Kirchartz and Uwe Rau. What Makes a Good Solar Cell? *Advanced Energy Materials*, 8(28):1703385, 2018.

[26] Dieter K. Schroder. *Semiconductor material and device characterization*. IEEE Press, Piscataway, NJ and Hoboken, N.J, 3. ed. edition, 2006.

[27] William Shockley and Hans J. Queisser. Detailed balance limit of efficiency of p-n junction solar cells. *Journal of Applied Physics*, 32(3):510–519, 1961.

[28] Jean-Francois Guillemoles, Thomas Kirchartz, David Cahen, and Uwe Rau. Guide for the perplexed to the Shockley–Queisser model for solar cells. *Nature Photonics*, 13(8):501–505, 2019.

[29] M. Planck. Faksimile aus den verhandlungen der deutschen physikalischen gesellschaft 2 (1900) s. 237: Zur theorie des gesetzes der energieverteilung im normalspectrum; von m. planck. *Physik Journal*, 4(4):146–151, 1948.

[30] Basita Das, Irene Aguilera, Uwe Rau, and Thomas Kirchartz. What is a deep defect? Combining Shockley-Read-Hall statistics with multiphonon recombination theory. *Physical Review Materials*, 4(2), 2020.

[31] Handong Jin, Elke Debroye, Masoumeh Keshavarz, Ivan G. Scheblykin, Maarten B. J. Roeffaers, Johan Hofkens, and Julian A. Steele. It's a trap! on the nature of localised states and charge trapping in lead halide perovskites. *Materials Horizons*, 7(2):397–410, 2020.

[32] Pamela Johnson. The effect of trapping defects on cigs solar-cell performance /. 01 2003.

[33] Su-Huai Wei and S. B. Zhang. Defect properties of CuInSe2 and CuGaSe2. *Journal of Physics and Chemistry of Solids*, 66(11):1994–1999, 2005.

[34] S. B. Zhang, Su-Huai Wei, Alex Zunger, and H. Katayama-Yoshida. Defect physics of the CuInSe2 chalcopyrite semiconductor. *Physical Review B: Condensed Matter*, 57(16):9642–9656, 1998.

[35] A. Urbaniak, K. Macielak, M. Igalson, P. Szaniawski, and M. Edoff. Defect levels in Cu(In,Ga)Se _2 studied using capacitance and photocurrent techniques. *Journal of Physics: Condensed Matter*, 28(21):215801, 2016.

[36] Sebastian Fiechter, Yvonne Tomm, Klaus Diesner, and Tilmann Weiss. Homogeneity Ranges, Defect Phases and Defect Formation Energies in A I B III C VI2 Chalcopyrites (A = Cu; B = Ga, In; C = S, Se). *Japanese Journal of Applied Physics*, 39(S1):123, 2000.

[37] M. Igalson, M. Cwil, and M. Edoff. Metastabilities in the electrical characteristics of CIGS devices: Experimental results vs theoretical predictions. *Thin Solid Films*, 515(15):6142–6146, 2007.

[38] Peter T. Erslev, Jin Woo Lee, William N. Shafarman, and J. David Cohen. The influence of Na on metastable defect kinetics in CIGS materials. *Thin Solid Films*, 517(7):2277–2281, 2009.

[39] Armin Richter, Martin Hermle, and Stefan W. Glunz. Reassessment of the Limiting Efficiency for Crystalline Silicon Solar Cells. *IEEE Journal of Photovoltaics*, 3(4):1184–1191, 2013.

[40] A. Haug. Band-to-band Auger recombination in semiconductors. *Journal of Physics and Chemistry of Solids*, 49(6):599–605, 1988.

[41] A. Froitzheim, R. Stangl, L. Elstner, M. Kriegel, and W. Fuhs. AFORS-HET: a computer-program for the simulation of heterojunction solar cells to be distributed for public use. In *Proceedings of 3rd World Conference onPhotovoltaic Energy Conversion, 2003*, volume 1, pages 279–282 Vol.1, 2003.

[42] R. Scheer. Activation energy of heterojunction diode currents in the limit of interface recombination. *Journal of Applied Physics*, 105(10):104505, 2009.

[43] J. Hedstrom, H. Ohlsen, M. Bodegard, A. Kylner, L. Stolt, D. Hariskos, M. Ruckh, and H.-W. Schock. ZnO/CdS/Cu(In,Ga)Se/sub 2/ thin film solar cells with improved performance. In *The conference record of the twenty third IEEE Photovoltaic Specialists Conference - 1993*, pages 364–371, New York, NY, 1993. Inst. of Electrical and Electronics Engineers.

[44] M. A. Contreras, B. Egaas, P. Dippo, J. Webb, J. Granata, K. Ramanathan, S. Asher, A. Swartzlander, and R. Noufi. On the role of na and modifications to cu(in,ga)se/sub 2/ absorber materials using thin-mf (m=na, k, cs) precursor layers [solar cells]. In *Conference record of the Twenty Sixth IEEE Photovoltaic Specialists Conference - 1997*, pages 359–362, Piscataway, NJ, 1997. IEEE Service Center.

[45] Su-Huai Wei, S. B. Zhang, and Alex Zunger. Effects of Na on the electrical and structural properties of CuInSe2. *Journal of Applied Physics*, 85(10):7214–7218, 1999.

[46] Zhen-Kun Yuan, Shiyou Chen, Yun Xie, Ji-Sang Park, Hongjun Xiang, Xin-Gao Gong, and Su-Huai Wei. Na-Diffusion Enhanced p-type Conductivity in Cu(In,Ga)Se 2 : A New Mechanism for Efficient Doping in Semiconductors. *Advanced Energy Materials*, 6(24):1601191, 2016.

[47] F. Couzinie-Devy, E. Cadel, N. Barreau, L. Arzel, and P. Pareige. Na distribution in Cu(In,Ga)Se2 thin films: Investigation by atom probe tomography. *Scripta Materialia*, 104:83–86, 2015.

[48] Anke Laemmle, Roland Wuerz, Torsten Schwarz, Oana Cojocaru-Mirédin, Pyuck-Pa Choi, and Michael Powalla. Investigation of the diffusion behavior of sodium in Cu(In,Ga)Se 2 layers. *Journal of Applied Physics*, 115(15):154501, 2014.

[49] Philip Jackson, Roland Wuerz, Dimitrios Hariskos, Erwin Lotter, Wolfram Witte, and Michael Powalla. Effects of heavy alkali elements in Cu(In,Ga)Se2 solar cells with efficiencies up to 22.6% // Effects of heavy alkali elements in Cu(In,Ga)Se 2 solar cells with efficiencies up to 22.6%. *physica status solidi (RRL) – Rapid Research Letters*, 10(8):583–586, 2016.

[50] Motoshi Nakamura, Koji Yamaguchi, Yoshinori Kimoto, Yusuke Yasaki, Takuya Kato, and Hiroki Sugimoto. Cd-Free Cu(In,Ga)(Se,S)2 Thin-Film Solar Cell With Record Efficiency of 23.35%. *IEEE Journal of Photovoltaics*, 9(6):1863–1867, 2019.

[51] Philip Jackson, Dimitrios Hariskos, Erwin Lotter, Stefan Paetel, Roland Wuerz, Richard Menner, Wiltraud Wischmann, and Michael Powalla. New world record efficiency for cu(in,ga)se 2 thin-film solar cells beyond 20%. *Progress in Photovoltaics: Research and Applications*, 19(7):894–897, 2011.

[52] Shankar Karki, Pran Paul, Grace Rajan, Benjamin Belfore, Deewakar Poudel, Angus Rockett, Evgeny Danilov, Felix Castellano, Aaron Arehart, and Sylvain Marsillac. Analysis of Recombination Mechanisms in RbF-Treated CIGS Solar Cells. *IEEE Journal of Photovoltaics*, 9(1):313–318, 2019.

[53] Tim Kodalle, Marc D. Heinemann, Dieter Greiner, Hasan A. Yetkin, Michael Klupsch, Chen Li, Peter A. van Aken, Iver Lauermann, Rutger Schlatmann, and Christian A. Kaufmann. Elucidating the Mechanism of an RbF Post Deposition Treatment in CIGS Thin Film Solar Cells. *Solar RRL*, 2(9):1800156, 2018.

[54] Anke Laemmle, Roland Wuerz, and Michael Powalla. Efficiency enhancement of Cu(In,Ga)Se 2 thin-film solar cells by a post-deposition treatment with potassium fluoride. *physica status solidi (RRL) - Rapid Research Letters*, 7(9):631–634, 2013.

[55] Christopher P. Muzzillo. Review of grain interior, grain boundary, and interface effects of K in CIGS solar cells: Mechanisms for performance enhancement. *Solar Energy Materials and Solar Cells*, 172:18–24, 2017.

[56] Thomas Paul Weiss, Shiro Nishiwaki, Benjamin Bissig, Romain Carron, Enrico Avancini, Johannes Löckinger, Stephan Buecheler, and Ayodhya N. Tiwari. Injection Current Barrier Formation for RbF Postdeposition-Treated Cu(In,Ga)Se 2 -Based Solar Cells. *Advanced Materials Interfaces*, 5(4):1701007, 2018.

[57] Thomas Lepetit, Sylvie Harel, Ludovic Arzel, Guy Ouvrard, and Nicolas Barreau. KF post deposition treatment in co-evaporated Cu(In,Ga)Se 2 thin film solar cells: Beneficial or detrimental effect induced by the absorber characteristics. *Progress in Photovoltaics: Research and Applications*, 25(12):1068–1076, 2017.

[58] M. Malitckaya, H.-P. Komsa, V. Havu, and M. J. Puska. Effect of Alkali Metal Atom Doping on the CuInSe 2 -Based Solar Cell Absorber. *The Journal of Physical Chemistry C*, 121(29):15516–15528, 2017.

[59] Arantxa Vilalta-Clemente, Mohit Raghuwanshi, Sébastien Duguay, Celia Castro, Emmanuel Cadel, Philippe Pareige, Philip Jackson, Roland Wuerz, Dimitrios Hariskos, and Wolfram Witte. Rubidium distribution at atomic scale in high efficient Cu(In,Ga)Se 2 thin-film solar cells. *Applied Physics Letters*, 112(10):103105, 2018.

[60] Philipp Schöppe, Sven Schönherr, Roland Wuerz, Wolfgang Wisniewski, Gema Martínez-Criado, Maurizio Ritzer, Konrad Ritter, Carsten Ronning, and Claudia S. Schnohr. Rubidium segregation at random grain boundaries in Cu(In,Ga)Se2 absorbers. *Nano Energy*, 42:307–313, 2017.

[61] Philipp Schöppe, Sven Schönherr, Philip Jackson, Roland Wuerz, Wolfgang Wisniewski, Maurizio Ritzer, Maximilian Zapf, Andreas Johannes, Claudia S. Schnohr, and Carsten Ronning. Overall Distribution of Rubidium in Highly Efficient Cu(In,Ga)Se2 Solar Cells. *ACS Applied Materials & Interfaces*, 10(47):40592–40598, 2018.

[62] Max Hilaire Wolter, Benjamin Bissig, Enrico Avancini, Romain Carron, Stephan Buecheler, Philip Jackson, and Susanne Siebentritt. Influence of Sodium and Rubidium Postdeposition Treatment on the Quasi-Fermi Level Splitting of Cu(In,Ga)Se 2 Thin Films. *IEEE Journal of Photovoltaics*, 8(5):1320–1325, 2018.

[63] Marc Daniel Heinemann, Tim Kodalle, Charles Hages, Michael Klupsch, Dieter Greiner, Lars Korte, Sergej Levcenco, Thomas Unold, Rutger Schlatmann, and Christian A. Kaufmann. Evaluation of recombination losses in thin film solar cells using an LED sun simulator – the effect of RbF post-deposition on CIGS solar cells. *EPJ Photovoltaics*, 9:9, 2018.

[64] S. A. Jensen, S. Glynn, A. Kanevce, P. Dippo, J. V. Li, D. H. Levi, and D. Kuciauskas. Beneficial effect of post-deposition treatment in high-efficiency Cu(In,Ga)Se2 solar cells through reduced potential fluctuations. *Journal of Applied Physics*, 120(6):063106, 2016.

[65] Evelyn Handick, Patrick Reinhard, Regan G. Wilks, Fabian Pianezzi, Thomas Kunze, Dagmar Kreikemeyer-Lorenzo, Lothar Weinhardt, Monika Blum, Wanli Yang, Mihaela Gorgoi, Eiji Ikenaga, Dominic Gerlach, Shigenori Ueda, Yoshiyuki Yamashita, Toyohiro Chikyow, Clemens Heske, Stephan Buecheler, Ayodhya N. Tiwari, and Marcus Bär. Formation of a K-In-Se Surface Species by NaF/KF Postdeposition Treatment of Cu(In,Ga)Se2 Thin-Film Solar Cell Absorbers. *ACS Applied Materials & Interfaces*, 9(4):3581–3589, 2017.

[66] Tim Kodalle, Tobias Bertram, Rutger Schlatmann, and Christian A. Kaufmann. Effectiveness of an RbF Post Deposition Treatment of CIGS Solar Cells in Dependence on the Cu Content of the Absorber Layer. *IEEE Journal of Photovoltaics*, 9(6):1839–1845, 2019.

[67] Tim Kodalle, Hasan A. Yetkin, Alejandra Villanueva Tovar, Tobias Bertram, Reiner Klenk, Rutger Schlatmann, and Christian A. Kaufmann. A Device Model for Rb-Conditioned Chalcopyrite Solar Cells. *IEEE Journal of Photovoltaics*, pages 1–9, 2020.

[68] Enrico Avancini, Romain Carron, Thomas P. Weiss, Christian Andres, Melanie Bürki, Claudia Schreiner, Renato Figi, Yaroslav E. Romanyuk, Stephan Buecheler, and Ayodhya N. Tiwari. Effects of Rubidium Fluoride and Potassium Fluoride Postdeposition Treatments on Cu(In,Ga)Se 2 Thin Films and Solar Cell Performance. *Chemistry of Materials*, 29(22):9695–9704, 2017.

[69] Marika Edoff, Tobias Jarmar, Nina Shariati Nilsson, Erik Wallin, Daniel Hogstrom, Olof Stolt, Olle Lundberg, William Shafarman, and Lars Stolt. High <italic>V</italic>oc in (Cu,Ag)(In,Ga)Se 2 Solar Cells. *IEEE Journal of Photovoltaics*, 7(6):1789–1794, 2017.

[70] Stephanie Essig, Stefan Paetel, Theresa Magorian Friedlmeier, and Michael Powalla. Challenges in the deposition of (Ag,Cu)(In,Ga)Se 2 absorber layers for thin-film solar cells. *Journal of Physics: Materials*, 4(2):024003, 2021.

[71] Shih-Chi Yang, Jordi Sastre, Maximilian Krause, Xiaoxiao Sun, Ramis Hertwig, Mario Ochoa, Ayodhya N. Tiwari, and Romain Carron. Silver–Promoted High–Performance (Ag,Cu)(In,Ga)Se 2 Thin–Film Solar Cells Grown at Very Low Temperature. *Solar RRL*, page 2100108, 2021.

[72] Shih-Chi Yang, Tzu-Ying Lin, Mario Ochoa, Huagui Lai, Radha Kothandaraman, Fan Fu, Ayodhya N. Tiwari, and Romain Carron. Efficiency boost of bifacial cu(in,ga)se2 thin-film solar cells for flexible and tandem applications with silver-assisted low-temperature process. *Nature Energy*, pages 1–12, 2022.

[73] Gregory M. Hanket, Jonathan H. Boyle, William N. Shafarman, and Glenn Teeter. Wide-bandgap (agcu)(inga)se2 absorber layers deposited by three-stage co-evaporation. In *2010 35th IEEE Photovoltaic Specialists Conference*, pages 003425–003429. IEEE, 062010.

[74] Yunhai Zhao, Shengjie Yuan, Dongxing Kou, Zhengji Zhou, Xinshou Wang, Haiqin Xiao, Yueqing Deng, Changcheng Cui, Qianqian Chang, and Sixin Wu. High efficiency cigs solar cells by bulk defect passivation through ag substituting strategy. *ACS Applied Materials & Interfaces*, 12(11):12717–12726, 2020.

[75] Alexandra M. Bothwell, Siming Li, Rouin Farshchi, Michael F. Miller, Jake Wands, Craig L. Perkins, Angus Rockett, Aaron R. Arehart, and Darius Kuciauskas. Large–area (ag,cu)(in,ga)se

2 thin–film solar cells with increased bandgap and reduced voltage losses realized with bulk defect reduction and front–grading of the absorber bandgap. *Solar RRL*, 6(8):2200230, 2022.

[76] Peter T. Erslev, JinWoo Lee, Gregory M. Hanket, William N. Shafarman, and J. David Cohen. The electronic structure of Cu(In1−xGax)Se2 alloyed with silver. *Thin Solid Films*, 519(21):7296–7299, 2011.

[77] Jan Keller, Kostiantyn V. Sopiha, Olof Stolt, Lars Stolt, Clas Persson, Jonathan J.S. Scragg, Tobias Törndahl, and Marika Edoff. Wide–gap (Ag,Cu)(In,Ga)Se 2 solar cells with different buffer materials—A path to a better heterojunction. *Progress in Photovoltaics: Research and Applications*, 28(4):237–250, 2020.

[78] Lei Chen, JinWoo Lee, and William N. Shafarman. The Comparison of (Ag,Cu)(In,Ga)Se$_ bf 2$ and Cu(In,Ga)Se$_
bf 2$ Thin Films Deposited by Three-Stage Coevaporation. *IEEE Journal of Photovoltaics*, 4(1):447–451, 2014.

[79] Kihwan Kim, Seung Kyu Ahn, Jang Hoon Choi, Jinsoo Yoo, Young-Joo Eo, Jun-Sik Cho, Ara Cho, Jihye Gwak, Soomin Song, Dae-Hyung Cho, Yong-Duck Chung, and Jae Ho Yun. Highly efficient ag-alloyed cu(in,ga)se2 solar cells with wide bandgaps and their application to chalcopyrite-based tandem solar cells. *Nano Energy*, 48:345–352, 2018.

[80] Kihwan Kim, Joo Wan Park, Jin Su Yoo, Jun-Sik Cho, Hi-Deok Lee, and Jae Ho Yun. Ag incorporation in low-temperature grown cu(in,ga)se2 solar cells using ag precursor layers. *Solar Energy Materials and Solar Cells*, 146:114–120, 2016.

[81] Marko Jošt, Eike Köhnen, Amran Al-Ashouri, Tobias Bertram, Špela Tomšič, Artiom Magomedov, Ernestas Kasparavicius, Tim Kodalle, Benjamin Lipovšek, Vytautas Getautis, Rutger Schlatmann, Christian A. Kaufmann, Steve Albrecht, and Marko Topič. Perovskite/cigs tandem solar cells: From certified 24.2% toward 30% and beyond. *ACS Energy Letters*, pages 1298–1307, 2022.

[82] Ana Kanevce, Stephanie Essig, Stefan Paetel, Wolfram Hempel, Dimitrios Hariskos, and Theresa Magorian Friedlmeier. Impact of Ag content on device properties of Cu(In,Ga)Se 2 solar cells. *EPJ Photovoltaics*, 13:28, 2022.

[83] Olivier Donzel-Gargand, Thomas Thersleff, Jan Keller, Tobias Törndahl, Fredrik Larsson, Erik Wallin, Lars Stolt, and Marika Edoff. Deep surface cu depletion induced by k in high-efficiency cu(in,ga)se 2 solar cell absorbers. *Progress in Photovoltaics: Research and Applications*, 26(9):730–739, 2018.

[84] Olivier Donzel-Gargand, Fredrik Larsson, Tobias Törndahl, Lars Stolt, and Marika Edoff. Secondary phase formation and surface modification from a high dose KF-post deposition treatment of (Ag,Cu)(In,Ga)Se 2 solar cell absorbers. *Progress in Photovoltaics: Research and Applications*, 27(3):220–228, 2019.

[85] Nicholas H. Valdes, Kevin J. Jones, Robert L. Opila, and William N. Shafarman. Influence of Ga and Ag on the KF Treatment Chemistry for CIGS Solar Cells. *IEEE Journal of Photovoltaics*, 9(6):1846–1851, 2019.

[86] Dimitrios Hariskos, Philip Jackson, Wolfram Hempel, Stefan Paetel, Stefanie Spiering, Richard Menner, Wiltraud Wischmann, and Michael Powalla. Method for a High-Rate Solution Deposition of Zn(O,S) Buffer Layer for High-Efficiency $\mathrm{Cu(In,Ga)Se_2}$-Based Solar Cells. *IEEE Journal of Photovoltaics*, 6(5):1321–1326, 2016.

[87] PhysTech. Hera-DLTS Software Manual, 2013.

[88] R. Wuerz, W. Hempel, and P. Jackson. Diffusion of Rb in polycrystalline Cu(In,Ga)Se 2 layers and effect of Rb on solar cell parameters of Cu(In,Ga)Se 2 thin-film solar cells. *Journal of Applied Physics*, 124(16):165305, 2018.

[89] Wolfram Hempel and Theresa Magorian Friedlmeier. Influence of temperature and sputter source on Cu(In,Ga)Se 2 SIMS depth profiles. *Surface and Interface Analysis*, 2022.

[90] Tim Helder, Ana Kanevce, Mario Zinßer, Rico Gutzler, Stefan Paetel, Wolfram Hempel, Theresa Magorian Friedlmeier, and Michael Powalla. How small changes make a difference: Influence of low silver contents on the effect of RbF–PDT in CIGS solar cells. *Progress in Photovoltaics: Research and Applications*, 2022.

[91] Shwu Yeng, T. Lin, and You-Feng Lin. The n -dimensional pythagorean theorem. *Linear and Multilinear Algebra*, 26(1-2):9–13, 1990.

[92] Patricio Farrell and Dirk Peschka. Challenges for drift-diffusion simulations of semiconductors: A comparative study of different discretization philosophies.

[93] Franz Aurenhammer. Voronoi Diagrams—a Survey of a Fundamental Geometric Data Structure. *ACM Computing Surveys*, 23(3):345–405, 1991.

[94] S. Rebay. Efficient Unstructured Mesh Generation by Means of Delaunay Triangulation and Bowyer-Watson Algorithm. *Journal of Computational Physics*, 106(1):125–138, 1993.

[95] Mario Zinßer. *FEM Modeling of Thin-Film Photovoltaic Modules used for Holistic Top-down Loss Analyses, Yield Optimizations and Efficiency Potential Studies*. Phd-thesis, KIT, Stuttgart, 2023.

[96] W. van Roosbroeck. Theory of the Flow of Electrons and Holes in Germanium and Other Semiconductors. *Bell Syst. Tech. J.*, 29(4):560–607, 1950.

[97] James C Maxwell. *A dynamical theory of the electromagnetic field*. Wipf and Stock Publishers, 1996.

[98] Benoit Gaury, Yubo Sun, Peter Bermel, and Paul M. Haney. Sesame: a 2-dimensional solar cell modeling tool. *Solar Energy Materials and Solar Cells*, 198:53–62, 2019.

[99] J S Blakemore. The Parameters of Partially Degenerate Semiconductors. *Proc. Phys. Soc.*, (A 65 450), 1952.

[100] Monica Morales-Masis, Stefaan De Wolf, Rachel Woods-Robinson, Joel W. Ager, and Christophe Ballif. Transparent Electrodes for Efficient Optoelectronics. *Advanced Electronic Materials*, 3(5):1600529, 2017.

[101] D. L. Scharfetter and H. K. Gummel. Large-signal analysis of a silicon Read diode oscillator. *IEEE Transactions on Electron Devices*, 16(1):64–77, 1969.

[102] Sanjoy Paul, Roberto Lopez, Md Dalim Mia, Craig H Swartz, and Jian V Li. A simulation study on radiative recombination analysis in cigs solar cell. In *2017 IEEE 44th Photovoltaic Specialist Conference (PVSC)*, pages 2749–2754. IEEE, 2017.

[103] Masafumi Yamaguchi, Hitoshi Tampo, Hajime Shibata, Kan-Hua Lee, Kenji Araki, Nobuaki Kojima, and Yoshio Ohshita. Analysis for non-radiative recombination and resistance loss in chalcopyrite and kesterite solar cells. *Japanese Journal of Applied Physics*, 60(SB):SBBF05, 2021.

[104] Markus Heinemann and Christian Heiliger. Auger recombination rates in ZnMgO from first principles. *Journal of Applied Physics*, 110(8):083103, 2011.

[105] D. V. Lang. Deep–level transient spectroscopy: A new method to characterize traps in semiconductors. *Journal of Applied Physics*, 45(7):3023–3032, 1974.

[106] Jian V. Li, Richard S. Crandall, Ingrid L. Repins, Alexandre M. Nardes, and Dean H. Levi. Applications of admittance spectroscopy in photovoltaic devices beyond majority-carrier trapping defects. In *2011 37th IEEE Photovoltaic Specialists Conference*, pages 000075–000078, 2011.

[107] Kow-Ming Chang, Jung-Yu Tsai, and Chun Yen Chang. New physical formulation of the thermionic emission current at the heterojunction interface. *IEEE Electron Device Letters*, 14(7):338–341, 1993.

[108] S. M. Durbin and J. L. Gray. Considerations for modeling heterojunction transport in solar cells. In *Proceedings of 1994 IEEE 1st World Conference on Photovoltaic Energy Conversion - WCPEC (A Joint Conference of PVSC, PVSEC and PSEC)*, volume 2, pages 1746–1749 vol.2, 1994.

[109] K. Horio and H. Yanai. Numerical modeling of heterojunctions including the thermionic emission mechanism at the heterojunction interface. *IEEE Transactions on Electron Devices*, 37(4):1093–1098, 1990.

[110] Kyounghoon Yang, Jack R. East, and George I. Haddad. Numerical modeling of abrupt heterojunctions using a thermionic-field emission boundary condition. *Solid-State Electronics*, 36(3):321–330, 1993.

[111] C. M. Wu and E. S. Yang. Carrier Transport Across Heterojunction Interfaces. *Solid-State Electronics*, 22:241–248, 1979.

[112] R. L. Anderson. Germanium-Gallium Arsenide Heterojunctions [Letter to the Editor]. *IBM Journal of Research and Development*, 4(3):283–287, 1960.

[113] Helena Wilhelm, Hans-Werner Schock, and Roland Scheer. Interface recombination in heterojunction solar cells: Influence of buffer layer thickness. *Journal of Applied Physics*, 109(8):084514, 2011.

[114] Mario Zinßer, Tim Helder, Theresa Magorian Friedlmeier, Andreas Bauer, Thomas Kirchartz, Uwe Rau, Rolf Wächter, and Michael Powalla. Holistic yield modeling, top-down loss analysis, and efficiency potential study of thin-film solar modules. *Submitted to Communications Physics*, 2022.

[115] Andreas Schenk, Pietro Altermatt, and Bernhard Schmithusen. Physical Model of Incomplete Ionization for Silicon Device Simulation. In *2006 International Conference on Simulation of Semiconductor Processes and Devices*, pages 51–54, Piscataway, NJ, 2006. IEEE Service Center.

[116] G. Xiao, J. Lee, J.J Liou, and A. Ortiz-Conde. Incomplete ionization in a semiconductor and its implications to device modeling. *Microelectronics Reliability*, 39(8):1299–1303, 1999.

[117] Thomas Kirchartz and Uwe Rau. Linking structural properties with functionality in solar cell materials – the effective mass and effective density of states. *Sustain. Energy Fuels*, 2(7):1550–1560, 2018.

[118] Joseph Raphson. *Analysis aequationum universalis seu ad aequationes algebraicas resolvendas methodus generalis, & expedita, ex nova infinitarum serierum methodo, deducta ac demonstrata : ; cui annexum est de spatio reali, seu ente infinito conamen mathematico-metaphysicum*. typis Tho. Braddyll, prostant venales apud Iohannem Taylor, 1697.

[119] E. Knapp, R. Häusermann, H. U. Schwarzenbach, and B. Ruhstaller. Numerical simulation of charge transport in disordered organic semiconductor devices. *Journal of Applied Physics*, 108(5):054504, 2010.

[120] H. A. van der Vorst. Bi-CGSTAB: A Fast and Smoothly Converging Variant of Bi-CG for the Solution of Nonsymmetric Linear Systems. *SIAM Journal on Scientific and Statistical Computing*, 13(2):631–644, 1992.

[121] Ulf Malm and Marika Edoff. 2D device modelling and finite element simulations for thin-film solar cells. *Solar Energy Materials and Solar Cells*, 93(6-7):1066–1069, 2009.

[122] Ivan Pisarenko and Eugeny Ryndin. Drift-Diffusion Simulation of High-Speed Optoelectronic Devices. *Electronics*, 8(1):106, 2019.

[123] S. Stodtmann, R. M. Lee, C. K. F. Weiler, and A. Badinski. Numerical simulation of organic semiconductor devices with high carrier densities. *Journal of Applied Physics*, 112(11):114909, 2012.

[124] Mark Lundstrom. Drift-diffusion and computational electronics - still going strong after 40 years! In *2015 International Conference on Simulation of Semiconductor Processes and Devices (SISPAD 2015)*, pages 1–3, Piscataway, NJ, 2015. IEEE.

[125] Mario Zinßer. Numerically Robust Methodology for Fitting Current-Voltage Characteristics of Solar Devices with the Single-Diode Equivalent-Circuit Model.

[126] Steven J. Byrnes. Multilayer optical calculations.

[127] E. Hecht. *Optics*. Pearson Education, Incorporated, 2017.

[128] G. Yin, C. Merschjann, and M. Schmid. The effect of surface roughness on the determination of optical constants of CuInSe 2 and CuGaSe 2 thin films. *Journal of Applied Physics*, 113(21):213510, 2013.

[129] Katsidis Charalambos C., Siapkas Dimitrios I. General transfer-matrix method for optical multilayer systems with coherent, partially coherent, and incoherent interference. *Applied Optics*, (41), 2002.

[130] Johann Heinrich Lambert. *Lamberts Photometrie:(Photometria, sive De mensura et gradibus luminis, colorum et umbrae)(1760)*. Number 31-33. W. Engelmann, 1892.

[131] August Beer. Bestimmung der absorption des rothen lichts in farbigen flussigkeiten. *Ann. Physik*, 162:78–88, 1852.

[132] Mario Zinßer, Moritz Loy, Tim Helder, Andreas Bauer, Theresa Magorian Friedlmeier, and Michael Powalla. Finite Element Simulation of Electrical Intradevice Physics of Thin-Film Solar Cells and Its Implications on the Efficiency. *IEEE Journal of Photovoltaics*, 12(2):483–492, 2022.

[133] Mario Zinßer, Benedikt Braun, Tim Helder, Theresa Magorian Friedlmeier, Bart Pieters, Alexander Heinlein, Martin Denk, Dominik Göddeke, and Michael Powalla. Irradiation-dependent Topology Optimization of Metallization Grid Patterns used for latitude-based Yield Gain of Thin-film Solar Modules. *MRS Advances*, 7(30):706–712, 2022.

[134] J. A. Nelder and R. Mead. A Simplex Method for Function Minimization. *The Computer Journal*, 7(4):308–313, 1965.

[135] Marti A., J. L. Balenzategui, and R. F. Reyna. Photon recycling and Shockley's diode equation. *Journal of Applied Physics*, 82(8):4067–4075, 1997.

[136] Uwe Rau, Beatrix Blank, Thomas C. M. Müller, and Thomas Kirchartz. Efficiency Potential of Photovoltaic Materials and Devices Unveiled by Detailed-Balance Analysis. *Physical Review Applied*, 7(4), 2017.

[137] Mario Zinßer, Tim Helder, Andreas Bauer, Theresa Magorian Friedlmeier, Julia Zillner, Jan-Philipp Becker, and Michael Powalla. Optical and Electrical Loss Analysis of Thin-film Solar Cells combining the Methods of Transfer-Matrix and Finite Elements. *IEEE Journal of Photovoltaics*, 12(5):1154–1161, 2022.

[138] Jian V. Li. Deep level transient spectroscopy characterization without the Arrhenius plot. *The Review of scientific instruments*, 92(2):023902, 2021.

[139] J. Lauwaert, S. Khelifi, and H. Vrielinck. Determination of Majority Carrier Capture Rates via Deep Level Transient Spectroscopy. *ECS Journal of Solid State Science and Technology*, 5(4):P3041–P3047, 2016.

[140] PhysTech. Phystech dlts faq, 2013.

[141] M. Igalson and P. Zabierowski. Reverse-bias DLTS for investigation of the interface region. *Opto-Electronics Review*, 8(4):346–349, 2000.

[142] S. Weiss and R. Kassing. Deep Level Transient Fourier Spectroscopy (DLTFS)—A technique for the analysis of deep level properties. *Solid-State Electronics*, 31(12):1733–1742, 1988.

[143] Boonton Model 7200 Capacitance Meter description. `https://boonton.com/applications/artmid/615/articleid/1105/dlts-measurements-with-boonton-model-7200-capacitance-meter`. Accessed: 202-11-28.

[144] M Gloeckler, AL Fahrenbruch, and JR Sites. Numerical modeling of cigs and cdte solar cells: setting the baseline. In *3rd World Conference onPhotovoltaic Energy Conversion, 2003. Proceedings of*, volume 1, pages 491–494. IEEE, 2003.

[145] Mario Ochoa, Stephan Buecheler, Ayodhya N. Tiwari, and Romain Carron. Challenges and opportunities for an efficiency boost of next generation Cu(In,Ga)Se 2 solar cells: prospects for a paradigm shift. *Energy & Environmental Science*, 13(7):2047–2055, 2020.

[146] Koen Decock, Samira Khelifi, and Marc Burgelman. Analytical versus numerical analysis of back grading in CIGS solar cells. *Solar Energy Materials and Solar Cells*, 95(6):1550–1554, 2011.

[147] Shota Minoura, Takuji Maekawa, Keita Kodera, Akihiro Nakane, Shigeru Niki, and Hiroyuki Fujiwara. Optical constants of Cu(In, Ga)Se2 for arbitrary Cu and Ga compositions. *Journal of Applied Physics*, 117(19):195703, 2015.

[148] Laura Friedl. *Störstellenanalyse an CIGS-Solarzellen mithilfe von kapazitiven Tieftemperatur-Messungen*. Bachelorthesis, Universität Stuttgart, Stuttgart, 2021.

[149] Romain Carron, Christian Andres, Enrico Avancini, Thomas Feurer, Shiro Nishiwaki, Stefano Pisoni, Fan Fu, Martina Lingg, Yaroslav E. Romanyuk, Stephan Buecheler, and Ayodhya N. Tiwari. Bandgap of thin film solar cell absorbers: A comparison of various determination methods. *Thin Solid Films*, 669:482–486, 2019.

[150] A. Czudek, A. Eslam, A. Urbaniak, P. Zabierowski, R. Wuerz, and M. Igalson. Evolution of the electrical characteristics of Cu(In,Ga)Se 2 devices with sodium content. *Journal of Applied Physics*, 128(17):173102, 2020.

[151] R. Herberholz, M. Igalson, and H. W. Schock. Distinction between bulk and interface states in CuInSe2/CdS/ZnO by space charge spectroscopy. *Journal of Applied Physics*, 83(1):318–325, 1998.

[152] P. Zabierowski, K. Stankiewicz, A. Donmez, F. Couzinie-Devy, and N. Barreau. Systematic study of the complex structure of N1 Deep Level Transient Spectroscopy signal in Cu(In,Ga)Se2 based heterojunctions. *Thin Solid Films*, 519(21):7485–7488, 2011.

[153] Nicoleta Nicoara, Roby Manaligod, Philip Jackson, Dimitrios Hariskos, Wolfram Witte, Giovanna Sozzi, Roberto Menozzi, and Sascha Sadewasser. Direct evidence for grain boundary passivation in Cu(In,Ga)Se2 solar cells through alkali-fluoride post-deposition treatments. *Nature Communications*, 10(1):3980, 2019.

[154] Thomas Feurer, Fan Fu, Thomas Paul Weiss, Enrico Avancini, Johannes Löckinger, Stephan Buecheler, and Ayodhya N. Tiwari. RbF post deposition treatment for narrow bandgap Cu(In,Ga)Se2 solar cells. *Thin Solid Films*, 670:34–40, 2019.

[155] L. E. Oikkonen, M. G. Ganchenkova, A. P. Seitsonen, and R. M. Nieminen. Effect of sodium incorporation into CuInSe 2 from first principles. *Journal of Applied Physics*, 114(8):083503, 2013.

[156] Tim Helder, Ana Kanevce, Andreas Bauer, Mario Zinßer, Stefan Paetel, Theresa Magorian Friedlmeier, and Michael Powalla. DLTS investigations on CIGS solar cells from an inline co-evaporation system with RbF post-deposition treatment. *EPJ Photovoltaics*, 13:7, 2022.

[157] Ronald A. Sinton and Andres Cuevas. Contactless determination of current–voltage characteristics and minority–carrier lifetimes in semiconductors from quasi–steady–state photoconductance data. *Applied Physics Letters*, 69(17):2510–2512, 1996.

[158] Julia I. Deitz, Pran K. Paul, Rouin Farshchi, Dmitry Poplavskyy, Jeff Bailey, Aaron R. Arehart, David W. McComb, and Tyler J. Grassman. Direct Nanoscale Characterization of Deep Levels in AgCuInGaSe 2 Using Electron Energy–Loss Spectroscopy in the Scanning Transmission Electron Microscope. *Advanced Energy Materials*, 9(35):1901612, 2019.

[159] L. L. Kerr, Sheng S. Li, S. W. Johnston, T. J. Anderson, O. D. Crisalle, W. K. Kim, J. Abushama, and R. N. Noufi. Investigation of defect properties in Cu(In,Ga)Se2 solar cells by deep-level transient spectroscopy. *Solid-State Electronics*, 48(9):1579–1586, 2004.

[160] Hisham Aboulfadl, Kostiantyn V. Sopiha, Jan Keller, Jes K. Larsen, Jonathan J. S. Scragg, Clas Persson, Mattias Thuvander, and Marika Edoff. Alkali Dispersion in (Ag,Cu)(In,Ga)Se2 Thin Film Solar Cells-Insight from Theory and Experiment. *ACS Applied Materials & Interfaces*, 2021.

[161] P. K. Paul, D. W. Cardwell, C. M. Jackson, K. Galiano, K. Aryal, J. P. Pelz, S. Marsillac, S. A. Ringel, T. J. Grassman, and A. R. Arehart. Direct nm-Scale Spatial Mapping of Traps in CIGS. *IEEE Journal of Photovoltaics*, 5(5):1482–1486, 2015.

[162] A. Urbaniak, K. Macielak, N. Barreau, P. Szaniawski, and M. Edoff. Signatures of extended defects in Cu(In,Ga)Se2 observed using capacitance spectroscopy techniques. *Journal of Physics and Chemistry of Solids*, 134:58–63, 2019.

[163] Sung Heo, JaeGwan Chung, Hyung-Ik Lee, Junho Lee, Jong-Bong Park, Eunae Cho, Kihong Kim, Seong Heon Kim, Gyeong Su Park, Dongho Lee, Jaehan Lee, Junggyu Nam, JungYup Yang, Dongwha Lee, Hoon Young Cho, Hee Jae Kang, Pyung-Ho Choi, and Byoung-Deog Choi. Defect visualization of Cu(InGa)(SeS)2 thin films using DLTS measurement. *Scientific Reports*, 6(1):30554, 2016.

[164] Ana Kanevce, Stefan Paetel, Dimitrios Hariskos, and Theresa Magorian Friedlmeier. Impact of RbF-PDT on Cu(In,Ga)Se 2 solar cells with CdS and Zn(O,S) buffer layers. *EPJ Photovoltaics*, 11:8, 2020.

[165] Maximilian Krause, José A. Márquez, Sergej Levcenco, Thomas Unold, Olivier Donzel-Gargand, Marika Edoff, and Daniel Abou-Ras. Microscopic insight into the impact of the KF post–deposition treatment on optoelectronic properties of (Ag,Cu)(In,Ga)Se 2 solar cells. *Progress in Photovoltaics: Research and Applications*, 30(1):109–115, 2022.

[166] Jan Keller, Hisham Aboulfadl, Lars Stolt, Olivier Donzel-Gargand, and Marika Edoff. Rubidium Fluoride Absorber Treatment for Wide–Gap (Ag,Cu)(In,Ga)Se 2 Solar Cells. *Solar RRL*, page 2200044, 2022.

[167] Natalia M. Martin, Tobias Törndahl, Erik Wallin, Konstantin A. Simonov, Håkan Rensmo, and Charlotte Platzer-Björkman. Surface/Interface Effects by Alkali Postdeposition Treatments of (Ag,Cu)(In,Ga)Se2 Thin Film Solar Cells. *ACS Applied Energy Materials*, 5(1):461–468, 2022.

[168] Ryan Kaczynski, JinWoo Lee, Jane van Alsburg, Yejiao Wang, and Baosheng Sang. Inline Rubidium Fluoride Treatment of (A)CIGS Absorbers Deposited onto Flexible Substrates in a Production-Scale Process Tool. In *2019 IEEE 46th Photovolt. Spec. Conf.*, pages 1420–1423. IEEE, 2019.

[169] Tomás S. Lopes, Jessica de Wild, Célia Rocha, André Violas, José M. V. Cunha, Jennifer P. Teixeira, Marco A. Curado, António J. N. Oliveira, Jérôme Borme, Gizem Birant, Guy Brammertz, Paulo A. Fernandes, Bart Vermang, and Pedro M. P. Salomé. On the Importance of Joint Mitigation Strategies for Front, Bulk, and Rear Recombination in Ultrathin Cu(In,Ga)Se2 Solar Cells. *ACS Applied Materials & Interfaces*, 13(23):27713–27725, 2021.

[170] Michał Ćwil, Małgorzata Igalson, Paweł Zabierowski, Chrystian A. Kaufmann, and Axel Neisser. Capacitance profiling in the CIGS solar cells. *Thin Solid Films*, 515(15):6229–6232, 2007.

[171] A. Urbaniak, M. Igalson, F. Pianezzi, S. Bücheler, A. Chirilă, P. Reinhard, and A. N. Tiwari. Effects of Na incorporation on electrical properties of Cu(In,Ga)Se2-based photovoltaic devices on polyimide substrates. *Solar Energy Materials and Solar Cells*, 128:52–56, 2014.

[172] G. P. Li and K. L. Wang. A novel technique for studying electric field effect of carrier emission from a deep level center. *Applied Physics Letters*, 42(9):838–840, 1983.

[173] O. S. Elsherif, K. D. Vernon-Parry, J. H. Evans-Freeman, and P. W. May. Effect of doping on electronic states in B-doped polycrystalline CVD diamond films. *Semiconductor Science and Technology*, 27(6):065019, 2012.

[174] Tran Thien Duc, Galia Pozina, Erik Janzén, and Carl Hemmingsson. Investigation of deep levels in bulk GaN material grown by halide vapor phase epitaxy. *Journal of Applied Physics*, 114(15):153702, 2013.

[175] Tadeusz Wosiński. Evidence for the electron traps at dislocations in GaAs crystals. *Journal of Applied Physics*, 65(4):1566–1570, 1989.

[176] Shogo Ishizuka, Noboru Taguchi, Jiro Nishinaga, Yukiko Kamikawa, Shingo Tanaka, and Hajime Shibata. Group III Elemental Composition Dependence of RbF Postdeposition Treatment Effects on Cu(In,Ga)Se 2 Thin Films and Solar Cells. *The Journal of Physical Chemistry C*, 122(7):3809–3817, 2018.

[177] D. A. G. Bruggeman. Berechnung verschiedener physikalischer Konstanten von heterogenen Substanzen. I. Dielektrizitätskonstanten und Leitfähigkeiten der Mischkörper aus isotropen Substanzen. *Annalen der Physik*, 416(7):636–664, 1935.